Summer 2019

Synthesis and applications of ceramic (silicon carbide and silicon nitride), metallic (cobalt(0)) and polymeric (polyurethane) aerogels

Parwani M. Rewatkar

Department: Chemistry

Recommended Citation

Rewatkar, Parwani M., "Synthesis and applications of ceramic (silicon carbide and silicon nitride), metallic (cobalt(0)) and polymeric (polyurethane) aerogels" (2019). *Doctoral Dissertations*. 2811.
https://scholarsmine.mst.edu/doctoral_dissertations/2811

SYNTHESIS AND APPLICATIONS OF CERAMIC (SILICON CARBIDE AND SILICON NITRIDE), METALLIC (COBALT(0)) AND POLYMERIC (POLYURETHANE) AEROGELS

by

PARWANI M. REWATKAR

A DISSERTATION

Presented to the Faculty of the Graduate School of the

MISSOURI UNIVERSITY OF SCIENCE AND TECHNOLOGY

In Partial Fulfillment of the Requirements for the Degree

DOCTOR OF PHILOSOPHY

in

CHEMISTRY

2019

Approved by:

Dr. Chariklia Sotiriou-Leventis, Advisor
Dr. Manashi Nath
Dr. Jeffrey G. Winiarz
Dr. Amitava Choudhury
Dr. Ali Rownaghi

TO

MY PARENTS

PUBLICATION DISSERTATION OPTION

This dissertation consists of the following three manuscripts that have been published, accepted or submitted for publication:

Paper I, pages 20–74, was published in *Chemistry of Materials*.

Paper II, pages 75–109, has been accepted in *ACS Applied Materials and Interfaces*.

Paper III, pages 110–161, has been submitted to the *ACS Applied Materials and Interfaces*.

ABSTRACT

A new method has been demonstrated for the synthesis of monolithic ceramic and purely metallic aerogels from xerogel powder compacts, and the use of polyurethane aerogels based on cyclodextrins as efficient desiccants.

I. Highly porous (>80%) monolithic SiC and Si_3N_4, aerogels were prepared from compressed compacts of polyurea-crosslinked silica xerogel powders. The process is time efficient as solvent-exchange through powders is fast, and energy efficient as it bypasses drying with supercritical fluids. The final ceramic objects were chemically pure, sturdy, with compressive moduli at 37 ± 7 MPa and 59 ± 7 MPa, and thermal conductivities at $0.16_3 \pm 0.010$ W m^{-1} K^{-1} and 0.070 ± 0.001 W m^{-1} K^{-1}, for SiC and Si_3N_4, respectively.

II. Monolithic metallic Co(0) aerogels, synthesized from polyurea-crosslinked cobaltia xerogel powder compacts, were porous (69% v/v) and extremely sturdy (compressive modulus at 688 ± 10 MPa). They were infiltrated with molten $LiClO_4$, and were ignited with a hot NiCr wire. The temperature during combustion reached 1515 ^{o}C. The heat released (-55.17 ± 2.01 kcal mol^{-1}) was near the theoretical value for the reaction:

$4\ Co + LiClO_4$ ----> $4\ CoO + LiCl$ (-58.5 kcal mol^{-1}).

III. Polyurethane (PU) aerogels are low-density hierarchical nano-structured solids with high open nanoporosity, and high surface areas. Using α- and β-cyclodextrin (CD) as polyols, an aromatic triisocyanate and dibutyltin dilaurate (DBTDL) as a catalyst we obtained hyperbranched CD-based polyurethane aerogels (α- and β-CDPU-xx). Those materials show high water uptake capacities (108% w/w with α-CDPU-2.5) and can be reused multiple times by regeneration at room temperature by changing the relative humidity of the environment.

ACKNOWLEDGEMENTS

I ought to profoundly thank my advisor Dr. Chariklia Sotiriou-Leventis, and my mentor Dr. Nicholas Leventis, who are wonderful sources of ideas and insights. Dr. Sotiriou-Leventis’ caring nature has made her more than just an advisor. Dr. Leventis’ positive attitude towards research is something I am going to carry with me for lifetime. They have played a major role in sculpting ‘the improved me’. Pursuing Ph.D. under them was one of the best decisions I happened to make, and I have realized it at various stages throughout my somewhat difficult yet wonderful journey of doctorate.

I would also like to thank my committee members Dr. Manashi Nath, Dr. Amitava Choudhury, Dr. Jeffrey G. Winiarz, and Dr. Ali Rownaghi for their valuable suggestions.

I would like to thank Mr. Shannon D. Roark and Ms. Tina M. Balch, our departmental secretaries, and Mr. Jonathon Sidwell, senior research specialist, for all their help and nice behavior. I also thank Mr. David Satterfield and Dr. Nathan Leigh for providing training on various instruments.

My parents and grandparents have been a great source of support and positive energy. They believed on my abilities more than me, which has enabled me to visualize the success. My brother has always stood by me and played a vital role in keeping me calm and tension-free throughout my journey. I would also like to thank my fiancé, whose recent entry has made the final stages of this journey even more beautiful, joyful, and simple.

I would like to extend a thank you note to all my colleagues: Dr. Adnan Malik Saeed (special thanks), Dr. Hojat Majedi Far, Dr. Suraj Donthula, Dr. Tahereh Taghvaee, Dr. Chandana Mandal, Rushi Soni, Shaheen ud Doulah, and Vaibhav Edlabadkar and Dr. Saidulu Gorla for their valuable discussions, assistance in the lab, and friendship.

TABLE OF CONTENTS

Page

SECTION

PAPER

SECTION

LIST OF ILLUSTRATIONS

Figure Page

SECTION

PAPER I

PAPER II

PAPER III

LIST OF SCHEMES

LIST OF TABLES

Table Page

PAPER I

PAPER III

LIST OF ABBREVIATIONS

Abbreviation	**Description**
SCF	supercritical fluid
RF	resorcinol-formaldehyde aerogel
PBO	polybenzoxazine aerogel
PAN	polyacrylonitrile
PUA	polyurea
PU	polyurethane
p-DCPD	polydicyclopentadiene
PMMA	polymethyl methacrylate
NCO	isocyanate group
TIPM	triisocyanate (tris(4-isocyanatophenyl) methane)
APTES	3-aminopropyltriethoxysilane
TMOS	tetramethylorthosilicate
α-CD	alpha-cyclodextrin
β-CD	beta-cyclodextrin
CDPU	cyclodextrin-based polyurethane

DBTDL	dibutyltin dilaurate
X-aerogel	cross-linked aerogel
TDI	toluene diisocyanate
DABCO	1,4-diazabicyclo[2.2.2]octane
DMAB	dimethylamine borane
CoOx	cobaltia
TGA	thermogravimetric analysis
SEM	scanning electron microscopy
XRD	X-ray diffraction
SAXS	small angle x-ray scattering
XPS	X-ray photoelectron spectroscopy
FTIR	fourier transformed infrared spectroscopy
DSC	differential scanning calorimetry
MDSC	modulated differential scanning calorimetry
CP MASS ^{13}C NMR	cross-polarization magic angle spinning ^{13}C-NMR
CP TOSS ^{13}C NMR	cross-polarization total suppression of spinning sidebands ^{13}C-NMR
UV-Vis	ultraviolet-visible spectroscopy
TEM	transmission electron microscopy

TMS	tetramethylsilane
BET	Brunauer–Emmett–Teller method in the analysis of surface area from N_2-sorption porosimetry
DFT	density functional theory in the analysis of micropore size distribution
DR	Dubinin-Radushkevich method in the analysis of micropore volume
Q_{st}	isosteric heat of adsorption
Q_{o}	Q_{st} at near zero gas uptake

1. INTRODUCTION

1.1. AEROGELS

Aerogels are a unique material that possess extremely low density (about 1000 times less dense than glass), high porosity (contain up to 99% v/v air),[1-6] high surface area (>500 m^2 g^{-1}), extremely high pore volume (>2 cm^3 g^{-1}),[7] low thermal conductivity, low sound velocity and high optical transparency. The set of those unique properties makes aerogels viable for numerous applications such as solar plate collectors,[8-9] Cherenkov counters,[10] battery separators,[11] materials for life jackets,[12] additives to drilling fluids,[13] catalysts, and catalyst supports,[14-15] energy materials,[16-18] ceramics[19-21] etc.

The question at this point is how do you make those unique materials? Aerogels are made via a sol-gel process,[22] which involves the mixing of appropriate precursors in a suitable solvent, usually in the presence of a catalyst. That mixture of solutions is called a 'sol', which solidifies or gels to give a wet-gel. A wet-gel is a nanostructured porous solid-network that forms in a liquid reaction medium by a polymerization process and thus a wet-gel contains solvent in its pores. The wet-gel is then aged for certain amount of time (ageing) and then dried to remove the solvent from pores. Drying of solvent by a simple evaporation method creates a liquid-vapor meniscus at the exit of the gel pores exerting the pressure on the pore walls due to surface tension of the liquid. That leads to an extensive shrinkage of the wet-gel (up to 30% of its initial volume[23]) and a dried solid network with collapsed pores, referred to as *xerogel*. The term *xerogel* is defined by IUPAC as an "open network formed by the removal of all swelling agents from a gel",[24] and was first introduced by Freundlich to designate shrinking (or swelling) gels.[25] So, to retain the "dry solid skeleton" of the initial wet material (wet-gel), there is a special drying technique, known as a supercritical fluid drying which allows to replace the liquid in the pores with a gas and thus minimizes the shrinkage. This drying technique was first applied by Kistler who introduced the term *aerogel* in 1932. According to Kistler, aerogels can be described as "gels in which the liquid has been replaced by air, with very moderate shrinkage of the solid network."[26] He worked with silica aerogels extensively. These inorganic aerogels were first prepared by Ebelmen in 1846, by exposure to the atmosphere of a silane obtained from $SiCl_4$ and ethanol.[27] Since then, silica aerogels have been the most studied type of inorganic materials and numerous literature can be found about their chemistry, properties and applications.[28] Figure 1.1 summarizes the formation of a wet-gel via a sol-gel method, and drying of a wet-gel by two different methods to yield either an aerogel or a xerogel, specifying the key properties of those two materials. The pictures shows a typical silica aerogel and a xerogel. The latter is obtained from ambient pressure drying.

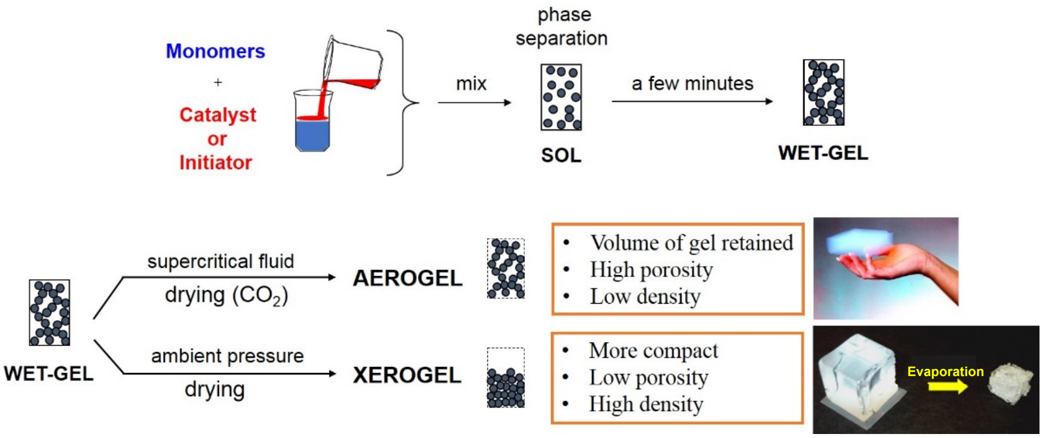

Figure 1.1. The schematic representation of preparation of a*erogel* versus *xerogel* by sol-gel method.

Over the years, tremendous amount of research has been carried out on several other kinds of non-silica inorganic aerogels such as rare earth metal oxide,[29] and chalcogenide aerogels.[30] A number of organic aerogels have also been introduced such as resorcinol formaldehyde (RF),[31] polybenzoxazine (PBO),[32] polydicyclopentadiene (p-DCPD),[33] and poly methyl methacrylate (PMMA) aerogels.[34] Recently, new types of aerogels have been added to the library of known aerogels. Carbon nanotubes,[35] graphene,[36] and silicon carbide[37] aerogels are few of those.

To summarize, aerogels are chemically identical to the bulk form of the skeletal material but posses many dramatically enhanced materials properties over the dense (non-porous) form of the same substance (e.g., substantially increased surface area and low thermal conductivity). The low densities of aerogels are due to their nanostructures that consist of 3D assemblies of nanoparticles. However, along with the low density and high porosity of aerogels, lies an issue of fragility and poor mechanical properties. The problem of fragility has been addressed before by Leventis et. al. group by introducing *Polymer-crosslinked Aerogels*.[38] Moreover, the use of supercritical drying makes the overall process costly, particularly at a commercial level. Making *Aerogels from Xerogels* by bypassing the supercritical drying offers a solution, which has been demonstrated here with ceramic and pure metallic aerogels.

1.1.1. Polymer-crosslinked Aerogels. Silica aerogels consist of a pearl-necklace-like skeletal framework and the interparticle neck of such structures is the weakest point, leading to the fragility of those aerogels. During ageing of those wet-gels, Ostwald ripening takes place, which is a dissolution and reprecipitation of silica at surfaces with negative curvature i.e. at the interparticle neck.[39] Clearly, longer ageing time can lead to relatively stronger silica aerogels. However, that increase in strength is obtained at the expense of the skeletal nanoparticles' density. A new approach to reduce the fragility of those aerogels is compounding the skeleton with an organic polymer by crosslinking the surface functional groups of silica with an isocyanate.[40] This forms a coating of polymer on the entire skeletal framework and reinforces the interparticle necks without compromising much the density. The resulting materials have been referred to as *X-aerogels*. The mechanical strength of X-aerogels was reported to be increased by 300 times for a nominal increase in density by only a factor of 3.[40] A variety of different chemistries, other than using isocyanate, can be carried out to crosslink the skeletal particles with polymers e.g., epoxy resins,[41] polystyrene,[40c] poly methyl methacrylate,[40d] polyacrylonitrile.[34]

An added advantage of thos cross-linked polymers is that they can act as sources of carbon to perform carbothermal reduction provided that the polymer contains enough carbonizable carbon. One such example of carbonizable polymer is tris(4-isocyanatophenyl)methane (TIPM) derived polyurea, which has 56% w/w carbonization yield.[42] To incorporate that polymer coating on silica nanoparticles, the surface of silica is modified by an amine functionality by cogelation of (3-aminopropyl)triethoxysilane (APTES) with tetramethyl orthosilicate (TMOS).[43] Those dangling -NH_2 groups have been then utilized to react with a triisocyanate (TIPM) to form a coating of polyurea on silica network.[40a,b] Scheme 1.1 shows the synthesis of polymer-crosslinked silica aerogels (*X-silic*a or *X-TMOS-co-APTES*) in a step-wise manner.

Not only amino groups but also adsorbed water can react with TIPM leading to increased amount of carbonizable carbon, which can be optimized as per stoichiometric requirement. In a similar fashion, metal-oxide aerogels can also be coated with polyurea, which can be converted to pure metallic aerogels, mimicking the age-old smelting process.[44]

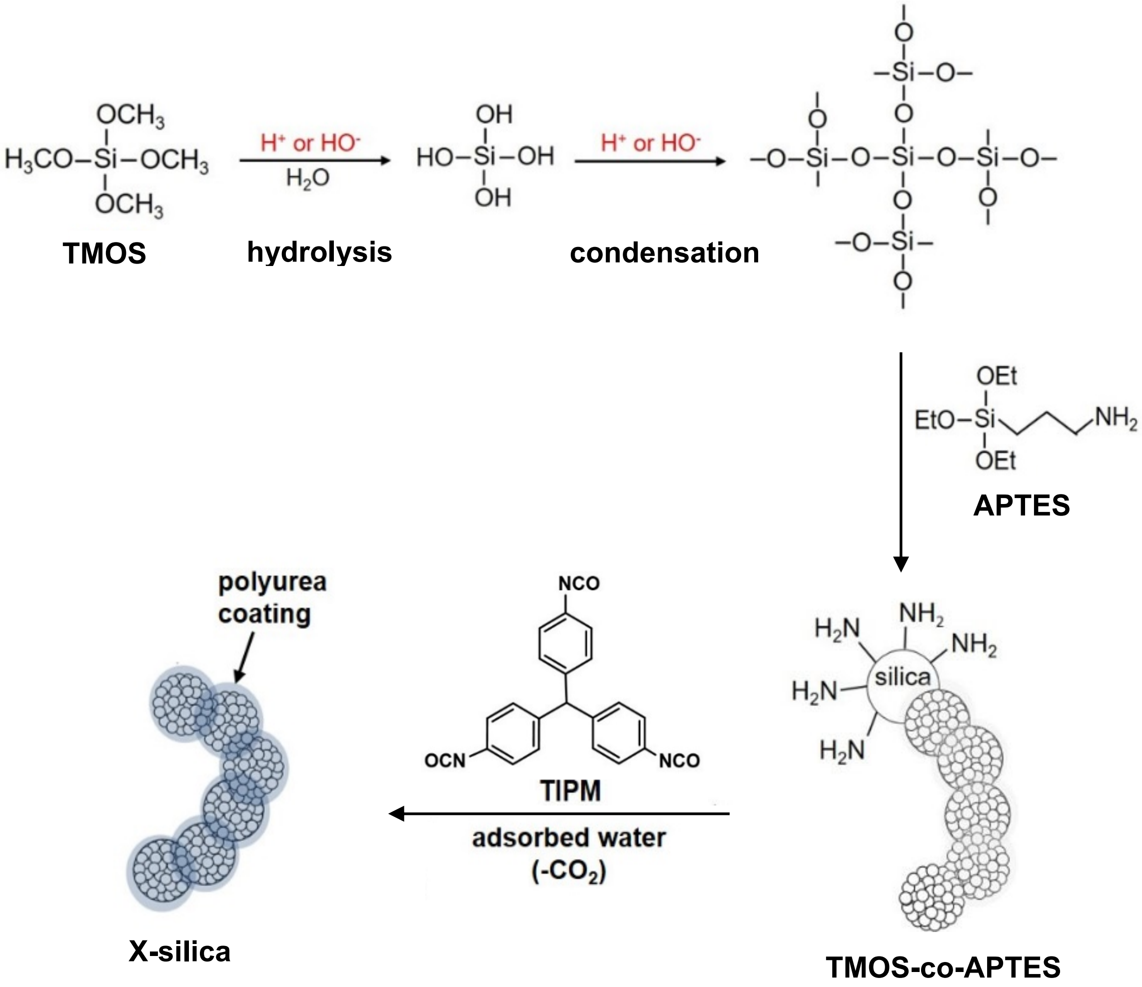

Scheme 1.1. Synthesis of polymer-crosslinked silica aerogels (*X-silica*).

1.1.2. Aerogels from Xerogels. As discussed earlier, many aerogels exhibit fragility issue and are produced by methods that require a costly, time consuming supercritical fluid (SCF) extraction step. Those shortcomings have hampered commercialization. One solution could be the synthesis of aerogels from xerogels. The proposed method has been utilized to fabricate SiC, Si_3N_4 and Co(0) aerogels and has the potential of extending to other ceramic or metallic aerogels.

That method uses polymer-crosslinked *xerogel powder* compacts as the ceramic precursors, rather than monolithic polymer-crosslinked aerogels. It takes into consideration the topology of the carbothermal reactions, and for porosity it relies on the void space created by carbon reacting away during pyrolysis. That allows making aerogels from xerogels. Moreover, the compact structure provided by xerogels plays a vital role in an efficient utilization of the material. That can be explained by considering the topology of the reaction between SiO_2 and C (Scheme 1.2). The mechanism of formation of SiC and Si_3N_4 starts with the common preliminary reaction of SiO_2 with C at the interface of C-on-SiO_2 particle producing SiO and CO gases. The generated in-situ CO diffuses through another particle of C-on-SiO_2 and eventually reacts with SiO_2 as in Scheme 1.2. If the CO gas encounters the pores in an aerogel precursor, however it will escape and thus the resulting ceramic aerogel would end up with unreacted silica in it. However, the compactness of the xerogel assembly forces the CO gas always through C-on-SiO_2 interface. Figure 1.2 shows the topology of the reaction between SiO_2 and C, release of CO gas, and efficient utilization of CO gas in a compact assembly. Moreover, realizing the importance of the close proximity between particles, the xerogel can be used in the form of powders, compression of which allows more room for compactness and introduces an added advantage of casting shaped compacts of any size by simply pressing the precursor xerogel powder in a suitable die, thus liberating synthesis of ceramic aerogels from the size of the autoclave. The use of *xerogel powders* clearly indicates the most efficient utilization of the carbonizable polymer. Indeed, as discussed in paper I, it was sufficient to work with

C:SiO_2 ratios near the stoichiometric level to make pure SiC or Si_3N_4, while in the acrylonitrile-crosslinked silica aerogels methodology reported in the literature, that ratio had to be at least 2.5 times higher than the stoichiometric requirement.[45]

$$\mathbf{SiO_2(s) + C(s) \longrightarrow SiO(g) + CO(g) \qquad (1)}$$

$$\mathbf{SiO_2(s) + CO(g) \longrightarrow SiO(g) + CO_2(g) \qquad (2)}$$

Scheme 1.2. Common preliminary steps in the formation of SiC or Si_3N_4.

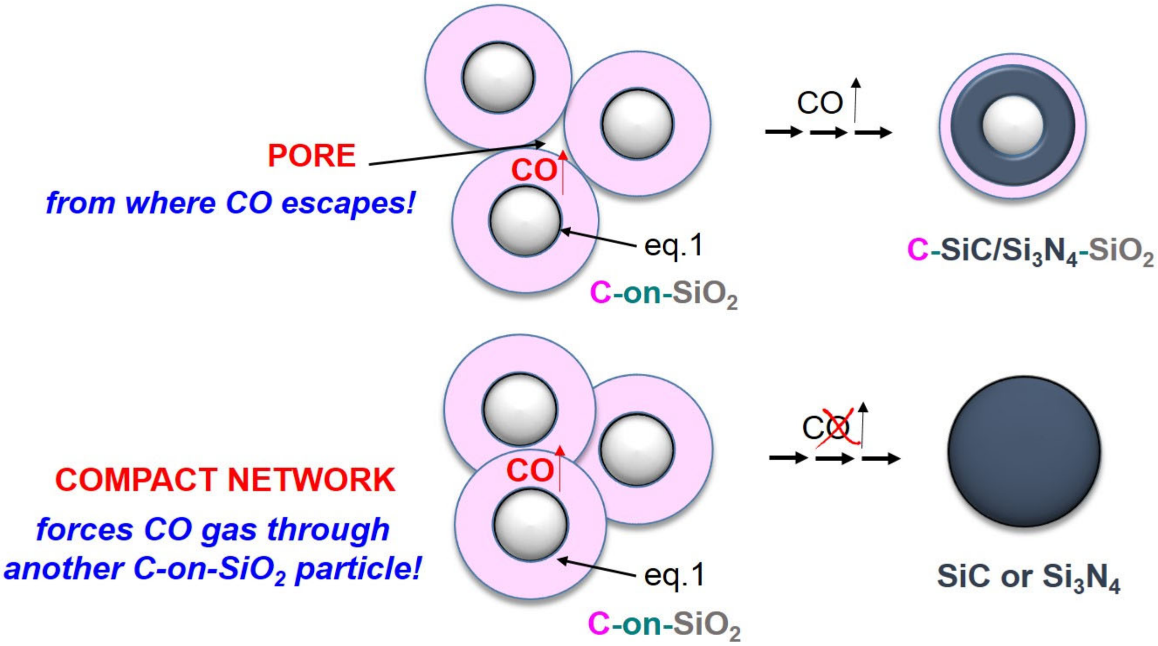

Figure 1.2. Topology of formation of SiC or Si_3N_4.

In summary, the *aerogel from xerogel powder* methodology has certain distinct advantages:

(a) Energy efficient: using xerogel bypasses supercritical fluid drying.

(b) Time efficient: using powders allow faster solvent exchange within grains of powder.

(c) Material efficient: almost stoichiometric utilization of the carbon due to the xerogel compactness.

(d) Generalizable: gelation of any system can be diverted to powders by vigorous agitation.

The proposed synthetic design can be extended to other refractory materials such as ZrC, HfC, ZrB_2, HfB_2 and several other metals such as Fe, Ni, Co, Cu, etc. Specifically for a system like Co, which resists or takes relatively longer time (about 10 days) to form gel, the proposed xerogel powder route is advantageous. In that regard, porous purely metallic Co(0) aerogel has been synthesized and is demonstrated as a thermite by filling the pores of Co(0) aerogel with perchlorate salt (Paper II).

1.2. ISOCYANATE CHEMISTRY

The isocyanate group (-N=C=O) is a highly reactive electrophile due to the electron withdrawing ability of oxygen and nitrogen atoms attached to the carbon atom (Scheme 1.3) That creates electron deficiency on this carbon atom making it available for a nucleophilic attack (Scheme 1.4). Thus, the isocyanate group can reac with numerous compounds such as amines, alcohols, carboxylic acids, water, etc. The reactivity of the NCO depends on the type of groups attached on the nitrogen i.e. electron withdrawing or electron donating groups. In that regard, the aromatic isocyanates are more reactive than aliphatic isocyanates.[46]

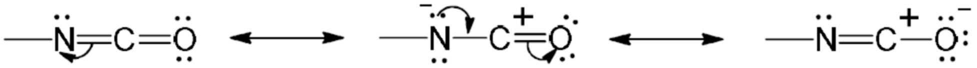

Scheme 1.3. Possible resonance structures of the isocyanate group.

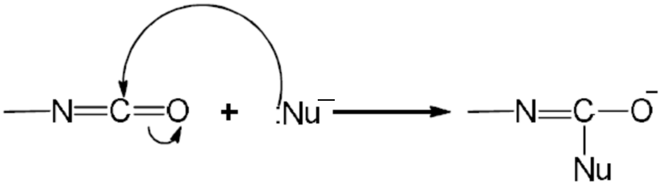

Scheme 1.4. Nucleophilic attack on the isocyanate group.

The rich chemistry of NCO group makes it an important precursor for the synthesis of many organic aerogels. Also, the isocyanate group can be used as a crosslinker for inorganic aerogels as discussed previously (Section 1.1.1). In this thesis, an aromatic triisocyanate (TIPM) has been used to crosslink silica and cobalt oxide to form polyurea coating on their skeletal networks, which are used to synthesize ceramic (Paper I) and purely metallic aerogels (Paper II), respectively. TIPM has also been used to form a hierarchical polyurethane aerogel by reacting the isocyanate with polyols: α- and β-cyclodextrins (Paper III).

1.2.1. Reaction of Isocyanate with Amine. The nucleophilic nitrogen of an amino group attacks the carbonyl carbon of NCO to form urea as shown below. This reaction is exothermic and occurs extremely fast. Scheme 1.5 represents the reaction of isocyanate with amine yielding urea.

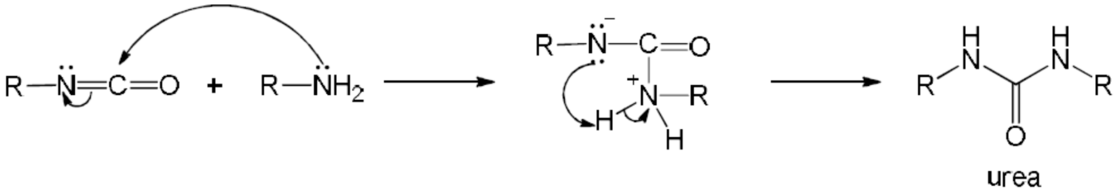

Scheme 1.5. Reaction of isocyanate with amines to form urea.

1.2.2. Reaction of Isocyanate with Water. The reaction of water with NCO proceeds via formation of unstable carbamic acid, which decomposes to amine and carbon dioxide. The amine generated *in-situ* then reacts with the unreacted isocyanate to form urea. The reaction is generally catalyzed by a small amount of amine such as triethylamine (Et_3N). Scheme 1.6 represents the reaction of isocyanate with water yielding urea.

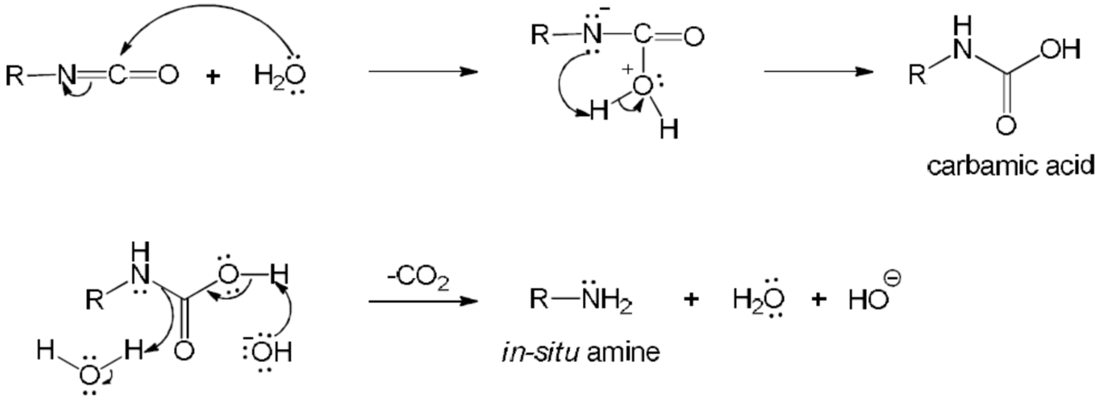

Scheme 1.6. Reaction of isocyanate with water to form urea.

1.2.3. Reaction of Isocyanate with Alcohol. The reaction of alcohol with isocyanate is most commonly catalyzed by a tin-based catalyst dibutyltin dilaurate (DBTDL) to form urethane. Scheme 1.7 represents the reaction of isocyanate with an alcohol yielding urethane.

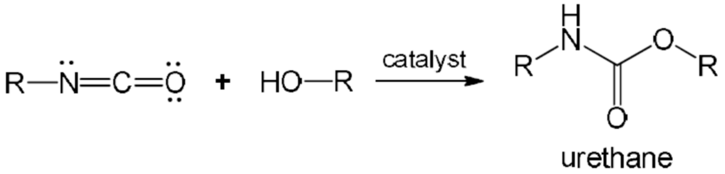

Scheme 1.7. Reaction of isocyanate with alcohol to form urethane.

The third paper of this dissertation is based on hierarchical polyurethanes and thus they are discussed briefly below.

1.3. POLYURETHANES

Polyurethanes (PUs) were discovered by Bayer and his coworkers in 1947. They reacted diisocyanates with polyester diols.[47] Polyurethanes were used during World War II as coatings for aircraft[48] but their use was limited. Early work on PUs was focused on fibers and flexible foams. With the commercialization of polyisocyanates in 1952, production of flexible polyurethane foam began in 1954 using toluene diisocyanate (TDI) and polyester polyols. Those materials were used to produce rigid foams, gum rubber and elastomers. Since then, this research on polyurethanes has grown very fast as various polyisocyanates and polyols became available, which allowed the synthesize of numerous kinds of polyurethanes for specialized applications.

The properties of polyurethanes can be altered by using various combinations of alcohols and isocyanates with different catalysts. Long, flexible segments, of polyols, give soft, elastic polymers. High amounts of crosslinking give tough or rigid polymers, while long chains and low crosslinking give polymers that are very flexible. Due to the crosslinking present, PUs consist of three-dimensional networks of high molecular weights.

Polyurethanes are being used in medical devices, construction, adhesives, coatings, textiles, plastics, etc.[49] Polyurethane foams in particular are useful in thermal insulation.[50] Because aerogels are also highly desirable for thermal insulation, polyurethane aerogels are a natural choice of interest.

1.3.1. Polyurethane Aerogels. The first cellulosic aerogels have been synthesized by Kistler in the 1930s with nitrocellulose[51] while the first isocyanate and polyurethane-based aerogels were reported in the 1990s by Tabor[52] and by Biesman, Perrut and their co-workers.[53]

In 2001, Tan et. al.[54] reported cellulose aerogels crosslinked with toluene diisocyanate (TDI) with an impact strength ten times higher than that of resorcinol-formaldehyde (RF) aerogels. Many such contributions were made in the area of polyurethane aerogels. In 2013, Leventis et. al. synthesized polyurethane aerogels from multifunctional small-molecules yet inexpensive monomers, allowing control of the onset of the phase separation, which is translated into control of the particle size, morphology, pore structure and ultimately the mechanical properties. Molecular parameters of interest included the molecular rigidity vs. flexibility of the isocyanate.[55]

Other than studying the polyurethanes for thermal insulating properties and basic study of structure-property relationships, polyurethane aerogels are being synthesized for targeted applications. Recently, in 2018, Leventis et. al. synthesized shape memory polyurethanes.[56]

It has been very clear that the rigidity and multifunctionality of polyol and polyisocyanate play an important role in fabricating the material properties of polyurethane aerogels. In that regard, the idea was to utilize the polyol functionality of cyclodextrin molecules with a triisocyanate (TIPM) to yield a hierarchical polyurethane structure. The porous structure and surface area that will be provided by such structure was aimed to be utilized to capture either gases or organic molecules or simply water, depending upon the pore sizes.

1.3.2. Cyclodextrin-based Polyurethanes. Cyclodextrins (CD) are readily available cyclic compounds consisting of six to eight glucose units with well-known host-guest chemistry.[57] Incorporation of cyclodextrins in polymers renders them water-insoluble, and those materials have found applications in extraction of organic pollutants from air and water.[58]

The first cyclodextrin-polyurethane (CDPU) resins were reported in 1980 by reacting cyclodextrins with three different diisocyanates (hexamethylene diisocyanate, 1,3-bis(isocyanatomethyl)cyclohexane, 1,3-bis(isocyanatomethyl)benzene. Their interaction with various organic compounds were studied with gas-solid chromatography. Those resins were able to distinguish between xylene isomers and pyridine derivatives.[59] In 1996, K. Sreenivasan reported the synthesis of hydrophilic biodegradable polyurethanes by chain extention of a prepolymer formed between a polyethylene glycol, hexamethylene diisocyanate and β-CD, and demonstrated dye absorption from aqueous media.[60] Many subsequent studies were focused on the synthesis of CD-based polymers made by reacting CD with various monomers such as different aliphatic and aromatic diisocyanates and epichlorohydrin. Those polymeric materials were used in the removal of direct azo dyes and aromatic amines from aqueous solutions, patulin extraction, and differential adsorption of many organic compounds such as benzaldehyde, aniline, nitrophenol isomers, etc.[61-63] Recently, R. Mirzajani et. al. demonstrated an application of β-CD-based polyurethane, synthesized via reaction of β-CD and hexamethylene diisocyanate in DMF, in adsorption and determination of Pb(II) ions in dust and water samples.[64]

In the third part of this dissertation, α- and β-CD molecules are utilized together with a triisocyanate (TIPM) in the presence of dibutyltin dilaurate (DBTDL) as a catalyst. The resulting hyperbranched CD-based polyurethanes are referred to as α- and β-CDPU-xx**.** The discussion is focused on the synthesis and characterization (chemical and physical) of α- and β-CDPU-xx 3D structures, and the study of their desiccant behavior.

1.4. SCOPE OF THE PRESENT WORK

Since 1930s tremendous amount of research, improvement and actual implementation has occurred in the field of aerogels due to the need for novel functional materials for betterment of life. Aerogels are being commercially used in various fields. To mention few, silica aerogels are used as Cerenkov radiation detectors, in aboard spacecrafts as collectors for cosmic particles (NSASA's Stardust program), Cabot aerogels by Cabot Corporation for architecture daylighting, building insulation, specialty chemicals and coatings, etc., insulating aerogels (inside Toasty Feet) by Aspen, *Aerocore* (an organic aerogel for vacuum insulation) by American Aerogel Corporation. And that list can continue even further. The unique combination of properties makes aerogels useful in numerous fields despite the fragility and cost issues and therefore, there has been a continuous demand for improvisation, as well as for new research. Here, we have made an attempt to propose a cost effective method for synthesizing **ceramic aerogels** (SiC and

Si_3N_4) with potential applications as high-temperature thermal insulators, as catalyst supports for high-temperature gas-phase reactions, to make composites, etc. The proposed method has also been demonstrated for fabricating **metallic aerogels** (Co(0) aerogels), which can be used as monolithic thermites. Also, cyclodextrin-based polyurethane aerogels are developed as efficient **desiccants** that can be regenerated with minimal energy requirement.

1.4.1. Ceramic Aerogels. Thermal insulation under extreme conditions, such as rapid temperature changes and long-term high-temperature exposure in aerospace and thermal power fields, requires exceptional stability.[65] Ceramic aerogels are attractive candidates for thermal insulation under such harsh conditions due to their low density, low thermal conductivity, and excellent fire and corrosion resistance.[66] Ample porous ceramics have been discussed in the literature starting from pure ultrahigh-temperature ceramic (UHTC)[67] such as ZrB_2, HfB_2, to several ceramic composites.[68] Silicon-based porous ceramic materials derived from organosilicon polymers are well known for their low bulk density, large surface area, and excellent thermal and mechanical stability. They have attracted attention in many applications, including high-temperature resistance, catalyst supports, Li-ion batteries, and gas sensors.[69] Sorarù and co-workers prepared highly porous polymer-derived SiOC and SiCN ceramic aerogels with Li-ion storage ability[70] and electrochemistry properties.[71] This research inspired many similar efforts for fabricating novel aerogels.[72–75]

Silicon carbide and silicon nitride are the most studied Si-based ceramics. Monolithic porous SiC was first prepared by Acheson Process by carbothermal reduction of silica with carbon in 1891.[76] Similarly, the synthesis of silicon nitride powders by reaction between silica, carbon and nitrogen has been well known since a German patent was granted in 1896 to Mehner.[77] Since then porous forms of those ceramics have been synthesized in various forms such as fibers, whiskers, powders using various techniques, including oxidation bonding method, combustion synthesis, chemical vapor reaction, sol-gel method and carbothermal reduction reaction, preceramic foam processing, and coatmix method.[78] Considering sol-gel method and the required costly and time consuming supercritical drying method, few attempts have been made previously to synthesize those ceramic aerogels via freeze-drying or from xerogels. For example, Zheng et al. demonstrated the synthesis of mesoporous SiC via the carbothermal reduction reaction of saccharose-containing silicon xerogel at 1450 °C.[79] Novel porous Si_3N_4-SiO_2 composites were obtained by sol-gel and freeze-drying processes using Si_3N_4-SiO_2, Al_2O_3 and MgO as raw materials.[80] In most of those processes, however, the final ceramics are in powder or composite form. In the first paper of this thesis, we report a method by which monolithic ceramic aerogels of various shapes and sizes can be made via a cost effective, time efficient and materials efficient method, which can also be extended to other systems whose surface can be functionalized with hydroxy or amino groups.

1.4.2. Metallic Aerogels. Burpo et. al. synthesized noble metal (Au, Pd, Pt) aerogels via a direct solution-based method. Reduction of noble metal salts was carried out using dimethyl amine borane (DMAB) and sodium borohydride, which takes place very fast (within few minutes) resulting into gels when carried out above a critical concentration. Those were then freeze-dried to aerogels having high surface area, capacitance and conductivity, which is useful in catalytic, energy storage and sensor applications.[81] Noble metal aerogels have also been previously prepared by a sol-gel method either through a single step gelation process or by gelation of noble metal nanoparticles produced by reduction of the corresponding salt solutions.[82] As an alternative to those precious metals, several other metallic aerogels have been synthesized and demonstrated in energy conversion, biomedicine, batteries and catalysis.[83] Leventis et. al. reported an efficient synthesis of metal aerogels through carbothermal reduction of polymer coated metal oxide aerogels.[32] In this work, co-gelation of iron oxide networks with resorcinol formaldehyde (RF) networks was carried out. Pyrolysis of the interpenetrating networks of RF-iron oxide under inert atmosphere resulted in porous iron monoliths. Those iron aerogels were demonstrated as thermites.[84]

In the second paper of this thesis, cobalt aerogels are synthesized from xerogel powders as discussed in previous section (Section 1.1.2 Aerogels from Xerogel). The cobalt system was specifically chosen since it resists or takes very long time to form gel and thus a powder route is beneficial for such system. The final Co aerogels were about 70% (v/v) porous. Those pores were filled with lithium perchlorate ($LiClO_4$) and ignited with the help of a nichrome wire. The temperature of the thermite reaction reached above 1500 °C.

1.4.3. Desiccants. Desiccant materials are hygroscopic solids that induce or sustain a state of dryness in the surrounding air.[85] Generally, desiccants can be categorized in two types based on the factors responsible for water uptake:

(1) Chemical reaction

e.g., $P_4O_{10} + 6\ H_2O \text{ ----> } 4\ H_3PO_4$

$MgSO_4 + 7\ H_2O \text{ ----> } MgSO_4.7H_2O$

(2) Adsorption

e.g., silica gels, molecular sieves, clays

The materials of the second category are generally porous materials. In order to be considered as good desiccants, those materials need to be hydrophilic and highly adsorbent. Hydrophilicity can be introduced by the presence of functional groups that attract water, while adsorption capacity depends on physical properties such as surface area, porosity, and pore volumes. For example, some relatively hydrophobic carbon-based materials show high water sorption capacity due to their high porosity, but the speed of adsorption is low because of inappropriate surface chemistry that lacks the affinity for water.[86] Silica gel, on the other hand, is the most commonly known desiccant since the XVII century.[87] It's fairly good desiccant behavior is the result of the presence of hydrophilic hydroxyl groups on its surface and its porous properties.

Desiccants have a wide range of applications e.g., controlling the level of water in industrial gas streams, in air conditioning systems, in food packaging, storing and shipping purposes, or as energy-saving alternatives to heat drying.[88] Due to the demanding applications of desiccants, ample amount of research has been carried out to investigate the moisture adsorption capacities by various kinds of materials including carbons,[89] polymers,[90] clays,[91] zeolites,[92] etc. Along with the high water adsorption capacity by desiccants, it becomes very important to consider the regeneration aspect of those since it can save a lot of energy and money. The most commonly known desiccants: zeolites and silica gel are known to adsorb up to 0.45 g of water per g of material. Zeolites require heating above 200°C for regeneration,[92d,93] while silica gels or nanoporous carbons can be regenerated by heating to about 120 °C.[93] However, it will be better if a desiccant can be designed that can adsorb above 0.5 g of water per g of material and most importantly can be dried and reused by heating up to 40 – 50 ˚C or just by lowering the relative humidity of the environment. In order to accomplish this, the cyclodextrin-based polyurethane (CDPU) aerogels with heterogeneous hydrophilic sites, high surface areas and suitable pore structures were synthesized and tested as desiccants (Paper III).

The best desiccant of this study adsorbs about 1 g per g of material and is shown to be regenerated by simply lowering the humidity of the environment. Figure 1.3 shows a comparison of the materials of this study with the commonly known commercial desiccants.

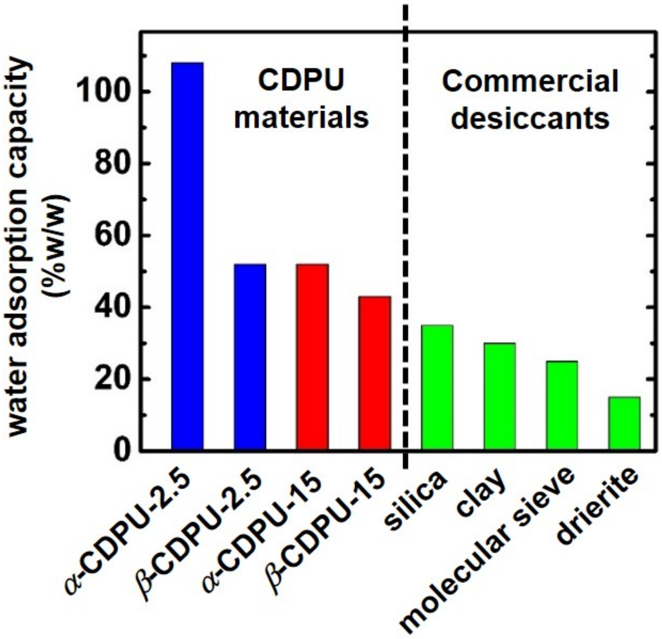

Figure 1.3. Comparison of moisture adsorption capacities of CDPU aerogels with commercial desiccants.

PAPER

I. STURDY, MONOLITHIC SiC AND Si_3N_4 AEROGELS FROM COMPRESSED POLYMER-CROSSLINKED SILICA XEROGEL POWDERS

Parwani M. Rewatkar, Tahereh Taghvaee, Adnan Malik Saeed, Suraj Donthula, Chandana Mandal, Naveen Chandrasekaran, Theodora Leventis,[#] T. K. Shruthi,[†] Chariklia Sotiriou-Leventis[*] and Nicholas Leventis[*]

Department of Chemistry, Missouri University of Science and Technology, Rolla, MO 65409, U.S.A. [#]Summer student via the ARO High School Student Apprenticeship Program. [†]S. N. Bose Scholar. [*]Correspondence: Tel.: 573-341-4391 (NL) 573-341-4353 (CSL). E-mail: leventis@mst.edu, cslevent@mst.edu

ABSTRACT

We report the carbothermal synthesis of sturdy, highly porous (>85%) SiC and Si_3N_4 monolithic aerogels from compressed compacts of polyurea-crosslinked silica *xerogel* powders. The high porosity in those articles did not pre-exist pyrolysis, but was created via reaction of core silica nanoparticles with their carbonized polymer coating toward the new ceramic framework and CO that escaped. Sol-gel silica powder was obtained by disrupting gelation of a silica sol with vigorous agitation. The grains of the powder were about 50 μm in size, irregular in shape, and consisted of 3D assemblies of silica nanoparticles as in any typical silica gel. The individual elementary silica nanoparticles within the grains of the powder were coated conformally with a nano-thin

layer of carbonizable polyurea derived from the reaction of an aromatic triisocyanate (TIPM: triisocyanatophenyl methane) with the innate –OH, deliberately added $–NH_2$ groups, and adsorbed water on the surface of silica nanoparticles. The wet-gel powder was dried at ambient temperature under vacuum. The resulting free-flowing silica/polyurea xerogel powder was vibration-settled in suitable dies and was compressed to convenient shapes (discs, cylinders, donut-like objects), which in turn were converted to same-shape SiC or Si_3N_4 artifacts by pyrolysis at 1500 °C under Ar or N_2, respectively. The overall synthesis was time-, energy- and materials-efficient: (a) solvent exchanges within grains of powder took seconds, (b) drying did not require high-pressure vessels and supercritical fluids, and (c) due to the xerogel compactness, the utilization of the carbonizable polymer was at almost the stoichiometric ratio. Chemical and materials characterization of all intermediates and final products included solid-state ^{13}C and ^{29}Si NMR, XRD, SEM, N_2-sorption and Hg intrusion porosimetry. Analysis for residual carbon was carried out with TGA. The final ceramic objects were chemically pure, sturdy, with compressive moduli at 37±7 and 59±7 MPa for SiC and Si_3N_4, respectively, and thermal conductivities (using the laser flash method) at 0.16_3±0.010 and 0.070±0.001 W m^{-1} K^{-1}, respectively. The synthetic methodology of this report can be extended to other sol-gel derived oxide networks and is not limited to ceramic aerogels. Work-in-progress includes metallic Fe(0) aerogels.

TOC Graphic

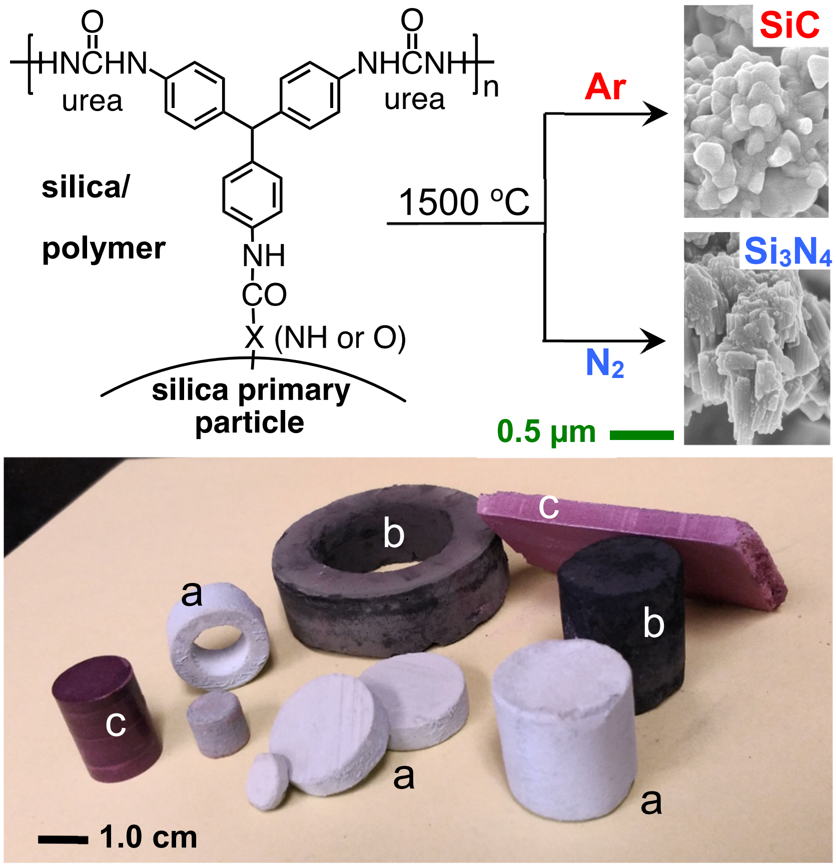

(a) SiC (b) Si_3N_4 (c) silica/polymer compact

Large SiC and Si_3N_4 aerogel monoliths with porosities over 85% were prepared carbothermally at 1500 °C under Ar or N_2 respectively, from compressed-to-shape silica xerogel powders coated conformally with a carbonizable polyurea. Use of xerogel precursors disengages synthesis of ceramic aerogels from expensive and time-consuming drying with supercritical fluids.

1. INTRODUCTION

Aerogels are solid objects derived from wet-gels by converting their pore-filling solvent into a supercritical fluid that is vented off like a gas.[1] In principle, that process preserves the volume of the original wet-gel into the final dry object, thereby aerogels are highly porous, low-density materials.[2,3] Conversely, simple evaporation of the pore-filling solvent causes extensive shrinkage; those materials are referred to as xerogels and consist of the same elementary building blocks as aerogels, however due to shrinkage-induced compaction, xerogels have lower porosities and higher densities than aerogels.[4]

Silica is the most common type of aerogels, but a wide array of other inorganic and polymeric aerogels are known, including organic/inorganic interpenetrating networks,[5] and polymer-crosslinked oxide aerogel composites.[6,7,8,9] In the latter variety, the skeletal inorganic-oxide framework is coated conformally with a nano-thin layer of polymer, and those materials have been investigated extensively for their mechanical strength.[10] Eventually, the term 'aerogel' has been broadened and includes "secondary" materials best represented by carbon aerogels,[1] which are obtained from pyrolysis of several sol-gel derived polymeric aerogels.[11] The present study describes such secondary SiC and Si_3N_4 aerogels derived from xerogels rather than aerogels. The conceptual point of departure of this approach is traced to organic/inorganic interpenetrating networks.[5]

Organic/inorganic interpenetrating networks include oxide aerogels (e.g., of Cr, Fe, Co, Ni, Cu, Ti, Hf, Sn) whose skeletal framework is intertwined with a second network of a carbonizable phenolic-resin aerogel (e.g., resorcinol-formaldehyde, or polybenzoxazine).[5,12,13] Mimicking the age-old smelting process,[14] those materials undergo carbothermal reduction, and have been a source for several metallic (Fe, Co, Ni, Cu) and ceramic (TiC, Cr_3C_4, HfC) aerogels.[13,15] Importantly, along those studies it was observed that chemically identical interpenetrating xerogels undergo carbothermal reduction at up to 400 °C lower temperatures than the corresponding aerogels, pointing to the fact that reactions, even amongst nanostructured reagents, can still benefit from a more intimate contact like the one that is found in a more compact structure – i.e., that of a xerogel versus that of an aerogel. Along these lines, the ultimate proximity between an inorganic oxide framework and a carbonizable polymer will be found in nanostructured oxide networks coated conformally with the latter.

A generalizable synthetic protocol that implements that line of reasoning is illustrated here by the carbothermal synthesis of SiC and Si_3N_4 aerogels as large shaped-objects using Eqs 1[16,17] and 2,[18,19,20] respectively. The substrate converted to those two

$$SiO_2 + 3\ C \longrightarrow SiC + 2\ CO \tag{1}$$

$$3\ SiO_2 + 2\ N_2 + 6\ C \longrightarrow Si_3N_4 + 6\ CO \tag{2}$$

ceramics was sol-gel silica coated conformally and cross-linked covalently with carbonizable polyurea from reaction of: (a) innate –OH, and deliberately added $–NH_2$ groups on silica, and (b) adsorbed water, with triisocyanatophenyl methane (TIPM), an available-in-bulk triisocyanate. The crosslinking process is shown in Scheme 1.

Monolithic SiC aerogels have been described before from silica aerogels crosslinked via free-radical surface-initiated polymerization (FR-SIP) of acrylonitrile.[21] Apart from the inherent synthetic complexity involved with FR-SIP, a main drawback of that approach was also that for porosity it relied on the innate, pre-pyrolysis porosity of the monolithic, crosslinked silica aerogel network. In addition, the topology of the reactants in that arrangement led to mechanically weak materials, and to low utilization of polyacrylonitrile-derived carbon. In contrast, the TIPM-based methodology that is described in this report was fast, energy and materials efficient and can be extended to the preparation of other large monolithic ceramic and/or metallic aerogels. For high-speed, we moved away from the idea of using cross-linked monolithic silica aerogels as the ceramic precursors, adopting instead the concept of pyrolysis of dry compressed crosslinked silica *xerogel* powders. Those powders have the same nanoparticulate structure as typical monolithic aerogels, but, owing to the short diffusion path in the powder grains, they can be solvent-exchanged and processed from one step to the next within seconds rather than hours – or days. Second, the TIPM-derived polyurea coating acts as a binder for the underlying silica particles, so that dry, crosslinked silica powders can be compressed into large, sturdy compacts with any desirable shape, which effectively removes the autoclave-size limitation from the accessible size of the resulting aerogel articles. And as importantly, taking isomorphic carbothermal synthesis[22-26] one step further, it was realized that for porosity, polymer crosslinked *xerogel* powders would rely not on the porosity of the pre-

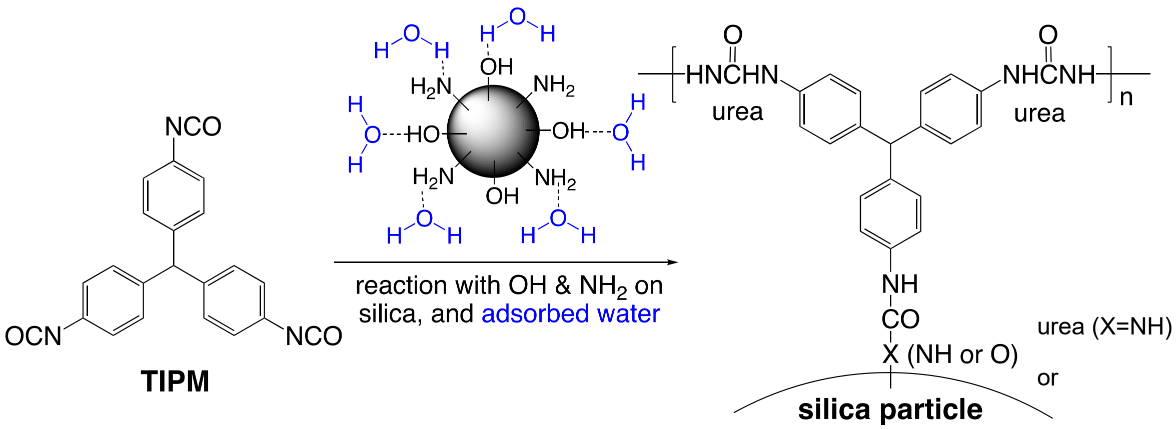

Scheme 1. Cross-linking of skeletal silica nanoparticles (native or –NH_2 modified) with a triisocyanate (TIPM)[6]

carbothermal object, but rather on the fact that in the course of the carbothermal reduction the carbonizable polymer coating would react away (to the ceramic and CO – see Eq.s 1 and 2) creating *new* porosity that did not exist before. That synthetic design has certain distinct advantages over all prior ceramic aerogel work: First, use of xerogel precursors bypasses supercritical drying, and thus improves energy efficiency. Second, a more subtle feature of working with compressed cross-linked xerogel powders, rather than aerogel monoliths, is that in principle none (or very little) of the reducing agent, CO, which is generated in situ during the course of the reaction, would be carried away: no matter which way from the SiO_2/C interface CO wants to move, the compactness of the assembly forces it always through silica, resulting in the most efficient utilization of the carbonizable polymer. As it turned out, it was just sufficient to work with C:SiO_2 ratios near the stoichiometric level, while in acrylonitrile-crosslinked silica aerogels that ratio had to be at least 2.5 times higher than the stoichiometric. Eventually, pyrolysis of compressed shaped compacts under Ar or N_2 yielded same-shape, highly porous (>85%) monolithic SiC or Si_3N_4. Those porous ceramic objects were mechanically robust, chemically inert at high temperatures, and good thermal insulators. In more general terms, SiC and Si_3N_4 are hard ceramics useful as abrasives, in cutting tools, and in biomedicine as bone replacement materials. Porous SiC and Si_3N_4 are used industrially as catalyst supports, or as filters for molten metals, and are prepared by annealing powders under compression. Oftentimes, porosities up to 30% are considered high. Apart from the immediate relevance of the two model materials of this study to all those industrial applications, the generalizable methodology that is described herewith brings other porous ceramic and metallic aerogels within its reach.

2. RESULTS

2.1. FABRICATION OF SHAPED SiC AND Si_3N_4 POROUS OBJECTS

In order to facilitate latching of polyurea onto the surface of silica, the long-standing strategy has been to provide silica with amines.[27,28] Based on the higher reactivity of (a) terta- versus tri-alkoxysilanes,[3] and of (b) methoxy versus the ethoxysilanes,[29] it has been suggested that co-gelation of tetramethoxysilane (TMOS) with 3-aminopropyl triethoxysilane (APTES), leads to a TMOS-derived 3D network of silica nanoparticles, which are surface-modified later with slower-reacting APTES (Scheme 2).[6] Overall, it is noted that hydrolysis and polycondensation of TMOS is catalyzed by the high concentration of base (APTES),[6] and such TMOS/APTES sols gelled *in seconds*.[27] For comparison, such one-pot, one-step TMOS/APTES gel networks have been reproduced here in monolithic aerogel form, and are referred to as TMOS-co-APTES.

Being extremely fast, co-gelation of TMOS and APTES does not leave much room for manipulation, and the course of the reaction could not be diverted away from monolithic gels into micron-sized particles (powders). To that end, a viable approach was to deconvolute gelation of TMOS from incorporation of APTES operationally (Scheme 2). Thus, referring to Scheme 3, materials preparation started with conventional NH_4OH-catalyzed hydrolysis and polycondensation of TMOS.[30] That reaction is typically carried out by mixing two solutions: Solution A (TMOS in methanol) and Solution B (water+catalyst in methanol).[30] Given the monomer and catalyst concentrations of Solutions A and B (see Experimental), the undisturbed combined solution yields monolithic gels in about 20 min. Here, gelation was disrupted by adding Solutions A and B in hexane under vigorous mechanical stirring. APTES, in a APTES:TMOS mol/mol ratio of 0.2, was added to the reaction mixture as soon as it turned milky-white (in approximately 20 min, as expected). The suspension was aged for 24 h under continuous vigorous stirring to ensure that latching of APTES on the surface of the silica particles was complete. The resulting new wet-silica suspension, and materials from that point on are referred to as APTES@TMOS. That abbreviation is intended to trace the material to its monomers, and to underline the synthetic sequence of events. As it turns out (refer to section 2.2), APTES@TMOS and TMOS-co-APTES were chemically indistinguishable as emphasized in Scheme 2. The APTES@TMOS suspension was separated from the gelation solvents using centrifugation, and the resulting wet APTES@TMOS paste was washed successively (i.e., re-suspended and centrifuged) with ethyl acetate (EtOAc, 2×), water-saturated EtOAc (1×), and once with acetone. Those conditions were the result of an optimization study (refer to Appendix I in Supporting Information) that related acetone washes to the amount of carbonizable polymer uptaken during the crosslinking step. In that regard, the combination of one wash with water-saturated EtOAc and one wash with acetone provided silica with a reproducible amount of adsorbed water for the reaction with the required amount of TIPM. For characterization purposes, some of the APTES@TMOS slurry from the last acetone wash was washed again with pentane and was dried at room temperature under vacuum. The rest of the APTES@TMOS slurry was crosslinked at 65 ºC for 72 h in Desmodur RE (a commercial solution of TIPM in dry EtOAc, courtesy of Covestro, LLC). The resulting polymer-crosslinked wet-silica suspension was washed with acetone and then with pentane. Excess pentane was removed with a centrifuge, and the wet, crosslinked silica paste was dried under vacuum at ambient temperature to a free-flowing fine powder that is referred to as X-APTES@TMOS. Dry X-APTES@TMOS powder was placed in suitable dies and was compressed under 15,000 psi into sturdy monolithic compacts. To test the latitude of this technology, large donut-shaped objects (Scheme 3) were fabricated with a die made to spec by a commercial machine shop. Finally, X-APTES@TMOS shaped compacts were converted to SiC and Si_3N_4 monoliths via pyrolysis at 1500 ºC for 36 h under flowing Ar or N_2, respectively. Those conditions were identified using solid-state ^{29}Si NMR analysis of a series of X-APTES@TMOS compacts that were pyrolyzed according to a pre-determined matrix of temperatures and pyrolysis times (see Appendix II in Supporting Information). Residual unreacted carbon in the SiC or the Si_3N_4 objects was oxidized off with air at elevated temperatures as shown in Scheme 3.

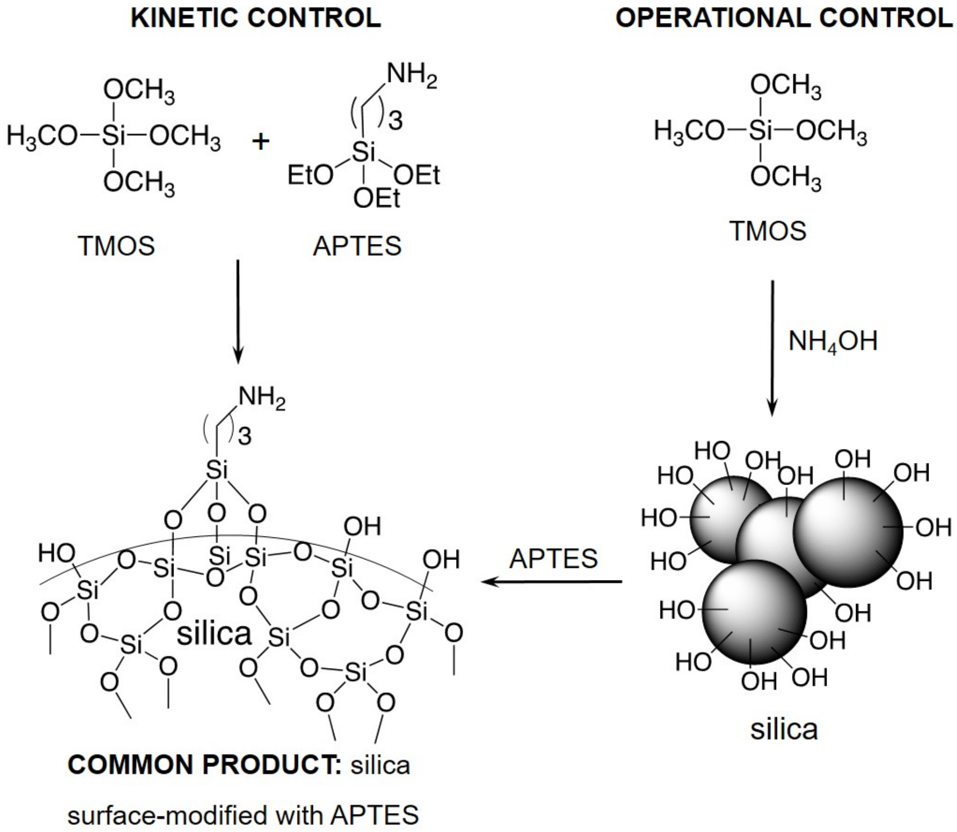

Scheme 2. Two routes to a common product: silica-gels surface-modified with APTES. (Powders can be prepared only via operational control.)

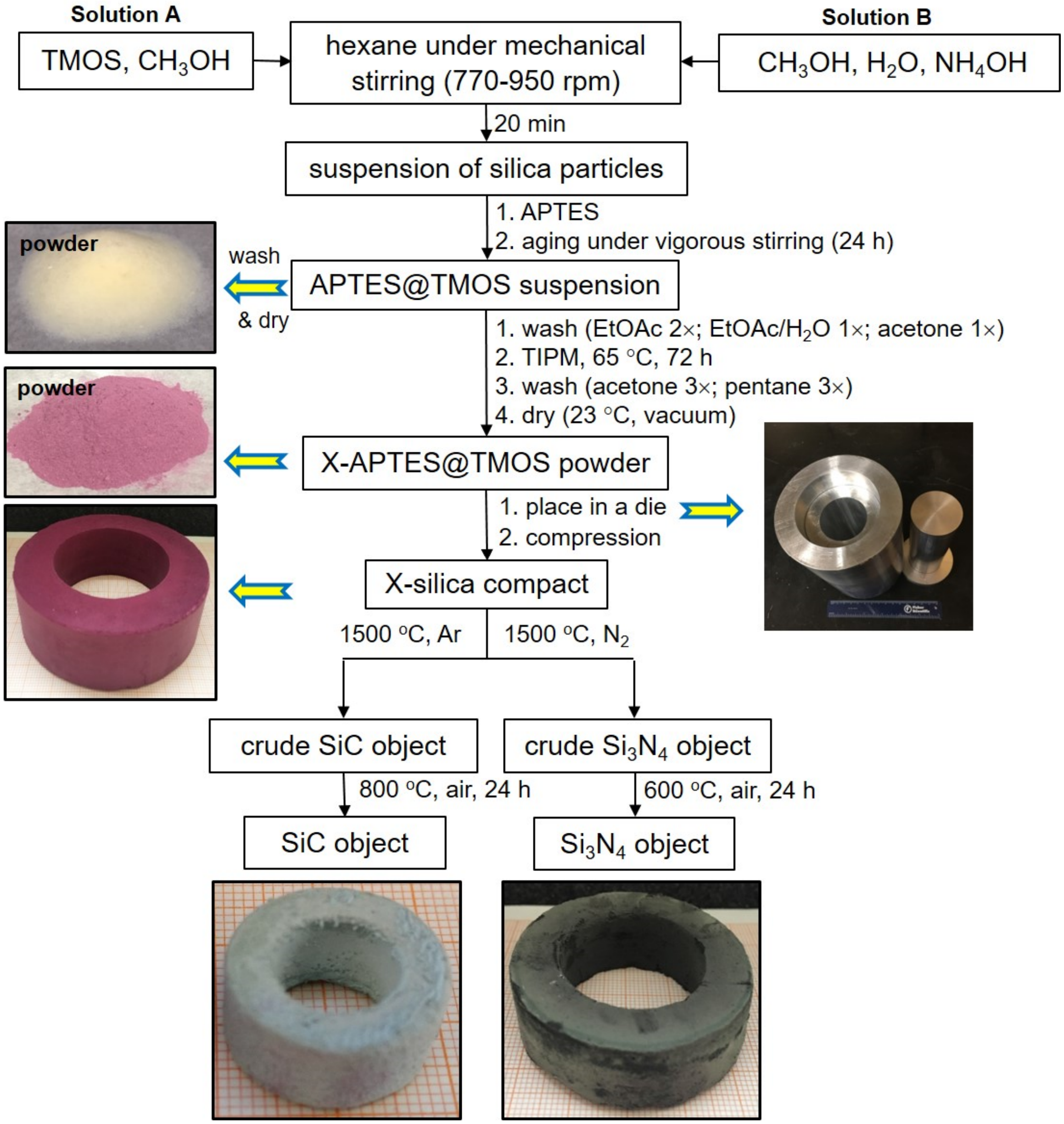

Scheme 3. Fabrication of highly porous SiC and Si_3N_4 shaped objects

2.2. CHEMICAL CHARACTERIZATION ALONG SYNTHESIS

Latching of APTES on TMOS-derived silica particles was confirmed with solid-state CPMAS ^{29}Si NMR. The spectrum of APTES@TMOS (Figure 1) shows two features:

(a) a peak at -66 ppm with a shoulder at –59 ppm, which were assigned to the T3 and T2 silica atoms from APTES, and (b) two peaks at –110 ppm and at –101 ppm with a shoulder at -92 ppm, which were assigned respectively to the Q4, Q3 and Q2 silicon atoms from TMOS. The presence of Q3 and T2 silicon atoms points to dangling Si-OH groups, thereby APTES@TMOS offers two kinds of possible sites for reaction with the isocyanate: $-NH_2$ and -OH. Figure 1 also includes the ^{29}Si NMR spectrum of a TMOS-co-APTES aerogel prepared with the same APTES:TMOS mol ratio (0.2) as APTES@TMOS. The two spectra were in all aspects identical, including both the integrated Q:T ratio of 1.635±0.015, as well as the T3:T2 and the Q4:Q3:Q2 ratios, leading to the conclusion that: (a) preventing gelation by vigorous agitation; and, (b) separating operationally (experimentally) the incorporation of APTES from gelation of TMOS did not have any adverse effects on the product, which was chemically indistinguishable from well-known TMOS-co-APTES.

Uptake of TIPM-derived polyurea in X-APTES@TMOS was confirmed with solid-state CPMAS ^{13}C NMR. The intimate connection of the polymer to the silica framework was investigated with ^{29}Si NMR. The amount of polyurea was quantified with thermogravimetric analysis (TGA).

The CPMAS ^{13}C NMR spectrum of native APTES@TMOS powder (Figure 2) shows three upfield peaks of about equal intensity at 42, 25, and 9.5 ppm, which were assigned to the three carbons of APTES. The spectrum of TIPM-crosslinked X-APTES@TMOS powder (Figure 2) was dominated by the resonances of TIPM-derived polyurea. (A spectrum of the latter[31] is included in Figure 2 for comparison.) Owing to massive polymer uptake, the relative intensity of the $–\underline{C}H_2–$ groups of APTES in X-APTES@TMOS was suppressed. Next, turning to the solid-state CPMAS ^{29}Si NMR spectrum of X-APTES@TMOS powder (Figure 1), it is noted that the Q4:Q3 ratio changed in favor of Q3 relative to the spectrum of APTES@TMOS: Indeed, in native APTES@TMOS powder the Q4:Q3 area ratio (after deconvolution and Gaussian fitting) was 1.11, in X-APTES@TMOS that ratio was found equal to 0.69. Similarly, the T3:T2 ratio was also reduced from 2.33 before, to 1.33 after crosslinking, i.e., in favor of T2. Those data mean that the triisocyanate (TIPM) gets attached to the surface of silica not only via the $–NH_2$ groups that were provided deliberately for that purpose, but also via any other reactive group that it could find available, like for example –SiOH at the Q3 and T2 positions, and here is the justification: since all relevant ^{29}Si NMR spectra of Figure 1 were run using cross-polarization (CP), after crosslinking Q3 and T2 positions found themselves closer to an abundance of protons, from TIPM, hence their intensity increased relative to Q4 and T3, respectively. To cross-check this proposition, we also run the spectra of APTES@TMOS and of X-APTES@TMOS using direct polarization (Appendix III in Supporting Information), and we observed that the intensity ratios of Q4:Q3 and T3:T2 stayed the same before and after crosslinking, as expected. Considering both sets of ^{29}Si NMR data together (i.e., with direct and with cross-polarization), we concluded that: (a) neither the crosslinking process, nor the accumulated polymer had any adverse effect on the silica backbone, and thereby (b) the intensity increase of Q3 and T2 in CPMAS, could only be attributed to polymer uptake at both the innate –OH and the deliberately added $–NH_2$ positions on silica. The next task was to quantify the amount of TIPM-derived polyurea in X-APTES@TMOS powders.

Using thermogravimetric analysis under O_2 (TGA, Figure 3), the APTES@TMOS powder lost 24.5% of its mass, which was attributed to its organic component. Thereby, it was concluded that APTES@TMOS consisted of 75.5% of SiO_2. Under the same conditions X-APTES@TMOS lost 65.4% of its mass. That mass loss corresponded to the sum of the organic component coming from APTES plus TIPM-derived polyurea. From those data, it was calculated that X-APTES@TMOS consisted of 34.6% w/w SiO_2 and 54.2% w/w of TIPM-derived polyurea. Considering the carbonization yield of the latter (56% w/w, by pyrolysis at 800 °C/Ar),[32] it was calculated that the C:SiO_2 mol/mol ratio that was expected to enter carbothermal reactions towards SiC or Si_3N_4 was equal to 4.4. Considering that the C:SiO_2 mol ratio for converting SiO_2 to SiC is equal to 3 (see Eq 1),[16,17] and for converting to Si_3N_4 is equal to 2 (refer to Eq 2),[18-20] it was concluded that the expected C:SiO_2 mol ratio of 4.4 from X-APTES@TMOS would be sufficient for the complete conversion of SiO_2 to either ceramic.

Consistently with the stoichiometry of Eqs 1 and 2 and the expected C:SiO_2 mol ratio of 4.4, the crude products from pyrolysis at 1500 °C in Ar (SiC) or N_2 (Si_3N_4) contained vastly different amounts of carbon. As-prepared SiC articles contained only 0.29 ± 0.07 % carbon, while those of Si_3N_4 contained 49 ± 1 % carbon (in both cases, those values were averages of 3 independent experiments – i.e., from different batches). Clearly, some carbon was wasted in the process, but its utilization in the xerogel compacts was much more efficient than in aerogels: for instance, for complete conversion of polyacrylonitrile-crosslinked silica aerogels to SiC, the C:SiO_2 ratio *had to* be ≥ 7.[21]

After removing carbon (Scheme 3), the solid-state ^{29}Si NMR spectra of the terminal SiC objects showed only one peak at -20 ppm (Figure 4). The broadness of that resonance was attributed to three overlapping resonances from α-SiC (at -14, -20 and -25 ppm) and one resonance from β-SiC (at -18 ppm).[33] (The spectra of commercial α-SiC and β-SiC are included in Figure 4 for comparison.) Similarly, the ^{29}Si NMR spectra of the Si_3N_4 objects showed a resonance at -48 ppm and a low-intensity peak at -112 ppm. Based on literature values,[33,34] as well as the spectra of commercial Si_3N_4 and silica sand (both included in Figure 4), the former peak was assigned to Si_3N_4, and the latter one to Q4 type of silicon in SiO_2. Based on the relative integrated intensity of the peaks corresponding to Si_3N_4 and SiO_2 (19:1), and the silica:Si_3N_4 response factor (6.82:1.00) at the given acquisition parameters (see Experimental and Appendix II in Supporting Information), it was calculated that the SiO_2 impurity in the Si_3N_4 objects was 0.33% w/w. (It is noted that SiO_2 was also present as an impurity in our commercial Si_3N_4 source at a level of 1.16% w/w – see Figure 4).

XRD (Figure 5) confirmed the presence of both the α- and β- phases of SiC and Si_3N_4 in the respective ceramic objects. No peaks corresponding to remaining crystalline silica were present. Quantitative phase analysis for SiC was difficult owing to overlapping, or partially overlapping reflections from the α- and β- phases. From analysis of the pattern generated from the (101) and (102) reflections of α-SiC, and the (111) reflection of β-SiC, an approximate composition of 68% of α-SiC and 32% of β-SiC was obtained. On the other hand, Si_3N_4 consisted of 78% of α-Si_3N_4 and 22% of β-Si_3N_4. The proximity/overlap of the (102)/(111), (110)/(220), and (116)/(311) reflections of α-SiC / β-SiC caused additional peak broadening, thereby the average crystallite size calculated via the Scherrer equation[35] from those three reflections (11.9 ± 2.8 nm) is considered as the lowest limit. On the other hand, the average crystallite size of α-Si_3N_4 was calculated at 46.9 nm (from the (101) reflection at $2\theta=20.4^{o}$), and the crystallite size of β-Si_3N_4 was calculated at 52.5 nm (from the (101) reflection at $2\theta=33.5^{o}$).

Table 1. Materials characterization data along processing

Sample I.D.	Linear shrinkage (%) [a]	Bulk density, ρ_b (g cm^{-3})	Skeletal density, ρ_s (g cm^{-3}) [d]	Porosity, Π (% v/v) [e]	Specific pore volume (cm^3 g^{-1})			BET surface area, σ (m^2 g^{-1})	Average pore diameter Φ, (nm) [i]
					V_{Total} [f]	$V_{1.7\text{-}300\_\text{nm}}$ [g]	$V_{>300\text{ nm}}$ [h]		
TMOS-co-APTES monolith	14.30 ± 0.02 [b]	0.190 ± 0.007 [a]	1.79 ± 0.02	89	4.52	2.50	2.02	554	32.6
X-TMOS-co-APTES monolith	$13.1_8 \pm 0.19$ [b]	0.56 ± 0.04 [a]	1.670 ± 0.002	62	1.19	1.26	0	374	12.7
APTES@TMOS powder	-	0.35	1.770 ± 0.001	80	2.29	1.32	0.97	294	31.2
X-APTES@TMOS powder	-	0.81	1.470 ± 0.005	45	0.55	0.15	0.40	113	19.5
X-APTES@TMOS compact	-	1.04 ± 0.01 [a]	1.470 ± 0.001	29	0.28	0.09	0.19	119	9.4
Crude SiC object	$18.6_9 \pm 0.88$ [c]	0.390 ± 0.003 [a]	3.04 ± 0.05	88	2.23	0.02	2.21	5.8	1538
SiC object	$20.8_0 \pm 0.93$ [c]	0.410 ± 0.002 [a]	3.19 ± 0.09	88	2.12	0.02	2.10	3.2	2642 [6226]
Crude Si_3N_4 object	$18.8_4 \pm 0.85$ [c]	$0.6_9 \pm 0.18$ [a]	2.67 ± 0.02	74	1.07	0.69	0.38	152	28.1
Si_3N_4 object	$21.3_8 \pm 0.88$ [c]	0.35 ± 0.02 [a]	2.98 ± 0.01	85	2.52	0.02	2.50	4.7	2158 [8027]

[a] Average of 3 samples. [b] Shrinkage = 100 × (mold diameter – sample diameter)/(mold diameter). [c] Shrinkage relative to the X-APTES@TMOS compact. [d] Single sample, average of 50 measurements. [e] Porosity, $\Pi = 100\times(\rho_s - \rho_b)/\rho_s$. [f] V_{Total} was calculated via $V_{\text{Total}} = (1/\rho_b) - (1/\rho_s)$. [g] $V_{1.7\text{-}300\text{ nm}}$ from N_2- sorption data via the BJH desorption method. [h] $V_{>300\text{ nm}} = V_{\text{Total}} - V_{1.7\text{-}300\text{ nm}}$. [i] For single number entries, or the first of two number entries: average pore diameters were calculated via the $4V/\sigma$ method by setting $V = V_{\text{Total}} = (1/\rho_b) - (1/\rho_s)$; numbers in [brackets] are weighted averages calculated from the pore size distribution curves obtained using Hg-intrusion porosimetry.

2.3. MATERIALS CHARACTERIZATION

That focused on: (a) the evolution of the micromorphology and the pore structure along the operations of Scheme 3, and (b) application-related properties such as oxidation resistance at high temperatures, thermal conductivity and mechanical strength.

2.3.1. Structural Evolution along Processing. The evolution of the micromorphology along processing is illustrated in Figures 6 and 7. Relevant material characterization data are summarized in Table 1. For setting a reference point relative to previous literature both Figure 6 and Table 1 include corresponding data for TMOS-co-APTES and X-TMOS-co-APTES aerogel monoliths. Figures 6C and 6D concern powders and include insets showing typical grains of the respective materials – irregular shaped, about 50 μm in size; the main subject of Figures 6C and 6D is the interior of those grains, in high magnification.

Referring to Figure 6, and cross-referencing with Table 1, there is a clear increase in compactness from a TMOS-co-APTES aerogel monolith (Figure 6A) to the APTES@TMOS xerogel powder (Figure 6C): the arrangement of the elementary building blocks (nanoparticles) is more dense in the xerogel powder, and both the porosity, Π, and the BET surface area, σ, decreased from 89% to 80%, and from 554 m^2 g^{-1} to 294 m^2 g^{-1}. Also, as expected from all previous literature on polymer-crosslinked aerogels,[6,9] both Π and σ decreased from the TMOS-co-APTES aerogel (Figure 6A: 89% and 554 m^2 g^{-1}) to the crosslinked X-TMOS-co-APTES aerogel (Figure 6B: 62% and 374 m^2 g^{-1}). The same trend was noted with xerogel powders: by going from APTES@TMOS to X-APTES@TMOS, elementary particles in SEM became fuzzier (Figures 6C and 6D), and the Π and σ values decreased from 80% and 294 m^2 g^{-1}, to 45% and 113 m^2 g^{-1}, respectively. (It is noted that porosities reported for powders should be considered as the upper limits for the correct values of Π inside granules, because bulk densities used for calculating Π were what is referred to as tapped-densities.[36]) Overall, all data together show that polymer-coated nanoparticles in polyurea-crosslinked xerogel powders were squeezed closer together relative to their position in aerogel monoliths.

Next, by putting crosslinked xerogel powders in a die under pressure yielded compacts in which the overall porosity was reduced even further (from 45% to 29% v/v), however the BET surface area (119 $m^2\ g^{-1}$) was not affected. Those data suggest that on one hand grains of powder were squeezed together, which (a) was anticipated from the nature of the compacting process, and (b) is evident in lower-resolution SEM (Figure 6E); on the other hand, however, the fundamental building blocks of the network inside crosslinked granules were not affected by compaction – not much difference was observed between Figure 6D and 6F, and the BET surface area, as just mentioned, remained unaffected.

Carbothermal reduction towards either SiC or Si_3N_4 caused about 19% shrinkage in linear dimensions relative to the compacts. In both cases, high-temperature treatment in air in order to remove residual carbon caused an additional 2% shrinkage. As expected from the very low amount of residual carbon in as-prepared SiC samples (section 2.2), microscopically, as-prepared and clean-of-residual-carbon SiC (Figure 7, top row) looked very similar to one another, consisting of macroporous networks formed by almost dendritic kind of structures. Using a higher magnification, the skeletal framework consisted of fused nanoparticles (pointed with arrows), reminiscent, both in shape and size, of the polyurea crosslinked particles in X-APTES@TMOS. On the other hand, the case with

Si_3N_4 was different. As-prepared Si_3N_4 appeared grainy at all magnifications (Figure 7 – lower row). However, after pyrolytic removal of unreacted carbon, the skeletal framework of Si_3N_4 appeared macroporous and particulate; using a higher magnification it appeared consisting of stacked-and-fused rectangular-shaped platens. The approximate size of those platens (confined with arrows in SEM) matches with the crystallite size calculated from XRD via the Scherrer equation (about 50 nm). On the contrary, the size of the fused particles in SiC was larger than the calculated crystallite size (around 10 nm), meaning that those particles were polycrystalline.

The evolution of several key material properties (Table 1) was consistent with the evolution of the microscopic appearance of the samples before and after C removal (Figure 7). Specifically, bulk and skeletal densities, porosities, pore volumes and BET surface areas of as-prepared, and of clean-of-carbon SiC were quite close to one another. On the other hand, after removing unreacted carbon, Si_3N_4 objects were less dense (0.35 vs. 0.69 g cm^{-3}), more porous (85% vs. 74%) and their BET surface area was much lower (4.7 m^2 g^{-1}) compared to as-prepared samples (152 m^2 g^{-1}). SEM and materials characterization data considered together were consistent with the fact that as-prepared SiC had hardly any unreacted carbon (0.29% w/w, see section 2.2), while as-prepared Si_3N_4 included a significant amount (49% w/w) of unreacted carbon.

Overall, clean-of-carbon SiC and Si_3N_4 objects had similar bulk densities (0.410 vs. 0.352 g cm^{-3}, respectively), similar porosities (87% vs. 85% v/v, respectively), similar total specific pore volumes (V_{Total}, 2.12 vs. 2.52 cm^3 g^{-1}, respectively, calculated from bulk and skeletal density data), they both had low BET surface areas (3.2 vs. 4.7 m^2 g^{-1}), and they were void of mesopores and smaller macropores: in both cases the pore volumes of pores with sizes in the 1.7-300 nm range (by N_2 sorption) were just 0.02 cm^3 g^{-1} (i.e., a very small fraction of V_{Total}).

Finally, the macropore structure of both materials was quantified with Hg intrusion porosimetry (Figure 8). The Hg intrusion curves for both materials were smooth, sigmoidal, they started rising early and both leveled off by 500 psi. Samples were recovered intact after the experiments (see inset photograph in Figure 8). The intrusion curve of Si_3N_4 was steeper. Along increasing pressure, SiC showed two clear steps with a smaller deflection in the middle. Pore size distribution curves derived from those data (Figure 8, lower inset) showed that SiC had a trimodal distribution of pores, with about half of the pore volume distributed around 2.5 μm, while most of the other half of the pore volume was assigned to pores centered around 11.0 μm, with the balance to pores distributed around 5.7 μm. The overall average pore size in SiC was calculated by integration of the pore size distribution curve, and was found equal to 6.23 μm. Si_3N_4 included one main kind of pores with a distribution maximum at 7.9 μm; two small bumps (shoulders, pointed at with blue arrows) at the left of that maximum were at positions where SiC showed maxima, namely at around 6 μm and 2.5-3 μm. The average pore size in Si_3N_4 was calculated in a similar fashion to that of SiC and was found equal to 8.0 μm.

2.3.2. Thermal Characterization of SiC and Si_3N_4 Articles. Properties of interest included thermal stability in oxidizing environments, and thermal conductivity. The thermal stability of the porous SiC and Si_3N_4 ceramic objects was investigated up to 1000 °C using TGA under N_2 and under O_2. Under O_2, Si_3N_4 appeared more stable than SiC. The latter started gaining mass at about 800 °C (Figure 9A), presumably due to oxidation processes akin to sintering SiC powders.[37,38]

The thermal conductivity of both ceramic artifacts was determined at room temperature using thermal diffusivity data obtained with the laser flash method (see Experimental). Representative data are shown in Figure 9B. The voltage at the detector was proportional to the temperature of the sample at the side opposite to excitation. Fitting those data to Fick's first law,[39,40] yielded the thermal diffusivity, R, of each sample. Thermal conductivities, λ, were calculated via $\lambda = \rho_b \times c_P \times R$, where c_P is the heat capacity of each sample and was measured using modulated differential scanning calorimetry (MDSC, see Experimental). All relevant data are presented in Table 2. The thermal conductivities of the two materials were: $\lambda_{SiC} = 0.163$ W m^{-1} K^{-1} and $\lambda_{Si3N4} = 0.070$ W m^{-1} K^{-1}, meaning that in general both porous ceramics were very good thermal insulators, despite that the corresponding dense ceramics are fairly good thermal *conductors* with conductivities equal to 120 W m^{-1} K^{-1} and 30 W m^{-1} K^{-1}, for SiC and Si_3N_4, respectively.[41] Further analysis of the relative thermal insulation properties of those two materials gave insight about the relative connectivity of their fundamental building blocks along their skeletal frameworks. To that end, first we had to deconvolute the thermal conduction through the solid network, λ_s, from: (a) the gaseous thermal conduction through the air-filled porous network, λ_g, and (b) the thermal conduction via irradiation, λ_{irr}. The latter was eliminated completely by coating samples with carbon black: no early irradiation spike is observed in the data of Figure 9B. On the other hand, λ_g was calculated using Knudsen's equation (see footnote 'd' of Table 2),[42,43] and it was found equal to 0.0220 W m^{-1} K^{-1} and 0.0214 W m^{-1} K^{-1} for SiC and Si_3N_4, respectively (Table 2). As expected from the large pore sizes of both materials, those λ_g values were close to the thermal conductivity of still open air ($\lambda_{g,o} = 0.02619$ W m^{-1} K^{-1}, at 300 K, 1 bar). The thermal conductivities through the two solid frameworks, $\lambda_{s,SiC}$ and $\lambda_{s,Si3N4}$, were then calculated by subtracting their λ_g values from their λ values ($\lambda_s = \lambda - \lambda_g$), and they were found: $\lambda_{s,SiC} = 0.141$ W m^{-1} K^{-1} and $\lambda_{s,Si3N4} = 0.049$ W m^{-1} K^{-1}.

2.3.3. Mechanical Characterization of SiC and Si_3N_4 Articles. The elastic moduli of the two aerogels were measured under quasi-static compression in the spirit of ASTM D1621-04a using cylindrical specimens with length/diameter ratio of about 0.6 (see Experimental). The shape of the stress-strain curves of Si_3N_4 showed brittle behavior, while the curves of SiC were polymer-aerogel-like,[44] showing some ductility with a compaction onset at about 40% strain (Figure 9C). At comparable bulk densities (0.410 g cm^{-3} versus 0.352 g cm^{-3} for SiC and Si_3N_4, respectively) the ultimate strengths of the two materials were also similar, 7.47 ± 0.30 MPa for SiC versus 7.35 ± 0.41 MPa for Si_3N_4, however, because the Si_3N_4 curves were steeper, they reached the ultimate strength at lower strains (17.1 ± 5.1 %, versus 49.3 ± 3.9% for SiC). The elastic moduli of the two materials, E, were calculated from the early slopes of the stress-strain curves (at <3% strain) and were found $E_{SiC} = 36.7 \pm 6.6$ MPa, and $E_{Si3N4} = 59.4 \pm 7.4$ MPa. Curiously, Si_3N_4 appeared stiffer than SiC, even though the intrinsic elastic modulus of pure Si_3N_4 ($E^o_{Si3N4} = 304$ GPa) is lower than that of SiC ($E^o_{SiC} = 430$ GPa).[45]

3. DISCUSSION

3.1. MATERIALS SYNTHESIS

The comparative chemical characterization of TMOS-co-APTES monolithic aerogels and of APTES@TMOS powders (Figure 1) provided proof to the long-standing

Table 2. Thermal conductivity data

Sample	Bulk density ρ_b (g cm^{-3})	Heat capacity @ 23 ºC c_P (J g^{-1} K^{-1})	Thermal diffusivity R (mm^2 s^{-1})	Thermal conductivity, λ (W m^{-1} K^{-1}) [a]	Π [b] (% v/v)	Avg. pore diameter Φ (nm) [c]	Gaseous thermal conductivity, λ_g (W m^{-1} K^{-1}) [d]	Solid thermal conductivity, λ_s (W m^{-1} K^{-1}) [e]
SiC	0.410 ± 0.002	0.72_6 ± 0.074	0.54_8 ± 0.049	0.16_3 ± 0.010	0.8772	6226	0.02198	0.141
Si_3N_4	0.35_2 ± 0.024	0.76_4 ± 0.028	0.262 ± 0.005	0.070 ± 0.001	0.8467	8027	0.02142	0.049

[a] Via $\lambda = \rho_b \times c_P \times R$, average of 3 samples. [b] Porosity in decimal notation. [c] From Hg intrusion porosimetry. [d] From Knudsen's equation: $\lambda_g = (\lambda_{g,o}\Pi)/(1+ 2\beta\ (l_g/\Phi))$,[42,43] whereas: $\lambda_{g,o}$ is the intrinsic conductivity of the pore-filling gas (for air at 300 K at 1 bar, $\lambda_{g,o} = 0.02619$ W m^{-1} K^{-1}), β is a parameter that accounts for the energy transfer between the pore-filling gas and the aerogel walls (for air $\beta = 2$), l_g is the mean free path of the gas molecules (for air at 1 bar pressure, $l_g \approx 70$ nm). [e] Via $\lambda_s = \lambda - \lambda_g$.

hypothesis that during co-gelation of TMOS/APTES, APTES first catalyzes the formation of a TMOS-derived network, to which it gets attached later.

Disruption of gelation with vigorous agitation has been an efficient method to produce sol-gel silica powders. The powder particles were irregular-shaped. It is understood that other methods involving use of surfactants may yield spherical silica particles,[46] however, it is well-established that vibrated irregular particles pack more densely,[47] thereby those alternative approaches to more spherical particles were not considered. TIPM-derived polyurea is attached to the surface of silica via the APTES-supplied –NH_2 groups, but as ^{29}Si NMR evidence suggests (Figure 1), TIPM is really an opportunistic crosslinker that engages not only –NH_2 groups, but also dangling –SiOH groups at Q3 and T2 positions.

The polymer (polyurea) layer coating of silica nanoparticles acts as a binder that, under compression, glues the powder grains together yielding sturdy compacts. Carrying out the whole process with xerogel-like powders, dried via solvent evaporation rather than via supercritical fluids, has brought core-shell-like skeletal silica particles coated with a carbonizable polymer in close contact with one another. Taking, for the sake of this discussion, SiC as an example, intitial reaction of SiO_2 with C at their interface yields a thin layer of SiC[48] that prevents further direct reaction between the two. Complete consumption of SiO_2 and its conversion to SiC relies on CO, produced via SiC + 2 SiO_2 ---> 3 SiO + CO, passing though the SiO_2 core.[21,49,50] However, owing to the topology of that reaction (at the SiC/SiO_2 interface) only half of CO goes through silica; the other half moves through carbon and once it reaches the nearest pore (at the other side of the C-coating) it is carried away and is lost. In xerogel compacts, however, most of the CO moving through the C shell does not reach a pore; instead, it enters the C-shell of another C-on-SiO_2 particle at a nearby strand, and eventually reaches silica again. The result was that complete conversion of SiO_2 to SiC was achieved with a near stoichiometric ratio of C:SiO_2 (4.4), while conversion of more loosely-packed aerogels requires a large excess of carbon (>7 mol/mol) in order to compensate for the loss of CO.[21] Finally, the fact that conversion of X-APTES@TMOS compacts to Si_3N_4 left half of the carbon unreacted, implies that Si_3N_4 and SiC were produced in parallel processes, namely SiC was *not* an intermediate to Si_3N_4. That understanding was further confirmed by control experiments in which SiC aerogel articles were pyrolyzed under conditions that produce pure Si_3N_4 (1500 °C, N_2) and remained intact.

3.2. APPLICATION-RELEVANT MATERIAL PROPERTIES AND RELATIONSHIP TO THE NANOSTRUCTURE

Both types of porous ceramics of this work were highly porous, yet sturdy, and thermally stable in air up to fairly high temperatures (near 1000 °C). Although at first glance Si_3N_4 aerogel articles appeared stiffer and better thermal insulators that their SiC counterparts, a more sound comparison of the two materials may be obtained by further analysis of their solid thermal conduction, λ_s, and their elastic moduli, E, from the perspective of their skeletal frameworks.

3.2.1. The Skeletal Framework from a Thermal Conductivity Perspective. In porous materials, λ_s depends on their bulk density, ρ_b, and is usually modeled according to Eq 3.[51,52]

$$\lambda_s = C(\rho_b)^{\alpha} \tag{3}$$

Exponent α depends on how material fills space, and typically varies between 1 and 1.5. For foams, for example, α = 1,[53] in base-catalyzed silica aerogels α = 1.5,[54] in resorcinol-formaldehyde aerogels $1.2 \leq \alpha \leq 1.5$,[51] and for several polyurethane aerogels, on average $1.0 \leq \alpha \leq 1.5$.[44] Here, owing to the similarity of the two materials in terms of their origin, bulk density and pore structure, it is reasonable to assume that $\alpha_{SiC}=\alpha_{Si3N4}$. Pre-exponential factor C on the other hand depends on the chemical identity of the material and the pore geometry, which controls the thermal efficiency of interparticle contacts along the skeletal framework. For instance, larger contacts conduct heat more efficiently hence the C value is higher. Using Ashby's approach to modeling the pre-exponential factor (in a similar expression describing the evolution of Young's modulus as a function of density - see section 3.2b below),[55] C was expressed as $C = \lambda_{pure\_SiC}$ (or λ_{pure_Si3N4}) $\times$ C_G, where C_G is the geometric factor of interparticle contacts, in the context of what was just described. Considering the experimental ratio $\lambda_{s,SiC}/\lambda_{s,Si3N4}$ of the two materials (=2.878), and setting the other values accordingly (i.e., the ρ_b's of SiC and Si_3N_4 – see Table 2), it is calculated that for α = 1.0, $C_{G,SiC} = 0.62 \times C_{G,Si3N4}$, and that for α = 1.5, $C_{G,SiC} = 0.57 \times C_{G,Si3N4}$. Thereby, the interparticle contacts in the Si_3N_4 aerogel framework render its porous structure a more efficient (by about 2×) thermal conductor than the SiC porous structure, which is the opposite than what is suggested by considering the ratio of the intrinsic thermal conductivities of the two materials: $\lambda_{pure\_SiC} / \lambda_{pure\_Si3N4} = 4$. That inverted behavior of our nanostructured Si_3N_4 is attributed to the large-area, face-to-face contacts between its skeletal platens (Figure 7).

3.2.2. The Skeletal Framework from a Stiffness Perspective. The higher stiffness of the Si_3N_4 aerogels can be attributed to the more efficient contacts between skeletal platens as identified via analysis of λ_s. Yet, the question is how can a significantly stiffer material (SiC) end up with lower modulus? The modulus of low-density porous materials like aerogels is modeled as a function of their relative density, ρ_b/ρ_s (calculated from values in Table 1), according to Eq 4,[51,52,55,56,57,58] where E^o is the intrinsic modulus of

$$E = E^o A_G \left(\frac{\rho_b}{\rho_s} \right)^X \tag{4}$$

the pure, non-porous material, A_G is a geometric factor similar to C_G (refer to section 3.2a above), and "X" is an exponent that expresses the sensitivity of E to ρ_b, and is related to the network morphology. Here, E^o_{SiC} = 430 GPa, and E^o_{Si3N4} = 304 GPa.[45] By considering the experimental ratio E_{SiC}/E_{Si3N4} (=0.618), and by setting A_G=C_G (=0.60, i.e., equal to the average C_G values discussed in section 3.2a), it was calculated that exponents X_{SiC} and X_{Si3N4} were related via Eq 5, namely $X_{SiC} > X_{Si3N4}$, thereby SiC aerogels were more sensitive

$$X_{SiC} = 1.05 \times X_{Si3N4} + 0.156 \tag{5}$$

to changes in bulk density than Si_3N_4 aerogels, which justifies the observed crossover, whereas stiffer SiC in the bulk form, ended up with lower modulus in the porous form. In conclusion, the higher stiffness of the Si_3N_4 artifacts is attributed to both the apparently efficient contact between its skeletal platens, and the different way the two materials fill space (platens vs fused particles).

3.2.3. Overall Assessment of SiC versus Si_3N_4 Aerogel Articles. Comparing the mechanical properties and the thermal conductivity of the SiC aerogels of this study with those reported recently for SiC foams at the same relative density (ρ_b/ρ_s = 0.12), and porosity (88%) as in this paper,[59] the materials of this study are slightly stronger (7.5 vs. 3.5 MPa), much less stiff (37 MPa vs. 2.5 GPa), and much better thermal insulators (0.163 vs. ca. 3.5 W m^{-1} K^{-1}) than SiC foams. Those trends are attributed to, actually expected from, the morphological differences between SiC of this study, and the literature SiC foams.[59] On the other hand, owing to the lower intrinsic thermal conductivity of silica (1.38 W m^{-1} K^{-1} at room temperature),[41] together with the smaller, more numerous particles filing space at similar porosities like those reported here for SiC and Si_3N_4, silica aerogels are much better thermal insulators[60] than both porous ceramics of this study. By the same token, however, owing to its lower melting point, silica is not suitable for very high temperature applications. In that regime, data presented herewith suggest that Si_3N_4 aerogels are better overall materials than SiC: they display higher oxidation resistance (up to 1000 °C), lower overall thermal conductivity (despite the penalty due to the efficient contact of platens) and higher modulus.

4. CONCLUSION

3D Assemblies of polymer-coated silica nanoparticles have been investigated extensively in aerogel form as strong lightweight materials.[6,61] Here, we have described an alternative application for such 3D assemblies of nanoparticles, namely in the carbothermal preparation of sturdy, highly porous SiC and Si_3N_4 ceramics. Our methodology takes into consideration the topology of the carbothermal reactions, and for porosity it relies on the void space created by carbon reacting away. That allowed making aerogels from xerogels. Indeed, using polymer-crosslinked *xerogel* powder compacts as the ceramic precursors, rather than monolithic polymer-crosslinked aerogels, processing moves fast, it is energy and materials efficient, and most importantly it is generalizable. In that regard, (a) gelation of any system that does so relatively slowly (minutes or longer) can be diverted to powders by vigorous agitation, (b) the surface of any sol-gel derived skeletal oxide particle is rich with –OH groups, where isocyanate-derived polymers, like carbonizable TIPM-derived polyurea, can latch on covalently,[64] and (c) crosslinked powders can be compressed to shaped compacts of any size, thus liberating synthesis of ceramic aerogels from the size of the authoclave. In addition to other ceramic aerogels based on refractory materials (e.g., zirconium carbide), work-in-progress includes Fe(0) metallic aerogels that may alleviate certain issues in thermite applications.[62,63]

5. EXPERIMENTAL

5.1. MATERIALS

All reagents and solvents were used as received, unless noted otherwise. Tetramethylorthosilicate (TMOS), 3-aminopropyltriethoxysilane (APTES) and ammonium hydroxide (NH_4OH, ACS reagent) were purchased from the Sigma Aldrich Chemical Co. HPLC grade solvents including hexane, methanol (CH_3OH), ethyl acetate (EtOAc), n-pentane were purchased from Sigma Aldrich Chemical Co. Technical grade acetone was purchased from Univar (St. Louis, MO). Tris(4-isocyanatophenylmethane) (TIPM) was donated by Covestro LLC (Pittsburg, PA) as a 27% w/w solution in dry EtOAc under the trade name Desmodur RE. Ultra-high purity Ar (grade 5), N_2 (grade 4.8) and Ar (99.99999%) gases were purchased from Ozarc Gas (Rolla, MO). For comparison and chemical identification purposes, authentic samples of α-SiC (Grade UF-25) and of Si_3N_4

(Grade M11) were purchased from H. C. Stark Inc. (Euclid, OH); *β*-SiC was purchased from Performance Ceramics Co. (Peninsula, OH).

5.1.1. Preparation of APTES@TMOS Silica Powder. Hexane (43 mL, 3× the volume of the intended sol) was added under flowing dry (drying tube) Ar (99.99999%) to a three-neck round bottom flask equipped with a mechanical stirrer and a drying tube. To that flask, Solution A consisting of 4.5 mL of CH_3OH and 3.85 mL (0.026 mol) of TMOS, and solution B consisting of 4.5 mL of CH_3OH, 1.5 mL (0.083 mol) of water and 40 μL NH_4OH were added successively at room temperature under vigorously stirring (770 – 950 rpm). As soon as the mixture developed fine particles and turned white (approximately 20 min), 1.28 mL of APTES (approximately 1/3× the volume of TMOS) was added to the flask, and the reaction mixture was stirred at the same rate for 24 h at room temperature. The resulting APTES@TMOS suspension was transferred to centrifuge tubes (50 ml, Fisher Scientific) and the solvent was exchanged twice with ethyl acetate and once with water-saturated ethyl acetate (EtOAc/H_2O). After standing for 15 h in EtOAc/H_2O, the APTES@TMOS suspension was given one acetone wash and was either processed to X-APTES@TMOS powder (see next section), or was dried under vacuum at room temperature after three more washes with pentane. All washes and solvent exchanges were carried out with centrifugation for 15-20 min at 2450 rpm. Each time, the supernatant solvent was removed and the volume of the new solvent that was brought in was 2× the volume of the compacted slurry (paste) at the bottom of the centrifuge tubes. Before every new centrifugation step, the compacted slurry was re-suspended with vigorous agitation with a glass rod.

5.1.2. Preparation of Cross-linked X-APTES@TMOS Silica Powder. Desmodur RE (6× the volume of the centrifuged paste) was added to the centrifuge tubes containing the APTES@TMOS slurry from the last acetone wash, the tubes were sealed tightly with their caps, and the suspension was heated in an oven at 65 °C for 72 h. The mixture was swirled slowly every 10 to 12 h to re-distribute the settled powder and increase the diffusion rate. At the end of the 3-day period, the tubes were allowed to cool to room temperature and they were centrifuged for 15 to 20 min followed successively by three acetone washes and three pentane washes. Always, the wash solvent was removed by centrifugation. Again, for all washes, the volume of solvent added was twice the volume of the paste at the bottom of the tubes. After removing the solvent from the last pentane wash, the contents of the tubes were transferred with the aid of small portions of pentane and were combined in a round bottom flask. Pentane was removed and the product was dried under reduced pressure (water aspirator connected via a drying tube) at room temperature into a dry, freely flowing X-APTES@TMOS powder.

5.1.3. Preparation of TMOS-co-APTES AND X-TMOS-co-APTES Monolithic Aerogels. They were prepared by mixing Solution A and Solution B from above, following standard procedures that involve drying with supercritical fluid CO_2.[27]

5.1.4. Preparation of Porous SiC and Si_3N_4 Monoliths. Dry X-APTES@TMOS powder was compressed into various cylindrical and annular monolithic objects using aluminum dies of different sizes and shapes and a hydraulic press operated at 15,000 psi. Placement of the powder in the dies was carried out in small portions under continuous tapping. Compressed objects were converted to porous SiC or Si_3N_4 pyrolytically in a tube furnace set at 1500 °C for 36 h under flowing ultra-high purity Ar or N_2, respectively. In both cases the gas flow rate was set at 325 mL min^{-1}. Residual carbon from the crude SiC and Si_3N_4 samples was removed by heating in air for 24 h in a muffle furnace at 800 ºC and 600 ºC, respectively.

5.2. METHODS

Pyrolytic conversion of X-APTES@TMOS compacts to SiC and Si_3N_4 was carried out in a programmable MTI GSL1600X-80 tube furnace (outer and inner tubes both of 99.8% pure alumina; outer tube: 1022 mm × 82 mm × 70 mm; inner tube: 610 mm × 61.45 mm × 53.55 mm; heating zone at set temperature: 457 mm). The temperature of the tube furnace was raised under flowing Ar or N_2 from ambient to the carbothermal reaction temperature at 2.5 ºC min^{-1}. The temperature was maintained at that level for the prescibed length of time. Cooling back to room temperature was carried out under constant flow of Ar or N_2, again at 2.5 ºC min^{-1}.

5.2.1. Physical Characterization. Bulk densities (ρ_b) were calculated from the weight and the physical dimensions of the samples. Skeletal densities (ρ_s) were determined with helium pycnometry using a Micromeritics AccuPyc II 1340 instrument. Samples for skeletal density measurements were outgassed for 24 h at 80 °C under vacuum before analysis. Percent porosities, Π, were determined from the ρ_b and ρ_s values via $\Pi = 100 \times (\rho_s - \rho_b)/\rho_s$.

5.2.2. Chemical Characterization. Solid-state ^{13}C NMR spectra were obtained for powder samples on a Bruker Avance III 400 MHz spectrometer with a carbon frequency of 100 MHz using a 7 mm Bruker MAS probe and magic-angle spinning at 5 kHz. Broadband proton suppression along with CPTOSS pulse sequence were used for cross-polarization and spin sideband suppression. Solid-state ^{13}C NMR spectra were referenced externally to glycine (carbonyl carbon at 176.03 ppm). Solid-state ^{29}Si NMR spectra were also obtained on the same Bruker Avance III 400 MHz spectrometer with a 59.624 MHz silicon frequency using again a 7 mm Bruker MAS probe and magic angle spinning at 5 kHz. ^{29}Si NMR spectra of samples without protons (SiC, Si_3N_4 – Figure 4) were acquired using a single pulse excitation (i.e., direct polarization). ^{29}Si NMR spectra of all other samples were obtained using both cross-polarization (CPMAS pulse sequence – Figure 1), and direct polarization (Figure S.4 in Supporting Information). ^{29}Si NMR spectra were referenced externally to neat tetramethylsilane (TMS, 0 ppm). The relaxation delay was set at 5 s in all experiments, while the number of scans was set at 2,048 and 16,384 for ^{13}C and ^{29}Si, respectively. The cross-polarization contact time was set at 3000 μs.

X-ray diffraction analysis was performed with powders of the corresponding materials using a PANalytical X'Pert Pro multipurpose diffractometer (MPD) with Cu Kα radiation (λ = 1.54 Å) and a proportional counter detector equipped with a flat graphite monochromator. Crystallite sizes were calculated using the Scherrer equation,[35] from the full-width-at-half-maxima of selected reflections (see Section 2.2) after subtracting the instrument line broadening.

5.2.3. Solid Framework Characterization. Scanning electron microscopy (SEM) was conducted with Au-coated samples on a Hitachi Model S-4700 field-emission microscope.

5.2.4. Pore Structure Analysis. BET surface areas were determined with N_2-sorption porosimetry at 77 K using a Micromeritics ASAP 2020 surface area and porosity analyzer. Samples for N_2-sorption analysis were outgassed for 24 h at 80 °C under a vacuum before analysis. The pore size distribution of both the SiC and Si_3N_4 objects was also investigated with Hg-intrusion porosimetry using a Micromeritics AutoPore IV 9500 instrument.

5.2.5. Thermal Characterization. Thermogravimetric analysis (TGA) was conducted under N_2 or O_2 with a TA Instruments Model TGA Q50 thermogravimetric analyzer, using a heating rate of 5 °C min^{-1}.

Modulated Differential Scanning Calorimetry (MDSC) was conducted under N_2 with a TA Instruments Differential Scanning Calorimeter Model Q2000. Heat capacities, c_P, at 23 °C of powders (4–8 mg), needed for the determination of their thermal conductivity, λ, were measured using the MDSC method with a TA Instruments Differential Scanning Calorimeter Model Q2000 calibrated against a sapphire standard and run from 0 °C to 40 °C at 0.5 °C min^{-1} in the modulated T4P mode, using 100 s as the modulation period and 0.13 °C as the modulation amplitude. Raw c_P data were multiplied with a correction factor (1.008 ± 0.041) based on measuring the heat capacities of a rutile and of a corundum sample just before running the SiC and Si_3N_4 aerogel samples, and taking the ratios with the corresponding literature values for heat capacities.

Thermal conductivities, λ, were determined via $\lambda = \rho_b \times c_P \times R$, whereas the thermal diffusivity, R, was measured with a Netzsch NanoFlash Model LFA 447 flash diffusivity instrument using disk samples about 1 cm in diameter, 1.8−2.5-mm-thick.[65] Samples were first sputter-coated with gold and then spray-coated with carbon on both faces to minimize radiative heat transfer and ensure complete absorption of the heat pulse.[66] Before every run, the instrument was checked with manufacturer provided standards (Pyrex 7740, Pyrocream 9606, 99.8% Alumina and AXM-5Q Poco Graphite). Samples were heated with a heat pulse from one side, and the temperature increase was observed as a function of time on the other. Subsequently, data (Figure 9B) were fitted with the pulse-corrected Cowan model that approximates the heat-transfer equation using an initial value for the thermal diffusivity estimated from the time it takes the detector voltage (proportional to the temperature) to reach its half-maximum value (denoted as t_{50}).[39,40]

5.2.6. Mechanical Characterization. Quasi-static compression testing at low strain rates (2.5 mm/mm) was conducted on an Instron 4469 Universal Testing Machine using a 500 N load cell, following testing procedures and specimen length/diameter ratios in the spirit of ASTM D1621-04a (Standard Test Method for Compressive Properties of Rigid Cellular Plastics), as described before.[67] The specimens had a nominal diameter of 1.0 cm and a length/diameter ratio of 0.6. The recorded force as a function of displacement (machine-compliance corrected) was converted into stress as a function of strain.

ACKNOWLEDGEMENTS

This project was supported by the ARO under Award No. W911NF-14-1-0369 and the NSF under Award No. 1530603. We are grateful to Covestro LLC (formerly Bayer Corporation U.S.A.) for the generous supply of Desmodur RE (TIPM), and we thank the Materials Research Center of MS&T for support with materials characterization (SEM, XRD).

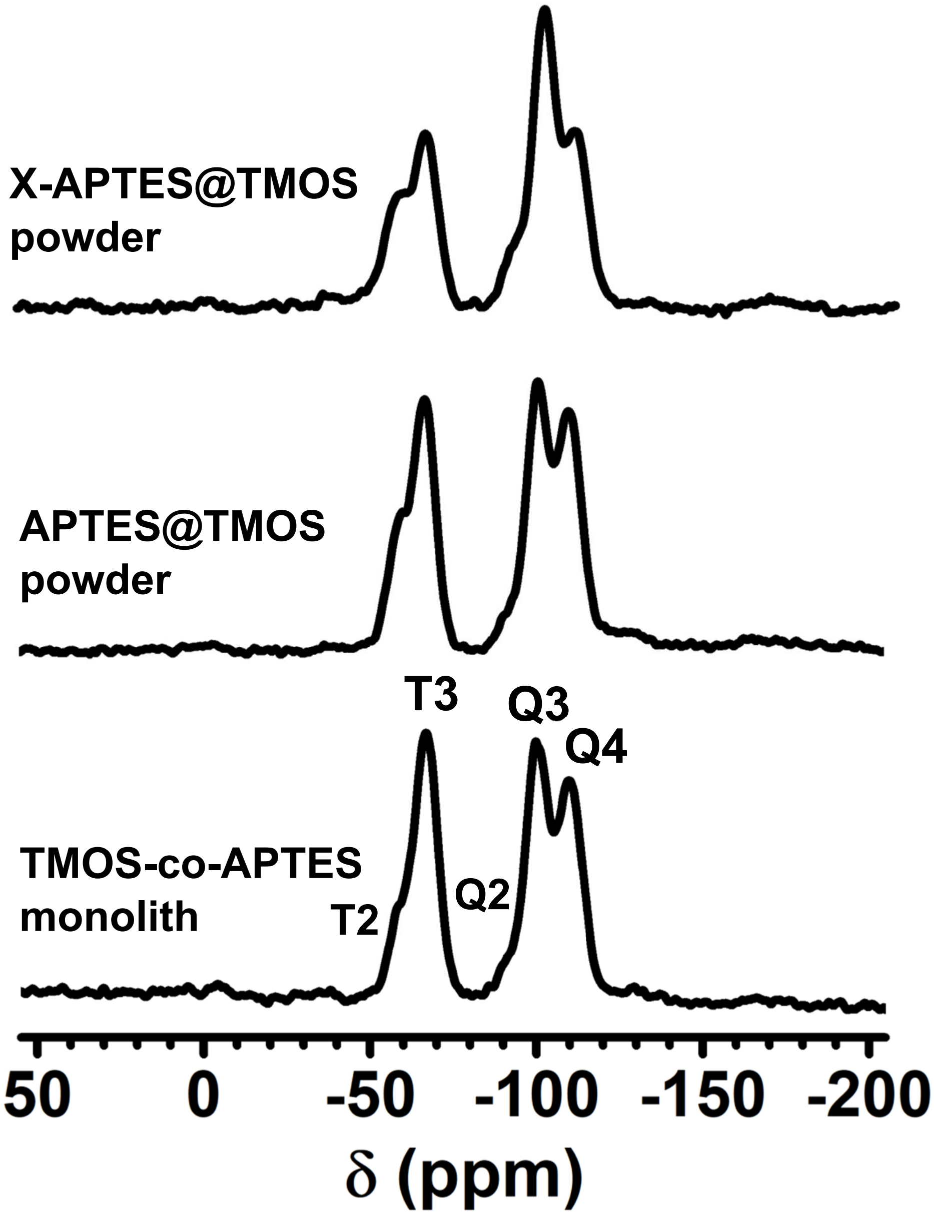

Figure 1. Solid-state CPMAS ^{29}Si NMR spectra of samples as shown. (For the corresponding spectra under direct polarization see Figure S.4 in the Supporting Information.)

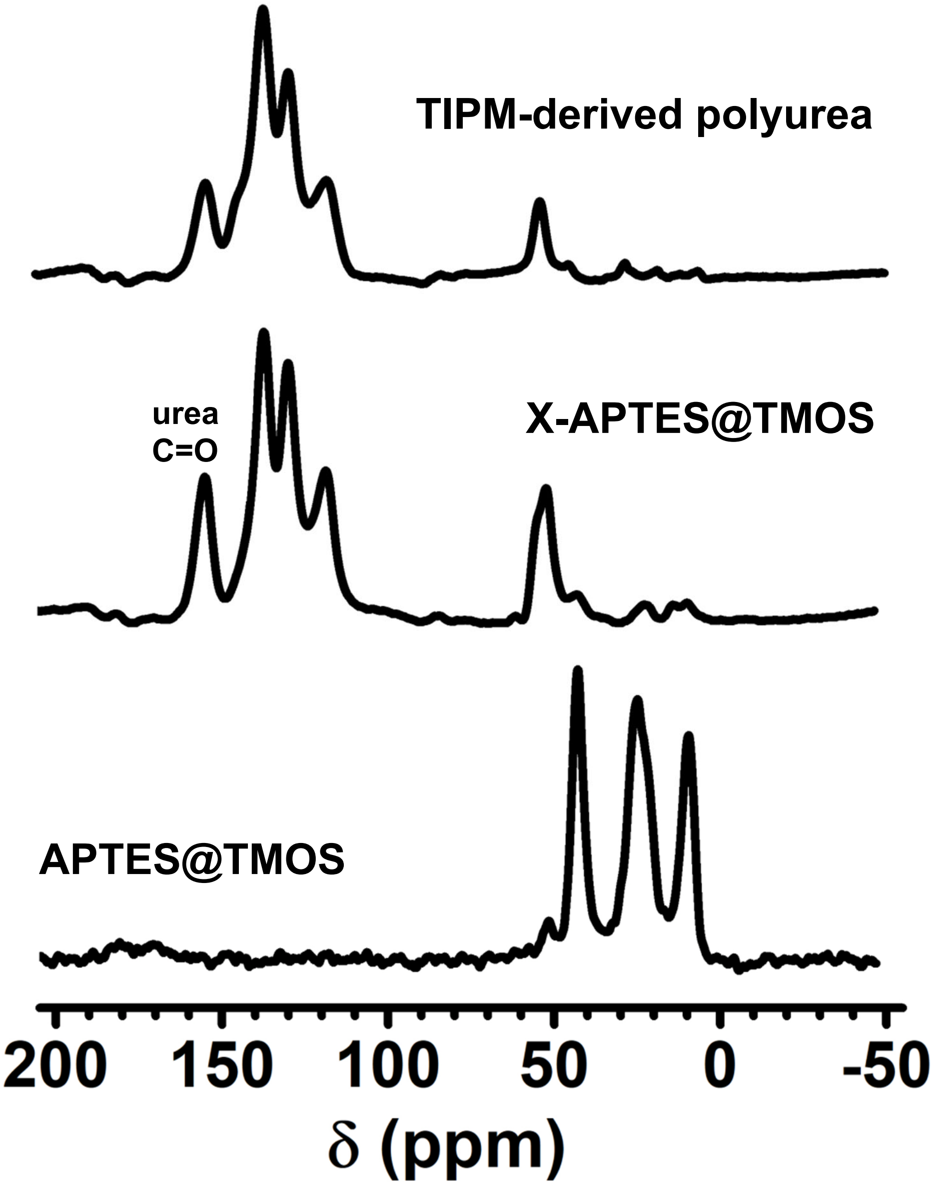

Figure 2. Solid-state CPMAS ^{13}C NMR of materials as shown.

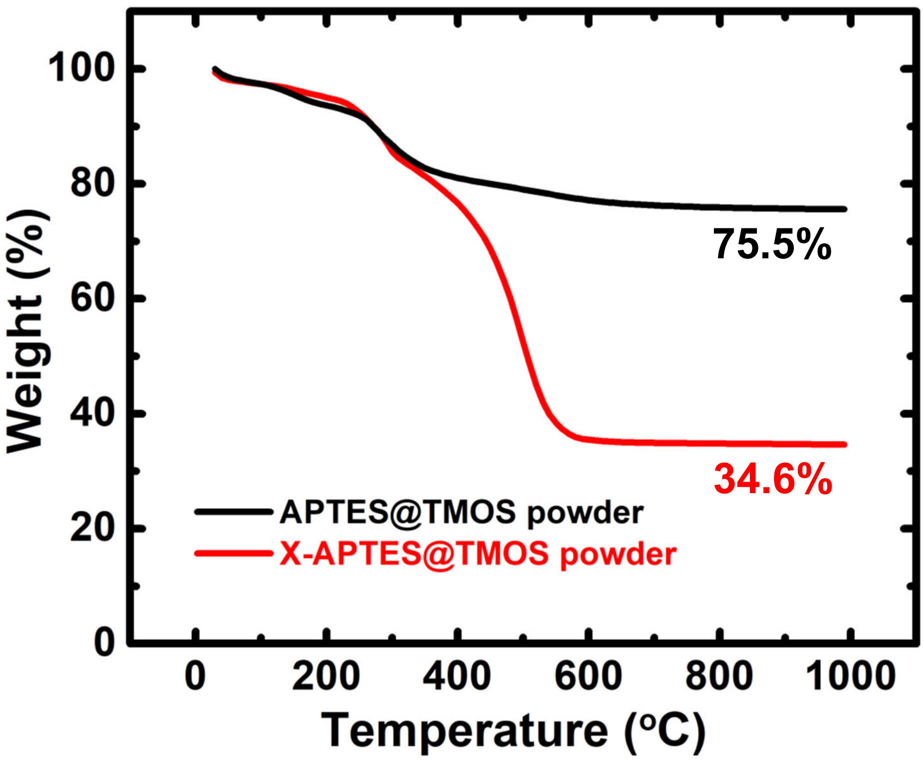

Figure 3. Thermogravimetric analysis (TGA) under N_2 of samples as shown. (Heating rate 5 ºC min^{-1}.)

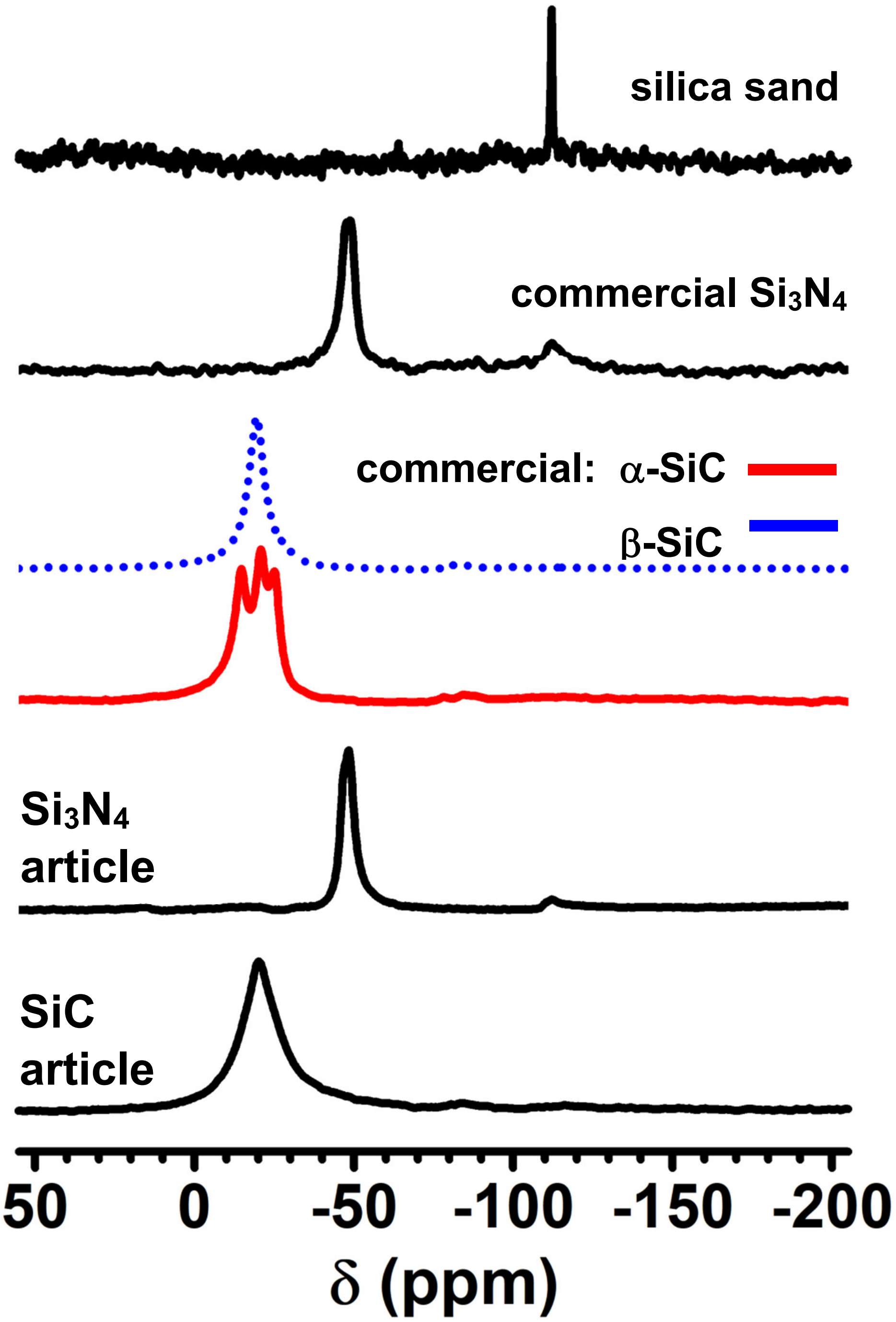

Figure 4. Solid-state MAS ^{29}Si NMR spectra of samples as shown. (All spectra were obtained using excitation with direct polarization.)

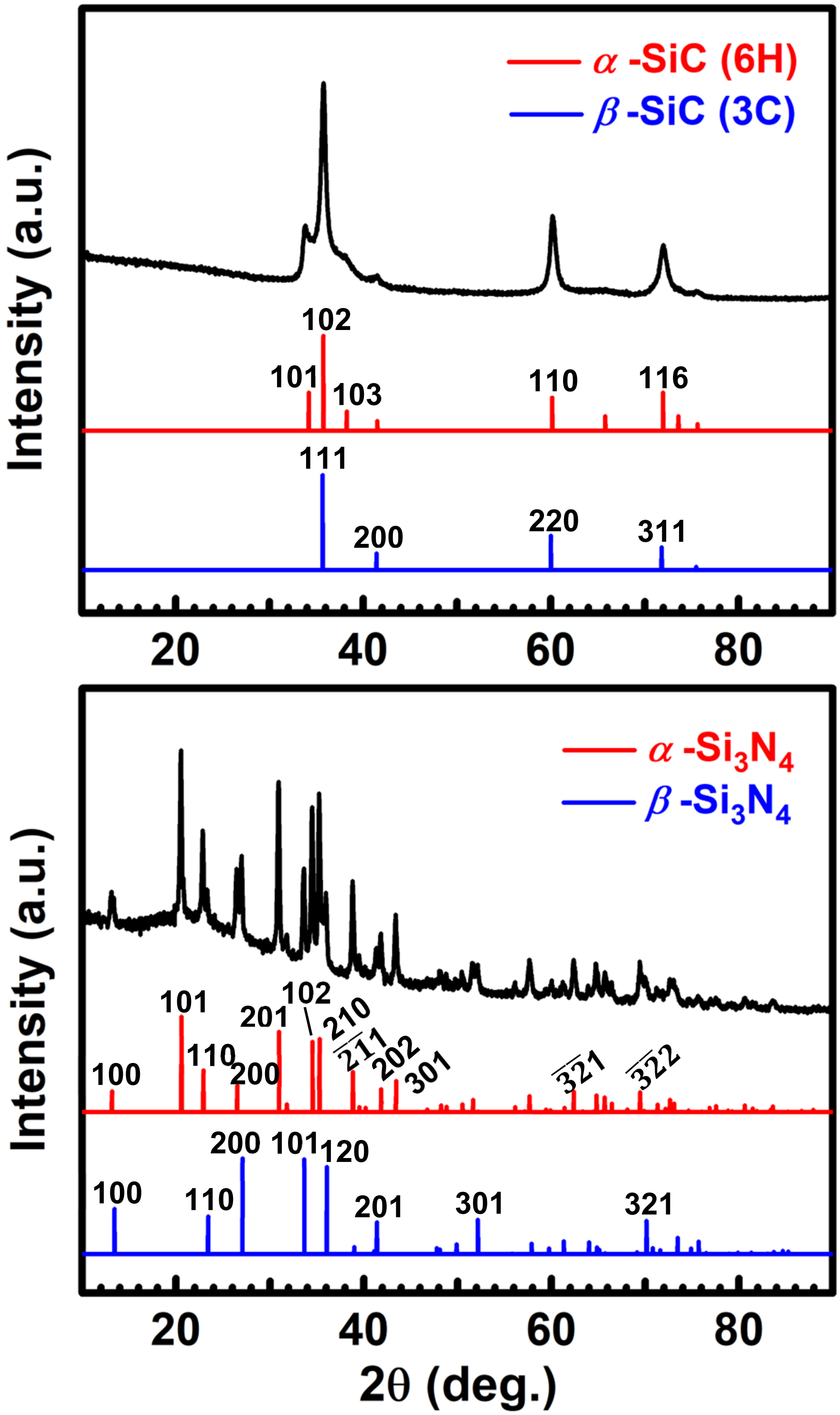

Figure 5. X-Ray diffraction of porous ceramic artifacts: Top: SiC; Bottom: Si_3N_4.

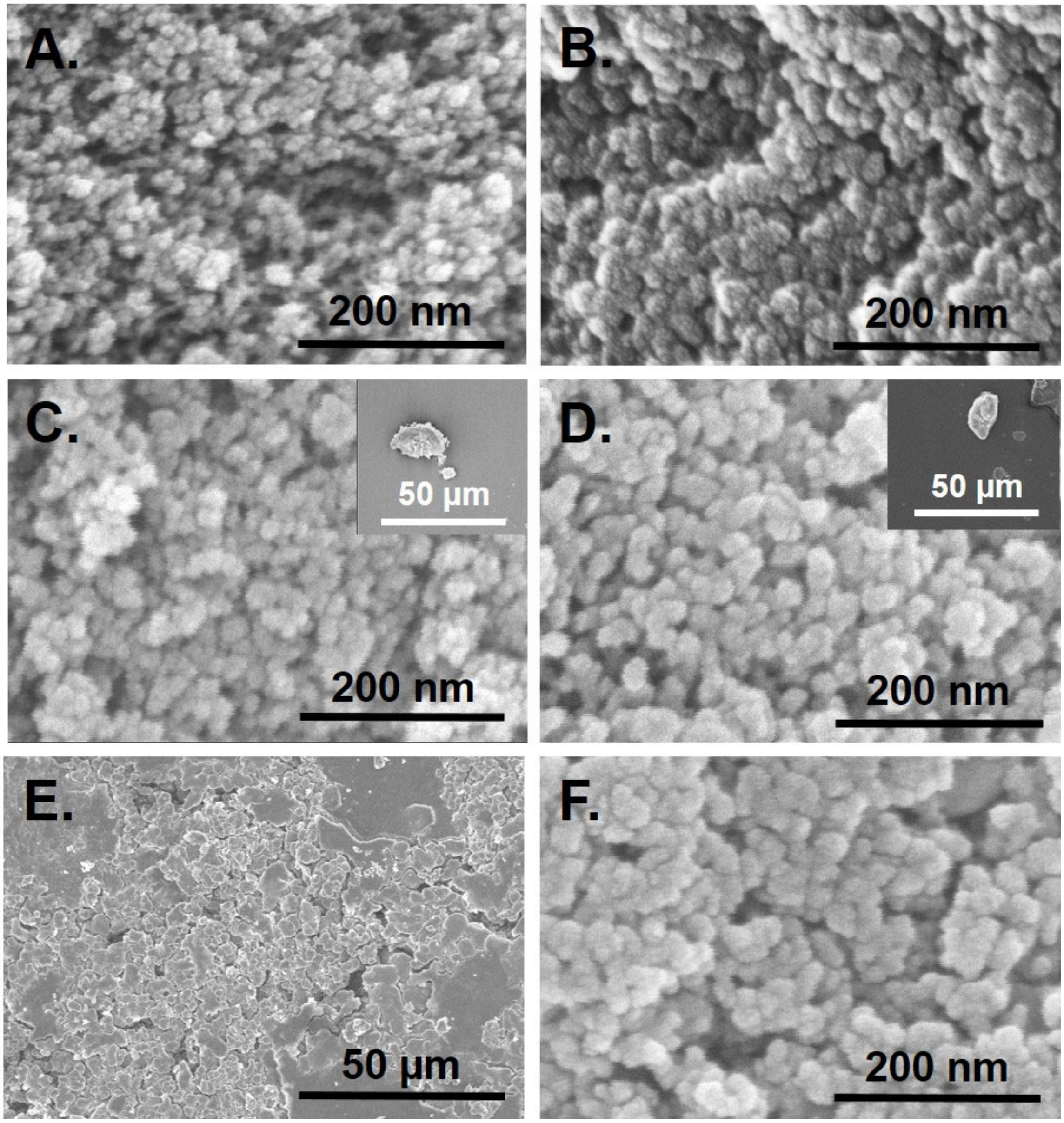

Figure 6. SEM of: (A) TMOS-co-APTES aerogel; (B) X-TMOS-co-APTES aerogel; (C) Inside a grain (see Inset) of a APTES@TMOS powder; (D) Inside a grain (see Inset) of a X-APTES@TMOS powder; (E) Low magnification image from inside a X-APTES@TMOS compact; and, (F) High magnification image from inside a X-APTES@TMOS compact.

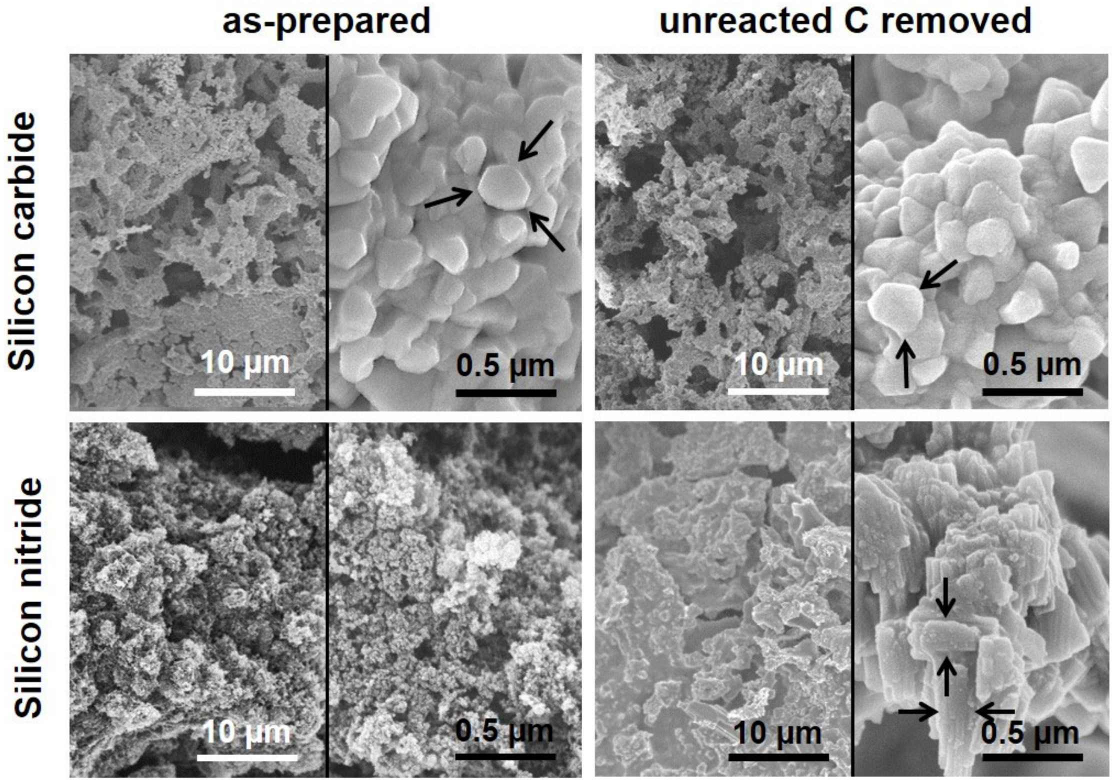

Figure 7. SEM from a fracture cross-section of a SiC and a Si_3N_4 aerogel artifact at two different magnifications, before and after removal of unreacted carbon as, indicated. Arrows show features that correspond to features in the precursors (the X-APTES@TMOS compacts – case of SiC) or to crystallite sizes calculated from the XRD data (case of Si_3N_4).

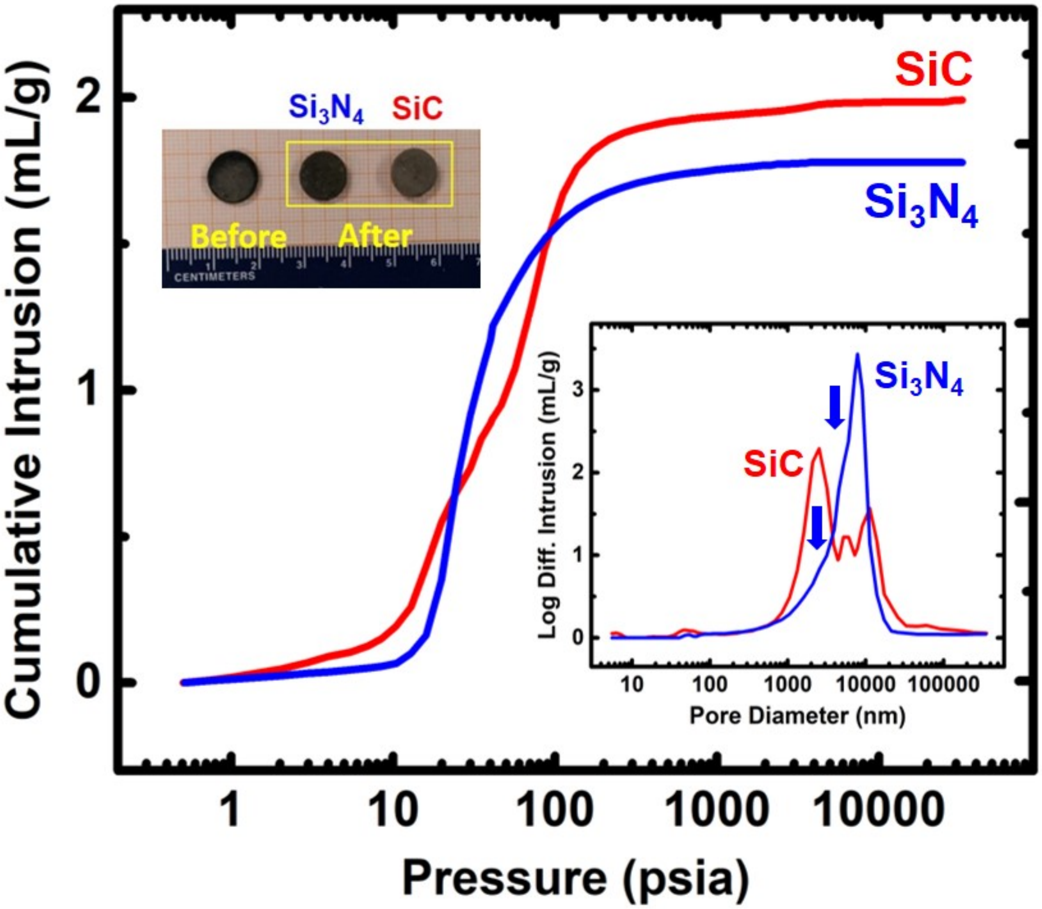

Figure 8. Hg-Intrusion porosimetry of porous SiC and Si_3N_4 artifacts. Lower Inset: Pore size distributions. Upper Inset: Before testing, as shown.

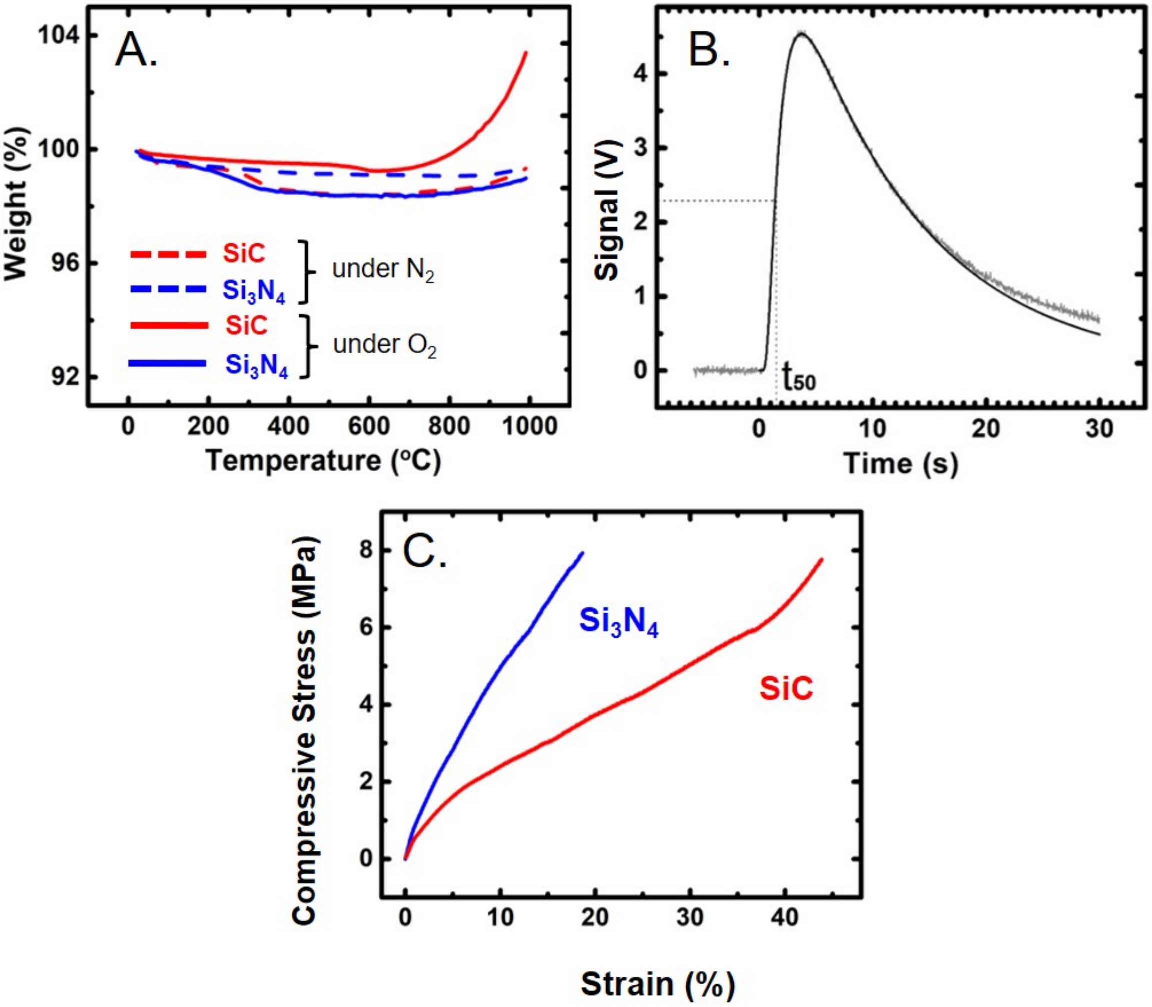

Figure 9. Representative applications related data for SiC amd Si_3N_4 artifacts: (A) TGA data related to the thermal stability of the two porous ceramic artifacts up to 1000 °C under O_2 vs N_2. (B) Laser flash data for finding the thermal diffusivity, *R*, of the final C-free SiC and Si_3N_4 samples. The detector voltage was proportional to the temperature. Data shown are for SiC. t_{50} is the time it takes for the temperature at the back side of the sample to reach 50% of its maximum value. (C) Compressive stress-strain data for the two porous ceramics at the densities given in Table 1.

SUPPORTING INFORMATION

Appendix I. Optimization of washing procedures for an optimal amount of carbon available for carbothermal reduction

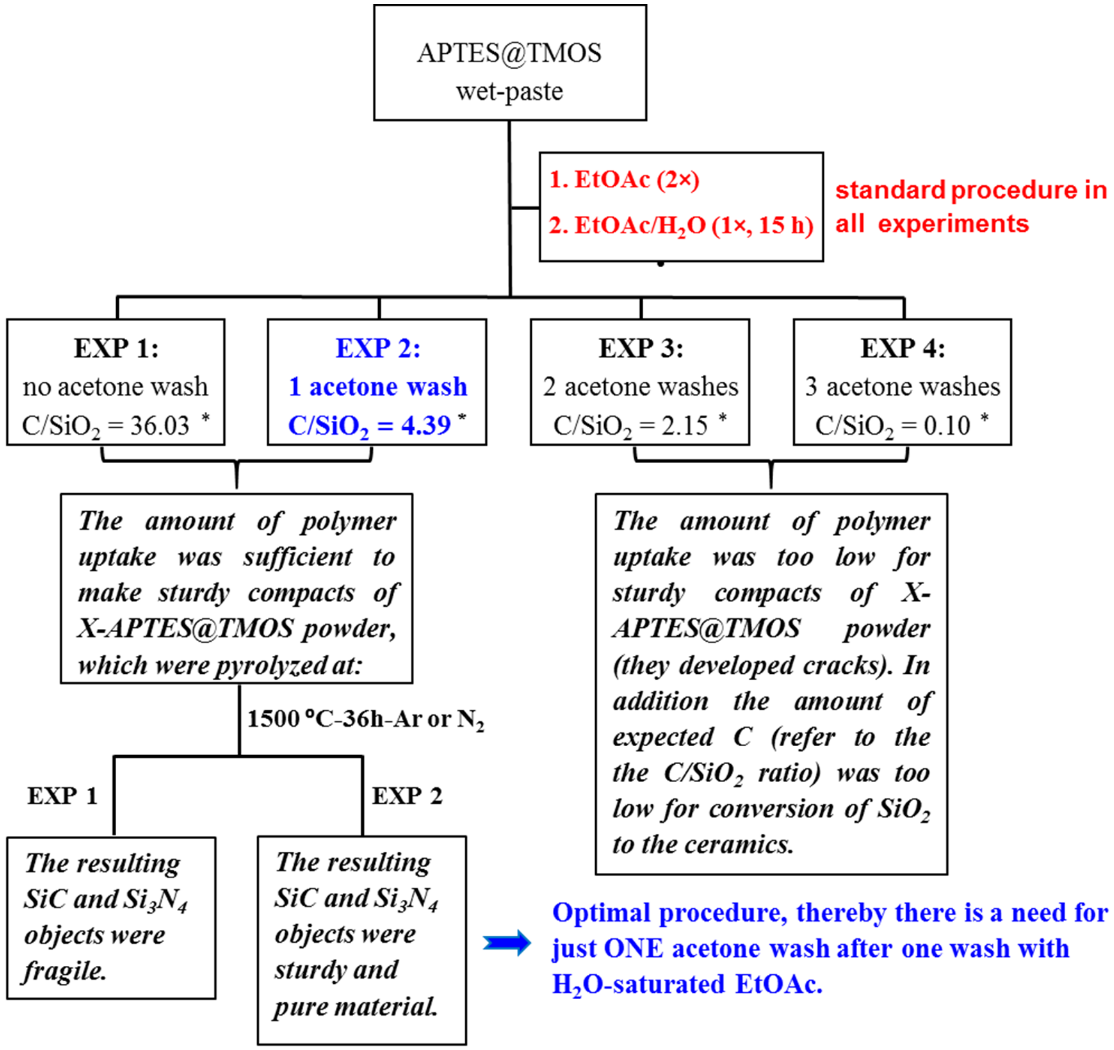

* This is the amount of carbon relative to silica that is expected based on the carbonization yield of TIPM-derived polyurea (56% w/w, by pyrolysis at 800 °C/Ar) and the amount of polyurea in the resulting X-APTES@TMOS powder determined with TGA (as in Figure 3 of the main article.)

Scheme S.1. Optimization of washing procedure for optimal polymer uptake during crosslinking, and thereby optimal amount of carbon produced and available for carbothermal reduction

Appendix II. Optimization of pyrolytic conditions for converting compressed silica compacts to Si_3N_4 aerogels

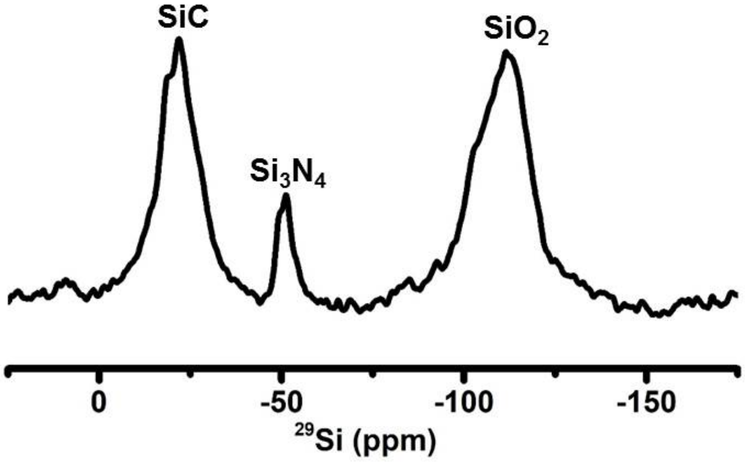

Figure S.1. Solid-state MAS ^{29}Si NMR of a mixture consisting of SiC:Si_3N_4:SiO_2 in a ratio of 1:1:1 mol:mol:mol, using a ZrO rotor spun at 7kHz and direct polarization (zg pulse sequence). Acquisition parameters: number of scans: 16384; relaxation delay: 5 sec; acquisition time: 0.0129 sec; power level for pulse: 250 W. Integrated areas: SiC: 39.02; Si_3N_4: 7.77; SiO_2: 53.02.

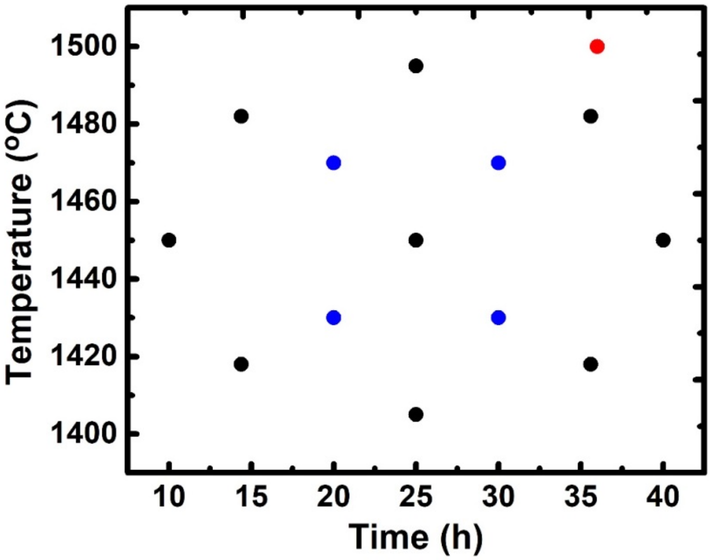

Figure S.2. Samples prepared in order to identify the optimal conditions (pyrolysis temperature and time) for Si_3N_4. Black points: samples suggested by a *Central Composite Rotatable Design* (CCRD) statistical method. Blue points: extra points added to the CCRD design in order to increase confidence. Red point: conditions predicted to produce pure Si_3N_4.

Table S.1. Quantitative analysis using solid-state ^{29}Si NMR under the conditions indicated in the legend of Figure S.1 of samples prepared by pyrolysis of X-APTES@TMOS compacts according to the conditions of Figure S.2.

Sample	Pyrolysis Time - Temperature	Quantitative Analysis from NMR (Lorentzian fitting)			
		wt% Si_3N_4	wt% SiC	wt% SiO_2	Mole Ratio [Si_3N_4] : [SiC] : [SiO_2]
1	10 h – 1450 °C	42.15	19.04	38.81	1 : 1.58 : 2.15
2	14.39 h – 1418 °C	69.38	6.55	24.07	1 : 0.33 : 0.81
3	14.39 h – 1482 °C	71.14	13.02	15.84	1 : 0.64 : 0.52
4	20 h – 1430 °C	74.24	5.73	20.03	1 : 0.27 : 0.63
5	20 h – 1470 °C	83.14	6.18	10.68	1 : 0.26 : 0.30
6	25 h – 1405 °C	79.83	3.42	16.75	1 : 0.15 : 0.49
7	25 h – 1450 °C	80.37	5.52	14.11	1 : 0.24 : 0.41
8	25 h – 1450 °C	80.47	7.13	12.40	1 : 0.31 : 0.36
9	25 h – 1495 °C	88.72	7.10	4.18	1 : 0.28 : 0.11
10	30 h – 1430 °C	81.88	6.55	11.57	1 : 0.28 : 0.33
11	30 h – 1470 °C	84.96	6.31	8.73	1 : 0.26 : 0.24
12	35.61 h – 1418 °C	86.97	2.98	10.05	1 : 0.12 : 0.27
13	35.61 h – 1482 °C	90.10	6.43	3.47	1 : 0.25 : 0.09
14	40 h – 1450 °C	85.06	5.83	9.11	1 : 0.24 : 0.25
15	36 h – 1500 °C	99.68	0	0.32	1 : 0.00 : 0.007

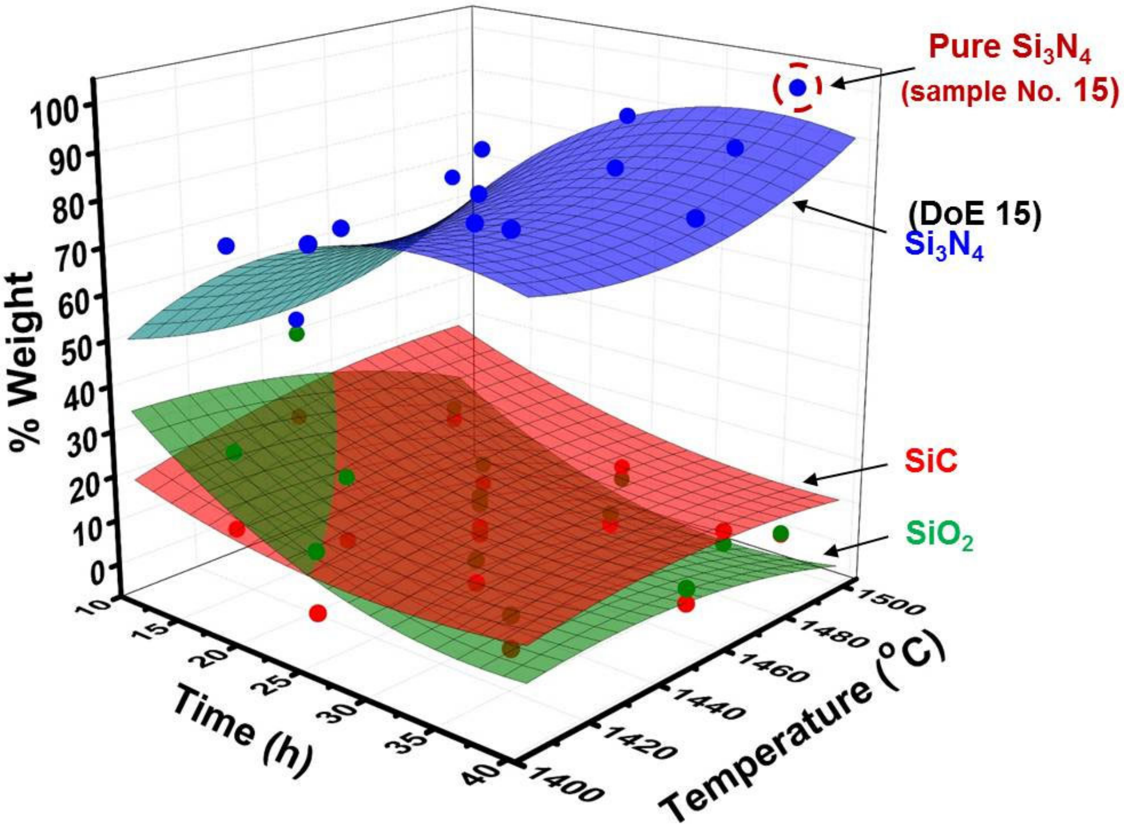

Figure S.3. Fitting the weight percent data for SiC, Si_3N_4 and unreacted SiO_2 (from Table S.1) in samples produced by pyrolysis of X-APTES@TMOS compacts for the time periods (t) and at the specific temperatures (θ) as indicated. The fitting equations are:

$$\%SiC = (0.022_1)t^2 + (-0.001_4)\theta^2 + (-0.004_2)t\theta + (4.66_9)t + (4.30_7)\theta + (-3199)$$

$R^2 = 0.82904$

$$\%Si_3N_4 = (-0.063_6)t^2 + 0.003_4)\theta^2 + (0.001_1)t\theta + (2.73_5)t + (-9.80_7)\theta + (7078)$$

$R^2 = 0.91297$

$$\%SiO_2 = (0.042_5)t^2 + (-0.002_9)\theta^2 + (0.003_1)t\theta + (-7.39_4)t + (5.50_0)\theta + (-3780)$$

$R^2 = 0.93479$

Appendix III. Solid-state ^{29}Si NMR of APTES@TMOS and of X-APTES@TMOS under two different acquisition conditions

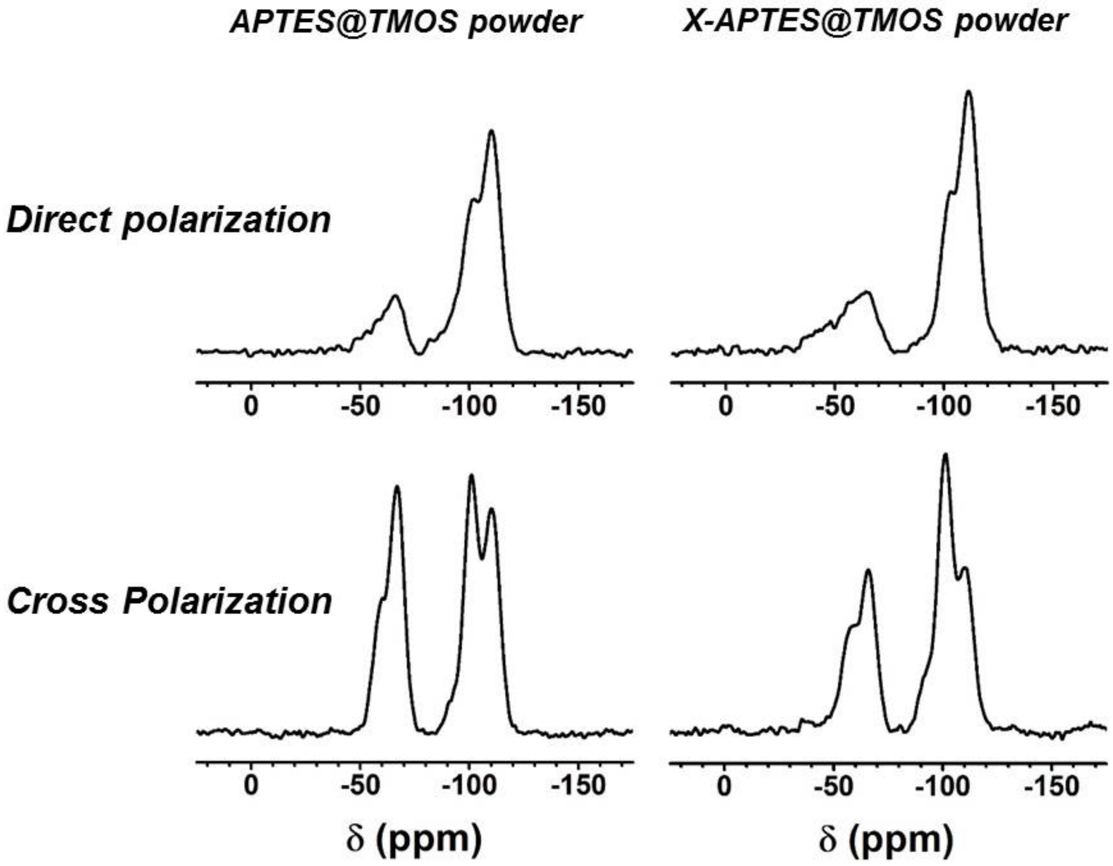

Figure S.4. Solid-state ^{29}Si NMR data for the two materials as indicated taken using two different modes: Direct and cross-polarization (CP). Note the enhancement of Q3 and T2 under CP, and the even higher enhancement of Q3 relative to Q4 after crosslinking, signifying that the TIPM-derived crosslinking polymer (polyurea) laches not only on APTES-provided –NH_2 groups, but also on –OH groups of Q3 positions.

REFERENCES

1. Vareda, J. P.; Lamy-Mendes, A.; Durães, L. A Reconsideration on the Definition of the Term Aerogel Based on Current Drying Trends. *Micropor. Mesopor. Mat.* **2018**, *258*, 211-216.

2. Pierre, A. C.; Pajonk, G. M. Chemistry of Aerogels and Their Applications. *Chem. Rev.* **2002**, *102*, 4243−4265.

3. Hüsing, N.; Schubert, U. Aerogels-airy Materials: Chemistry, Structure, and Properties. *Angew. Chem., Int. Ed.* **1998**, *37*, 22–45.

4. Brinker, C. J.; Scherer, G. W. *Sol-Gel Science*. The Physics and Chemistry of Sol-gel Processing. Academic Press: New York, 1990.

5. Leventis, N. Interpenetrating Organic/Inorganic Networks of Resorcinol-Formaldehyde / Metal Oxide Aerogels in *Aerogels Handbook - Advances in Sol-Gel Derived Materials and Technologies.* Aegerter, M.; Leventis, N.; Koebel, M. Eds., Springer: New York, NY, **2011**, Chapter 14, pp 287-313.

6. Leventis, N. Three-Dimensional Core-Shell Superstructures: Mechanically Strong Aerogels. *Acc. Chem. Res.* **2007**, *40*, 874–884.

7. While, L. S.; Echard, D. R.; Bertino, M. F.; Gao, X.; Donthula, S.; Leventis, N.; Shukla, N.; Kosny, J.; Saeed, S.; Saoud, K. Fabrication of Native Silica, Cross-linked, and Hybrid Aerogel Monoliths with Customized Geometries. *Transl. Mater. Res.* **2016**, *3*, 015002.

8. Maleki, H.; Durães, L.; Portugal, A. A. Development of Mechanically Strong Ambient Pressure Dried Silica Aerogels with Optimized Properties. *J. Phys. Chem. C* **2015**, *119*, 7689-7703.

9. Mohite, D. P.; Larimore, Z. J.; Lu, H.; Mang, J. T.; Sotiriou-Leventis, C.; Leventis, N. Monolithic Hierarchical Fractal Assemblies of Silica Nanoparticles Cross-Linked with Polynorbornene via ROMP: A Structure-Property Correlation from Molecular to Bulk through Nano. *Chem. Mater.* **2012**, *24*, 3434-3448.

10. Leventis, N.; Lu, H. Polymer Crosslinked Aerogels in Aerogels Handbook - Advances in Sol-Gel Derived Materials and Technologies. Aegerter, M.; Leventis, N.; Koebel, M. Eds., Springer: New York, NY, **2011**, pp 251-285.

11. Al-Muhtaseb, S A.; Ritter, J. A. Preparation and Properties of Resorcinol–Formaldehyde Organic and Carbon Gels. *Adv. Mater.* **2003**, *15*, 101–114.

12. Leventis, N.; Chandrasekaran, N.; Sadekar, A. G.; Sotiriou-Leventis, C.; Lu, H. One-Pot Synthesis of Interpenetrating Inorganic/Organic Networks of CuO/Resorcinol-Formaldehyde Aerogels: Nanostructured Energetic Materials. *J. Am. Chem. Soc.* **2009**, *131*, 4576-4577.

13. Mahadik-Khanolkar, S.; Donthula, S.; Bang, A.; Wisner, C.; Sotiriou-Leventis, C.; Leventis, N. Polybenzoxazine Aerogels. 2. Interpenetrating Networks with Iron Oxide and the Carbothermal Synthesis of Highly Porous Monolithic Pure Iron(0) Aerogels as Energetic Materials. *Chem. Mater.* **2014**, *26*, 1318-1331.

14. Leventis, N.; Chandrasekaran, N.; Sotiriou-Leventis, C.; Mumtaz, A. Smelting in the Age of Nano: Iron Aerogels. *J. Mater. Chem.* **2009**, *19*, 63-65.

15. Leventis, N.; Chandrasekaran, N.; Sadekar, A. G.; Mulik, S.; Sotiriou-Leventis, C. The Effect of Compactness on the Carbothermal Conversion of Interpenetrating Metal Oxide / Resorcinol-Formaldehyde Nanoparticle Networks to Porous Metals and Carbides. *J. Mater. Chem.* **2010**, *20*, 7456 – 7471.

16. Saito, M.; Nagashima, S.; Kato, A. Crystal Growth of SiC Whisker from the SiO(g)-CO System. *J. Mater. Sci. Lett.* **1992**, *11*, 373–376.

17. Klinger N.; Strauss E.; Komarek K.; Reactions Between Silica and Graphite. *J. Am. Ceram. Soc*. **1966**, *9*, 369–375.

18. Bandyopadhyay, S.; Mukerji, J. Reaction Sequences in the Synthesis of Silicon Nitride from Quartz. *Ceram. Int.* **1991**, *17*, 171–179.

19. Ličko, T.; Figusch, V.; Púchyová, J. Synthesis of Silicon Nitride by Carbothermal Reduction and Nitriding of Silica: Control of Kinetics and Morphology. *J. Eur. Ceram. Soc.* **1992**, *9*, 219–230.

20. Chung, S. L.; Chang, C. W. Carbothermal Reduction and Nitridation Synthesis of Silicon Nitride by Using Solution Combustion Synthesized Precursors. *J. Mater. Sci.* **2009**, *44*, 3784–3792.

21. Leventis, N.; Sadekar, A.; Chandrasekaran, N.; Sotiriou-Leventis, C. Click Synthesis of Monolithic Silicon Carbide Aerogels from Polyacrylonitrile-Crosslinked 3D Silica Networks. *Chem. Mater.* **2010**, *22*, 2790-2803.

22. Ledoux, M. J.; Pham-Huu, C**.** Silicon Carbide: A Novel Catalyst Support for Heterogeneous Catalysis**.** *CATTECH* **2001**, *5*, 226–246.

23. Moene, R.; Makkee, M.; Moulijn, J. A. High Surface Area Silicon Carbide as Catalyst Support. Characterization and Stability. *Appl. Catal., A* **1998**, *167*, 321–330.

24. Greil, P. Biomorphous Ceramics from Lignocellulosics. *J. Eur. Ceram. Soc.* **2001**, *21*, 105–118.

25. Qian, J.-M.; Wang, J.-P.; Qiao, G.-J.; Jin, Z.-H. Preparation of Porous SiC Ceramic with a Woodlike Microstructure by Sol-gel and Carbothermal Reduction Processing. *J. Eur. Ceram. Soc.* **2004**, *24*, 3251–3259.

26. Sonnenburg, K.; Adelhelm, P.; Antonietti, M.; Smarsly, B.; Nöske, R.; Strauch, P. Synthesis and Characterization of SiC Materials with Hierarchical Porosity Obtained by Replication Techniques. *Phys. Chem. Chem. Phys.* **2006**, *8*, 3561–3566.

27. Katti, A.; Shimpi, N.; Roy, S.; Lu, H.; Fabrizio, E. F.; Dass, A.; Capadona, L. A.; Leventis, N. Chemical, Physical and Mechanical Characterization of Isocyanate-Crosslinked Amine-Modified Silica Aerogels. *Chem. Mater.* **2006**, *18*, 285-296.

28. M. A. B. Meador, M. A. B.; Capadona, L. A.; MacCorkle, L.; Papadopoulos, D. S.; Leventis, N. Structure-Property Relationships in Porous 3D Nanostructures as a Function of Preparation Conditions: Isocyanate Cross-Linked Silica Aerogels. *Chem. Mater.* **2007**, *19*, 2247-2260.

29. Hüsing, N.; Schubert, U.; Mezei, R.; Fratzl, P.; Riegel, B.; Kiefer, W.; Kohler, D.; Mader, W. Formation and structure of gel networks from $Si(OEt)_4/(MeO)_3Si(CH_2)_3NR_2'$ mixtures (NR_2' = NH_2 or $NHCH_2$-CH_2NH_2). *Chem. Mater.* **1999**, *11*, 451–457.

30. Leventis, N.; Elder, I. A.; Rolison, D. R.; Anderson, M. L.; Merzbacher, C. I. Durable Modification of Silica Aerogel Monoliths with Fluorescent 2,7-Diazapyrenium Moieties - Sensing Oxygen near the Speed of Open-Air Diffusion. *Chem. Mater.* **1999**, *11*, 2837-2845.

31. Leventis, N.; Sotiriou-Leventis, C.; Saeed, A. M.; Donthula, S.; Majedi Far, H.; Rewatkar, P. M.; Kaiser, H.; Robertson, J. D.; Lu, H.; Churu, G. Nanoporous Polyurea from a Triisocyanate and Boric Acid: A Paradigm of a General Reaction Pathway for Isocyanates and Mineral Acids. *Chem. Mater.* **2016**, *28*, 67-78.

32. Leventis, N.; Sotiriou-Leventis, C.; Chandrasekaran, N.; Mulik, S.; Larimore, Z. J.; Lu, H.; Churu, G.; Mang, J. T. Multifunctional Polyurea Aerogels from Isocyanates and Water. A Structure-Property Case Study. *Chem. Mater.* **2010**, *22*, 6692-6710.

33. Zujovic, Z. D.; Etzion, R.; Metson, J. B. Solid-State NMR Characterization of Silicon Nitride Bonded Silicon Carbide Refractories. *Ind. Eng. Chem. Res.* **2008**, *47*, 9913–9918.

34. Leonova, E.; Grins, J.; Shariatgorji, M; Ilag, L. L.; Edén, M. Solid-state NMR investigations of Si-29 and N-15 enriched silicon nitride. *Solid State Nucl. Mag. Res.* **2009**, *36*, 11–18.

35. Patterson, A. The Scherrer Formula for X-Ray Particle Size Determination. *Phys. Rev.* **1939**, *56*, 978–982.

36. Bulk Density and Tapped Density of Powders. World Health Organization Document QAS/11.450, March 2012.)

37. Roy, J.; Chandra, S.; Das, S.; Maitra, S. Oxidation Behaviour of Silicon Carbide - A Review. *Rev. Adv. Mater. Sci* **2014**, *38*, 29–39.

38. She, J. H.; Obji, T.; Kanzaki, S. Oxidation Bonding of Porous Silicon Carbide Ceramics with Synergistic Performance. *J. Eur. Ceram. Soc.* **2003**, *24*, 331–334.

39. Cowan, R. D. Proposed Method of Measuring Thermal Diffusivity at High Temperatures. *J. Appl. Phys.* **1961**, *32*, 1363−1369.

40. Cowan, R. D. Pulse Method of Measuring Thermal Diffusivity at High Temperatures. *J. Appl. Phys.* **1963**, *34*, 926−927.

41. http://accuratus.com/materials.html (10-10-2017)

42. Lu, X.; Arduini-Schuster, M. C.; Kuhn, J.; Nilsson, O.; Fricke, J.; Pekala, R. W. Thermal Conductivity of Monolithic Organic Aerogels. *Science* **1992**, *255*, 971−972.

43. Reichenauer, G.; Heinemann, U.; Ebert, H.-P. Relationship between Pore Size and the Gas Pressure Dependence of the Gaseous Thermal Conductivity. *Colloids Surf. A* **2007**, *300*, 204−210.

44. Chidambareswarapattar, C.; McCarver, P. M.; Luo, H.; Lu, H.; Sotiriou-Leventis, C.; Leventis, N. Fractal Multiscale Nanoporous Polyurethanes: Flexible to Extremely Rigid Aerogels from Multifunctional Small Molecules. *Chem. Mater.* **2013**, *25*, 3205−3224.

45. Calister, W. D. Jr. Materials Science and Engineering an Introduction, Fourth Edition, John Wiley & Sons, Inc. New York, N.Y.: 1997, Chapter 13.8, p 401.

46. Alnaief, M.; Smirnova, I. In Situ Production of Spherical Aerogel Microparticles. *J. Supercrit. Fluid* **2011**, *55*, 1118-1123.

47. Mounfield, C. C.; Edwards, S. F. A Model for the Packing of Irregularly Shaped Grains. *Physica A* **1994**, *210*, 301-316.

48. Matrin, H. P.; Ecke, R.; Muller, E. Synthesis of Nanocrystalline Silicon Carbide Powder by Carbothermal Reduction. *J. Eur. Ceram. Soc*. **1998**, *18*, 1737–1742.

49. Paccaud, O.; Derré, A. Silicon Carbide Coating by Reactive Pack Cementation. Part 1. Silicon Carbide/ Silica Interaction. *Chem. Vap. Deposition* **2000**, *6*, 33–40.

50. Vix-Guterl, C.; McEnaney, B.; Ehrburger, P. SiC Material Produced by Carbothermal Reduction of a Freeze Gel Silica-carbon Artefact. *J. Eur. Ceram. Soc.* **1999**, *19*, 427–432.

51. Lu, X.; Caps, R.; Fricke, J.; Alviso, C. T.; Pekala, R. W. Correlation between Structure and Thermal Conductivity of Organic Aerogels. *J. Non-Cryst. Solids* **1995**, *188*, 226−234.

52. Lu, X.; Nilsson, O.; Fricke, J.; Pekala, R. W. Thermal and Electrical Conductivity of Monolithic Carbon Aerogels. *J. Appl. Phys.* **1993**, *73*, 581−584.

53. Weigold, L.; Mohite, D. P.; Mahadik-Khanolkar, S.; Leventis, N.; Reichenauer, G. Correlation of Microstructure and Thermal Conductivity in Nanoporous Solids: The Case of Polyurea Aerogels Synthesized from an Aliphatic Triisocyanate and Water. *J. Non-Cryst. Solids* **2013**, *368*, 105-111.

54. Fricke, J.; Lu, X.; Wang, P.; Büttner, D.; Heinemann, U. Optimization of Monolithic Silica Aerogel Insulants. *Int. J. Heat Mass Transfer* **1992**, *35*, 2305−2309.

55. Ashby, M. F. The Properties of Foams and Lattices. *Phil. Trans. R. Soc. A* **2006**, *364*, 15-30.

56. Gross, J.; Fricke, J.; Pekala, R. W.; Hrubesh, L. W. Elastic Nonlinearity of Aerogels. *Phys. Rev. B* **1992**, *45*, 12774−12777.

57. Gross, J.; Fricke, J. Ultrasonic Velocity Measurements in Silica, Carbon and Organic Aerogels. *J. Non-Cryst. Solids* **1992**, *145*, 217−222.

58. Pekala, R. W.; Alviso, C. T.; Lemay, J. D. Organic Aerogels: Microstructural Dependence of Mechanical Properties in Compression *J. Non-Cryst. Solids* **1990**, *125*, 67−75.

59. Jana, D. C.; Sundararajan, G.; Chattopadhyay, K. Effect of Porosity on Structure, Young's Modulus, and Thermal Conductivity of SiC foams by Direct Foaming and Gelcasting. *J. Am. Ceram. Soc.* **2017**, *100*, 312-322.

60. Li, Z.-Y.; Liu, H.; Zhao, X.-P.; Tao, W.-Q. A Multi-Level Fractal Model for the Effective Thermal Conductivity of Silica Aerogel. *J. Non. Cryst. Solids* **2015**, *430*, 43–51.

61. Lu, H; Luo, H; Leventis N. Mechanical Characterization of Aerogels in *Aerogels Handbook - Advances in Sol-Gel Derived Materials and Technologies.* Aegerter, M.; Leventis, N.; Koebel, M. Eds., Springer: New York, NY, **2011**, Chapter 22, pp 499-536.

62. Leventis, N.; Donthula, S.; Mandal, C.; Ding, M. S.; Sotiriou-Leventis, C. Explosive versus Thermite Behavior in Iron(0) Aerogels Infiltrated with Perchlorates. *Chem. Mater.* **2015**, *27*, 8126-8137.

63. Mahadik-Khanolkar, S.; Donthula, S.; Bang, A.; Wisner, C.; Sotiriou-Leventis, C.; Leventis, N. Polybenzoxazine Aerogels. 2. Interpenetrating Networks with Iron Oxide and the Carbothermal Synthesis of Highly Porous Monolithic Pure Iron(0) Aerogels as Energetic Materials. *Chem. Mater.* **2014**, *26*, 1318-1331.

64. Leventis, N.; Vassilaras, P.; Fabrizio, E. F.; Dass, A. Polymer Nanoencapsulated Rare Earth Aerogels: Chemically Complex but Stoichiometrically Similar Core-Shell Superstructures with Skeletal Properties of Pure Compounds. *J. Mater. Chem.* **2007**, *17*, 1502-1508.

65. Parker, W. J.; Jenkins, R. J.; Butler, C. P.; Abbott, G. L. Flash Method of Determining Thermal Diffusivity, Heat Capacity, and Thermal Conductivity. *J. Appl. Phys.* **1961**, *32*, 1679−1684.

66. Lee, D.; Stevens, P. C.; Zeng, S. Q.; Hunt, A. J. Thermal Characterization of Carbon-opacified Silica Aerogels. *J. Non-Cryst. Solids* **1995**, *186*, 285−290.

67. Leventis, N.; Sotiriou-Leventis, C.; Mulik, S.; Dass, A.; Schnobrich, J.; Hobbs, A.; Fabrizio, E. F.; Luo, H.; Churu, G.; Zhang, Y.; Lu, H. Polymer Nanoencapsulated Mesoporous Vanadia with Unusual Ductility at Cryogenic Temperatures. *J. Mater. Chem.* **2008**, *18*, 2475–2482.

II. A COBALT SUNRISE: THERMITES BASED ON $LiClO_4$-FILLED Co(0) *AEROGELS* PREPARED *FROM* POLYMER-CROSSLINKED COBALTIA *XEROGEL* POWDERS

Parwani M. Rewatkar, Rushi U. Soni, Chariklia Sotiriou-Leventis* and Nicholas Leventis*

Department of Chemistry, Missouri University of Science and Technology, Rolla, MO 65409, U.S.A. *Corresponding authors: Tel.: 573-341-4391 (N.L.); 573-341-4353 (C.S.-L.). E-mail: leventis@mst.edu; cslevent@mst.edu

ABSTRACT

A new route to metallic aerogels that bypasses use of supercritical fluids and handling fragile wet-gel and aerogel precursors is exemplified by the carbothermal synthesis of monolithic Co(0) aerogels from compressed cobaltia xerogel powders coated conformally (crosslinked) at the primary particle level with a carbonizable polyurea. Residual carbon is removed and carbon-free samples are obtained by high-temperature treatment of as-prepared Co(0) aerogels under a flowing stream of H_2O/H_2 that prevents oxidation of the Co(0) network. The durability of Co(0) aerogels is demonstrated under harsh processing conditions in their application as thermites. For this, Co(0) aerogel discs are infiltrated with $LiClO_4$ from a melt, and are ignited at about 1100 °C with an electric resistor. As Co(0) "burns" to CoO, temperature exceeds 1500 °C, and the heat released ($55._2 \pm 2$ kcal mol^{-1}) is near to both the theoretical value (-58.47 kcal mol^{-1}) and that from well-known pressed-pellet iron/perchlorate thermites (66.6 kcal mol^{-1}). The advantage of

nanostructured thermites based on Co(0) aerogels is the efficiency (100%) by which the metal is consumed during its reaction with $LiClO_4$ filling the pores.

Keywords: cobalt, aerogel, xerogel, carbothermal, thermite

TOC Graphic

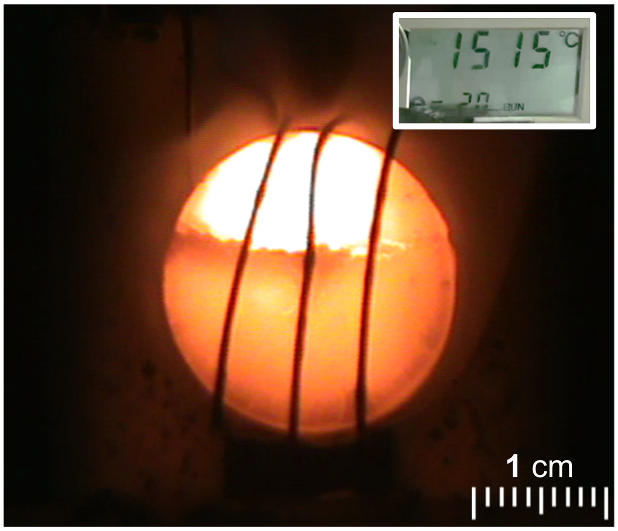

1. INTRODUCTION

Aerogels are open solid colloidal or polymer networks that are obtained by removing the swelling agents from a gel without substantial volume reduction or network compaction.[1] That definition has been expanded to include materials whose precursors are "regular" aerogels derived via the sol-gel route.[2,3] The most well-known class of materials in that category is carbon aerogels, but it also includes several porous metals and porous ceramics (*e.g.*, carbides, nitrides). Thus, although nanoporous metal foams can be prepared from suitable metal complex precursors *via*, for example, combustion synthesis,[4] and while monolithic noble metal aerogels can be prepared *via* direct sol-gel destabilization of colloids of noble metal nanoparticles,[5,6,7] a large sub-set of monolithic metallic aerogels can be prepared *via* carbothermal reduction of interpenetrating aerogel networks of a nanostructured oxide and a carbonizable polymer.[8,9,10,11,12] Interestingly, carbothermal reduction of interpenetrating xerogel networks takes place consistently at about 400 °C below the temperature needed for the exact same reduction in the corresponding aerogels, pointing to the importance of the proximity of the reactants at the nanoscopic level.[13] Thereby, the carbothermal route to metallic aerogels could be improved if the carbonizable polymer coats conformally the oxide network. That type of composite aerogels are referred to as polymer-crosslinked or X-aerogels, and are obtained by reaction of surface functional groups on wet-gels with suitable monomers.[14,15,16,17]

The X-aerogel route was first employed toward carbothermal synthesis of isomorphic SiC aerogels from polyacrylonitrile-crosslinked silica aerogel monoliths.[1] Unfortunately, however, any benefits from crosslinking are negated by the long diffusion time needed in order for crosslinking reagents and solvents to infiltrate the interior of large monolithic wet-gels, and thus reach, react and latch on the skeletal nanoparticles throughput. That issue is further compounded by the drying process of wet-gel to aerogels that typically involves converting the pore-filling solvent into a supercritical fluid (SCF) that is vented off like a gas. Alternatively, we have demonstrated recently that large monolithic SiC and Si_3N_4 aerogels can be prepared by pyrolysis of compressed compacts of X-silica *xerogel powders* obtained from suspensions of sol-gel particles, which in turn were obtained by disrupting gelation of silica sols with vigorous stirring.[18] That method does not involve molding and handling fragile wet-gels and/or aerogels, and bypasses the use of SCF for drying wet-gels into aerogels, or the need for long drying times for converting wet-gels into xerogels. That is, the short time/distance that reagents and solvents need to diffuse over in order to access the interior of the wet-gel grains of the suspension cuts down the crosslinking process from days to minutes. High porosity was created when the crosslinking polymer reacted away during carbothermal reduction of silica toward the carbide or the nitride.

Here, that methodology is extended to large-size monolithic metallic Co(0) aerogels, for which a route through monolithic aerogel precursors could not have even been practical, as reportedly only a few selected cobaltia sols can gel, and they do so with great difficulty (gelation time ~ 10 days).[19] The durability of the newly prepared Co(0) aerogels was probed under extreme processing conditions: the porous space of Co(0) aerogels was filled almost completely with molten $LiClO_4$, the resulting composites did not shrink, remained monolithic and were demonstrated as thermites[20] analogous to pressed Fe(0)/$KClO_4$ pellets that are used in thermal batteries.[21,22] Thermal batteries include an electrolytic salt that becomes an ionic conductor after melting through the heat provided by a thermite. Alternatively, the electrolytic salt can form an ionic conductor by dissolution, thereby the same concept has been extended to wet-condition indicators.[23]

2. RESULTS AND DISCUSSION

The overall process to Co(0) aerogels and their operation as thermites is summarized in Scheme 1. Synthetic procedures are detailed in the Experimental section.

Comprehensive materials characterization data have been compiled in Table S.1 of Appendix I in Supporting Information. The sections below discuss the rationale, chemical transformations, and characterization data of the various intermediates along processing.

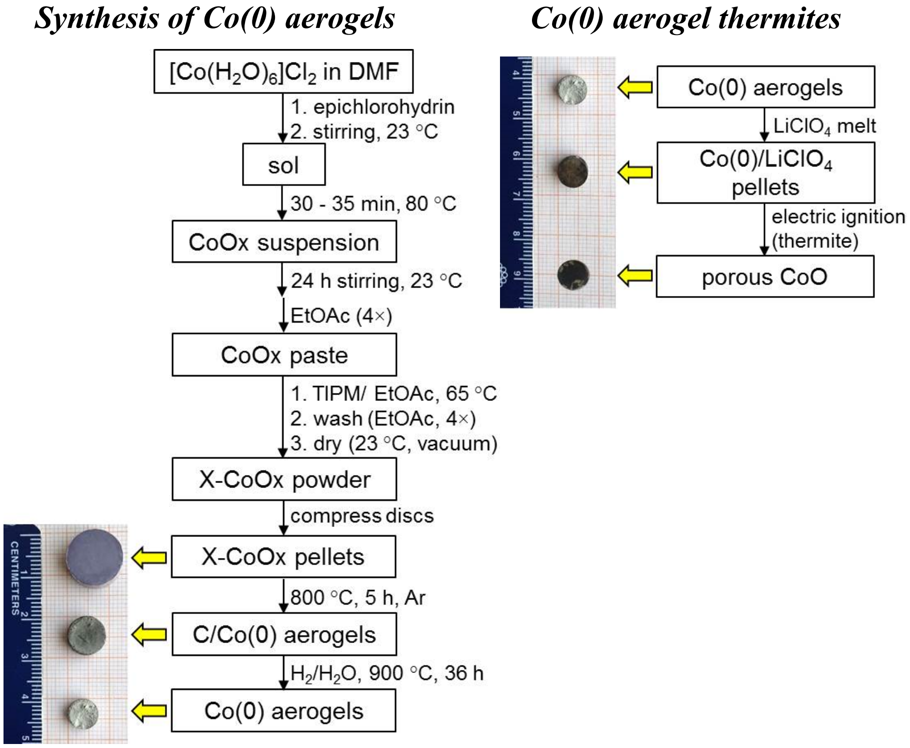

Scheme 1. Synthesis of Co(0) aerogels and their implementation as thermites

2.1. PREPARATION OF COBALTIA (CoOx) POWDER

Cobaltia (CoOx) suspensions were produced from DMF sols *via* reaction of $[Co(H_2O)_6]Cl_2$ with a proton acceptor (epichlorohydrin).[24,25,26] For characterization purposes part of the suspension was centrifuged and the precipitate was washed and dried under vacuum. Importantly, the $[Co(H_2O)_6]Cl_2$ salt is pink, but its DMF solutions were blue suggesting that octahedral $[Co(H_2O)_6]^{2+}$ was in equilibrium with tetrahedral $[CoCl_4]^{2-}$ (Scheme 2, Eq 1).[27] The position of that equilibrium was evaluated by titrating a DMF solution of $[Co(H_2O)_6](NO_3)_2$ (at the same concentration as in the sol: 0.43 M) with aqueous HCl. Figure 1 shows that the spectrum of the $[Co(H_2O)_6]Cl_2$ in DMF was practically the same as the spectrum of the nitrate salt plus 4 mol equivalents of HCl, suggesting that gelation of the hexahydtate salt with epichlorohydrin (Scheme 2, Eq 2) was convoluted with Eq 1, the equilibrium of which lies to the left. Reasonably, Eq 1 is expected to be also involved at the surface of the CoOx particles resulting from Eq 3. Indeed, prior TEM work has shown that cobaltia nanoparticles do form in our sol.[13] Furthermore, the thermogravimetric (TGA) profile of CoOx (Figure 2a) shows two mass loss events in the 200-400 °C range (pointed at by blue arrows); reasoning by analogy to $Co(OH)_2$ and $Co_2(OH)_3Cl$,[19,28] the first mass loss, which is observed at around 220 °C, is assigned to dehydroxylation of –OH capped cobaltia nanoparticles, while the second one, at around 300 °C, involves loss of chlorine from –Cl capped particles. Presence of a significant amount of surface –Cl caps suggests a reduced aptitude for cobaltia nanoparticles to develop interparticle Co–O–Co bridges, which are a prerequisite for gelation. Notwithstanding the reasons that prevent large-scale gelation, as outlined in the Introduction, this work bypasses the need to make monolithic cobaltia aerogels (or xerogels) toward metallic Co(0) aerogels.

The multidisperse irregular grains of the precipitate from Equation 3 (Figure 3a-left) had an internal nanostructure typical of an oxide sol-gel materials (xerogel or aerogel) (Figure 3a-right). The skeletal density, ρ_s, of the CoOx xerogel powder was 3.137 ± 0.003 g cm^{-3} and the BET surface area, σ, was 62.4 m^2 g^{-1}. The primary particle diameter was about 31 nm [= $6 / (\rho_s \times \sigma)$], and agreed with the minimum particle size in SEM (Figure 1a-right) and previous TEM results.[13] In TGA (Figure 2a), the CoOx xerogel powder lost

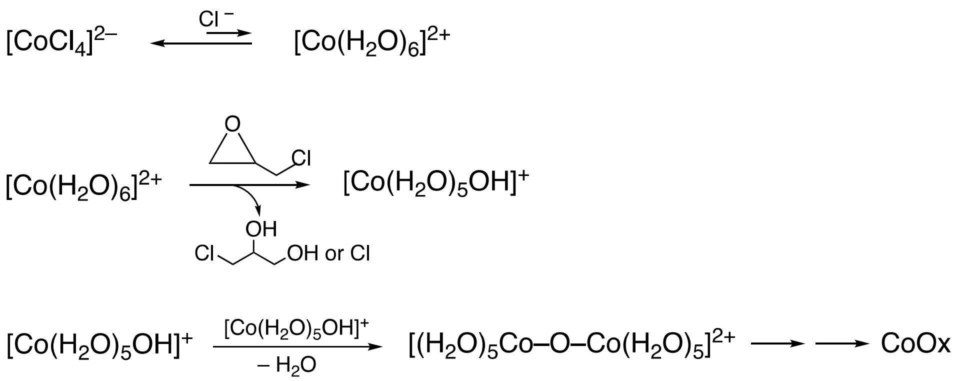

(1)

(2)

Scheme 2. Chemical processes during preparation of cobaltia (CoOx)

about 3% of its mass by 200 °C (attributed to solvent), and another 25% by 400 °C, attributed to dehydroxylation and loss of Cl as discussed above. By 900 °C, TGA under O_2 (Figure 2a) yielded a 73.20% w/w residue that was identified with XRD as Co_3O_4 (Figure 2b); by 1000 °C the residue was reduced to 68.49% w/w and was identified as CoO (Figure 2b). Thereby, CoOx contained about 54% w/w Co.

2.2. CROSSLINKING OF CoOx WITH A CARBONIZABLE POLYUREA – PREPARATION OF X-CoOx

Crosslinking was carried out by adding an aromatic triisocyanate (TIPM – see Eq 4) to CoOx suspensions and heating (Scheme 1). The size of the grains in the new material (X-CoOx) remained unchanged; under high magnification, skeletal particles were still visible, albeit a massive uptake of polymer. While both CoOx and X-CoOx powders were attracted by laboratory magnets, treating X-CoOx powder with aqueous HCl (12 M) yielded a residue that was not magnetic. TGA under O_2 showed that CoOx had been removed almost completely – the residue at 1000 °C was 3.3% w/w (Figure 2a). Solid-state

^{13}C NMR (Figure S.1 of Appendix II in Supporting Information) showed that the residue was chemically identical to polyurea (PUA) obtained *via* reaction of TIPM with water (Eq 4).[26]

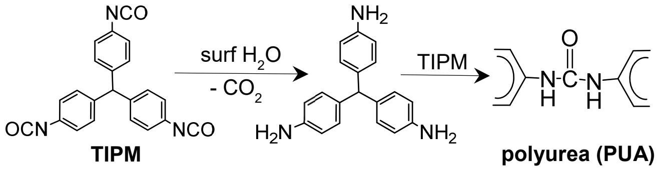

(4)

The skeletal density of the X-CoOx powder dropped to $\rho_s = 1.734 \pm 0.003$ g cm^{-3}, and the BET surface area also decreased to $\sigma = 36.2$ m^2 g^{-1}. Lower ρ_s and σ values increased the apparent particle diameter to about 96 nm. Concurrently, the specific pore volume in the 1.7-300 nm range, $V_{1.7\text{-}300\_\text{nm}}$ (Table S.1), decreased to 0.11 cm^3 g^{-1} (from 0.35 cm^3 g^{-1} in CoOx), consistent with PUA coating the primary CoOx particles, and filling the space in between them. At 1000 °C under O_2, X-CoOx gave a TGA residue of 30.3% w/w (CoO – see Figures 2a and 2b), therefore it was concluded that X-CoOx contained 23.8% w/w Co.

Considering the skeletal density of X-CoOx as the weighted average of the ρ_s values of CoOx (3.137 ± 0.003 g cm^{-3}) and of TIPM-derived polyurea (1.24 g cm^{-3}),[29] the PUA-to-CoOx mass ratio in X-CoOx was calculated equal to 0.74:0.26. Given that: (a) at 800 °C under Ar, the char yield of TIPM-derived polyurea is 56% w/w,[29] and (b) that char consists of 81% w/w C (the balance being N/O in ~1:1 atomic ratio),[29] the carbon yield of X-CoOx at 800 °C was expected to be about 33.6% w/w. Since X-CoOx contains 23.8 w/w Co (see last paragraph above), the expected C:Co mol/mol ratio from carbonization of X-CoOx was equal to 7.0. Given that at 800 °C CoOx yields Co_3O_4 (Figure 2b), the reduction process at 800 ºC requires 2 mol of C per mol of Co_3O_4 for conversion to Co(0) and CO_2.[10] Therefore, it was concluded that the expected C:Co ratio from X-CoOx was sufficient for reduction of the latter to Co(0).

2.3. COMPACTION OF X-CoOx POWDER TO DISCS

Using different dies, X-CoOx powder was compressed under 10,000 psi into different size discs (see Experimental Section). The compaction pressure has not been optimized; the value of 10,000 psi was selected because it is within the typical range used for compressing pellets for infrared spectroscopy, therefore it is easily accessible in most laboratories, rendering reproduction of this work rather straightforward. Compaction did not alter the oxidation state of cobalt. In XPS, the Co 2p spectra of CoOx powder, compressed CoOx powder (at 10,000 psi) and compressed X-CoOx (at 10,000 psi) discs were identical (Figure 4), consisting of two major peaks corresponding to the Co $2p_{1/2}$ and Co $2p_{3/2}$ energy levels (at around 797 and 781 eV, respectively), with a spin-energy separation of about 15.8 eV, and two higher-energy satellite features at around 802 and 785 eV, all characteristic of Co(II) species.[30,31] Just like the X-CoOx powders, compressed X-CoOx discs were attracted by laboratory magnets. Gram magnetic susceptibilities were measured and the values were reduced to magnetic susceptibilities per gram of Co. Thus, the susceptibilities per gram of Co of the CoOx powder and of the $[Co(H_2O)_6]Cl_2$ complex were close to one another (193.35 and 179.94, respectively; theoretical value for the hexahydrated complex: 164.76 – all in cgs units $\times 10^{-6}$); similarly, the susceptibilities per gram of Co of the X-CoOx powder and of the X-CoOx compressed discs were higher, yet close to one another (229.70 and 233.07, respectively – again in cgs units $\times 10^{-6}$), suggesting a direct chemical interaction (bonding) between Co(II) and the polymer, as expected from crosslinking,[14] and that interaction was not altered under 10,000 psi.

The skeletal density of the X-CoOx compacts (1.673 ± 0.009 g cm^{-3}) was practically unchanged from that of the loose X-CoOx powder (see Section 2.2). Based on the ρ_s value and the bulk density of the compact discs (1.340 ± 0.007 g cm^{-3}), their porosity was calculated at 19.9 % v/v. The values of $V_{1.7\text{-}300\_nm}$ and σ (0.0561 cm^3 g^{-1}, and 19.5 m^2 g^{-1}, respectively) were about half relative to those of the X-CoOx powders. The majority of the specific pore volume (62%) was assigned to pores with >300 nm in diameter. Fussion of the X-CoOx aggregates as well as macroporosity, presumably created when grains of X-CoOx were squeezed together, were both evident in SEM (Figure 3b).

2.4. CARBOTHERMAL REDUCTION OF X-CoOx COMPACT DISCS AND REMOVAL OF RESIDUAL CARBON

Reduction of X-CoOx compacts was carried out at 800 °C under flowing Ar (Scheme 1). Discs came out black and remained monolithic. Their bulk density was 2.14 ± 0.02 g cm^{-3}. XRD showed only one crystalline phase, α-Co (Figure 5), but the skeletal density (3.80 ± 0.09 g cm^{-3}) was much lower than the density of metallic Co (8.90 g cm^{-3}). SEM showed bright metallic protrusions embedded in amorphous matter (Figure 3c). CHN analysis yielded 41.55 ± 0.2 % C w/w. Despite shrinkage (31.5_6 ± 0.19 % in linear dimensions – see Table S.1), the porosity (44% v/v) was >2× than the porosity of the X-CoOx compressed discs (19.9 % v/v). In TGA under O_2, the product lost 31.31% of its mass up to 900 °C and an additional 4.49% by 1000 °C (Figure 6). The first mass loss was attributed to unreacted carbon and conversion of Co(0) to Co_3O_4, while the second mass loss was due to conversion of Co_3O_4 to CoO (as discussed in conjunction with Figure 2).

By either value, the atomic ratio of unreacted C-to-Co(0) was 4.83, which is in reasonable agreement with the after-pyrolysis expected atomic ratio of C:Co (7.0), and the 1:2 mol/mol stoichiometry of the reduction of Co_3O_4 to Co(0) and CO_2 (see above).[10]

A demanding application of Co(0) aerogels is as thermites for thermal batteries.[20,21] Because of the confined space in the latter devices, combustion of residual carbon would cause an explosion. A second cause of explosion is the rapid heating and expansion of the pore filling air.[11,32] This type of explosion is facilitated by weakening of the metallic network under oxidative carbon removal (*e.g.*, with O_2 at 600 °C).[32] Thereby, our approach here was first to remove carbon under conditions that would provide an overwhelmingly reducing environment around Co(0), and second to fill the pores with the oxidant ($LiClO_4$) almost completely.

Carbon was removed with water vapor using H_2 as the carrier gas at two different temperatures, 800 °C and 900 °C. (It is noted that if the carrier gas for the water vapor is Ar, while all other conditions remain the same, Co(0) is oxidized completely to CoO – by XRD, data not shown.) In SEM, the 800 °C samples had a more open structure than the 900 °C samples (compare Figures 3d and 3e). (For further comparison of the properties of the two materials refer to Table S.1) For thermites, we opted to proceed with the 900 °C samples, because smaller pores had the tendency to retain molten $LiClO_4$ longer, thus minimizing its spillage, which may reduce the amount of oxidizer available for combustion of the Co(0) network. Post carbon-removal CHN analysis yielded C: 0.12 ± 0.02% w/w; H: -0.03±0.00$_5$% w/w; N: 0.02±0.00$_5$% w/w. XRD showed only one crystalline phase (α-Co) over a flat baseline (Figure 5). TGA under N_2 of carbon-free Co(0) aerogels showed essentially a flat profile up to 1000 °C (Figure 6). TGA under O_2 showed first a 135.9%

mass increase up to 922.2 ºC (expected for Co(0)-to-Co_3O_4: 136.20% w/w), and a subsequent decrease to 127.3% (expected for Co(0)-to-CoO: 127.15%). (The chemical identity of the two residues at the two temperatures was confirmed with XRD – just as in Figure 2b.)

Macroscopically, Co(0) aerogels from the 900 ºC treatment for carbon removal (referred to as Co(0)-900 samples) were silvery-gray and extremely sturdy with a Young's modulus = 689 ± 10 MPa and ultimate compressive strength = 1035 ± 19 MPa at over 80% strain (see Figure S.2 of Appendix III in Supporting Information). By comparison, the Young's moduli of ceramic SiC and Si_3N_4 aerogels made by the same method described here (*i.e.*, from xerogel powders) were much lower (37 and 59 MPa, respectively),[18] and iron aerogels made from interpenetrating networks had to be annealed at 1,200-1,300 ºC to reach the same density as the Co(0)-900 aerogels, yet their Young's modulus was less than half (316 MPa).[32] The distribution of open pores in the Co(0)-900 samples was centered at 11 μm (by Hg-intrusion – see Figure S.3 of Appendix IV in Supporting Information). The skeletal density of the same samples was 8.2 ± 0.1 g cm^{-3} (versus 8.90 g cm^{-3} for pure Co(0)) indicating 7.45% v/v of closed porosity along the metallic framework. Consistent with SEM, the BET surface area was low (0.46 m^2 g^{-1}). However, given that intimate contact of solid-state reagents is as important, or even more so, than how finely divided are the reagents (as pointed out in the Introduction, xerogels react more efficiently than corresponding aerogels[13]) the low surface area of Co(0)-900 was of low concern as long as the porous space was large enough to accommodate the amount of oxidizer ($LiClO_4$) needed for complete consumption of Co(0). Indeed, from skeletal and bulk density data (3.16 ± 0.07 g cm^{-3}), open porosity was sufficiently high (62% v/v), and it should be able to accommodate the amount of $LiClO_4$ needed for complete combustion of the Co(0) in the aerogel discs.

2.5. FILLING THE POROUS SPACE OF Co(0) AEROGELS WITH $LiClO_4$ AND INGNITION

Co(0) aerogels were filled with $LiClO_4$ via capillary action from a melt in a sublimation apparatus under vacuum at 270 °C. ***CAUTION:*** This is a highly energetic system, and all safety rules must be obeyed at all times (see Experimental section).

The Co(0)-$LiClO_4$ pellets did not shrink relative to the Co(0) aerogels (Scheme 1 and Table S.1). α-Co remained the only Co(0) phase. Based on bulk and skeletal density data ($3.8_6 \pm 0.20$ g cm^{-3} and $4.12_2 \pm 0.056$ g cm^{-3}, respectively) the porosity of the $LiClO_4$-loaded Co(0) pellets was reduced to 6.4 % v/v (from 62% v/v before infiltration with $LiClO_4$). Based either on those skeletal density data, or the mass gain of the Co(0)-$LiClO_4$ pellets, the amount of $LiClO_4$ was 1.01 ± 0.01 mol/mol relative to the amount required for complete combustion *via* Eq 5.

$$4\ Co(0) + LiClO_4 \longrightarrow 4\ CoO + LiCl \qquad (5)$$

For ignition, a Nichrome wire was wrapped around the Co(0)-$LiClO_4$ discs (Figure 7). Ignition started at one of the contact points of the disc with the wire, when the temperature of the latter was approximately 1100°C (calculated as described in the Experimental section). Once ignition started, the electric power to the wire was disconnected and further combustion was self-sustained. A very bright glow spread rapidly throughout the disk. Quickly, that glow turned red and then ceased altogether. It took about 20 s from ignition to complete combustion (see Ignition Movies). Using an infrared pyrometer, the disc temperature reached 1515 °C. Discs shrunk slightly during combustion (Table S.1), but kept their shape. Post-combustion, discs were washed with water and were dried. Yet, they remained monolithic (Scheme 1), and the only crystalline phase was CoO (Figure 5). Fused CoO particles were <100 nm in size (Figure 3f). The ρ_s value of the CoO network was 5.06 ± 0.03 g cm^{-3} (density of CoO = 6.44 g cm^{-3}), pointing to 27% v/v of closed porosity. The skeletal and the bulk density ($2.68_6 \pm 0.023$ g cm^{-3}) of the CoO discs together gave an open porosity of 47% v/v. The sum of open and closed porosity (74% v/v) was near the sum of those values in the Co(0)-900 aerogels (70% v/v).

Ignition of Co(0)-$LiClO_4$ in a bomb calorimeter under high-purity Ar (1 bar, 23 °C) yielded again CoO as the only cobalt phase (identical XRD profile as the one shown in Figure 5 - top). The heat released, -55.17 ± 2.01 kcal per mol of Co(0) reacted, was close to both the theoretical value (-58.47 kcal mol^{-1} from Eq 5), and the heat released from the analogous combustion of Fe(0) to FeO (-66.6 kcal mol^{-1}).[32] Thereby, $LiClO_4$-filled Co(0) aerogels comprise a reasonable alternative to pressed-pellet iron/$KClO_4$ thermites. One advantage of the nanostructured cobalt system over the pressed pellet technology is that Co(0) is consumed completely.

3. CONCLUSION

Deconvolution of the synthesis of monolithic non-oxide aerogels from monolithic aerogel precursors has been extended to smeltable metals. Other possible candidates include Fe, Ni, Sn and Cu. According to the new method, both metallic and ceramic aerogels can be prepared from X-xerogel powders, relying for porosity on the carbonizable crosslinking polymer reacting away. Using xerogel powders as precursors renders the whole process economic, because it speeds up solvent exchanges and bypasses time-consuming SCF- or freeze-drying. In the present case of Co(0) aerogels, further streamlining was achieved by removing unreacted C with H_2O/H_2. Application of Co(0) aerogels in thermites was a point of departure in order to demonstrate durability at high temperatures, in melts, and in contact with strong oxidizers. It follows that less demanding environments as in liquidized gasses, or electrolytic solutions will be tolerated easily.

Applications of Co(0) aerogels in catalysis, as porous electrodes and in magnetic separations are under way.

4. EXPERIMENTAL

4.1. MATERIALS

All reagents and solvents were used as received. Epichlorohydrin (EPH) was purchased from the Sigma Aldrich Chemical Co. Cobalt chloride hexahydrate ($CoCl_2.6H_2O$), and HPLC grade dimethylformamide (DMF) and ethylacetate (EtOAc) were purchased from Fisher Scientific International, Inc. Tris(4-isocyanatophenylmethane) (TIPM) was donated by Covestro LLC (Pittsburg, PA) as a 27% w/w solution in dry EtOAc under the trade name Desmodur RE. Ultra-high purity Ar (grade 5), and H_2 (99.999% purity) gases were purchased from Ozarc Gas (Rolla, MO).

4.1.1. Preparation of CoO_x Suspensions. $CoCl_2.6H_2O$ (15.756 g, 0.06622 mol) was dissolved in DMF (100 mL) under vigorous stirring. Epichlorohydrin (55 mL, 0.632 mol) was added and the blue solution was heated at 80 °C for 120 min. A suspension (CoOx) started forming in about 15-20 min. After the heating period, the mixture was allowed to cool down to room temperature and stirring continued for another 24 h. The

CoO_x suspension was transferred to centrifuge tubes (50 mL, Fischer Scientific), and the solvent was exchanged three times with ethylacetate. All washes and solvent exchanges were carried out with centrifugation for 15-20 min at 2,450 rpm. For each solvent exchange / wash step the new solvent that was brought in was 2× the volume of the compacted slurry (paste) at the bottom of the centrifuge tubes. Before every new centrifugation step, the compacted CoOx slurry was re-suspended with a glass rod. For characterization purposes, a portion of the slurry from the last wash was dried under reduced pressure at 80 ºC into a dry, freely flowing CoO_x powder.

4.1.2. Preparation of Crosslinked X-CoO_x Powder. As-received Desmodur RE (*i.e.,* a solution of TIPM in ethylacetate), 1× the volume of the centrifuged paste, was added to the centrifuge tubes containing the CoO_x slurry from the last ethylacetate wash, the tubes were sealed tightly with their caps, and the suspension was heated in an oven at 65 ºC for 24 h. The mixture was swirled frequently to re-distribute the settled powder and increase the diffusion rate. At the end of the 24 h period, the tubes were allowed to cool to room temperature, they were centrifuged for 15 to 20 min and the suspension was washed 5× with ethylacetate as above. Always, the wash solvent was removed using centrifugation. Again, for all washes, the volume of solvent was 2× the volume of the paste at the bottom of the centrifuge tubes. After removing the solvent from the last ethylacetate wash, the contents of the tubes were transferred with the aid of small portions of ethylacetate and were combined in a round bottom flask. Ethylacetate was removed and the product was dried under reduced pressure at 80 ºC into a dry, freely flowing X-CoO_x powder.

4.1.3. Preparation of Monolithic Co(0) Aerogels. Dry X-CoO_x powder was compressed into discs using aluminum dies and a hydraulic press operated at 10,000 psi.

Two different dies were used yielding two different size discs (diameter/thickness, mm/mm): 41.9/7.6 and 13.0/3.9. Placement of the powder in the dies was carried out in small portions under continuous tapping to ensure even distribution and settling of the X-CoOx powder. Compressed discs were reduced at 800 ºC for 5 h under flowing high-purity Ar. At the end of the heating period, the furnace was allowed to cool down under flowing Ar, pellets were removed and it was found that they contained unreacted carbon. Those samples are referred to as Co(0)/C-800, whereas the numerical extension indicates that temperature of their treatment. Unreacted carbon was removed with H_2O-saturated H_2. For this, the temperature of the tube furnace was raised to either 800 ºC or 900 ºC under flowing Ar, the gas was switched to H_2O-saturated H_2 and the temperature was held at that point for 36 h. (Flowing H_2 was saturated with water vapor by bubbling through water before directed to the furnace.) At the end of this period, the furnace was allowed to cool down under continuous flow of H_2. The resulting samples are refereed to as Co(0)-800 or as Co(0)-900 where the numerical extension indicates the temperature used for their preparation.

4.1.4. Preparation of $LiClO_4$-Loaded Co(0)-900 Aerogels. Co(0)-900 samples were degassed at 80 °C overnight under vacuum prior to perchlorate infiltration. The infiltration process was carried out in a sublimation apparatus under vacuum at 270 °C (melting point of $LiClO_4$ = 236 ºC). The sublimation apparatus containing solid $LiClO_4$ and a hanging Co(0) aerogel pellet at the bottom of the top lid was sealed and heated under vacuum to the intended temperature using a sand bath. The pellet was held in place with a magnetic rod placed inside the “cold” finger of the sublimation apparatus. After $LiClO_4$ melted completely, the magnetic rod was pulled out of the cold finger, and the Co(0)-900 aerogel pellet dropped in the pool of molten $LiClO_4$. In the beginning, the Co(0)-900 pellet floated on the liquid perchlorate, but eventually it sunk as it was filled with the liquid salt. The process took 15 – 20 min. At the end of this period, the pellet was removed from the molten salt, always under vacuum, with the help of a powerful Nd-Fe-B magnet from outside. Subsequently, the apparatus was allowed to cool to room temperature, the vacuum was broken and the perchlorate-infiltrated pellet was removed. The amount of perchlorate was determined gravimetrically.

CUATIONARY NOTE: With the understanding that one deals with a highly energetic system, all safety precautions must be obeyed during infiltration: (a) use of face and body protection; (b) the infiltration vessel must be placed behind a Plexiglass™ shield inside a fume hood; (c) a Class D[33] *fire extinguisher must be kept next to the fume hood at all times.*

4.2. METHODS

4.2.1. Pyrolytic Synthesis of Co(0). Pyrolytic conversion of X-CoO_x compacts to pure metallic cobalt aerogels was carried out in a programmable MTI GSL1600X-80 tube furnace (outer and inner tubes both of 99.8% pure alumina; outer tube: 1022 mm × 82 mm × 70 mm; inner tube: 610 mm × 61.45 mm × 53.55 mm; length of the heating zone at the set temperature: 457 mm). The rate of heating and cooling was always maintained at 2.5 ºC min^{-1}. All gas flow rates were set at 325 mL min^{-1}.

4.2.2. Ignition of $LiClO_4$-loaded Co(0)-900 Aerogel Pellets. For ignition in the open air, a Nichrome wire (0.65 mm in diameter) was wrapped around $LiClO_4$-loaded Co(0)-900 pellets, and power was supplied to the wire with a Variac. The voltage across the wire (8.5 V) was measured with a multimeter and the electric current flowing through the wire (13.0 A) was measured using a Fluke i400 inductive current probe. Using the diameter of the wire, the current flowing through it, and by consulting tables,[34] the temperature at the point of ignition was about 1,100 °C. That temperature was also confirmed with an infrared thermometer. The whole set-up was placed in a fume hood behind a Plexiglass^{TM} shield. Video was recorded with a Sony Handycam Model DCR-SR68, placed on a tripod. The temperature of the $LiClO_4$-loaded Co(0)-900 pellets during thermite operation was monitored with an Infrared Thermometer (Model 0S3708) from Omega Engineering, Inc. focused at the center of the disc. The maximum temperature recorded was 1515 °C (See Ignition Movie S.M.2).

4.2.3. Physical Characterization. Bulk densities (ρ_b) were calculated from the weight and the physical dimensions of the samples. Skeletal densities (ρ_s) were determined with helium pycnometry using a Micromeritics AccuPyc II 1340 instrument. Samples for skeletal density measurements were outgassed for 24 h at 80 °C under vacuum before analysis. Percent porosities, Π, were determined from the ρ_b and ρ_s values via $\Pi = 100 \times (\rho_s - \rho_b)/\rho_s$.

4.2.4. Thermogravimetric Analysis (TGA). TGA was conducted under N_2 or O_2 with a TA Instruments Model TGA Q50 thermogravimetric analyzer, using a heating rate of 5 °C min^{-1}.

4.2.5. Chemical Characterization. Different methods were applied at different stages of processing as follows.

CHN elemental analysis was conducted with an Exeter Analytical Model CE440 elemental analyzer, calibrated with acetanilide. The combustion furnace was operated at 925 °C. The calibration standard and samples were run three times and results are given as averages.

The crosslinking polymer was identified as TIPM-derived polyurea with solid-state CPMAS ^{13}C NMR on a Bruker Avance III 400 MHz spectrometer with a carbon frequency of 100 MHz, using a 7 mm Bruker MAS probe at a magic angle spinning rate of 5 kHz with broadband proton suppression, and CP TOSS pulse sequence. The Total Suppression of Spinning Sidebands (TOSS) pulse sequence was applied by using a series of four properly timed 180º pulses on the carbon channel at different points of a cycle before the acquisition of the FID, after an initial excitation with a 90º pulse on the proton channel. The 90º excitation pulse on the proton and the 180º excitation pulse on carbon were set to 4.2 μs and 10 μs, respectively. The cross-polarization contact time and the relaxation delay were set at 2000 μs and 5 s, respectively. The number of scans was set at 2,048. Spectra were referenced externally to glycine (carbonyl carbon at 176.03 ppm). Chemical shifts are reported versus TMS (0 ppm). For this, dry X-CoOx powder was treated for 30 min with aqueous HCl (12 M). At the end of the period, the suspension was washed several times with water and several times with acetone. The final slurry was dried under vacuum at 80 ºC overnight. X-CoOx powders were attracted by magnets; after removal of the CoOx component with HCl, they were not. The NMR spectrum of the residue was compared with the spectrum of polyurea obtained from the reaction of TIPM with water.

Powder X-ray diffraction (XRD) analysis was performed with powders of the corresponding materials using a PANalytical X'Pert Pro multipurpose diffractometer (MPD) with Cu Kα radiation (λ = 1.54 Å) and a proportional counter detector equipped with a flat graphite monochromator.

X-ray photoelectron spectroscopic analysis (XPS) was carried out with a Kratos Axis 165 Photoelectron Spectroscopy System. Samples were mixed and ground together with Au powder (5% w/w) as internal reference. Samples were analyzed as powders. Each sample was placed on a piece of conductive carbon tape that was adhered to a stainless steel sample holder. Samples were introduced into the analysis chamber one at a time and the chamber was evacuated at 10^{-8} Torr or lower. No ion sputtering was performed on any of the samples. An Al monochromatic source (150 W) was used for excitation. A charge neutralizer was used to reduce the effects of differential or sample charging. The analysis area was 700 × 300 microns. Elemental quantification calculations were based on broad survey results from single sweeps at higher sensitivity (Pass energy = 80) and were carried out with the Kratos Axis Vision processing software taking into consideration the appropriate relative sensitivity factors for the particular XPS system. High-resolution elemental scans where carried out at a lower sensitivity (Pass energy = 20), using multiple sweeps to improve the signal-to-noise ratios. Deconvolution of Co 2p spectra was performed with Gaussian function fitting using the OriginPro 8.5.1 software package.

UV-Vis spectroscopy was carried out in DMF solutions of $CoCl_2.6H_2O$, $Co(NO_3)_2.6H_2O$, and $Co(NO_3)_2.6H_2O$ with varying concentrations of HCl using a Cary 5000 UV-Vis Spectrophotometer Model # G9825A. Absorbance was recorded from 270 to 800 nm. Samples were referenced against DMF. The salt concentration in each solution were 0.43 M, equal to the concentration of $CoCl_2.6H_2O$ in the DMF sol used for making CoOx suspensions. Five different solutions of $Co(NO_3)_2.6H_2O$ in DMF were prepared by varying the molar ratio of HCl : $[Co(NO_3)_2.6H_2O]$ as follows: 1:4, 1:2, 1:1, 2:1 and 4:1.

Magnetic susceptibilities were measured with powders of the corresponding samples using a Johnson Matthey Model Mark I Magnetic Susceptibility Balance. A five-point calibration curve was constructed with $CoCl_2.6H_2O$, $CuSO_4.6H_2O$, $K_3[Fe(CN)_6]$, CoO and H_2O. The mass magnetic susceptibility, χ_g (in cgs units), was calculated using the following equation:[35]

$\chi_g = CL(R - R_o)/[1\times10^9\ (m)]$, where, C = balance calibration constant, L = sample height in cm, R = reading from the digital display when the sample and the tube are in place in the instrument, R_o = reading from the display when the empty sample tube is placed in the instrument, m = sample mass in grams.

4.2.6. Solid Framework Characterization. Scanning electron microscopy (SEM) was conducted with Au-coated samples on a Hitachi Model S-4700 field-emission microscope.

4.2.7. Pore Structure Analysis. N_2-sorption porosimetry at 77 K was conducted with a Micromeritics ASAP 2020 surface area and porosity analyzer. Samples for N_2-sorption analysis were outgassed for 24 h at 80 °C under vacuum before analysis. The pore size distribution of Co pellet was also probed with Hg-intrusion porosimetry using a Micromeritics AutoPore IV 9500 instrument.

4.2.8. Mechanical Characterization of Co(0) Aerogels. Quasi-static compression testing of Co(0)-900 aerogels at low strain rates (2.5 mm/mm) was conducted on an Instron 4469 Universal Testing Machine using a 50 kN load cell, following testing procedures and specimen length/diameter ratios in the spirit of ASTM D1621-04a (Standard Test Method for Compressive Properties of Rigid Cellular Plastics), as described before.[16] The recorded force as a function of displacement (machine-compliance corrected) was converted into stress as a function of strain.

4.2.9. Calorimetry. The enthalpy of the reaction taking place in $LiClO_4$-impregnated Co(0) was measured in a 200 mL bomb calorimeter (Parr Instrument

Company, Model 1108 Oxygen Combustion Vessel and Model 1341 Plain Jacket Calorimeter). The heat capacity of the calorimeter was measured using benzoic acid as standard. The sample was ignited with a Nichrome fuse wire (0.65 mm in diameter, 10 cm in length) connected to the terminal socket on the apparatus head, which in turn was connected to the ignition unit (a Variac). The experiment was carried out by heating the Nichrome wire with a supply of 13.0 A of current for 15 sec under an atmosphere of high-purity Ar. The heat released by the fuse was measured independently with the calorimeter and was taken into consideration in the calculations. After each experiment, the residue was collected and analyzed with XRD.

ACKNOWLEDGEMENTS

This project was supported by ARO (W911NF-14-1-0369) and the NSF (1530603). We thank Covestro LLC for the generous supply of Desmodur RE (TIPM), and Dr. J. Watts for access to his infrared thermometer.

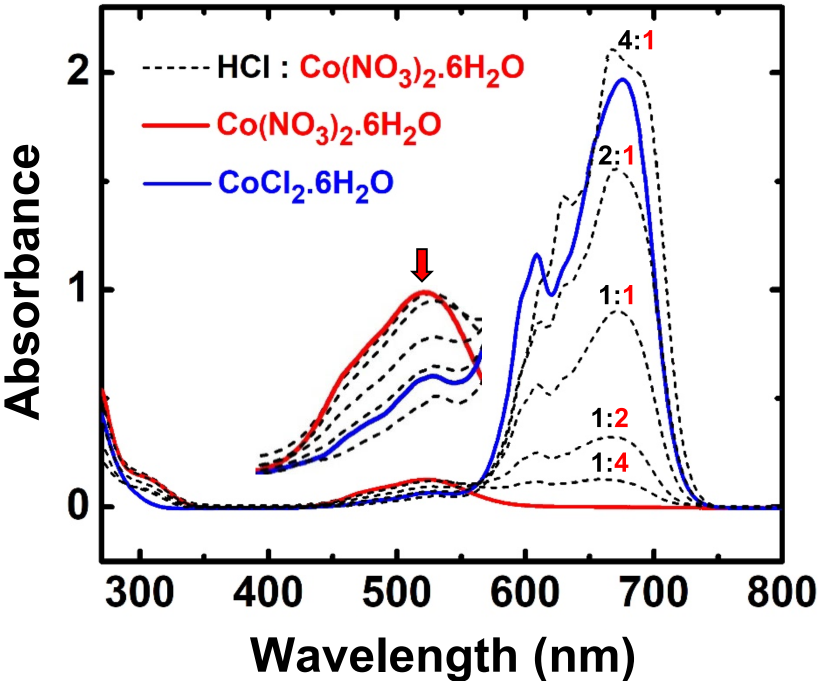

Figure 1. Spectrophotometric titration of a $[Co(H_2O)_6](NO_3)_2$ solution in DMF (0.43 M – red line) with HCl (black dashed lines – fractions denote the HCl : $[Co(H_2O)_6](NO_3)_2$ mol/mol ratio. As the concentration of HCl increases, the intensity of the absorption at 523 nm decreases (red arrow pointing down) and the intensity at 675 nm increases. The blue line shows the spectrum of $[Co(H_2O)_6]Cl_2$ in DMF at the same concentration (0.43 M). (Concentrations of the cobalt complexes were equal to those used in the sol. Spectra were taken from undiluted solutions using a sample holder with an optical path of 0.09 mm.)

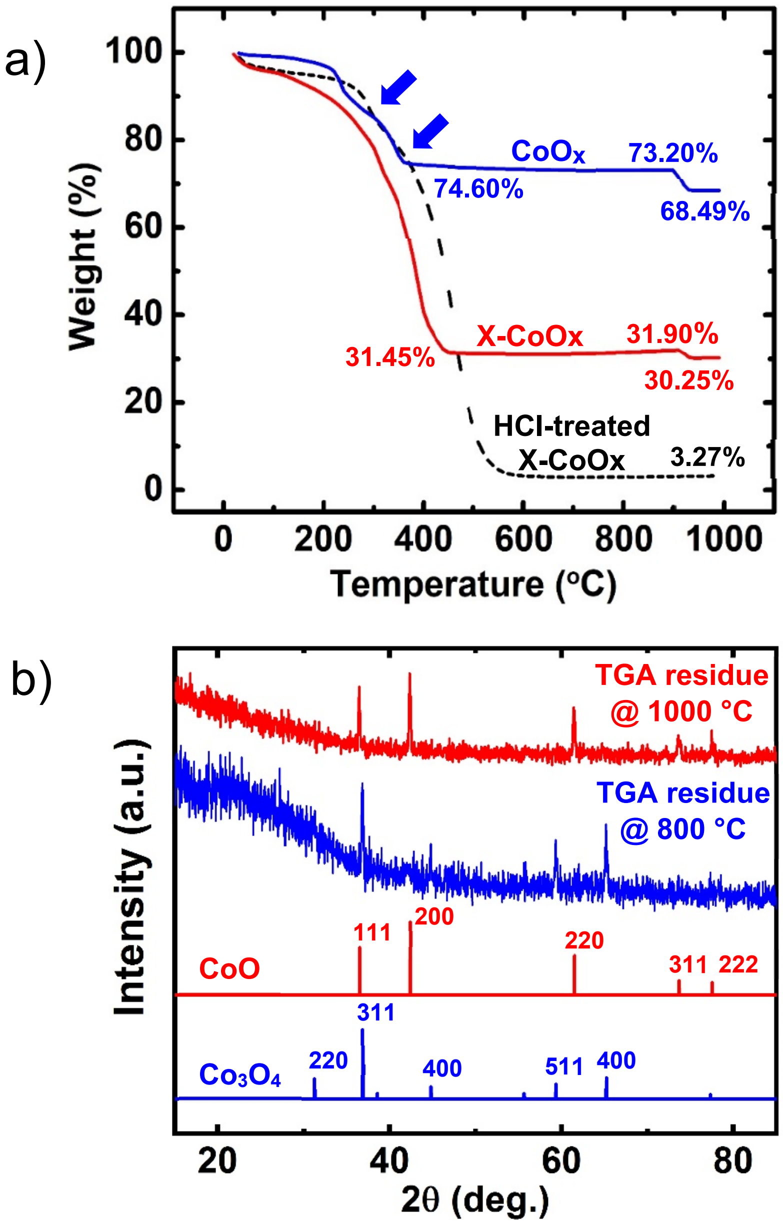

Figure 2. a) TGA under O_2 at 5 °C min^{-1} of: CoOx (blue line), X-CoOx (red line), and HCl-treated X-CoOx (dashed black line). Blue arrows point at the two decomposition steps of CoOx in the 200-400 °C range (see text). b) Referring to part (a) (blue line): XRD of the residue from TGA under O_2 collected at 800 °C and at 1000 °C, as indicated.

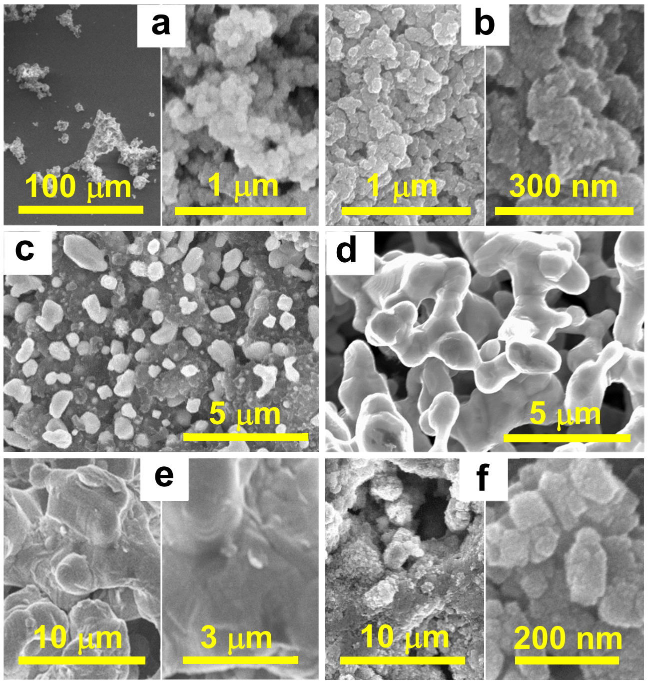

Figure 3. SEM of: a) CoOx powder (left: grains; right: interior of the grains). b) X-CoOx compressed disc at two magnifcations. c) As-prepared Co(0)/C (before carbon removal). d) Co(0)-800: Co(0) after carbon removal with H_2O/H_2 at 800 ºC. e) Co(0)-900: Co(0) after carbon removal with H_2O/H_2 at 900 ºC. f) Monolithic CoO after ignition of $LiClO_4$-loaded Co(0)-900 aerogels and washing with water.

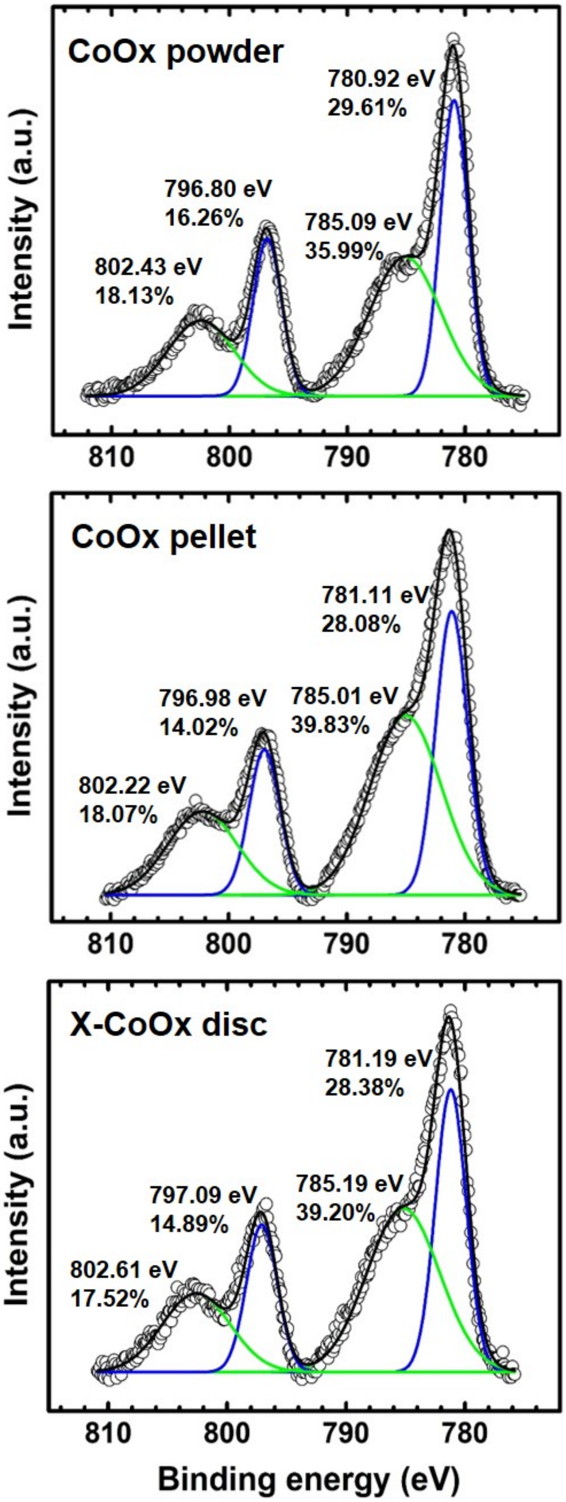

Figure 4. High resolution Co 2p XPS spectra of CoOx powder (top), a CoOx compressed pellet (middle), and of a X-CoOx compressed disc (bottom).

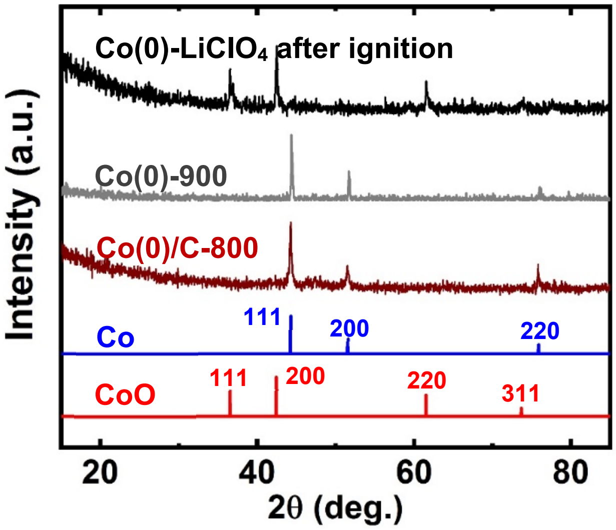

Figure 5. Powder XRD spectra of samples as shown. Numerical extensions denote the temperature of the last processing step (see text).

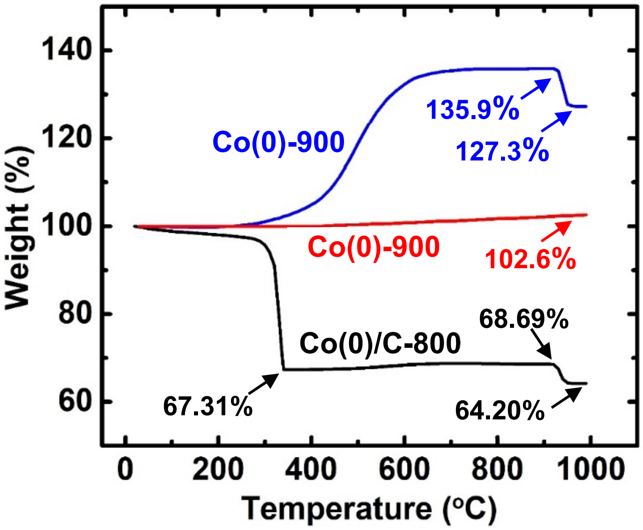

Figure 6. TGA (at 5 °C min^{-1}) of samples and conditions as follows. Black line: Under O_2 of an as-prepared Co(0)/C-800 disc; Blue line: Under O_2 of a carbon-free Co(0)-900 disc; Red line: Under N_2 of a carbon-free C(0)-900 disc. Numerical extensions denote the temperature of the last processing step (see text).

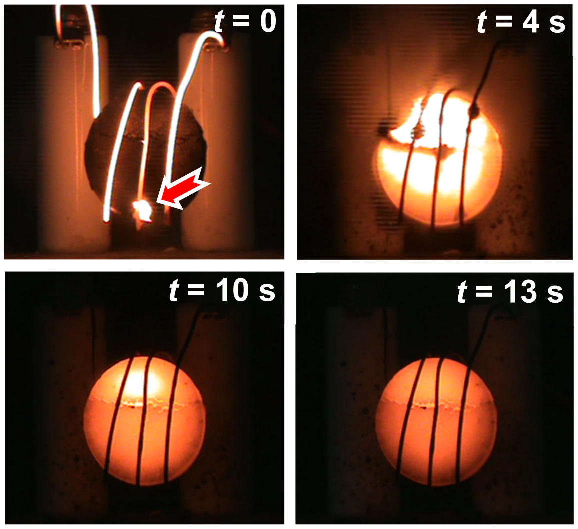

Figure 7. Ignition (t = 0) and combustion of a $LiClO_4$-infiltrated Co(0)-900 aerogel disc (21.8 diam. 3.7 mm thick). Arrow shows the point of ignition. The temperature at the center of the disk at t = 4 s after ignition reached 1515 ºC (see Movie S.M.2).

Appendix I. Material Characterization Data

Table S.1. Materials Characterization Data along All Stages of Processing as well as before and after Ignition

Sample I.D.	linear shrinkage (%) [b,c]	bulk density, ρ_b (g cm^{-3}) [b]	skeletal density, ρ_s (g cm^{-3}) [d]	porosity, Π (% v/v) [e]	specific pore volume (cm^3 g^{-1}) V_{Total} [f]	$V_{1.7\text{-}300\_nm}$ [g]	$V_{>300\ nm}$ [h]	BET surface area, σ (m^2 g^{-1}) [i]	Average pore diameter Φ, (nm) [j]
Powders and Compacts									
CoOx powder	-	-	3.137 ± 0.003	-	-	0.3500	-	62.40	-
X-CoOx powder	-	-	1.734 ± 0.003	-	-	0.1124	-	36.20	-
X-CoOx compact	-	1.340 ± 0.007	1.673 ± 0.009	19.87	0.1485	0.0561	0.0924	19.53	30.41
Monoliths from Compacts after Pyrolysis at 800 °C / Ar									
C/Co-800 monolith	31.56 ± 0.19	2.134 ± 0.020	3.802 ± 0.091	43.88	0.2345	0.0221	0.2124	62.69	14.87
Monoliths after Carbon Removal (H_2O/H_2) at the Temperatures Indicated as Extensions to the Sample I.D.s									
Co(0)-800 monolith [a]	42.14 ± 0.32	1.685 ± 0.063	8.127 ± 0.043	79.25	0.4704	0.0014	0.4690	1.34	1404.18
Co(0)-900 monolith [a]	45.78 ± 0.73	3.155 ± 0.073	8.237 ± 0.113 [b]	61.69	0.1979	0.0006	0.1973	0.46	1720.87 [11325.74]
Co(0)-900 monolith loaded with $LiClO_4$ [a]	no differential shrinkake	3.860 ± 0.201	4.122 ± 0.056	6.35	-	-	-	-	-
$LiClO_4$-loaded Discs after Ignition									
Co(0)-900/$LiClO_4$ after ignition	47.90 ± 0.61	3.762 ± 0.124	5.382 ± 0.265	30.11	-	-	-	-	-
Co(0)-900/$LiClO_4$ after ignition & wash	no additional shrinkage	2.686 ± 0.023	5.060 ± 0.029	46.91	-	-	-	-	-

[a] The numerical extension of Co(0) indicates the last processing temperature. [b] Average of 3 samples. [c] Shrinkage = 100 × (mold diameter – sample diameter)/(mold diameter). All shrinkges are reported with respect to the X-CoOx compact. [d] Single sample, average of 50 measurements. [e] Porosity, $\Pi = 100\times(\rho_s - \rho_b)/\rho_s$. [f] V_{Total} was calculated via $V_{Total} = (1/\rho_b) - (1/\rho_s)$. [g] $V_{1.7\text{-}300\ nm}$ from N_2- BJH desorption volume. [h] $V_{>300\ nm}$ was calculated by subtracting $V_{1.7\text{-}300\ nm}$ from V_{Total}. [i] BET surface area from N_2 sorption. [j] For the first number, V was calculated via $4V/\sigma$ by setting $V_{Total} = (1/\rho_b) - (1/\rho_s)$; the number in [brackets] is the peak maximum from the pore size distribution curve obtained using Hg-intrusion porosimetry (see Appendix IV).

Appendix II. Solid-state ^{13}C NMR Data

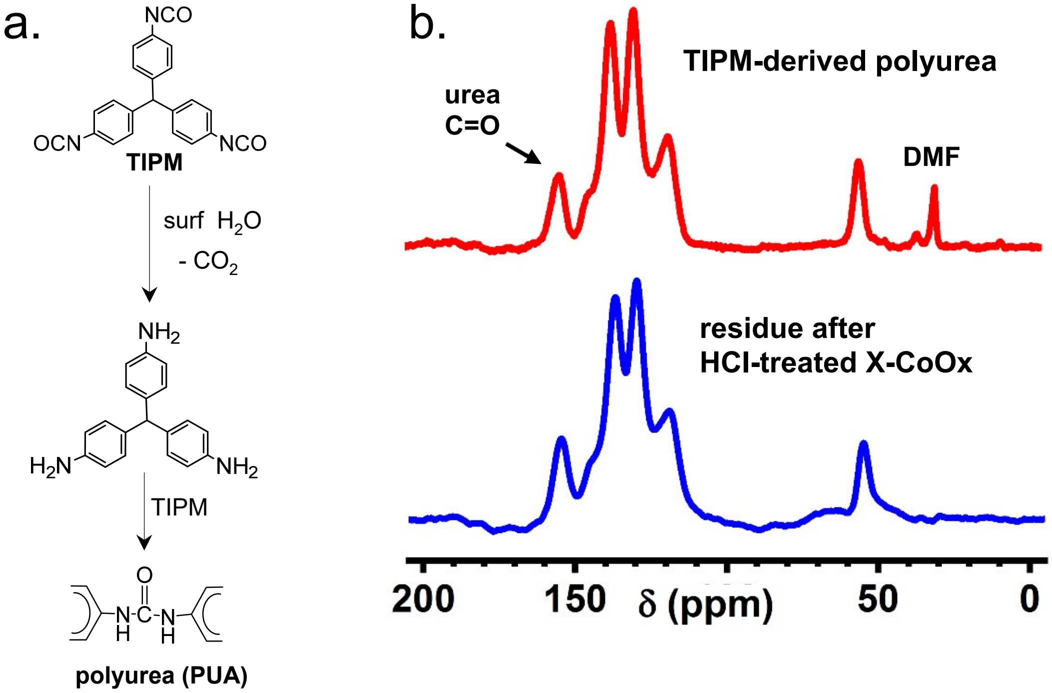

Figure S.1. a) Formation reaction of a TIPM-derived polyurea coating on the surface of the cobaltia nanoparticles. b) Comparison of the solid-state ^{13}C CPTOSS NMR spectrum of TIPM-derived polyurea via reaction of TIPM with water,[S.R.1] with the spectrum of the residue after HCl-treatment of X-CoOx powder.

Appendix III. Mechanical Characterization of a Co(0)-900 Aerogel Monolith

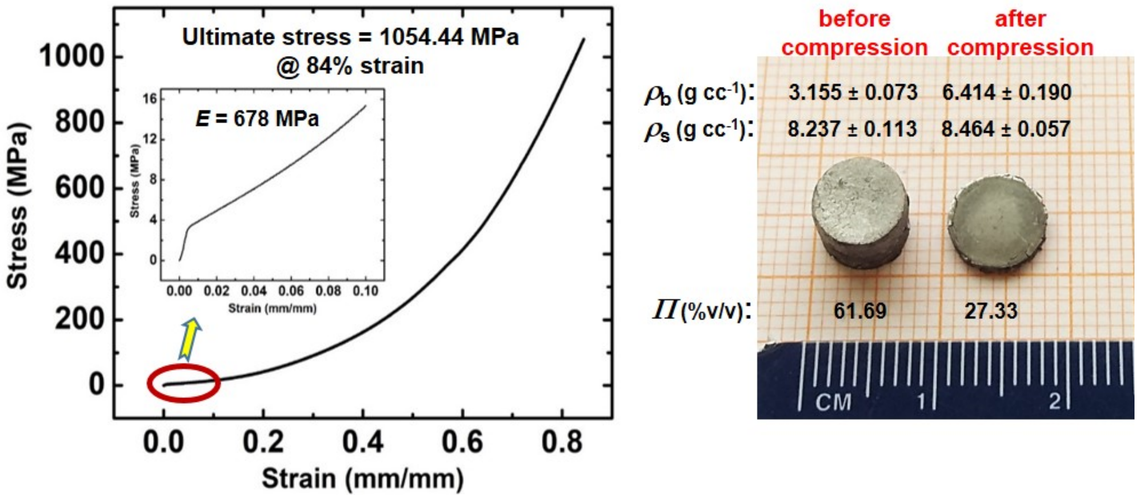

Figure S.2. Quasi-static (2.5 mm min^{-1}) compression testing of a cylindrical Co(0)-900 aerogel monolith (6 mm in length, 3 mm in diameter). The experiment was repeated two times with different monoliths. (The numerical extension in Co(0)-900 indicates the processing temperature at which flowing H_2O/H_2 was used in order to remove unreacted carbon from Co(0)/C-800 aerogels.)

Appendix IV. Hg-intrusion Porosimetry of a Co(0)-900 Aerogel Disc

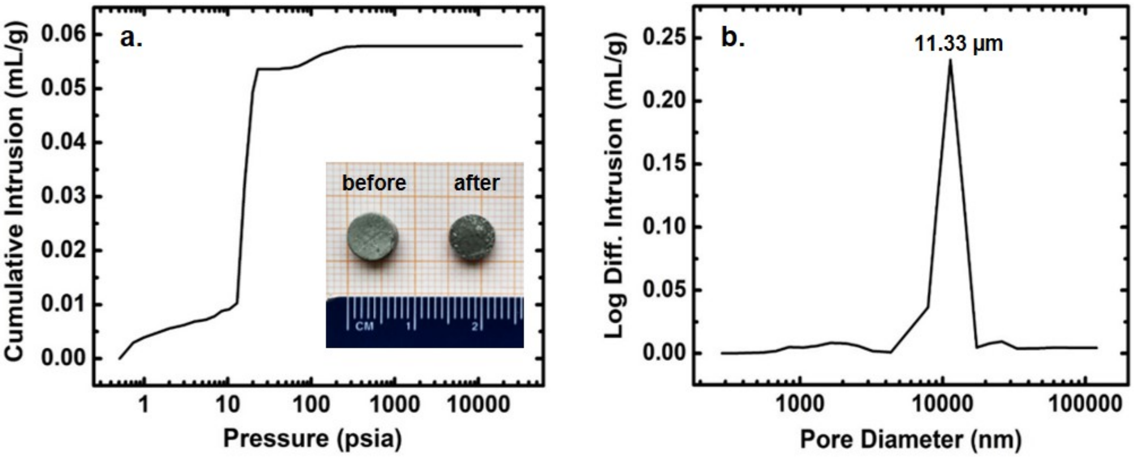

Figure S.3. a) Hg-intrusion isotherm. b) Pore size distribution of a Co(0)-900 aerogel disc. (The numerical extension in Co(0)-900 indicates the processing temperature at which flowing H_2O/H_2 was used in order to remove unreacted carbon from Co(0)/C-800 aerogels.)

Appendix V. Supplementary References

S.R.1 Leventis, N.; Sotiriou-Leventis, C.; Saeed, A. M.; Donthula, S.; Far H. M.; Rewatkar, P. M.; Kaiser, H.; Robertson, J. D.; Lu, H.; Churu, G. Nanoporous Polyurea from a Triisocyante and Boric Acid: A Paradigm of a General Reaction Pathway for Isocyanates and Mineral Acids. *Chem. Mater.* **2016**, *28*, 67−78.

REFERENCES

1. Leventis, N.; Sadekar, A.; Chandrasekaran, N.; Sotiriou-Leventis, C. Click Synthesis of Monolithic Silicon Carbide Aerogels from Polyacrylonitrile-Crosslinked 3D Silica Networks. *Chem. Mater.* **2010**, *22*, 2790–2803.

2. Vareda J. P.; Lamy-Mendes, A.; Durães, L. A Reconsideration on the Definition of the Term Aerogel based on Current Drying Trends. *Microporous Mesoporous Mater*. **2018**, *258*, 211–216.

3. Du, A.; Zhou, B.; Zhang, Z.; Shen, J. A Special Material or a New State of Matter: A Review and Reconsideration of the Aerogel. *Materials* **2013**, *6*, 941–968.

4. Tappan, B. C.; Steiner, S. A.; Luther, E. P. Nanoporous Metal Foams. *Angew. Chem. Int. Ed.* **2010**, *49*, 4544–4565.

5. Cai, B.; Dianat, A.; Hübner, R. Liu, W.; Wen, D.; Benad, A.; Sontag, L.; Gemming, T.; Cuniberti, G.; Eychmüller, A. Multimetallic Hierarchical Aerogels: Shape Engineering of the Building Blocks for Efficient Electrocatalysis. *Adv. Mater.* **2017**, *29*, 1605254.

6. Liu, W.; Herrmann, A.-K.; Bigall, N. C.; Rodriguez, P.; Wen, D.; Oezaslan, M.; Schmidt, T. J.; Gaponik, N.; Eychmüller, A. Noble Metal Aerogels–Synthesis, Characterization, and Application as Electrocatalysts. *Acc. Chem. Res.* **2015**, *48*, 154–162.

7. Wen, D.; Herrmann, A.-K.; Borchardt, L.; Simon, F.; Liu, W.; Kaskel, S.; Eychmüller, A. Controlling the Growth of Palladium Aerogels with High-Performance toward Bioelectrocatalytic Oxidation of Glucose. *J. Am. Chem. Soc.* **2014**, *136*, 2727–2730.

8. Wakayama, H.; Fukushima, Y. Porous Platinum Fibers Synthesized Using Supercritical Fluid. *Chem. Commun.* **1999**, 391–392.

9. Bozbag, S. E.; Sanli, D.; Erkey, C. Synthesis of Nanostructured Materials Using Supercritical CO_2: Part II. Chemical Transformations. *J. Mater. Sci.* **2012**, *47*, 3469–3492.

10. Shen, Y. Carbothermal Synthesis of Metal-functionalized Nanostructures for Energy and Environmental Applications. *J. Mat. Chem. A* **2015**, *3*, 13114–13188.

11. Mahadik-Khanolkar, S.; Donthula, S.; Bang, A.; Wisner, C.; Sotiriou-Leventis, C.; Leventis, N. Polybenzoxazine Aerogels. 2. Interpenetrating Networks with Iron Oxide and the Carbothermal Synthesis of Highly Porous Monolithic Pure Iron(0) Aerogels as Energetic Materials. *Chem. Mater.* **2014**, *26*, 1318–1331.

12. Leventis, N.; Chandrasekaran, N.; Sotiriou-Leventis, C.; Mumtaz, A. Smelting in the Age of Nano: Iron Aerogels. *J. Mater. Chem.* **2009**, *19*, 63–65.

13. Leventis, N.; Chandrasekaran, N.; Sadekar, A. G.; Mulik, S.; Sotiriou-Leventis, C. The Effect of Compactness on the Carbothermal Conversion of Interpenetrating Metal Oxide / Resorcinol-Formaldehyde Nanoparticle Networks to Porous Metals and Carbides. *J. Mater. Chem.* **2010**, *20*, 7456–7471.

14. Leventis, N. Three Dimensional Core-Shell Superstructures: Mechanically Strong Aerogels. *Acc. Chem. Res.* **2007**, *40*, 874–884.

15. Leventis, N.; Sotiriou-Leventis, C.; Zhang, G.; Rawashdeh, A.-M. M. Nano Engineering Strong Silica Aerogels. *NanoLetters* **2002**, *2,* 957–960.

16. Leventis, N.; Sotiriou-Leventis, C.; Mulik, S.; Dass, A.; Schnobrich, J.; Hobbs, A.; Fabrizio, E. F.; Luo, H.; Churu, G.; Zhang, Y.; Lu, H. Polymer Nanoencapsulated Mesoporous Vanadia with Unusual Ductility at Cryogenic Temperatures. *J. Mater. Chem.* **2008**, *18*, 2475–2482.

17. Meador, M. A. B.; Capadona, L. A.; MacCorkle, L.; Papadopoulos, D. S.; Leventis, N. Structure-Property Relationships in Porous 3D Nanostructures as a Function of Preparation Conditions: Isocyanate Cross-Linked Silica Aerogels. *Chem. Mater.* **2007**, *19*, 2247-2260.

18. Rewatkar, P. M.; Taghvaee, T.; Saeed, A. M.; Donthula, S.; Mandal, C.; Chandrasekaran, N.; Leventis, T.; Shruthi, T. K.; Sotiriou-Leventis, C.; Leventis, N. Sturdy, Monolithic SiC and Si_3N_4 Aerogels from Compressed Polymer-Cross-Linked Silica Xerogel Powders. *Chem. Mater.* **2018**, *30*, 1635–1647.

19. Peterson, G. R.; Hung-Low, F.; Gumeci, C.; Bassett, W. P.; Korzeniewski, C.; Hope-Weeks, L. J. Preparation−Morphology−Performance Relationships in Cobalt Aerogels as Supercapacitors. *ACS Appl. Mater. Interfaces* **2014**, *6*, 1796–1803.

20. Overviews of Recent Research on Energetic Materials. In Advanced Series in Physical Chemistry; Shaw, R. W., Brill, T. B., Thompson, D. L., Eds.; World Scientific Publishing, Co.: London, U.K., 2005; Vol. 16.

21. Guidotti, R. A.; Masset, P. Thermally Activated ("Thermal") Battery Tchnology Part I: An Overview. *J. Power Sources* **2006**, *161*,1443−1449.

22. Guidotti, R; Odinek, J; Reinhardt, F. W. Characterization of Fe/$KClO_4$ Heat Powders and Pellets. *J. Energ. Mater.* **2006**, *24*, 271−305.

23. Leventis, N.; Galison, W. A. Apparatus for Detecting Moisture in Garments. U.S. Patent No. 5,796,345 (1998).

24. Gash, A. E.; Tillotson, T. M.; Satcher, J. H.; Poco, J. F.; Hrubesh, L. W.; Simpson, R. L. Use of Epoxides in the Sol−gel Synthesis of Porous Iron(III) Oxide Monoliths from Fe(III) Salts. *Chem. Mater.* **2001**, *13*, 999−1007.

25. Fears, T. M.; Sotiriou-Leventis, C.; Winiarz, J. G.; Leventis, N. Economical Synthesis of Vanadia Aerogels via Epoxide-Assisted Gelation of $VOCl_3$. *J. Sol-Gel Sci. Technol.* **2016**, *77*, 244–256.

26. Leventis, N.; Vassilaras, P.; Fabrizio, E. F.; Dass, A. Polymer Nanoencapsulated Rare Earth Aerogels: Chemically Complex but Stoichiometrically Similar Core-Shell Superstructures with Skeletal Properties of Pure Compounds. *J. Mater. Chem.* **2007**, *17*, 1502–1508.

27. Greenwood, N. N.; Earnshaw, A. Chemistry of the Elements. Butterworth-Heinemann, Woburn, MA 1998, p 1131.

28. Garciamartinez, O.; Millan, P.; Rojas, R. M.; Torralvo, M. J. Cobalt Basic Salts as Inorganic Precursors of Cobalt Oxides and Cobalt Metal: Thermal Behavior Dependence on Experimental Conditions. *J. Mater. Sci.* **1988**, *23*, 1334−1350.

29. Leventis, N.; Sotiriou-Leventis, C.; Chandrasekaran, N.; Mulik, S.; Larimore, Z. J.; Lu, H.; Churu, G.; Mang, J. T. Multifunctional Polyurea Aerogels from Isocyanates and Water. A Structure-Property Case Study. *Chem. Mater.* **2010**, *22*, 6692–6710.

30. https://xpssimplified.com/elements/cobalt.php (Accessed 05-27-2019)

31. Xie, S.; Liu, Y.; Deng, J.; Yang, J.; Zhao, X.; Han, Z.; Zhang, K.; Dai, H. Insights into the Active Sites of Ordered Mesoporous Cobalt Oxide Catalysts for the Total Oxidation of *o*-xylene. *J. Catal.* **2017**, *352*, 282–292.

32. Leventis, N.; Donthula, S.; Mandal, C.; Ding, M. S.; Sotiriou-Leventis, C. Explosive versus Thermite Behavior in Iron(0) Aerogels Infiltrated with Perchlorates. *Chem. Mater.* **2015**, *27*, 8126–8137.

33. http://www.strikefirstusa.com/2016/05/five-classes-of-fires-fire-extinguishers-stop-them/ (Accessed 05-27-2019)

34. https://web.archive.org/web/20120920075813/http://www.pelicanwire.com/category/formulas-resistance/ (Accessed 05-27-2019)

35. https://www.unf.edu/~michael.lufaso/chem3610L/instructions_magnetic_susceptibility.pdf (Accessed 05-27-2019)

III. POLYURETHANE AEROGELS BASED ON CYCLODEXTRINS: HIGH CAPACITY DESICCANTS REGENERATED AT ROOM TEMPERATURE BY REDUCING THE RELATIVE HUMIDITY OF THE ENVIRONMENT

Parwani Rewatkar, Adnan Malik Saeed, Hojat Majedi Far, Suraj Donthula, Chariklia Sotiriou-Leventis*, Nicholas Leventis*

Department of Chemistry, Missouri University of Science and Technology, Rolla, MO 65409, U.S.A. *Corresponding authors: Tel.: 573-341-4391 (N.L.); 573-341-4353 (C.S.-L.). E-mail: leventis@mst.edu; cslevent@mst.edu

ABSTRACT

Polyurethane aerogels were prepared from a rigid aromatic triisocyanate (tris(4-isocyanatophenyl)methane) and cage-shaped α- and β-cyclodextrins as rigid polyols. Gelation was carried out in DMF using dibutyltin dilaurate (DBTDL) as catalyst. Wet-gels were dried to aerogels (abbreviated as α- or β-CDPU-xx) with supercritical fluid CO_2. "xx" stands for the percent weight of the two monomers in the sol, and was varied at two levels for each cyclodextrin: 2.5% and 15%. All aerogels were characterized with solid-state ^{13}C and ^{15}N NMR, CHN analysis, FTIR, XPS, SEM and gas (N_2 and CO_2) sorption porosimetry. α- and β-CDPU-xx aerogels were investigated as desiccants at room temperature. All materials had relatively higher capacities for water adsorption from high-humidity environments (99%) than typical commercial desiccants like silica or Drierite^{TM}. However, α-CDPU-2.5 aerogels did stand out with a water uptake capacity reaching 1 g of H_2O per g of material. Most importantly though, adsorbed water could be released quantitatively without heating, by just reducing the relative humidity of the environment to 10%. All *α*- and *β*-CDPU-xx aerogel samples were cycled between humid and dry environments 10 times. Their unusual behavior was traced to filling smaller mesopores with water and was attributed to a delicate balance of enthalpic (H-bonding) and entropic factors, whereas the latter are a function of pore sizes.

Keywords: desiccant, polyurethane, aerogels, cyclodextrin, water adsorption, regenerated, reused, relative humidity

TOC Graphic

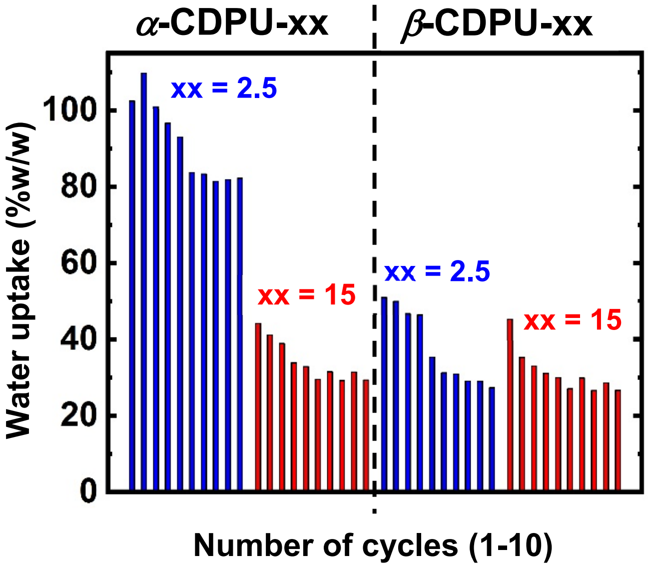

1. INTRODUCTION

Desiccants absorb water vapor and reduce the humidity of their environment. Most familiar is the use of desiccants to keep foodstuffs,[1,2] pharmaceuticals,[3] electronics,[4] and other products dry during shipment and storage.[5] Larger-scale applications of desiccants, mostly under consideration, include use as gas dryers,[6] in fresh water production by atmospheric moisture absorption,[7] in heat pumps and refrigeration,[8,9] or as energy-saving alternatives to heat-drying.[10] Desiccants can be anhydrous metal salts,[11-14] zeolites,[15-17] clays,[18-21] activated carbons[22-25] and polymers.[26-29] The mechanism of water uptake has been investigated extensively, and varies with the type of material.[30] In open-pore desiccants, water is first absorbed on hydrophilic sites on the pore surfaces and then proceeds with pore filling.[31,32]

The typical barriers of new desiccants to entry practical application are cost and performance. Both factors depend on the application, and are linked by whether a desiccant can go through a sufficient number of high-capacity sorption-desorption cycles. The latter should take into consideration the energy that needs to be expended in order to remove absorbed water and regenerate the desiccant for reuse. The water sorption capacity of the two most commonly used materials, silica gel and zeolites, reaches 0.45 g of water per gram of material.[33,34] High surface area silica aerogels have demonstrated an even higher water uptake capacity than other forms of silica (reaching up to 1.35 g of water per g of silica aerogel),[35] however performance deteriorates rapidly because of hydrolysis of the silica framework by the adsorbed water. Regarding regeneration, zeolites require heating up to more than 200 °C, while silica gels or nanoporous carbons, which can be dried at say 120 °C, are considered advantageous.[36] If, however, we consider a demanding application as the benchmark, as for example fresh water production, an attractive desiccant will be reuseable it will adsorb over 0.5 g of water per g of its mass, and it should be regenerated with minimum expenditure of energy, *e.g.*, at 40-50 °C.[30] As described herewith, certain polyurethane-based aerogels that incorporate α- or β-cyclodextrin within every polymeric repeat unit may meet or exceed those requirements. It turns out that those materials can uptake up to 1 g of water per gram of aerogel, and can be regenerated by simply reducing the relative humidity of the environment. The latter are the typical cycling conditions encountered during regular operation of many consumer appliances, thereby implementation of those materials may lead to tremendous energy savings.

Cyclodextrins are cyclic oligosaccharides connected, just like open-chain starch, with α-glycosidic bonds. The α-cyclodextrin (α-CD) ring consists of 6 glucose units and bears 18 –OH groups pointing outward from the central cavity (5.7 Å in diameter); the β-cyclodextrin (β-CD) ring consists of 7- glucose moieties, the cavity is 7.8 Å in diameter, and bears 21 –OH groups pointing outward (Scheme 1).[37] At first, we were attracted to cyclodextrins as building blocks of aerogels because of their hydrophobic cavity, and polyurethanes was the rather obvious choice of materials.[38-44] As it turned out the capacity of those materials for CO_2 and CH_4 uptake inside the hydrophobic cavity was not competitive relative to other adsorbers, however, it was noted that cyclodextrin-based aerogels included a fair amount of mesoporous space, and necessarily the urethane-rich pore walls should be capable of developing H-bonding with water. Then, reasoning by analogy to the mechanism proposed recently for the very high CO_2 uptake by phenolic and polyamide-derived carbons,[45,46] new water molecules should hydrogen-bond to already adsorbed water molecules, and that process could continue until small pores would be filled. That mode of thinking led to the investigation of those materials as desiccants with noteworthy results, as mentioned in the previous paragraph.

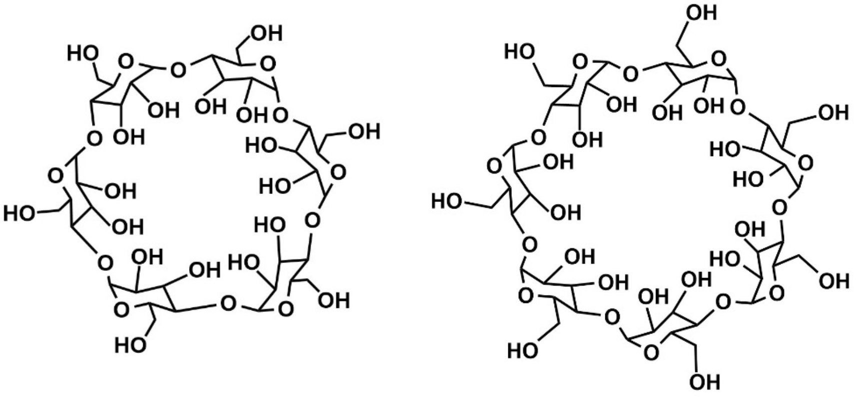

α-CD *β*-CD

Scheme 1. *α*- and *β*-Cyclodextrins bearing 18 and 21 –OH groups, respectively

2. RESULTS AND DISCUSSION

2.1. PREPARATION OF CYCLODEXTRIN-BASED POLYURETHANE AEROGELS – CHEMICAL AND GENERAL MATERIAL CHARACTERIZATION

The total dangling –OH groups on the glucose subunits (18 and 21 in *α*-CD and *β*-CD, respectively) were balanced stoichiometrically with the isocyanate groups of a rigid aromatic triisocyanate (TIPM). DMF solutions of the two reagents were polymerized and gelled at room temperature with DBTDL as catalyst (Scheme 2). The total amount of monomers (*i.e.*, TIPM + *α*-CD or *β*-CD) was set either at 2.5% w/w or at 15% w/w of the sol. Wet-gels were aged in their molds, solvent exchanged with acetone and were dried in an autoclave with liquid CO_2 taken out as a supercritical fluid following standard procedures. The resulting materials are referred to as *α*- and *β*-CDPU-xx, whereas "xx" stands for the total monomer concentration in the sol (*i.e.*, 2.5% w/w or 15% w/w). All formulations and gelation times are given in Table S.1 of Appendix I in Supporting Information.

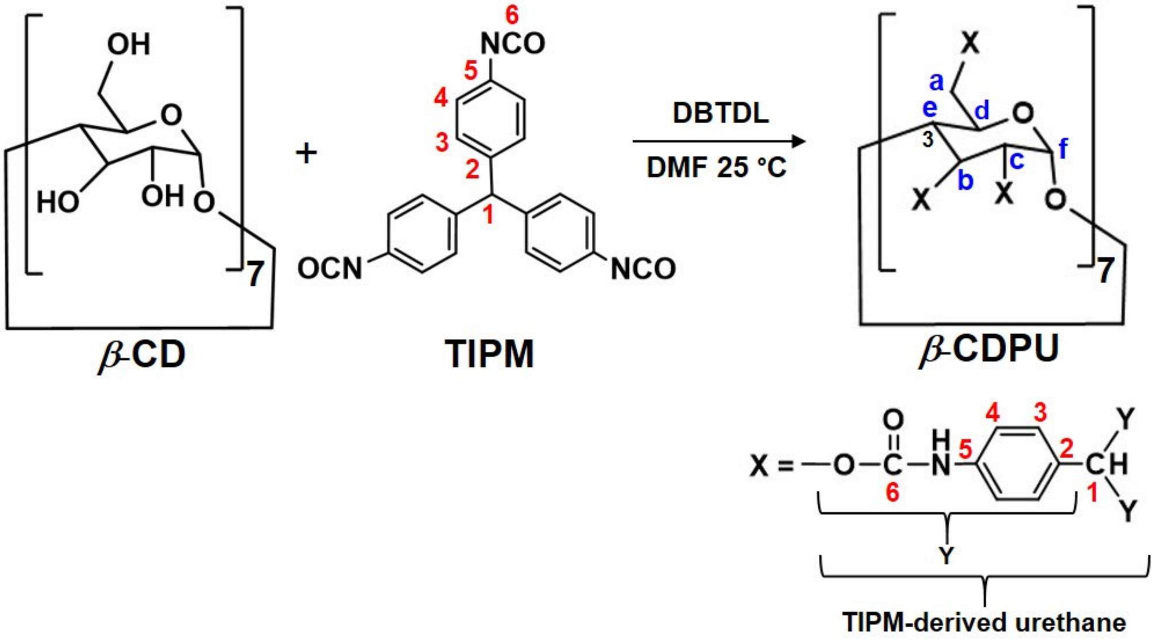

Scheme 2. Synthesis of cyclodextrin-based polyurethane aerogels, exemplified with *β*-CDPU-xx from *β*-CD and TIPM

The chemical identity of all *α*- and *β*-CDPU-xx was probed with FTIR, solid-state ^{13}C and ^{15}N NMR and CHN elemental analysis. The latter analysis was consistent with complete reaction and incorporation of both monomers in the product at their stoichiometric amounts. For *β*-CDPU-15, for example, we expected %C: 63.55; %H: 4.34; %N: 7.93. Experimentally it was found (average of 3 samples): %C: 63.55 ± 0.57; %H: 4.74 ± 0.20; %N: 8.19 ± 0.13. All aliphatic and aromatic carbons in the ^{13}C NMR spectra (Figure 1A) could be traced to the monomers. The new resonance at 153 ppm was assigned to the urethane carbonyl coming from the N=C=O groups of TIPM.[38] The solid-state ^{15}N

NMR spectra (Figure 1B) showed only one resonance at 102 ppm assigned to the urethane nitrogen.[47]

In FTIR (Figure 2), a strong urethane carbonyl stretch appeared at 1716 cm^{-1}, while the strongest peak at 1511 cm^{-1} was assigned to aromatic C=C stretching. A strong broad absorption band in the 3600-3100 cm^{-1} (with a peak maximum at 3405 cm^{-1}) was assigned to H-bonded N-H stretches.

The surface functionality that is available to interact with “intruders” from outside (like H_2O molecules) was investigated with XPS. The XPS spectrum of *α*-CD powder and a representative cyclodextrin-based aerogel sample, *α*-CDPU-15, are shown in Figure 3. The O1s XPS spectrum of *α*-CD showed a single peak at 532.12 eV that was assigned to both the C-OH and the glycosidic C-O-C. On the other hand, the deconvoluted O1s spectrum of *α*-CDPU-15 exhibited two absorptions, one at 532.17 eV and one at 530.62 eV; the first one was attributed to both the glycosidic C-O-C and the urethane oxygen (C=O)$\underline{\text{O}}$, while the second one to the urethane C=O.[48,49] Finally, consistent with the solid-state ^{15}N NMR data, the N1s XPS spectra showed just one symmetric peak at 398.66 eV that was assigned to urethane N.[50] In summary, *α*- and *β*-CDPU-xx were highly branched polyurethanes with surfaces decorated with –NH(C=O)O– groups.

In SEM (Figure 4), all four *α*- and *β*-CDPU-xx aerogels consisted of random assemblies of about equal-size nanoparticles. The porous structure was probed with N_2 and CO_2 sorption porosimetry. The skeletal framework was probed further with SAXS.

Table 1. Materials characterization data of α- and β-CDPU aerogels and α- and β-CD powders

Sample	Linear shrinkage (%) [a,b]	Bulk density, ρ_b (g cm^{-3}) [a]	Skeletal density, ρ_s (g cm^{-3}) [c]	Porosity Π (% v/v) [d]	BET surface area, σ (m^2 g^{-1})[e]	Particle radius (nm)			Fractal dimensions from SAXS [i]
						r [f]	R_1 [g]	R_2 [h]	
α-CDPU-2.5	51 ± 0.39	0.208 ± 0.015	1.296 ± 0.010	84	607 ± 2 [60 ± 8]	3.80	5.42 ± 0.36	30.21 ± 0.57	2.54 ± 0.28
β-CDPU-2.5	53 ± 0.27	0.257 ± 0.007	1.296 ± 0.014	80	457 ± 3 [45 ± 2]	5.04	4.94 ± 0.10	27.21 ± 0.76	3.00 ± 0.03
α-CDPU-15	40 ± 0.08	0.771 ± 0.004	1.334 ± 0.004	42	267 ± 11 [15 ± 3]	8.09	6.54 ± 0.03	[j]	[j]
β-CDPU-15	46 ± 0.12	0.942 ± 0.045	1.346 ± 0.010	30	246 ± 19 [7 ± 4]	9.82	7.97 ± 0.01	[j]	[j]
α-CD					0.9711 [0.1567]				
β-CD					0.9816 [0.1211]				

[a] Average of 3 samples. [b] Linear shrinkage = 100 × (mold diameter – sample diameter)/(mold diameter). [c] Single sample, average of 50 measurements. [d] Porosity, $\Pi = 100\times(\rho_s - \rho_b)/\rho_s$. [e] Average of 2 samples. Numbers in [brackets] are micropore surface areas via t-plot analysis according to the Harkins and Jura method. [f] Particle radii, $r = 3/(\rho_s\times\sigma)$; [g] R_1: primary particle radii from SAXS; [h] R_2: secondary particle radii from SAXS. [i] Fractal dimensions from power-law Region III of SAXS data (refer to Figure S.2 of Appendix III in Supporting Information). [j] SAXS intensity profiles could be fitted only in two regions.

Table 2. Pore structure data from N_2 and CO_2 adsorption by *α*- and *β*-CDPU aerogels and *α*- and *β*-CD powders

Sample	Specific pore volume (cm^3 g^{-1})					Pore size data		
	from N_2-sorption at 77 K			from CO_2-sorption at 273 K		Average pore diameter via 4V/σ (nm) [f]		BJH plot max [g]
	V_{Total} [a]	$V_{1.7\text{-}300\ nm}$ [b]	V_{max} [c]	V_{DR} [d]	V_{DFT} [e]	$V = V_{Total}$	$V = V_{max}$	
α-CDPU-2.5	4.0361 ± 0.3466	0.8876 ± 0.0972	1.1282 ± 0.1505	0.1246 ± 0.0162	0.0441 ± 0.0044	26	7.43	17 (21.5)
β-CDPU-2.5	3.1194 ± 0.1056	0.9272 ± 0.0738	1.0260 ± 0.0558	0.1131 ± 0.0002	0.0409 ± 0.0001	27	8.98	42 (30.2)
α-CDPU-15	0.5474 ± 0.0063	0.6382 ± 0.1982	0.5714 ± 0.0725	0.0737 ± 0.0011	0.0290 ± 0.0004	7.8	8.56	6.7 (1.1)
β-CDPU-15	0.3186 ± 0.0504	0.4076 ± 0.0001	0.4188 ± 0.0016	0.0618 ± 0.0065	0.0310 ± 0.0060	5.6	6.81	3.8 (0.2)
α-CD		0.0036	0.0038	0.0664	0.0319		15.65	
β-CD		0.0040	0.0040	0.0047	0.0014		16.30	

[a] V_{Total} was calculated via $V_{Total} = (1/\rho_b)-(1/\rho_s)$. The uncertainty was calculated by the rules of propagation of error. [b] Cumulative volume of pores between 1.7 and 300 nm from N_2-sorption and the BJH desorption method. [c] The maximum volume of N_2 adsorbed along the isotherm at 77K as P/P_o approached 1.0. [d] Total pore volume of micropores from CO_2-sorption data at 273K using the Dubinin-Radushkevich method (see Figure S.1 of Appendix II). [e] Total pore volumes for pores <1 nm, obtained *via* the DFT method from CO_2-sorption data at 273K. All pore volumes are reported as average of the results from two runs. [f] Calculated using the BET surface areas from Table 1, and by setting V equal to V_{Total}, or V_{max} as indicated. [g] From the BJH plots: first values are the peak maxima; numbers in (parentheses) are the full widths at half maxima.

Materials properties of α- and β-CDPU-xx are summarized in Tables 1 and 2, which also include corresponding data, whenever possible, for α– and β–CD for reference. As shown by the data of Table 1, upon drying, all gels shrunk 40%-50% in linear dimensions, and bulk densities (ρ_b) varied from 0.21 g cm^{-3} (α-CDPU-2.5) to 0.94 g cm^{-3} (β-CDPU-15). Correspondingly, the porosity (Π, calculated from bulk and skeletal (ρ_s) density data *via* $\Pi = (\rho_s - \rho_b) / \rho_s$) dropped from 84% v/v to 30% v/v, respectively. The latter materials could hardly be classified as aerogels, however, since their BET surface areas (σ, *via* N_2-sorption) remained high (>220 m^2 g^{-1}), they were still considered further for water adsorption.

2.2. THE PORE STRUCTURE AND THE SKELETAL FRAMEWORK OF α- AND β-CDPU-xx AEROGELS

All N_2-sorption isotherms (Figure 5) were Type IV. Hysteresis loops signified mesoporosity and were observed with all samples. However, the overall shape of the isotherms obtained with xx = 2.5 and xx = 15 materials were different. The isotherms of both α- and β-CDPU-15 aerogels showed broad saturation plateaus, characteristic of strictly mesoporous materials. The hysteresis loops were type H1 signifying ink-bottle type of mesopores (*e.g.*, as those formed by close packing of spherical particles – see below). Although the isotherms of both α- and β-CDPU-2.5 aerogels also reached saturation, the plateaus were narrow and a rapid increase of the adsorbed volume was observed at partial pressures (P/P_o) > 0.8, signifying a significant amount of macroporosity. The latter was attributed to the lower amount of material filling the same space as in the xx = 15 samples. The amount of N_2-adsorbed per unit mass (g) of either α- and β-CDPU-2.5 aerogels was

>3× higher than the amount adsorbed by the α- and β-CDPU-15 samples, signifying a structural change as density went up.

Pore volumes in the mesopore size regime ($V_{1.7\text{-}300\_nm}$) were calculated from the medium-to-high pressure N_2-sorption data of Figure 5 using the BJH desorption method. Data are summarized in Table 2 and are compared with: (a) the maximum volume adsorbed along the isotherms as P/P_o approached unity (V_{max}); and, (b) the total pore volumes (V_{Total}) calculated independently from bulk and skeletal density data ($V_{Total} = (1/\rho_b)-(1/\rho_s)$). In all cases V_{max} and $V_{1.7\text{-}300\_nm}$ matched closely one another. In α- and β-CDPU-15, $V_{1.7\text{-}300\_nm}$ (or V_{max}) $\approx$ V_{Total} (all in the 0.4-0.6 cm^3 g^{-1} range), but, due to macroporosity, in both α- and β-CDPU-2.5, V_{Total} >> $V_{1.7\text{-}300\_nm}$ (by 2.6× to 4.5×). Most importantly, however, in α- and β-CDPU-<u>2.5</u> $V_{1.7\text{-}300\_nm}$ was up to twice as much as the $V_{1.7\text{-}300\_nm}$ of α- and β-CDPU-<u>15</u>, supporting the structural change alluded to above.

Attempted use of low-pressure N_2-sorption (with a low-pressure transducer) in order to probe the micropore volume that necessarily exists in the α- and β-CD cavities,[37] did not produce any data, and it was concluded that N_2 could not probe the CD cavities. Instead, the micropore volume and pore size distribution was probed with CO_2 adsorption (see Appendix II in Supporting Information). Pore volumes of micropores with sizes <1 nm were calculated from analysis of the CO_2 adsorption isotherms with the DFT method (V_{DFT}), and they were found low (all in the 0.029-0.044 cm^3 g^{-1} range) and comparable for all materials (see Table 2). Pore volumes were also calculated from the same CO_2 adsorption data using the Dubinin-Radushkevich (DR) method (Figure S.1 - Table 2);[51,52] the values, V_{DR}, were larger than V_{DFT}, yet still low (0.11-0.12 cm^3 g^{-1}) for both α- and β-

CDPU-2.5, and even lower (0.062-0.073 cm^3 g^{-1}) for α- and β-CDPU-15. Always pore volumes probed with CO_2 adsorption were ≤10% of $V_{1.7\text{-}300\_nm}$ (Table 2).

BET surface areas, σ, support the notion of structural changes between α- and β-CDPU-2.5 on one hand, and α- and β-CDPU-15 on the other. If there were no structural changes, specific surface areas should be invariant of the amount of material (density). Here, α- and β-CDPU-2.5 were found to have significantly higher BET surface areas (607 m^2 g^{-1} and 457 m^2 g^{-1}, respectively) than α- and β-CDPU-15 (both in the 250 m^2 g^{-1} range) (see Table 1). (It is noted that the BET surface areas of α- and β-CDPU-2.5 aerogels are the highest amongst all polyurethane aerogels we are aware of.[38-44])

Pore size distributions in the 1.7-300 nm were obtained via the BJH method (see insets in Figure 5) and were very different for the xx = 2.5 *vs* the xx = 15 samples. α- and β-CDPU-2.5 showed broad pore size distributions, well in the mesopore range, while α- and β-CDPU-15 showed narrow distributions near the lower end of that range. Clearly, we are dealing with two groups of structurally different materials. Average pore sizes were calculated *via* the $4V/\sigma$ method, where the specific pore volume, V, was set equal to either V_{Total} or $V_{1.7\text{-}300\_nm}$. Results are cited in Table 2 and it is noted that average pore volumes by the two methods track the differences between V_{Total} and $V_{1.7\text{-}300\_nm}$, as discussed above. Most importantly, however, in the cases of α- and β-CDPU-15 the average pore sizes by the $4V/\sigma$ method (with V set equal either to V_{Total} or to $V_{1.7\text{-}300\_nm}$) were very close (7.8-8.6 nm and 5.6-6.8 nm, respectively) to the narrow BJH pore size distributions noted in the insets of Figure 5, thus supporting the validity of those distributions, and thereby the fact that the xx = 2.5 and the xx = 15 aerogels were structurally different materials. Further insight about those structural differences should be traceable to the way nanoparticles get assembled.

A first estimate of the size of the fundamental building blocks (primary particles) was obtained from skeletal density, ρ_s, and BET surface area, σ, data *via* the relationship: particle radius (r) = $3/(\rho_s \times \sigma)$. Primary particles calculated *via* that method were all in the 3.8-9.8 nm size regime (Table 1). Structural information was also obtained with small angle X-ray scattering (SAXS).

SAXS scattering profiles could be fitted into two power-law regions only with the low-density samples (xx = 2.5 – see Figure S.2 in Appendix III of the Supporting Information). The high-Q slope of all samples-was near, yet somewhat lower than -4.00, indicating that all primary particles had fuzzy interfaces (see Table S.2 in Appendix III of the Supporting Information). Primary particle radii, (R_1 – included in Table 1) were calculated from the high-Q Guinier knee of each scattering profile (Region II, Figure S.2), and they were numerically close and matched the trend in r from N_2-sorption data. By focusing either at r or R_1 (Table 1), primary particles of the xx = 15 samples were equal or larger than those of the xx = 2.5 samples, and those of the β-CDPU-15 aerogels were larger than those of their α- counterparts. Now, the slope of the low-Q power law region (Region III, Figure S.2) of α-CDPU-2.5 aerogels was equal to -2.54 ± 0.28 (see Table S.2), signifying mass-fractal assembly of primary particles into secondary particles with mass-fractal dimension equal to 2.54 ± 0.28. The radius of the secondary particles, (R_2 – included in Table 1) was calculated from the second Guinier knee (Region IV – Figure S.2) and it was found about 30 nm. From the mass-fractal dimension and the radii of the primary and secondary particles, the (meso)porosity of the secondary particles in α-CDPU-2.5 was calculated at 66% v/v[53] – *versus* 26% expected for close-packed spheres. On the other hand, the low-Q slope of β-CDPU-2.5 aerogels was equal to -3.00 ± 0.03 pointing to secondary particles consisting of closely packed primary particles; it was found from the second Guinier knee that $R_2 \approx 27$ nm. As just mentioned above, neither a low-Q power law nor a Guinier knee region was present in the high-density (xx=15) samples. Given that α- and β-CDPU-15 aerogels were low-porosity (Table 1), strictly mesoporous materials with narrow pores (Figure 5 and inset) and no quantitative sign of secondary particles (SAXS), it is reasonable to entertain the idea that the primary particles of those materials were densely packed – just like in low-density β-CDPU-2.5. Just on geometric grounds then, pore diameters between closely packed primary particles can be calculated *via* $2R_1(\sqrt{2}-1)$ and are on the order of 5.42 nm for α-CDPU-15, and 6.60 nm for β-CDPU-15, namely on the same order as the average pore sizes calculated *via* the $4V/\sigma$ method, or found *via* the BJH method (Figure 5 – insets). Thereby, with α-CDPU-15 and β-CDPU-15 being nanostructured densely-packed materials, the only pore volume available (0.57 cm^3 g^{-1} and 0.42 cm^3 g^{-1}, respectively – see Table 2) is confined in the interstitial places between primary particles. It is noted then that access to those pores is restricted by narrower channels, thereby the H1 shape of the corresponding N_2-sorption isotherms in Figure 5.

2.3. WATER VAPOR UPTAKE AND DESICCANT PROPERTIES OF α- AND β-CDPU-xx AEROGELS

The desiccant properties of α- and β-CDPU-xx aerogels were investigated at room temperature using two chambers, one with low humidity (~10%) maintained with Drierite™ in a Petri dish placed inside the chamber, and another one with high humidity (~99%) maintained with water in a Petri dish as shown in Figure S.3 of Appendix IV in

Supporting Information. Samples were placed and remained for 24 h in each chamber and then they were transferred to the other one. Periodically, samples were removed from their chambers and were weighted for water uptake. Before any experiments with α- and β-CDPU-xx aerogels the experimental set up was tested with commercial silica used as a desiccant, and with Drierite^{TM} itself (Figure 6A). The amount of water vapor absorbed (20% w/w for silica and 15% w/w for Drierite^{TM}) were close to those expected for the two materials (35 – 40% w/w for silica, and 10 – 14% w/w for Drierite^{TM}).[54,55] (Note that both control materials retained a significant amount of water after the first cycle – that is, after they were placed in the dry chamber and so on. The amounts of the water uptaken and released by all samples after three such 24h-cycles are cited in Table S.3 of Appendix IV in Supporting Information.)

Although none of the α- and β-CDPU-xx aerogels seemed to have reached saturation in 24 h, Figures 6B and 6C show that overall α-CDPU-2.5 aerogels had adsorbed the highest amount of water, about 108% w/w, and they expelled it quantitatively in the low humidity chamber. All experiments were conducted at room temperature. In fact, both lower-density samples (xx=2.5) showed higher water uptakes compared to their higher-density counterparts, but that difference in the β-CDPU-xx aerogels was not as large as in their α- counterparts. In the same context, it is also noted that the water vapor adsorption by α-CDPU-15 was in the same range as by the two β-CDPU-xx aerogels. Figures 6B and 6C also include water adsorption data from the corresponding α-CD and β-CD powders; both powders adsorbed ≤20% w/w of water, β-CD uptook less (about 15% w/w) than α-CD and both retained most of the water (>50%) in subsequent cycles. It is noted that the amount of water uptaken by either α-CD or β-CD powder was less than what is expected (about 33% w/w) if one H_2O molecule is H-bonded to each –OH group of either cyclodextrin (Scheme 1), while involvement of the hydrophobic microporous cavities was unlikely. Finally, new samples of each of the α- and β-CDPU-xx aerogels were subjected to ten (10) 24h-adsorption/desorption cycles in the same experimental set up at room temperature (Figure S.3). Each round trip took 48 h. The weight gain or loss was monitored in 24 h intervals, and is referred to relative to the initial weight of the sample before the first cycle. Results are shown in Figure 6D. The relative water vapor uptake amongst the four new α- and β-CDPU-xx aerogels was in the same range as before (compare Figure 6D with Figures 6B and 6C). The additional information from Figure 6D is that all aerogels experienced a break-in period of 5 cycles over which the total water uptake was reduced, but again α-CDPU-2.5 aerogels settled at about 80% w/w of water uptake, which is >2.5 times the level of water uptake by all other samples, which settled at about 30% w/w.

With an eye on improving on the unusually high water uptake by all cyclodextrin-based polyurethane aerogels, we first looked at the energetics of water uptake by the best performer, α-CDPU-2.5. Figure 7A shows the water sorption isotherms obtained at two temperatures. The isotherms were Type IV with H3 type hysteresis loops. The existence of hysteresis loop in those isotherms suggests that water is first adsorbed on the stronger sites of the material, followed by formation, growth and coalescence of clusters due to the strong hydrogen bonding between water molecules.[56] One major difference from the corresponding N_2-sorption isotherm was the lack of saturation, and a second one was that the hysteresis loops did not close as P/P_o returned to zero meaning that some water (<10%) remained adsorbed on the material. It is also noted that the 24h dynamic water uptake (about 108% w/w – Figure 6A) was higher than the equilibrium water uptake (30% w/w).

Similar observations, albeit the difference was smaller, have been made before,[57] but in our opinion the reasons seem to remain elusive.

The two isotherms of Figure 7A were replotted as shown in Figure S.5 of Appendix V in Supporting Information, and were fitted together into a Virial expression (Eq 1) following an iterative segment-wise fashion with the isosteric heat of adsorption, Q_{st}, *vs* N (Eq 2) as described in the Experimental section. The segments along N are listed in Table S.4. The final fitted plot of Q_{st} as a function of N is shown in Figure 7B, and the coefficients of Eq 2 for each segment along N are given in Table S.5 of Appendix V in Supporting Information.

The zero-coverage isosteric heat of adsorption, Q_o, is the value of Q_{st} at near zero water uptake and is largely a function of the binding strength of the adsorbate to the strongest binding sites. Q_o for α-CDPU-2.5 was calculated via Eq 3 from the coefficients of the Q_{st} *vs* N plot (see Table S.5) and it was found at about 18 kJ mol^{-1}, which is a typical value for H-bonding between water and urethane groups that decorate the surfaces of cyclodextrin-based polyurethane aerogels (refer to Figure 3).[58] As noted in Figure 7B, Q_{st} increases rapidly with the quantity of water adsorbed and reaches to a value of about 55 kJ mol^{-1}, which is higher than the heat of condensation of water (44.0 kJ mol^{-1}).[59] This kind of "overshooting" in the Q_{st} plots of water adsorption has been noted before,[59,60] and the consensus is that it is an artifact.[60,61] Instead, the average asymptotic value of Q_{st} as N increases is a better indicator of the interactions that lead to the total water uptake.[59] That average asymptotic value (see dotted horizontal line in Figure 7B) was near the condensation heat of water, indicating multilayer adsorption of water on water. It is also important to note that the average asymptotic value of Q_{st} is reached at the early stages of water uptake, thereby the overall water uptake was due to pore filling. This conclusion is in accord with the fact that an assumed monolayer coverage (at 7.6×10^{-6} mol m^{2})[62] of the entire BET surface areas (from Table 1) can explain only up to a 10% w/w of the water uptake observed experimentally (Figures 6B and C and Table S.3). Consequently, following the pore-filling hypothesis, α-CDPU-2.5 should display the highest water uptake capacity due to its highest pore volume amongst its other counterparts. Further along this line of reasoning, it is noted that the total water vapor uptake by three of the four aerogels of this study (α-CDPU-2.5, α-CDPU-15 and β-CDPU-15 – see Figures 6B and 6C and Table S.3) practically matches the mass needed to fill the mesopore volume of the three materials (refer to the values of $V_{1.7\text{-}300\_\text{nm}}$ or $V_{\max}$ in Table 2). By the same token, the water vapor uptaken by β-CDPU-2.5 in 24 h was enough to fill only about 54% of the $V_{1.7\text{-}300\_\text{nm}}$ or $V_{\max}$. Focusing first on the former three aerogels, in which water uptake matches the $V_{1.7\text{-}300\_\text{nm}}$ or $V_{\max}$ values, the question becomes why water uptake stops after mesopores have been filled? This issue is addressed in conjunction with Scheme 3.

Focusing on translational degrees of freedom, the maximum entropy of a collection of molecules is in the vapor phase (S_{out}), and the minimum when they are bound to a surface (S_{sur}). Driven by pressure or chemical potential (*i.e.*, concentration), molecules may enter micropores, but once inside they have lost their degrees of translational freedom and $S_{\text{in-micro}} \sim S_{\text{sur}} = 0$. In mesopores the situation is somewhere in between. Thereby, $S_{\text{out}} > S_{\text{in-meso}} > S_{\text{in-micro}} \approx S_{\text{sur}}$, and therefore $(S_{\text{sur}} - S_{\text{out}}) < (S_{\text{sur}} - S_{\text{in-meso}}) < (S_{\text{sur}} - S_{\text{in-micro}}) \approx 0$. Correspondingly, at a given temperature, T, when a species gets adsorbed on a surface from its immediate environment the entropic term, $-T\Delta S$, changes in the opposite direction: $(-T\Delta S)_{\text{in the open}} > (-T\Delta S)_{\text{from mesopores}} > (-T\Delta S)_{\text{from micropores}} \approx 0$. In order for the Gibbs free enthalpy, ΔG, to be negative, or conversely for the adsorption process to be spontaneous, the enthalpic term, ΔH, in $\Delta G = \Delta H - T\Delta S$, must be negative enough to undo the unfavorable effect of the entropic term ($-T\Delta S$). In micropores, even an energy-neutral process could foot that bill, because $(-T\Delta S)_{\text{from micropores}} \approx 0$. This seems to be the case of CO_2 adsorption inside micropores lined with, for example, phenoxides (surf–O^-).[46] In the case of open smooth surfaces, chemisorption (σ or π bond formation) would be an obvious mechanism to overcome the large positive value of $(-T\Delta S)_{\text{in the open}}$. In the present case here, for the first monolayer of water adsorption $\Delta H \approx -5$ kcal mol^{-1}, and subsequently, $\Delta H \approx -11$ kcal mol^{-1}. Therefore, ΔG will remain <0, and (meso)pores will be filled until their size is such that $-T(S_{\text{sur}} - S_{\text{in-meso}}) > |\Delta H|$ (≈ 11 kcal mol^{-1}).

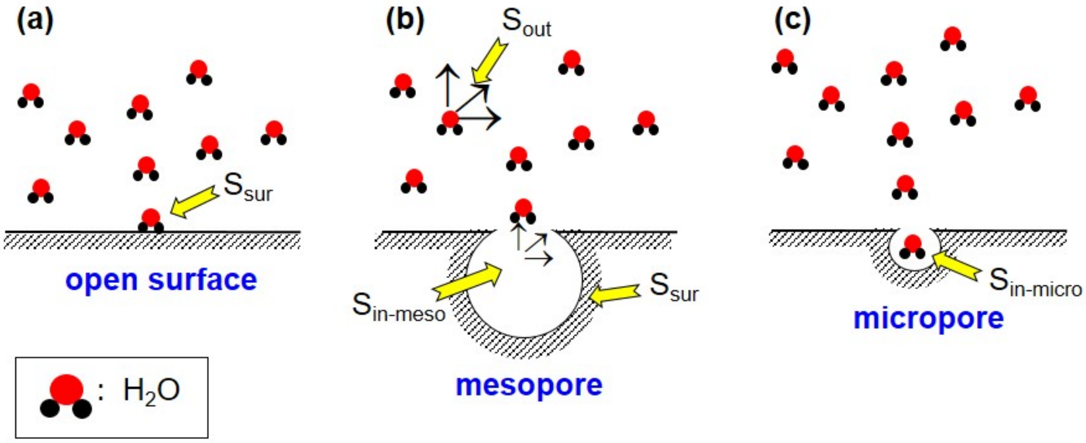

Scheme 3. Water adsorption on open smooth surfaces (a), inside mesopores (b) and inside micropores (c). (Entropy of water molecules: S_{out}, in the open vapor phase; $S_{\text{in-meso}}$, in mesopores; $S_{\text{in-micro}}$, in micropores; S_{sur}, on the surface)

And that brings us back to the case of β-CDPU-2.5. In those materials the pore size distribution in the mesopore range is shifted to significantly larger values (42 nm) relative to the pore sizes in α-CDPU-2.5 (17 nm) – see Figure 5. Furthermore, primary particles in β-CDPU-2.5 were closely packed (the fractal dimension was equal to 3.00 ± 0.03 – see Table 1). Owing to the similarity of primary particle sizes of that material with everything else, the specific interstitial volume within closely packed primary particles in β-CDPU-2.5 will be about equal to the specific volume of α-CDPU-15 and β-CDPU-15, hence the water uptake amongst those materials will be about the same – and it is. Clearly then, the larger mesopores in β-CDPU-2.5, always still within the mesopore range, are not small enough to contribute toward water adsorption in the spirit of Scheme 3.

Putting everything together, maximum water uptake will be observed with hydrophilic mesoporous materials consisting of fractal secondary particles with pore size distributions centered at about 20 nm or less.

3. CONCLUSION

The hydrophobic cavity in polyurethane aerogels incorporating α- and β-cyclodextrin in every repeat unit did not seem to be involved in any extraordinary adsorption effects. However, the high degree of crosslinking imposed by the multifunctionality of cyclodextrins, together with the rigid-aromatic triisocyanate employed in this study (TIPM) has lead to an early phase separation of small nanoparticles that yielded nanostructures with high surface areas decorated with urethane groups that can develop hydrogen bonding with water. That initiated a cascade of events upon exposure to a high-humidity (99%) environment, leading to exceptionally high water absorption capacities (up to 1 g of H_20 per g of adsorber). Data show that water uptake from the humid environment continues until small mesopores are filled completely, whereas the cutoff for “small” is pores with size distribution maxima at 20 nm or less. Such mesopores are formed within mass fractal secondary particles. Most importantly, however, owing to the balance of the enthalpic and entropic factors of water adsorption in such pores, adsorbed water is released by just reducing the relative humidity of the environment.

4. EXPERIMENTAL

4.1. MATERIALS

All reagents and solvents were used as received, unless noted otherwise. *α*- and *β*-Cyclodextrins (≥ 97%), and dibutyltin dilaurate (DBTDL) were purchased from Sigma Aldrich Chemical Co. and were dried at 120 °C under vacuum for 24 h prior to use. Anhydrous *N,N*-dimethylformamide (DMF) was purchased from Alfa Aesar. Tris(4-isocyanatophenyl)methane (TIPM) was donated by Covestro LLC as a 27% w/w solution in dry EtOAc under the trade name Desmodur RE. Deuterated solvents, chloroform ($CDCl_3$) and *N,N*-dimethylformamide-d_7 (99.5% atom D) containing tetramethylsilane (0.05% v/v) were purchased from Cambridge Isotope Laboratories, Inc.

4.1.1. Synthesis of Cyclodextrin-based Polyurethane Aerogels. In a typical procedure, *α*-cyclodextrin (0.5282 g, 0.000543 mol) was dissolved in anhydrous DMF and the solution was added to 4.44 g of Desmodur RE (containing 1.20 g, 0.00326 mol of TIPM in ethylacetate). The resulting sol was stirred at room temperature under N_2 for 10 min. At that point, DBTDL (48 μL) was added, and the resulting sol was stirred for another 5 min.

Subsequently, the sol was poured into molds (Wheaton 4 mL Polypropylene Omni-Vials 1.04 cm in inner diameter, Fisher part No. 225402), which were then sealed with their caps, wrapped with Parafilm^{TM}, and were kept at room temperature for 12-16 h for gelation and aging. The total weight percent of monomers (TIPM + α- or β-CD) in the sol was varied by changing the amount of solvent (DMF) and is denoted by extension -xx in the sample names, which are referred to as α-(or β-)CDPU-xx. "xx" was varied at two levels, 2.5% and 15% w/w. After aging, wet-gels were removed from the molds, washed with DMF (2×, 8h each time), acetone (4×, 8h each time, using 4× the volume of the gel for each wash) and were dried in an autoclave with liquid CO_2, which was removed as a supercritical fluid (SCF). Similarly, two formulations (xx = 2.5% w/w, or xx = 15% w/w) of β-CDPU-xx were synthesized by reacting β-cyclodextrin (0.5285 g, 0.000465 mol) and 4.44 g of Desmodur RE (containing 1.20 g, 0.00326 mol of TIPM) in the required amount of anhydrous DMF in the presence of DBTDL catalyst (48 μL, 0.0000815 mol). All formulations and gelation times are given in Table S.1 of Appendix I in Supporting Information.

4.2. METHODS

4.2.1. Drying with Supercritical Fluid (SCF) CO_2. Drying of acetone-exchanged wet-gels with supercritical fluid (SCF) CO_2 was carried out in an autoclave (SPIDRY Jumbo Supercritical Point Dryer, SPI Supplies, Inc. West Chester, PA). Samples were loaded into the autoclave and acetone was added till all samples were submerged. The pressure vessel was closed and liquid CO_2 was allowed in at room temperature until it displaced all acetone, which was then drained out. Liquid CO_2 was allowed in the vessel several more times until acetone was extracted out of the pores of the samples completely.

The criterion for the latter was that CO_2 released from the vessel formed powder of dry ice. Finally, the temperature of the autoclave was raised to 40 °C and SCF CO_2 was vented off like a gas.

4.2.2. Physical Characterization. Bulk densities (ρ_b) were calculated from the weight and the physical dimensions of the samples. Skeletal densities (ρ_s) were determined with helium pycnometry using a Micromeritics AccuPyc II 1340 instrument.

4.2.3. Chemical Characterization. Elemental analysis was conducted with an Exeter Analytical Model CE440 elemental analyzer, calibrated with acetanilide, urea, and glycine. The combustion furnace was operated at 1050 °C. All calibration standards and samples were run three times and results are given as averages.

Infrared (IR) spectra were obtained in KBr pellets, using a Nicolet-FTIR Model 750 spectrometer.

Liquid ^{13}C-NMR spectra were recorded with a 400 MHz Varian Unity Inova NMR instrument (100 MHz carbon frequency). Solid-state CPTOSS ^{13}C-NMR spectra were obtained from samples ground into fine powders on a Bruker Avance III 400 MHz spectrometer with a carbon frequency of 100 MHz, using a 7 mm Bruker MAS probe at a magic-angle spinning rate of 5 kHz, with broadband proton suppression and the CP TOSS pulse sequence for total suppression of side spinning bands. Solid-state ^{13}C-NMR spectra were referenced externally to glycine (carbonyl carbon at 176.03 ppm). Chemical shifts are reported versus TMS (0 ppm). Solid-state CPMAS ^{15}N-NMR spectra were also obtained on the same Bruker Avance III 400 MHz Spectrometer with a nitrogen frequency of 40.557 MHz, using a 7 mm Bruker MAS probe, with broadband proton suppression and magic angle spinning rate of 5 kHz. Chemical shifts were reported versus liquid ammonia (0 ppm) and were externally referenced to glycine (amine nitrogen at 33.40 ppm). In all solid-state NMR experiments the relaxation delay was set at 5 s.

X-ray photoelectron spectroscopic analysis (XPS) was carried out with a Kratos Axis 165 Photoelectron Spectroscopy System. Samples were mixed and ground together with Au powder (5% w/w) as internal reference. That was then pressed into a pellet for analysis. Each sample was placed on a piece of conductive carbon tape that was adhered to a stainless steel sample holder. Samples were introduced into the analysis chamber one at a time and the chamber was evacuated at 10^{-8} Torr or lower. No ion sputtering was performed on any of the samples. An Al monochromatic source (150 W) was used for excitation. A charge neutralizer was used to reduce the effects of differential or sample charging. The analysis area was 700 × 300 microns. Elemental quantification calculations were based on broad survey results from single sweeps at higher sensitivity (Pass energy = 80) and were carried out with the Kratos Axis Vision processing software taking into consideration the appropriate relative sensitivity factors for the particular XPS system. High-resolution elemental scans where carried out at a lower sensitivity (Pass energy = 20), using multiple sweeps to improve the signal-to-noise ratios. Deconvolution of the spectra was performed with Gaussian function fitting using the OriginPro 8.5.1 software package.

4.2.4. Solid Framework Characterization. Scanning electron microscopy (SEM) was conducted with Au-coated samples on a Hitachi Model S-4700 field-emission microscope.

The fundamental building blocks of all aerogels were also probed with small angle X-ray scattering (SAXS), using ~2 mm thick disks cut with a diamond saw. SAXS was conducted with a PANalytical X’Pert Pro multipurpose diffractometer (MPD) configured for SAXS, using Cu Kα radiation (wavelength = 1.54 Å), a 1/32° SAXS slit, a 1/16° antiscatter slit on the incident beam side, and a 0.1 mm antiscatter slit together with a Ni 0.125 mm automatic beam attenuator on the diffracted beam side. Samples were placed in circular holders between thin Mylar sheets, and scattering intensities were measured by running 20 scans from −0.1° to 5° with a point detector in the transmission geometry. All scattering data were reported in arbitrary units of scattering intensity as a function of Q, the momentum transferred during a scattering event. Scattering data (see Appendix III) were fitted to the Beaucage Unified Model,[63,64] applied with the Irena SAS tool for modeling and analysis of small angle scattering within the Igor Pro application (a commercial scientific graphing, image processing, and data analysis software from Wave Metrics, Portland, OR).

4.2.5. Gas and Water Vapor Sorption Analysis – Pore Structure Characterization. All samples were degassed at 150 °C for 24 h prior to each gas (N_2, CO_2, H_2O) sorption study. Brunauer-Emmett-Teller (BET) surface areas, σ, pore volumes, average pore sizes and pore size distributions for pores in the 1.7-300 nm range were determined with N_2-sorption porosimetry at 77 K using a Micromeritics ASAP 2020 surface area and porosity analyzer. A Micromeritics Tristar II 3020 operated through the MicroActive software version 4.0 was used for pore structure analysis by CO_2 sorption up to 760 torr (0.03 relative pressure) at 273 K (see Appendix II). Equilibrium water adsorption isotherms at 288 K and 298 K were outsourced at Micromeritics Particle Testing services.[65]

4.2.6. Dynamic Water Vapor Adsorption Studies. Water uptake experiments were carried out using two closed chambers at room temperature as shown in Figure S.3 of Appendix IV in Supporting Information. The two chambers were constructed with upside-down large Petri dishes (180 mm in diameter) covered with Al foil. The two chambers were maintained at 99% and 10% relative humidity for water adsorption and desorption, respectively. Humidity was monitored with two EEEKit Hygrometer/Thermometer Digital LCD monitors[66] placed inside each chamber (see Figure S.3). The 99% relative humidity environment was created by water placed in a Petri dish (88 mm in diameter) inside the closed chamber. The 10% relative humidity environment was created with 30 g Drierite™ placed in a similar Petri dish inside the other closed chamber. Fresh Drierite™ was used for every desorption experiment. Samples were placed in plastic caps and their size varied from 50 to 400 mg. Before the first water uptake cycle, α– or β–CDPU-xx samples were degassed at 80 ºC in a vacuum oven. (α- and β-CD powders were degassed at 130 ºC.) Up to 10 consecutive cycles of water adsorption-desorption were carried out, lasting 48 h each (allowing 24 h for adsorption and 24 h of desorption). The set-up was validated with three water adsorption-desorption cycles using Drierite™ and silica gel found in bags used to keep several commercial products dry.

4.2.7. Calculation of Isosteric Heats of H_2O Adsorption (Q_{st}). Those were calculated via the Virial fitting method.[67,68] For this, the H_2O adsorption isotherms at 288 K and 298 K were fitted simultaneously with a Virial-type equation (Eq 1) using the OriginPro 8.5.1 software package, where P is the pressure in Torr,

$$\ln P = \ln N + \frac{1}{T}\sum_{i=0}^{m} a_i N^i + \sum_{i=0}^{n} b_i N^i \qquad (1)$$

N is the adsorbed amount of water in mmol g^{-1}, *T* is the absolute temperature, a_i and b_i are the Virial coefficients, and *m* and *n* are the number of coefficients needed in order to fit the two isotherms. In general, Virial fitting starts by re-plotting the entire two adsorption isotherms at the two temperatures as Ln *P/N* vs *N* (see Figure S.5 of Appendix V in Supporting Information), and the two new isotherms are fitted simultaneously to Eq 1 using the least squares method; the values of *m* and *n* are varied gradually until the sum of the residuals (*i.e.*, the squared deviations of the experimental Ln *P/N* values from the fitted ones) is minimized. The *m* and *n* values in our case were $m = 5$ and $n = 2$. At that point, with the values of *m* and *n* at hand, in order to estimate the a_i and b_i coefficients of Eq 1, the latter equation was re-fitted as described by Bandosz.[69] According to that procedure, Eq 1 was fitted independently in six consecutive subsets of the data points along the two isotherms. The six subsets were chosen progressively with respect to *N* in a step-wise fashion as follows: The procedure started by fitting the experimental Ln *P*/*N* values within $0 \leq N \leq 6.0$. The upper limit (6 mmol g^{-1}) was the value of *N* at the maximum point of Ln *P*/*N*. The values of the parameters a_i were introduced into Eq 2 (*R* is the universal gas constant = 8.314 J mol^{-1} K^{-1}), thus obtaining Q_{st} (in kJ mol^{-1}) as a function of *N*.

$$Q_{st} = -R\sum_{i=0}^{m} a_i N^i \qquad (2)$$

The need to separate the Ln *P/N* vs *N* data (Eq 1) into subsets arises by the fact that after a certain value of *N*, the Q_{st} values calculated via Eq 2 tend to decrease, even become negative (see Table S.5 in Appendix V of the Supporting Information). The Ln *P*/*N* vs *N* data after the *N* value at which the Q_{st} values become negative ($N>1.4$) were rejected, and the remaining data points ($0 \leq N \leq 1.4$) comprise the first subset. Moving toward the second subset, the rejected part of the Ln P/N vs N data ($1.4 < N \leq 6.0$) was fitted to Eq 1 again, and the data points above which the new Q_{st} values became negative were rejected again ($3.0 < N \leq 6.0$). The remaining data points ($1.4 < N \leq 3.0$) and associated fitting coefficients comprised the second subset. The ranges of the six subsets that were used for Virial fitting of the entire isotherms, and for calculating the Q_{st} values as a function of N are tabulated in Table S.4 of Appendix V in Supporting Information. The parameters a_i and b_i for all six subsets are given in Table S.5 of Appendix V in Supporting Information.

The heat of adsorption as coverage goes to zero, Q_0, is given by Eq 3, and is a sensitive evaluator of the affinity of the adsorbate for the surface.[70]

$$Q_0 = -Ra_0 \qquad (3)$$

ACKNOWLEDGEMENTS

We thank the Army Research Office under Award No. W911NF-14-1-0369 for financial support. We also thank Covestro LLC for the generous supply of Desmodur RE (TIPM), and the Materials Research Center of the Missouri University of Science and Technology for support with materials characterization.

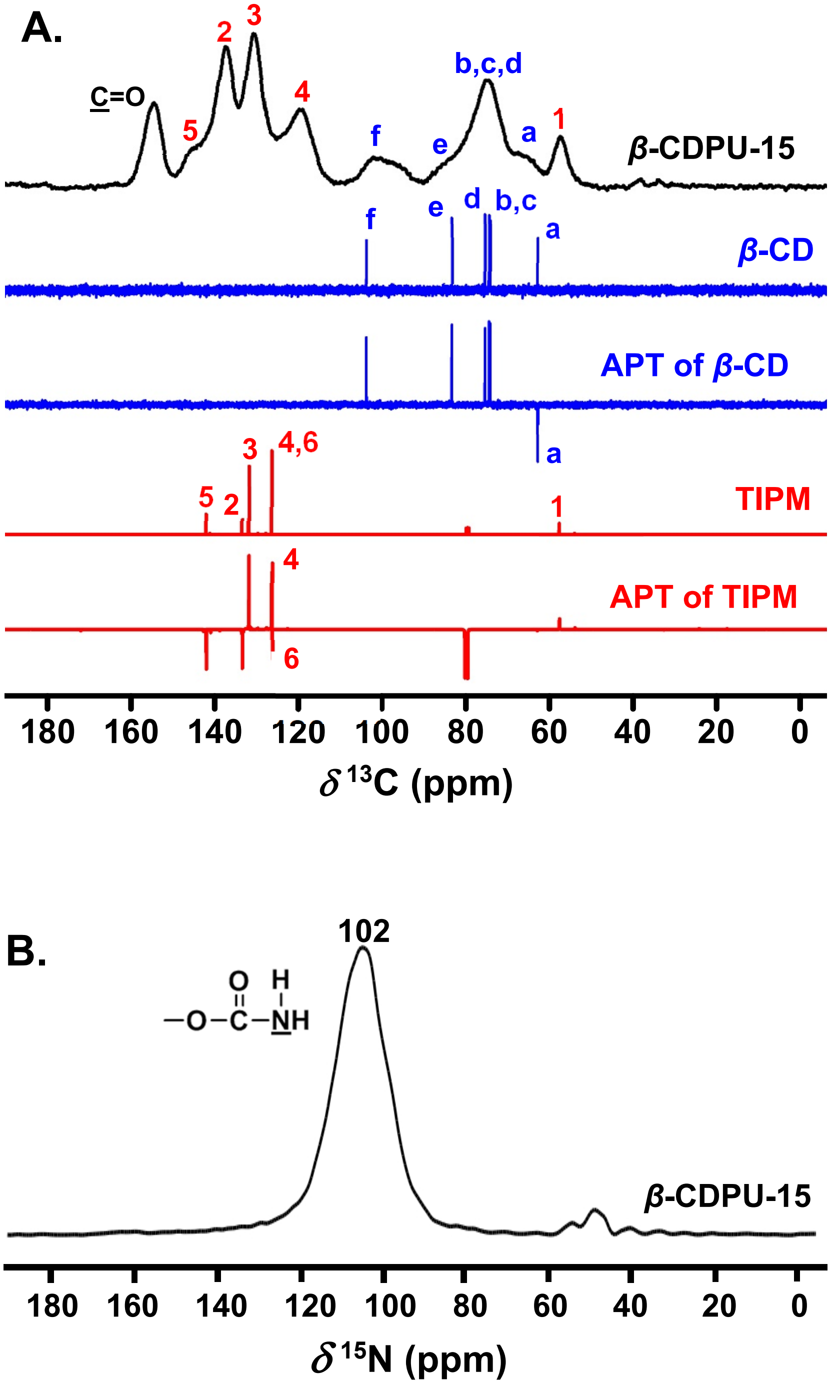

Figure 1. (A) Top: Solid-state CPMAS ^{13}C-NMR spectrum of a representative *β*-CDPU-xx (xx = 15). Bottom: Broad-band ^{1}H-decoupled liquid-state ^{13}C-NMR spectra of TIPM and *β*-CD including the ^{13}C-APT NMR spectra of TIPM and *β*-CD as indicated. (B) Solid-state CPMAS ^{15}N-NMR of *β*-CDPU-15.

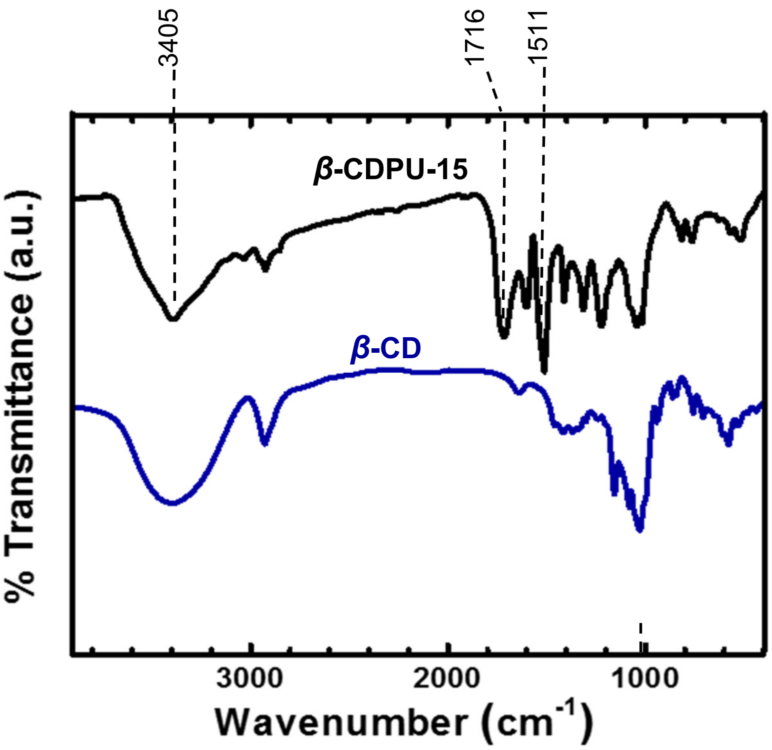

Figure 2. Infrared spectra of a representative *β*-CDPU-xx aerogel (xx = 15) and of *β*-cyclodextrin monomer. Absorptions marked with dashed lines are discussed in the text.

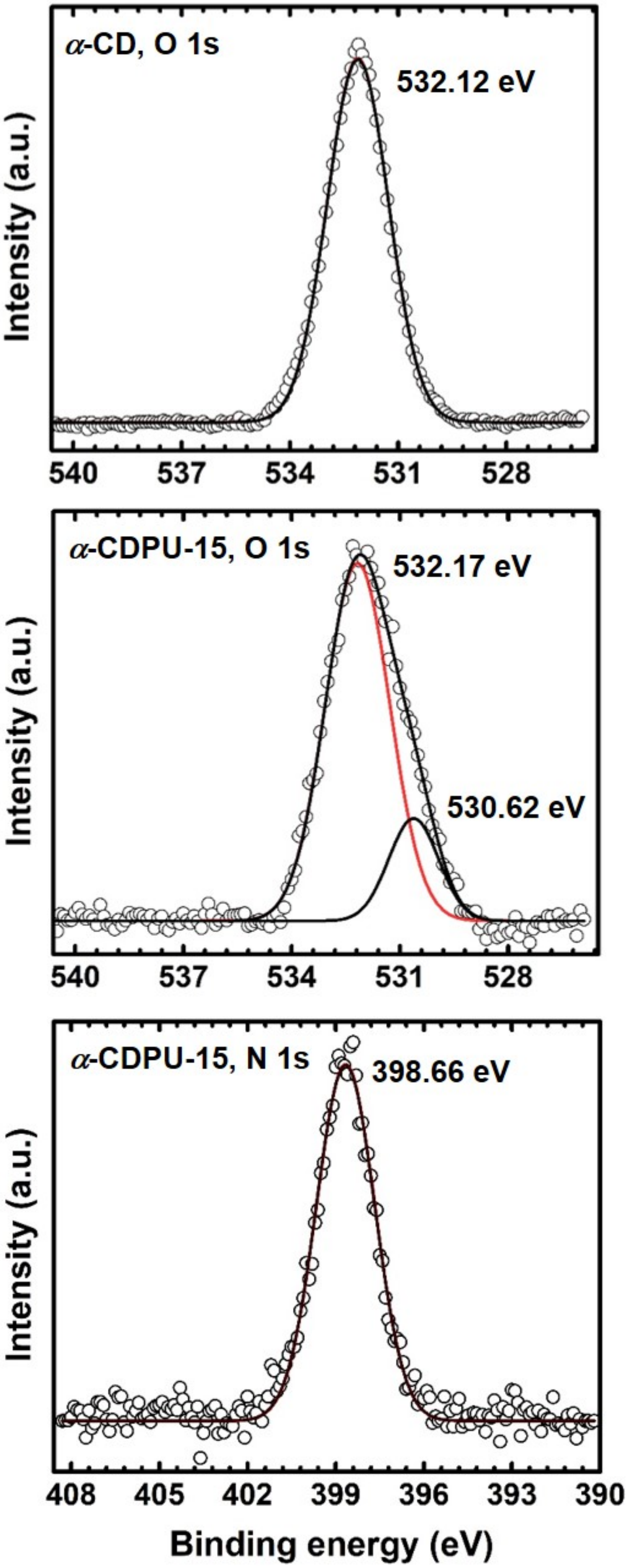

Figure 3. Representative XPS data of samples as shown.

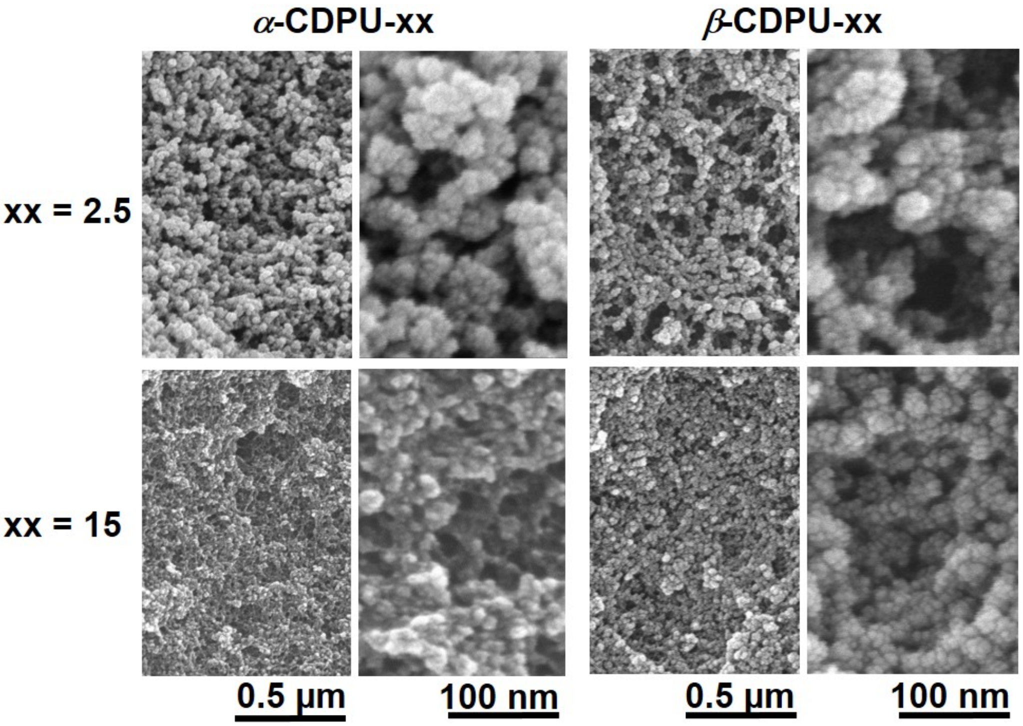

Figure 4. SEM of α- and β-CDPU-xx aerogels at two different magnifications as shown.

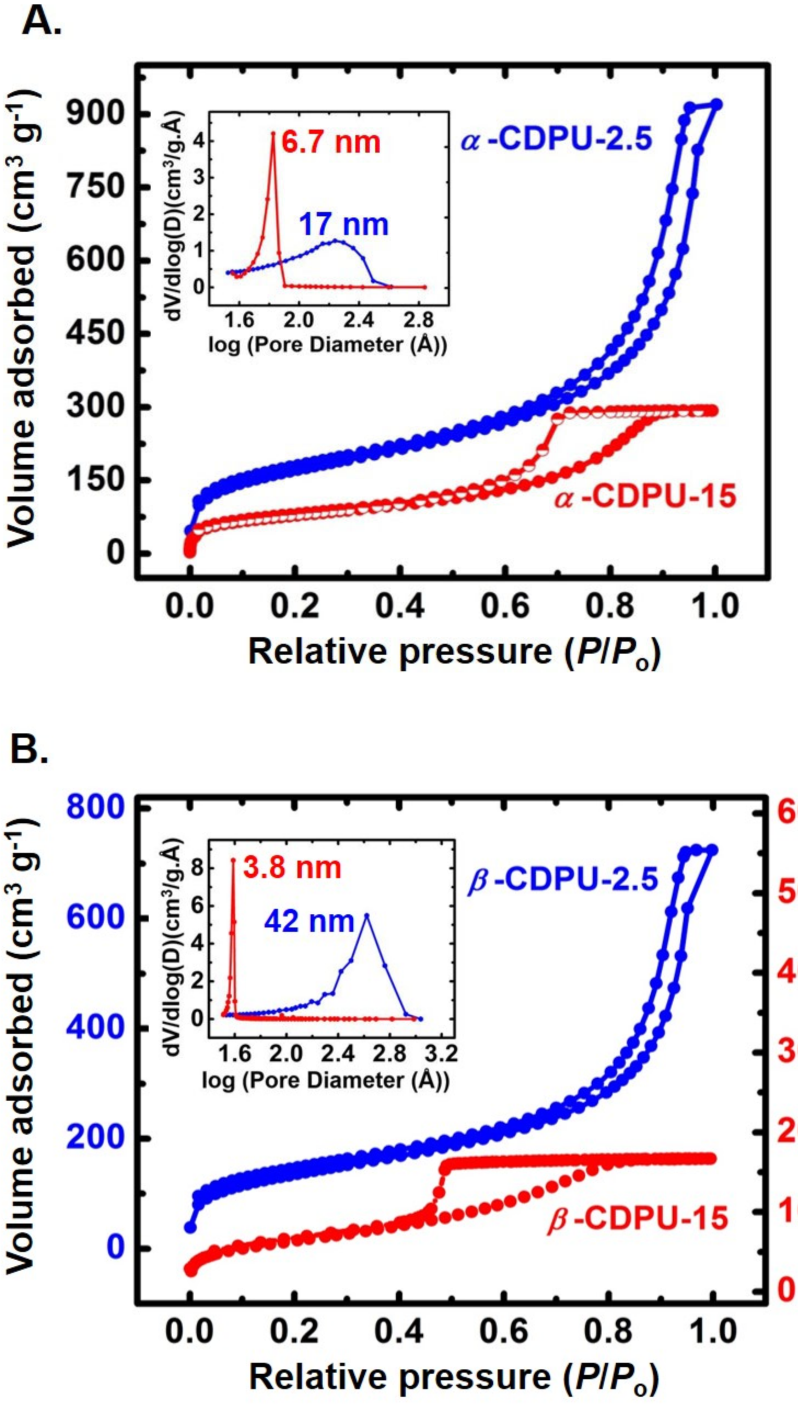

Figure 5. N_2 sorption isotherms of: (A) *α*-CDPU-2.5 and *α*-CDPU-15 at 77 K; (B) *β*-CDPU-2.5 and *β*-CDPU-15 at 77 K. Insets: pore size distributions via the BJH equation applied to the desorption branches of the isotherms.

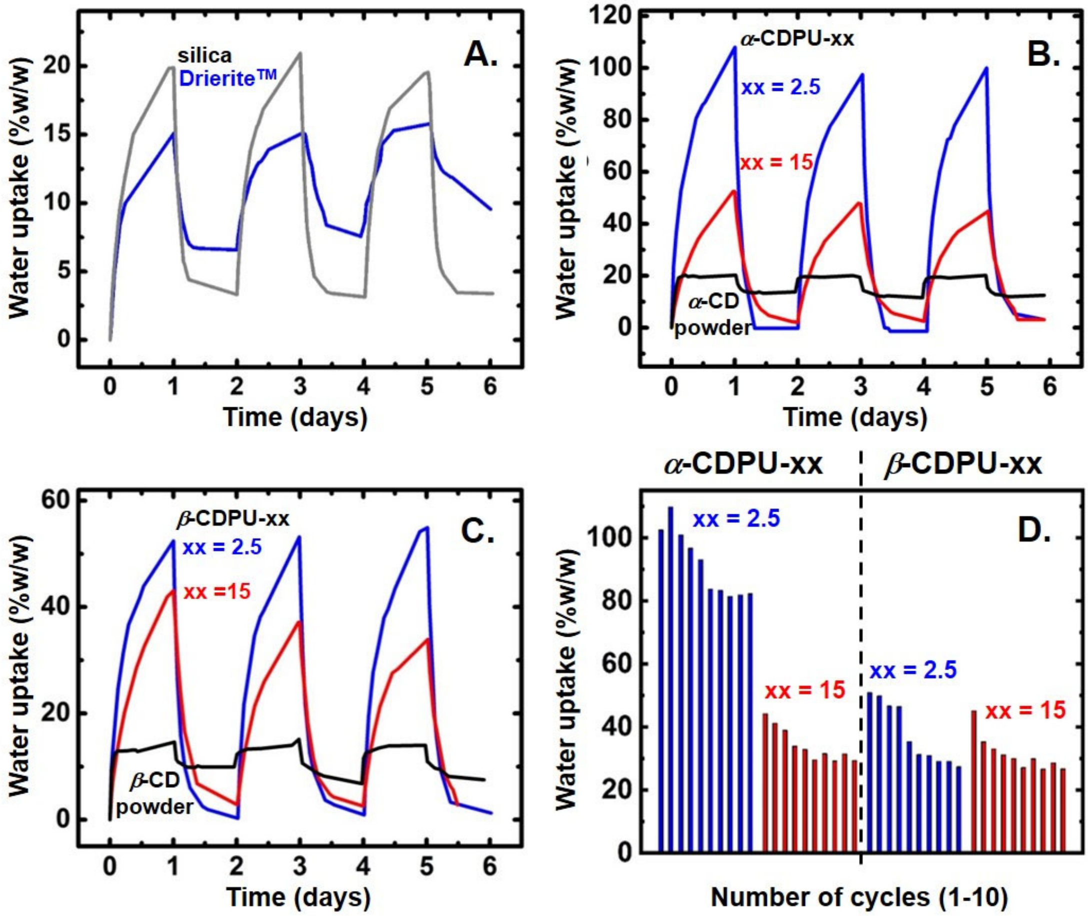

Figure 6. Three consecutive cycles of dynamic water uptake monitored frequently between a high (99%) and a low (10%) relative humidity environment by: silica gel and Drierite^{TM} (A); *α*-CDPU-2.5 and *α*-CDPU-15 (B); and, *β*-CDPU-2.5 and *β*-CDPU-15 (C). Ten consecutive cycles of the four aerogels monitored every 24h (D). (In all cases, the environment was changed from high to low humidity and *vice versa* every 24 h. All percent water uptake values are relative to the initial weight of the samples before the first water uptake in a humid environment.)

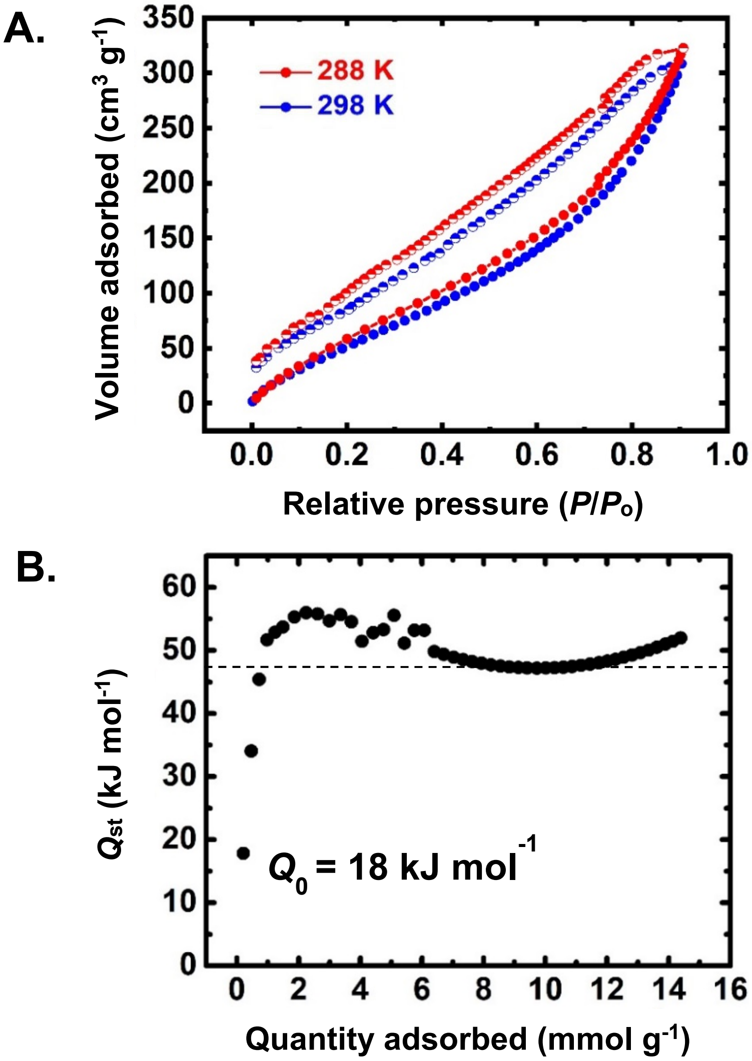

Figure 7. (A) Isotherms of water adsorption by α-CDPU-2.5 at two temperatures (298 K and 288 K). (B) Isosteric heat of water adsorption (Q_{st}) by α-CDPU-2.5 as a function of the water uptake, N. The dashed horizontal line in frame (B) shows the asymptotic value of Q_{st} as N increases.

Appendix I: Formulations and gelation times of *α*- and *β*-CDPU-xx aerogels

Table S.1. Formulations and gelation times of *α*- and *β*-CDPU-xx aerogels

Sample	*α*- or *β*-Cyclodextrin				Desmodur RE		TIPM			DMF		Gelation time [e] (min)
	mass (g)	volume [a] (mL)	mmol	C [b] (M)	volume (mL)	mass [c] (g)	mass [d] (g)	mmol	C [b] (M)	mass (g)	volume (mL)	
α-CDPU-2.5	0.973	0.649	1.00	0.007	7.979	8.156	2.202	6.00	0.045	117.87	124.34	25
β-CDPU-2.5	1.375	0.955	1.00	0.006	9.31	9.513	2.569	7.00	0.042	146.87	154.93	25
α -CDPU-15	0.973	0.649	1.00	0.047	7.979	8.156	2.202	6.00	0.281	12.04	12.70	6
β-CDPU-15	1.375	0.955	1.00	0.038	9.31	9.513	2.569	7.00	0.264	15.41	16.25	7

[a] The volumes of *α*- and *β*-cyclodextrin were calculated based on their densities 1.49 g cm^{-3} and 1.44 g cm^{-3}, respectively.

[b] Molar concentrations refer to the sol.

[c] The mass of commercial Desmodur RE was calculated based on its density 1.022 g cm^{-3} measured in our lab.

[d] The mass of TIPM in Desmodur RE was calculated based on the 27% w/w concentration given by the supplier.

[e] Phenomenological gelation times were determined at room temperature (23 ºC).

Appendix II. CO_2 and CH_4 adsorption by α- and β-CDPU-xx aerogels

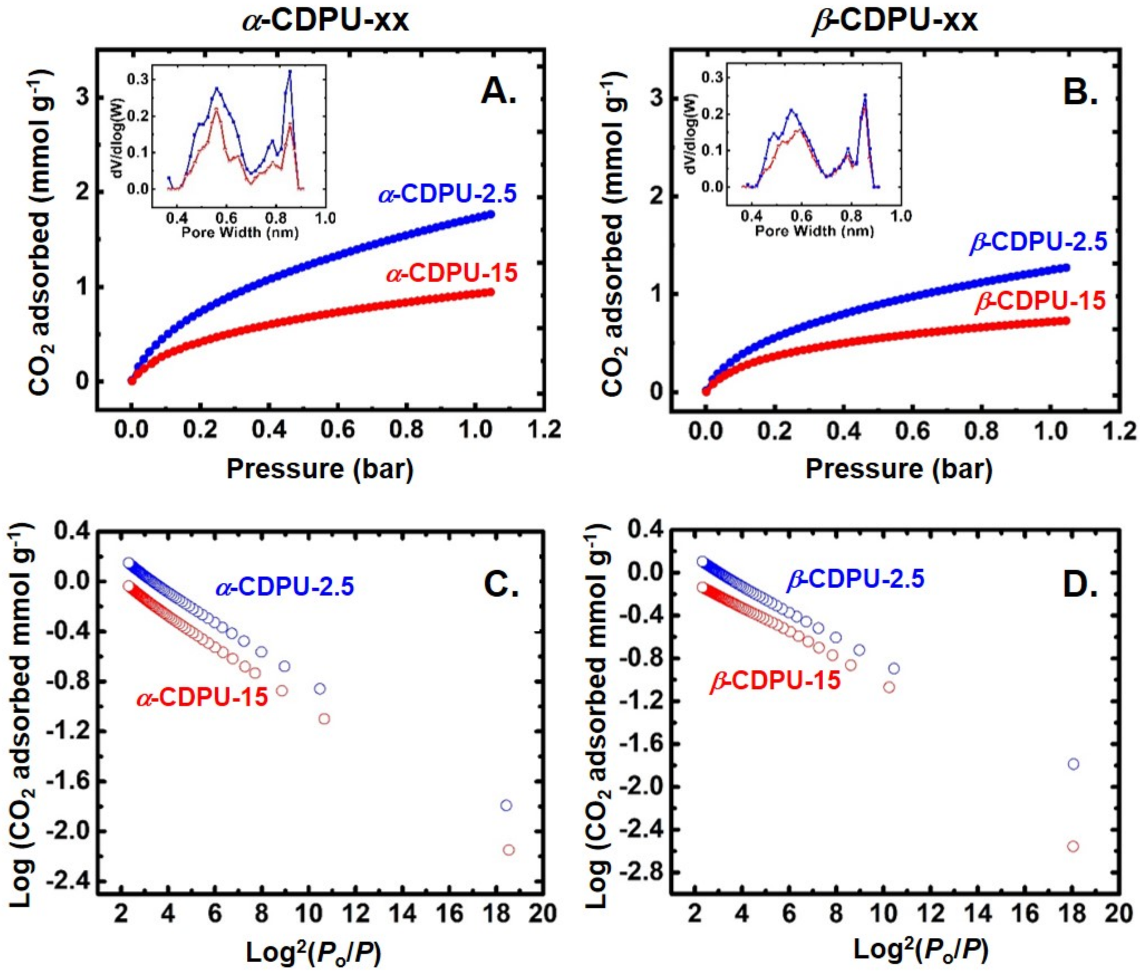

Figure S.1. (A),(B): CO_2 adsorption isotherms at 0 ˚C of aerogels as shown. Insets: pore size distributions by the DFT method. (C),(D): Dubinin-Rudushkevich (DR) plots from the data shown in frames (A) and (B), respectively. Pore volumes (V_{DR}) were calculated from the intercepts by extrapolating the linear parts of the plots, and are cited in Table 2 of the main article. (E),(F): CH_4 adsorption isotherms at 0 ˚C by aerogels as shown. (Continued)

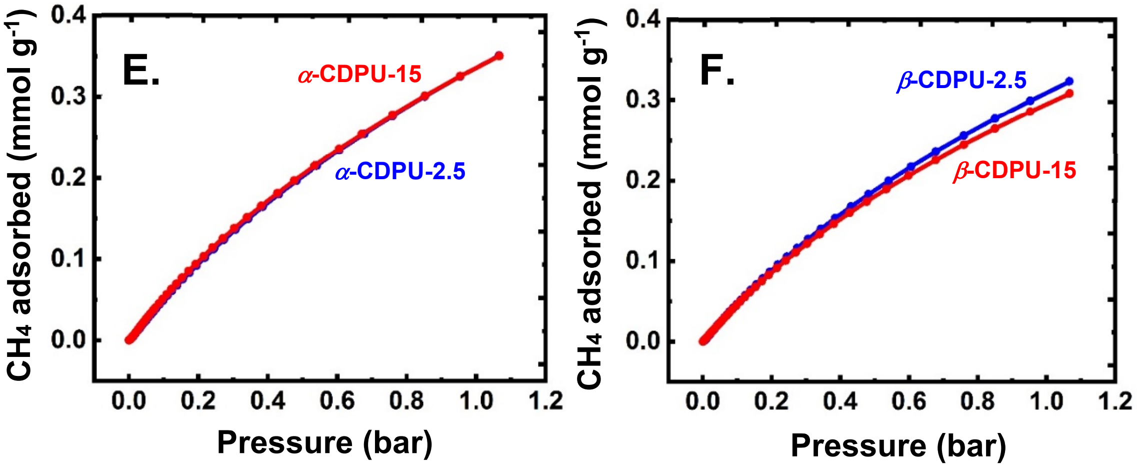

Figure S.1. (Continued) (A),(B): CO_2 adsorption isotherms at 0 ˚C of aerogels as shown. Insets: pore size distributions by the DFT method. (C),(D): Dubinin-Rudushkevich (DR) plots from the data shown in frames (A) and (B), respectively. Pore volumes (V_{DR}) were calculated from the intercepts by extrapolating the linear parts of the plots, and are cited in Table 2 of the main article. (E),(F): CH_4 adsorption isotherms at 0 ˚C by aerogels as shown.

Appendix III. Small angle x-ray scattering (SAXS) data for α- and β-CDPU-xx aerogels

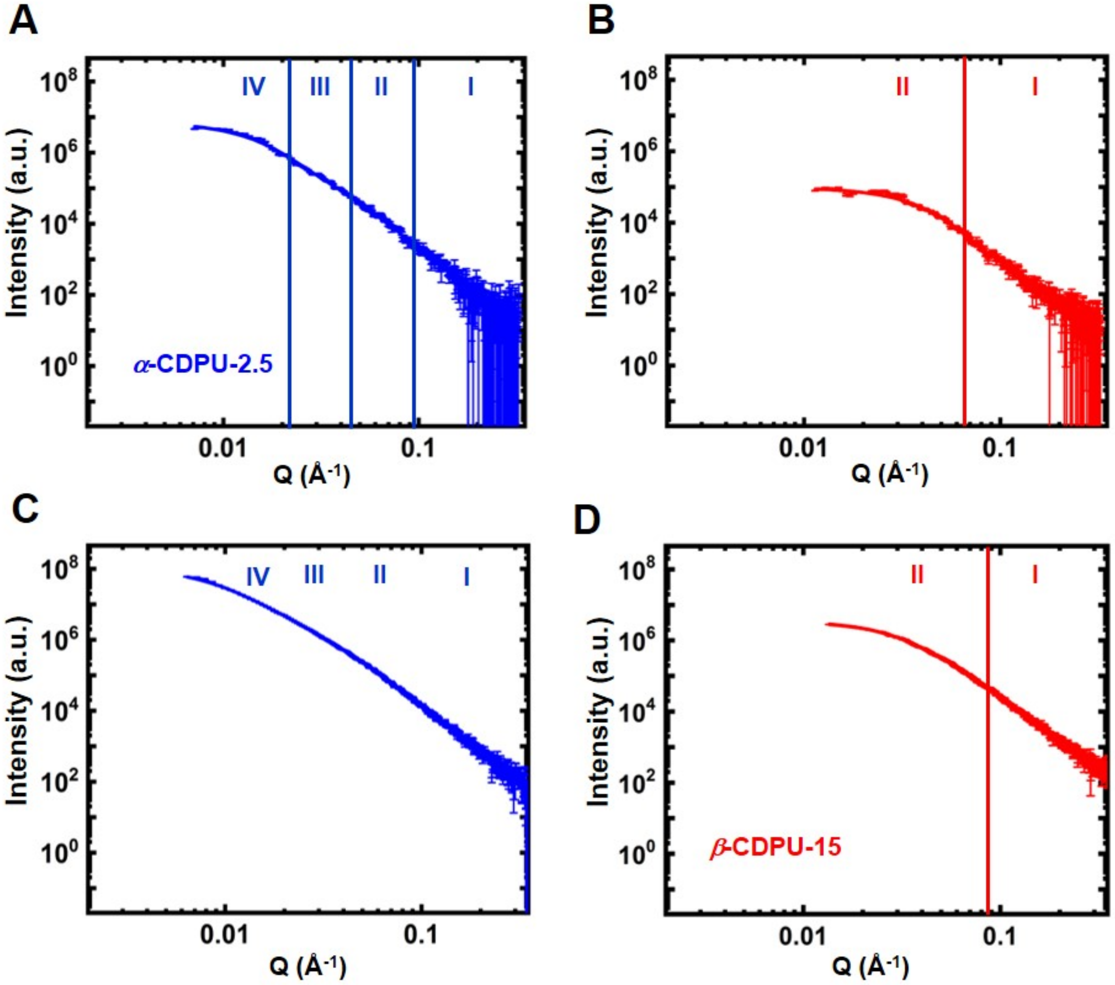

Figure S.2. SAXS intensity profiles as a function of the scattering vector, Q, of α- and β-CDPU-xx as shown.

Table S.2. SAXS data obtained by fitting the scattering profiles of Figure S.1 using the Beaucage Unified Model[S.R-1]

Sample	Primary Particles			Secondary Particles		
	high-Q slope [a]	R_G(I) [b] (nm)	R_1 [c] (nm)	low-Q slope [d]	R_G(II) [e] (nm)	R_2 [f] (nm)
α-CDPU-2.5	-4.22 ± 0.05	4.17 ± 0.28	5.42 ± 0.36	-2.54 ± 0.28	23.26 ± 0.44	30.21 ± 0.57
β-CDPU-2.5	-4.28 ± 0.02	3.80 ± 0.08	4.94 ± 0.10	-3.00 ± 0.03	20.95 ± 0.59	27.21 ± 0.76
α-CDPU-15	-3.98 ± 0.03	5.04 ± 0.02	6.54 ± 0.03	[g]	[g]	[g]
β-CDPU-15	-4.11 ± 0.01	6.14 ± 0.01	7.97 ± 0.01	[g]	[g]	[g]

Referring to Figure S.2:

[a] From power-law Region I.

[b] Radius of gyration of primary particles, R_G(I), from Region II (first Guinier knee).

[c] Primary particle radii R_1= (R_G(I)/0.77).

[d] From power-law Region III.

[e] Radius of gyration of secondary particles, R_G(II), from Region IV (second Guinier knee).

[f] Secondary particle radii, R_2 = (R_G(II)/0.77).

[g] Within our accessible range of *Q*, scattering profiles of α- (or β-)CDPU-15 aerogels could be fitted only with a high-*Q* power law and one Guinier knee.

S.R-1 (a) Beaucage G (1995) J Appl Crystallogr 28:717–728.
(b) Beaucage G (1996) J Appl Crystallogr 29:134–146.

Appendix IV: Dynamic water adsorption - experimental set-up

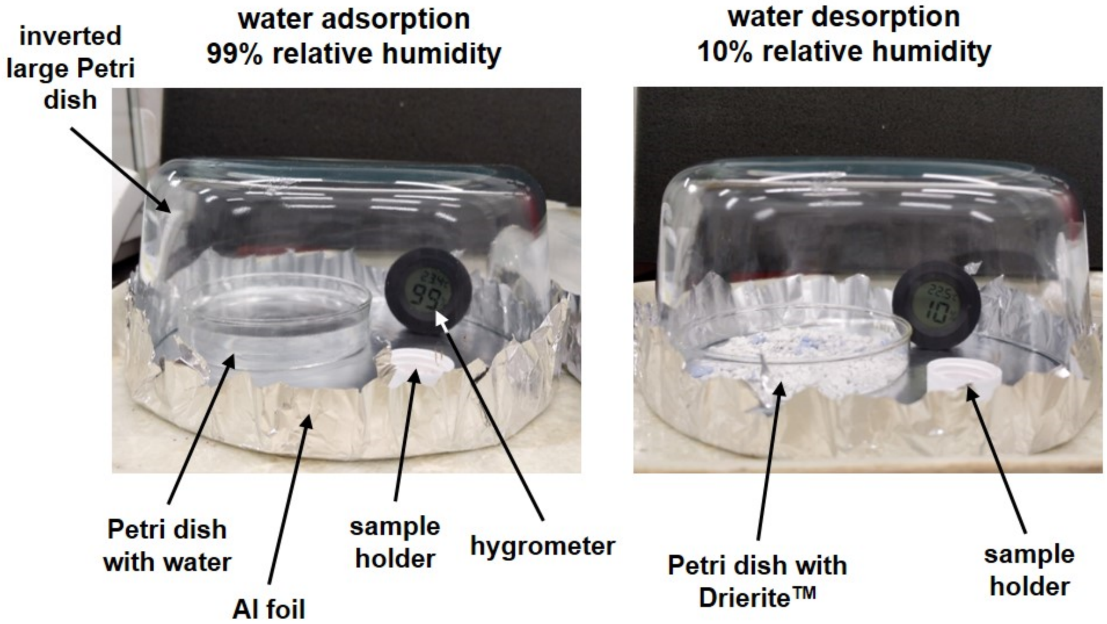

Figure S.3. Photographs of two closed chambers maintained at 99% and 10% humidity, respectively, as shown. The chambers were opened briefly for taking the samples out for weighing.

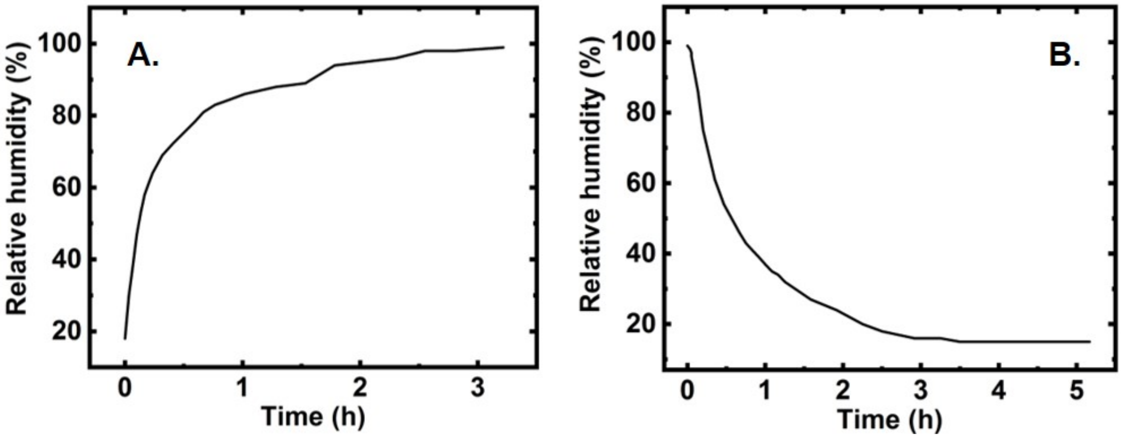

Figure S.4. (A) Increasing relative humidity with time in a closed chamber with a Petri dish with water. (B) Decreasing relative humidity with time in a closed chamber with a Petri dish with Drierite^{TM}.

Table S.3. Tabulated percent mass changes after three 24h-cycles of water vapor adsorption-desorption by materials as shown. The mass changes are relative to the masses before the adsorption-desorption experiments started.

Materials	Cycle 1		Cycle 2		Cycle 3	
	adsorption	desorption	adsorption	desorption	adsorption	desorption
silica	19.86	3.31	20.95	3.14	19.55	3.38
Drierite™	15.07	6.58	15.08	7.57	15.84	9.56
α-CDPU-2.5	107.98	-0.28	97.43	-1.42	77.78	3.05
α-CDPU-15	52.40	2.10	47.91	2.46	44.86	3.05
α-CD powder	20.18	13.81	19.47	11.54	20.14	12.48
β-CDPU-2.5	52.42	0.27	53.16	0.94	54.91	1.28
β-CDPU-15	43.10	2.81	37.11	2.54	33.93	2.83
β-CD powder	14.61	9.97	15.14	6.80	14.00	7.51

Appendix IV. Isosteric heats (Q_{st}) of water adsorption by α-CDPU-2.5

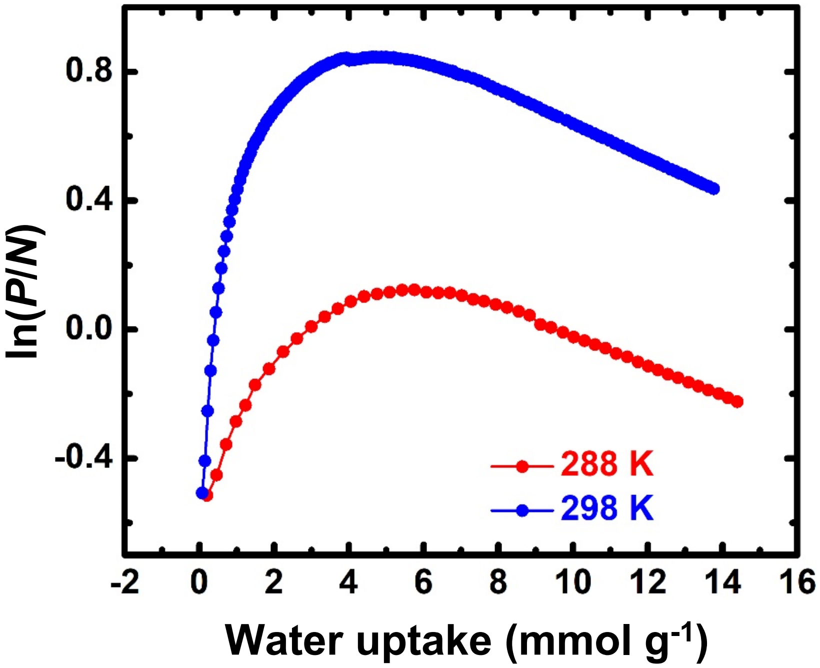

Figure S.5. Water adsorption isotherms of α-CDPU-2.5 at two different temperatures (red: 288 K; blue: 298 K). The two isotherms were fitted simultaneously using a Virial equation (refer to Equation 1 of the main article) for calculating the isosteric heats of adsorption, Q_{st}, as a function of water uptake, N. (Fitting was carried out in a stepwise fashion by diving the isotherms in six subsets as described in the Experimental Section.)

Table S.4. Six subsets (derived as shown in Table S.5) of the isotherms of Figure S.5, which were used for the Virial fitting, and for calculation of the isosteric heats of water adsorption (Q_{st}) by α-CDPU-2.5.

Subset	Range of N (mmol g^{-1}) for Virial fitting	Range of N (mmol g^{-1}) for calculating Q_{st} in the corresponding regions
Region 1	0.0 – 6.0	0.0 – 1.4
Region 2	1.4 – 6.0	1.4 – 3.0
Region 3	3.0 – 6.0	3.0 – 4.0
Region 4	4.0 – 6.0	4.0 – 5.0
Region 5	5.0 – 7.0	5.0 – 6.0
Region 6	6.0 – 14.4	6.0 – 14.4

Table S.5. Stepwise Virial fitting of the isotherms of Figure S.5. Q_{st} was first calculated in the entire region of N shown in each frame. Points outside the red dashed lines were rejected. Then moved to the rejected range of N and the process was repeated. The end Virial coefficients correspond to the range of N as indicated. (No. of terms used in Virial fitting: $m = 5$, $n = 2$)

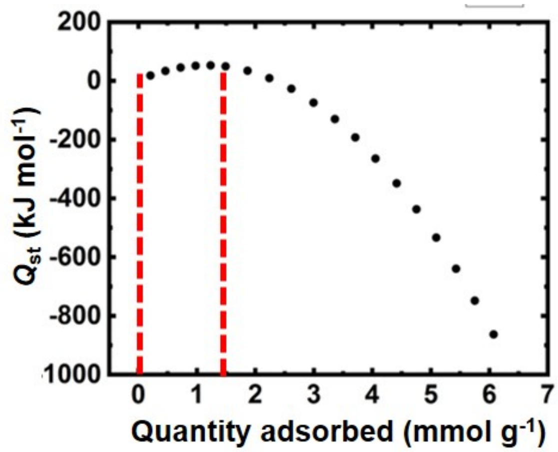

Region 1 [$0.0 \le N \le 1.4$]		
Parameters	Value	Standard Error
a_o	-135.04573	256.49389
a_1	-10663.91352	667.42805
a_2	4536.48086	386.93593
a_3	16.55311	10.31349
a_4	-2.41392	1.81526
a_5	0.13493	0.11561
b_0	-0.16065	0.86504
b_1	37.53614	2.24397
b_2	-15.95997	1.27922
χ^2_{red}	3.24968×10^{-4}	
R^2	0.9964	

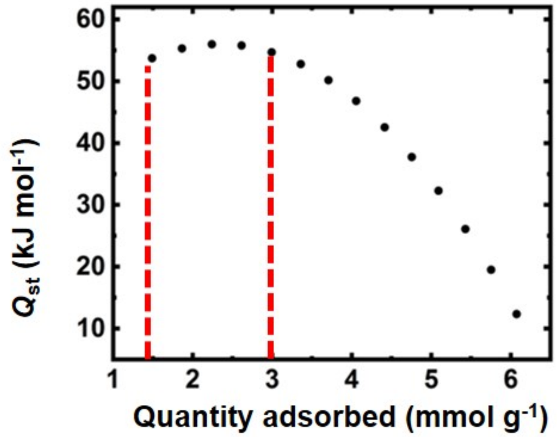

Region 2 [$1.4 < N \le 3.0$]		
Parameters	Value	Standard Error
a_o	-4638.13611	300.34945
a_1	-1805.68457	312.4587
a_2	398.5428	85.62435
a_3	-5.9749	6.19564
a_4	0.8051	0.85222
a_5	-0.04085	0.04496
b_0	15.73582	0.99866
b_1	6.35989	1.01344
b_2	-1.33086	0.25158
χ^2_{red}	3.17849×10^{-6}	
R^2	0.99997	

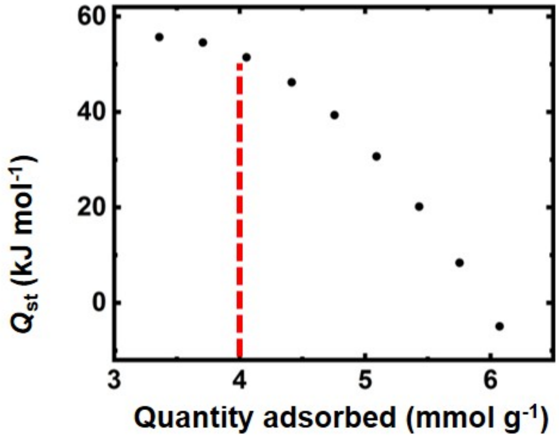

Region 3 [$3.0 < N \le 4.0$]		
Parameters	Value	Standard Error
a_o	7415.64519	3821.90217
a_1	-10265.52589	2600.91929
a_2	2677.08158	629.20542
a_3	-378.43741	85.42861
a_4	41.41509	9.13925
a_5	-1.79068	0.38724
b_0	-14.55069	10.64498
b_1	22.63662	6.12068
b_2	-3.38501	0.87971
χ^2_{red}	8.13087×10^{-7}	
R^2	0.99999	

Table S.5. (continued from last page)

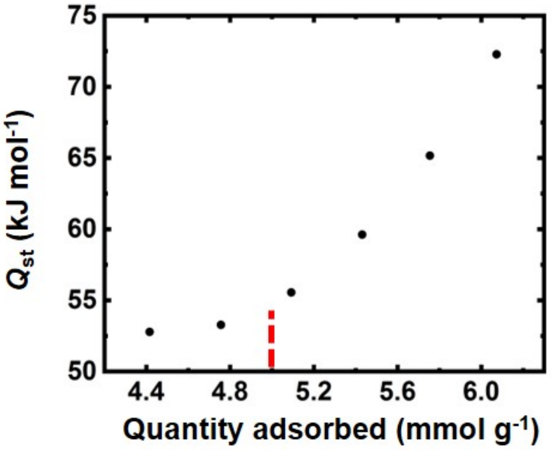

Region 4 [4.0 < N ≤ 5.0]		
Parameters	Value	Standard Error
a_o	-40982.74332	80697.1802
a_1	23091.5034	58102.28176
a_2	-6378.19322	17748.2565
a_3	1001.89891	3046.83459
a_4	-91.50295	291.21183
a_5	3.31094	11.0993
b_0	87.8246	134.52183
b_1	-29.26353	60.25142
b_2	3.25892	6.74597
χ^2_{red}	1.8409×10^{-6}	
R^2	0.99999	

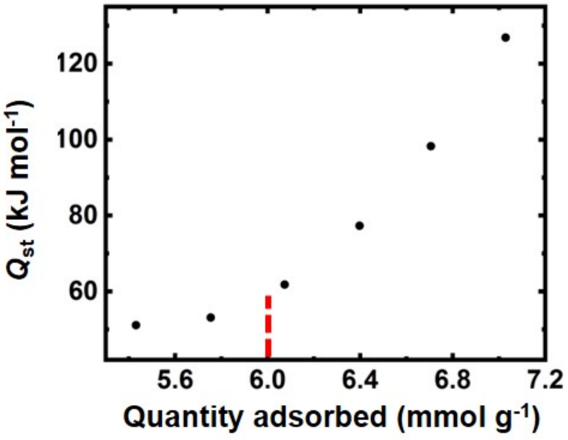

Region 5 [5.0 < N ≤ 6.0]		
Parameters	Value	Standard Error
a_o	-241573.471	182561.6875
a_1	134984.8732	118675.9631
a_2	-32587.03218	32847.82167
a_3	4442.25985	4949.89209
a_4	-342.22586	398.25257
a_5	10.50265	12.79124
b_0	427.23761	232.41215
b_1	-147.72087	85.1314
b_2	13.44292	7.79598
χ^2_{red}	1.92709×10^{-6}	
R^2	0.99999	

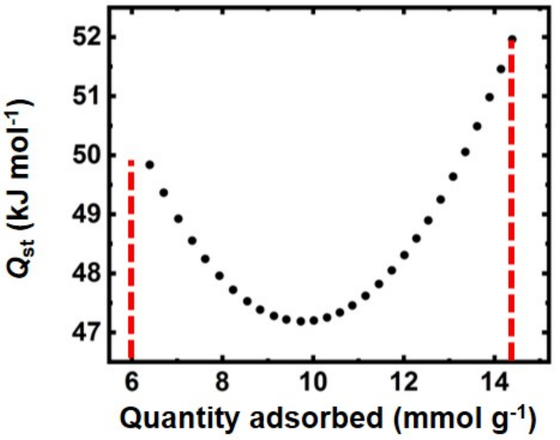

Region 6 [6.0 < N ≤ 14.4]		
Parameters	Value	Standard Error
a_o	-8772.81797	675.04831
a_1	725.06842	218.3768
a_2	-55.23643	28.54453
a_3	1.83272	2.31981
a_4	-0.04946	0.11432
a_5	3.04E-04	0.00222
b_0	29.1172	1.81695
b_1	-1.87891	0.4644
b_2	0.09365	0.0293
χ^2_{red}	5.94984×10^{-6}	
R^2	0.99997	

REFERENCES

1. Yildirim, S.; Röcker, B.; Pettersen, M. K.; Nilsen-Nygaard, J.; Zehera, A.; Rutkaite, R.; Radusin, T.; Suminska, P.; Marcos, B.; Coma, V. Active Packaging Applications for Food. *Compr. Rev. Food Sci. Food Saf.* **2018**, *17*, 165–199.

2. Gaikwad, K. K.; Singh, S.; Ajji, A. Moisture Absorbers for Food Packaging Applications. *Environ. Chem. Let.* **2019**, *17*, 609–628.

3. Waterman, K. C.; MacDonald, B. C. Package Selection for Moisture Protection for Solid, Oral Drug Products. *J. Pharm. Sci.* **2010**, *99*, 4437–4452.

4. Dahan, N.; Donaldson, N.; Taylor, S. J. G.; Sereno, N. The Application of PEEK to the Packaging of Implantable Electronic Devices: Water Permeation Calculation Method and Maximum Achievable Lifetime with Desiccant. *Journal of Microelectronics and Electronic Packaging* **2013**, *10*, 15–22.

5. Allinson, J. G.; Dansereau, R. J.; Sakr, A. The Effects of Packaging on the Stability of a Moisture Sensitive Compound. *Int. J. Pharm.* **2001**, *221*, 49–56.

6. Misha, S.; Mat, S.; Ruslan, M. H.; Sopian, K. Review of Solid/Liquid Desiccant in the Drying Applications and its Regeneration Methods. *Renew. Sust. Energ. Rev.* **2012**, *16*, 4686–4707.

7. Kumar, M.; Yadav, A. Composite Desiccant Material "$CaCl_2$/Vermiculite/Saw Wood: A New Material for Fresh Water Production from Atmospheric Air. *Applied Water Science* **2017**, *7*, 2103–2111.

8. Li, Z.; Hashimoto, K.; Hasegawa, H.; Saikawa, M. Performance Analysis of a Heat Pump System with Integrated Desiccant for Electric Vehicles. *Int. J. Refrig.* **2018**, *86*, 154–162.

9. She, X.; Yin, Y.; Luo, Y.; Lindeman, B.; Zhong, D.; Zhang, X. Experimental Study of a Novel Subcooling Method based on Liquid Desiccant Dehumidification for Vapor-compression Refrigeration Systems. *App. Therm. Eng.* **2018**, *130*, 1460–1471.

10. Henninger, S. K.; Schmidt, F. P.; Henning, H.-M. A Water Adsorption Characteristics of Novel Materials for Heat Transformation. *Applications Appl. Therm. Eng.* **2010**, *30*, 1692–1702.

11. Trusell, F.; Diehl, H. Efficiency of Chemical Desiccants. *Anal. Chem.* **1963**, *35*, 674–677.

12. Lenher, S.; Taylor, G. B. Anhydrous Magnesium Perchlorate as a Drying Agent. *Ind. Eng. Chem. Anal. Ed.* **1930**, *2*, 58.

13. Kallenberger, P. A.; Fröba, M. Water Harvesting from Air with a Hygroscopic Salt in a Hydrogel–derived Matrix. *Commun. Chem.* **2018**, *1*, 28.

14. Dai, L.; Yao, Y.; Jiang, F.; Yang, X.; Zhou, X.; Xiong, P. Sorption and Regeneration Performance of Novel Solid Desiccant based on PVA-LiCl Electrospun Nanofibrous Membrane. *Polym. Test* **2017**, *64*, 242–249.

15. Du, C.; Yang, H. Synthesis and Characterization of Zeolite 4A-type Desiccant from Kaolin. *American Mineralogist* **2010**, *95*, 741-746.

16. Jentys, A.; Warecka, G.; Derewinski, M.; Lercher, J. A. Adsorption of Water on ZSM5 Zeolites. *J. Phys. Chem.* **1989**, *93*, 4837–4843.

17. Kenyó, C.; Renner, K.; Móczó, J.; Fekete, E.; Kröhnke, C.; Pukánszky, B. Effect of Desiccant Characteristics on the Properties of PS/Zeolite Functional Packaging Materials. *Polym. Compos.* **2014**, *35*, 2112–2120.

18. Tretiak, C. S.; Abdallah, N. B. Sorption and Desorption Characteristics of a Packed Bed of Clay–$CaCl_2$ Desiccant Particles. *Solar Energy* **2009**, *83*, 1861–1870.

19. Mohan, R. P. An Expatiate View of Solid Clay based Desiccant Mould with Varying Void Fraction on Absorption. *Advanced Materials Research* **2014**, *984-985*, 94–99.

20. Bridgeman, C. H.; Buckingham, A. D.; Skipper, N. T.; Payne, M. C. Ab-initio Energy Study of Uncharged 2 : 1 Clays and their Interaction with Water. *Mol. Phys.* **1996**, *89*, 879–888.

21. Delville, A.; Letellier, M. Structure and Dynamics of Simple Liquids in Heterogeneous Condition: An NMR Study of the Clay-water Interface. *Langmuir* **1995**, *11*, 1361–1367.

22. Brennan, J. K.; Bandosz, T. J.; Thomson, K. T.; Gubbins, K. E. Water in Porous Carbons. *Colloids Surf A: Physicochemical Eng Aspects* **2001**, *187–188*, 539–568.

23. Furmaniak, S.; Gauden, P. A.; Terzyk, A. P.; Rychlicki, G. Water Adsorption on Carbons--Critical Review of the Most Popular Analytical Approaches. *Adv. Colloid Interface Sci.* **2008**, *137*, 82–143.

24. Slasli, A. M.; Jorge, M.; Stoekli, F. Water Adsorption by Activated Carbons in Relation to their Microporous Structure. *Carbon* **2003**, *41*, 479–486.

25. Fastyn, P.; Kornacki, W.; Gierczak, T.; Gawlowski, J.; Niedzielski, J. Adsorption of Water Vapor from Humid Air by Selected Carbon Adsorbents. *J. Chromatog. A* **2005**, *1078*, 7–12.

26. Cao, T.; Lee, H.; Hwang, Y.; Radermacher, R.; Chun, H.-H. Experimental Investigations on Thin Polymer Desiccant Wheel Performance. *Int. J. Refrigeration* **2014**, *44*, 1–11.

27. Mudiyanselage, T. K.; Neckers, D. C. Highly Absorbing Superabsorbent Polymer. *J. Polym. Sci. Part A: Polym. Chem.* **2008**, *46*, 1357–1364.

28. Yang, T. Poly(vinyl alcohol)/sulfated *β*-cyclodextrin for Direct Methanol Fuel Cell Applications. *Int. J. Hydrogen Energy* **2009**, *34*, 6917–6924.

29. Lee, J.; Lee, D.-Y. Sorption Characteristics of a Novel Polymeric Desiccant. *Int. J. Refrigeration* **2012**, *35*, 1940–1949.

30. Ng, E.-P.; Mintova, S. Nanoporous Materials with Enhanced Hydrophilicity and High-water Sorption Capacity. *Microporous Mesoporous Mater.* **2008**, *114*, 1–26.

31. Morishige, K.; Kittaka, S. Kinetics of Capillary Condensation of Water in Mesoporous Carbon: Nucleation and Meniscus Growth. *J. Phys. Chem. C* **2015**, *119*, 18287–18292.

32. Horikawa, T.; Sakao, N.; Do, D. Effects of Temperature on Water Adsorption on Controlled Microporous and Mesoporous Carbonaceous Solids. *Carbon* **2013**, *56*, 183–192.

33. Chen, C.-H.; Hsu, C.-Y.; Chen, C.-C.; Chen, S.-L. Silica Gel Polymer Composite Desiccants for Air Conditioning Systems. *Energy Buildings* **2015**, *101*, 122–132.

34. Tatlier, M.; Munza, G.; Henningera, S. K. Relation of Water Adsorption Capacities of Zeolites with their Structural Properties. *Microporous and Mesoporous Mater.* **2018**, *264*, 70–75.

35. Knez, Z.; Novak, Z. Adsorption of Water Vapor on Silica, Alumina, and their Mixed Oxide Aerogels. *J. Chem. Eng. Data* **2001**, *46*, 858–860.

36. Yuann, Y.; Zhang, H.; Yang, F.; Zhang, N.; Cao, X. Inorganic Composite Sorbents for Water Vapor Sorption: A Research Progress. *Renew. Sust. Energ. Rev.* **2016**, *54*, 761–776.

37. Harada, A. Cyclodextrin-based Molecular Machines. *Acc. Chem. Res.* **2001**, *34*, 456–464.

38. Chidambareswarapattar, C.; McCarver, P. M.; Luo, H.; Lu, H.; Sotiriou-Leventis, C.; Leventis, N. Fractal Multiscale Nanoporous Polyurethanes: Flexible to Extremely Rigid Aerogels from Multifunctional Small Molecules. *Chem. Mater.* **2013**, *25*, 3205−3224.

39. Donthula, S.; Mandal, C.; Leventis, T.; Schisler, J.; Saeed, A. M.; Sotiriou-Leventis, C.; Leventis, N. Shape Memory Superelastic Poly(isocyanurate-urethane) Aerogels (PIR-PUR) for Deployable Panels and Biomimetic Applications. *Chem. Mater.* **2017**, *29*, 4461−4477.

40. Donthula, S.; Mandal, C.; Schisler, J.; Leventis, T.; Meador, M. A. B.; Sotiriou-Leventis, C.; Leventis, N. Nanostructure-dependent Marcus-type Correlation of the Shape Recovery Rate and the Young's Modulus in Shape Memory Polymer Aerogels. *ACS Appl. Mater. Interfaces* **2018**, *10*, 23321−23334.

41. Bang, A.; Buback, C.; Sotiriou-Leventis, C.; Leventis, N. Flexible Aerogels from Hyperbranched Polyurethanes: Probing the Role of Molecular Rigidity with Poly(urethane acrylates) versus Poly(urethane norbornenes) *Chem. Mater.* **2014**, *26*, 6979−6993.

42. Papastergiou, M.; Chriti, D.; Damalas, D. E.; Raptopoulos, G.; Paraskevopoulou, P. Poly(urethane-acrylate) Aerogels from the Isocyanurate Trimer of Isophorone Diisocyanate. *J Supercritical Fluids* **2019**, *148*, 42–54.

43. Papastergiou, M.; Kanellou, A.; Chriti, D.; Raptopoulos, G.; Paraskevopoulou, P. Poly(urethane-acrylate) Aerogels via Radical Polymerization of Dendritic Urethane-acrylate Monomers. *Materials* **2018**, *11*, 2249.

44. Kanellou, A.; Anyfantis, G. C.; Chriti, D.; Raptopoulos, G.; Pitsikalis, M.; Paraskevopoulou, P. Poly(urethane-norbornene) Aerogels via Ring Opening Metathesis Polymerization of Dendritic Urethane-norbornene Monomers: Structure-property Relationships as a Function of an Aliphatic versus an Aromatic Core and the Number of Peripheral Norbornene Moieties. *Molecules* **2018**, *23*, 1007.

45. Saeed, A. M.; Rewatkar, P. M.; Majedi Far, H.; Taghvaee, T.; Donthula, S.; Mandal. C.; Sotiriou-Leventis, C.; Leventis, N. Selective CO_2 Sequestration with Monolithic Bimodal Micro/macroporous Carbon Aerogels Derived from Stepwise Pyrolytic Decomposition of Polyamide-polyimide-polyurea Random Copolymers. *Appl. Mater. Interfaces* **2017**, *9*, 13520−13536.

46. Majedi Far, H.; Rewatkar, P. M.; Donthula, S.; Taghvaee, T, Saeed, A. M.; Sotiriou-Leventis, C.; Leventis, N. Exceptionally High CO_2 Adsorption at 273 K by Microporous Carbons from Phenolic Aerogels: The Role of Heteroatoms in Comparison with Carbons from Polybenzoxazine and Other Organic Aerogels. *Macromol. Chem. Phys.* **2018**, *1800333*.

47. Rokosz, M. J.; Gerlock, J. L.; Kucherov, A. V.; Belfield, K. D.; Fryer, N. L.; Moad, G. ^{15}N CP/MAS Solid-state NMR Spectroscopy of a ^{15}N-enriched Hindered Amine Light Stabilizer Photolyzed in Acrylic/Melamine and Acrylic/Urethane Coatings. Polymer Degradation and Stability **2000**, *70*, 81−88.

48. Jeong, H. K.; Echeverria, E.; Chakraborti, P.; Lea, H. T.; Dowben, P. A. Electronic Structure of Cyclodextrin–carbon Nanotube Composite Films. *RSC Adv.* **2017**, *7*, 10968–10972.

49. Gao, B.; Sun, Y.; Miao, Y.; Min, H.; Xu, L.; Huang, C. Facile Preparation of Highly Luminescent Nitrogen-doped Carbonaceous Nanospheres and Potential Application in Intracellular Imaging of Quercetin. *Aust. J. Chem.* **2018**, *71*, 882–889.

50. Ederer, J.; Janoš, P.; Ecorchard, P.; Tolasz, J.; Štengl, V.; Beneš, H.; Perchaczc, M.; Pop-Georgievskid, O. Determination of Amino Groups on Functionalized Graphene Oxide for Polyurethane Nanomaterials: XPS Quantitation vs. Functional Speciation. *RSC Adv.* **2017**, *7*, 12464–12473.

51. Dubinin, M. M. Fundamentals of the Theory of Adsorption in Micropores of Carbon Adsorbents: Characteristics of their Adsorption Properties and Microporous Structures. *Carbon* **1989**, *27*, 457–467.

52. Garrido, J.; Linares-Solano, A.; Martin-Martinez, J. M.; Molina-Sabio, M.; Rodriguez-Reinoso, F.; Torregrosa, R. Use of Nitrogen vs. Carbon Dioxide in the Characterization of Activated Carbons. *Langmuir* **1987**, *3*, 76–81.

53. Mohite, D. P.; Larimore, Z. J.; Lu, H.; Mang, J. T.; Sotiriou-Leventis, C.; Leventis, N. Monolithic Hierarchical Fractal Assemblies of Silica Nanoparticles Cross-linked with Polynorbornene via ROMP: A Structure−property Correlation from Molecular to Bulk through Nano. *Chem. Mater.* **2012**, *24*, 3434−3448.

54. https://www.sorbentsystems.com/desiccants_charts.html

55. https://secure.drierite.com/catalog3/page3.cfm.

56. Pierce, C.; Smith, R. N. The Adsorption–desorption Hysteresis in Relation to Capillarity of Adsorbents. *J. Phys. Chem.* **1950**, *54*, 784–94.

57. Alonso-Buenaposada, I. D.; Calvo, E. G.; Montes-Morán, M. A.; Narciso, J.; Menéndez, J. A.; Arenillas, A. Desiccant Capability of Organic Xerogels: Surface Chemistry vs Porous Texture. *Microporous Mesoporous Mater.* **2016**, *232*, 70–76.

58. Steiner, T. The Hydrogen Bond in Solid State. *Angew. Chem. Int. Ed.* **2002**, *41*, 48–76.

59. Vartapetyan, R. S.; Voloshchuk, A. M.; Dubinin, M. M.; Yakubov, T. S. Adsorption of Water Vapors and the Micropore Structure of Carbon Adsorbents. Communication 14. Differential Heats of Adsorption of Water Vapors by Active Carbons. Bulletin of the Academy of Sciences of the USSR, Division of Chemical Science **1987**, pp. 1791–1795.

60. Salame, I. I.; Bagreev, A.; Bandosz, T. J. Revisiting the Effect of Surface Chemistry on Adsorption of Water on Activated Carbons. *J. Phys.Chem. B* **1999**, *103*, 3877–3884.

61. Liu, L.; Tan, S.; Horikawa, T.; Doa, D. D.; Nicholson, D.; Liu, J. Water Adsorption on Carbon - A Review. *Advances in Colloid and Interface Science* **2017**, *250*, 64–78.

62. Suroviec, A. H. Determining Surface Coverage of Self-assembled Monolayers on Gold Electrodes. *Chem. Educator* **2012**, *17*, 83–85.

63. Beaucage, G. Approximations Leading to a Unified Exponential/power-law Approach to Small-angle Scattering. *J. Appl. Crystallogr.* **1995**, *28*, 717−728.

64. Beaucage, G. Small-angle Scattering from Polymeric Mass Fractals of Arbitrary Mass Fractal Dimension. *J. Appl. Crystallogr.* **1996**, *29*, 134−146.

65. https://particletesting.com/submit-a-sample/ (06-05-2019)

66. https://www.amazon.com/gp/product/B07BLY177S/ref=ppx_yo_dt_b_asin_title_o04_s00?ie=UTF8&psc=1

67. Bimbo, N.; Sharpe, J. E.; Ting, V. P.; Noguera-Díaz, A.; Mays, T. J. Isosteric Enthalpies for Hydrogen Adsorbed on Nanoporous Materials at High Pressures. Adsorption **2014**, *20*, 373−384.

68. Li, R.-J.; Li, M.; Zhuo, X.-P.; Li, D.; O'Keeffe, M. A Highly Stable MOF with a Rod SBU and a Tetracarboxylate Linker: Unusual Topology and CO_2 Adsorption Behaviour Under Ambient Conditions. *Chem. Commun.* **2014**, *50*, 4047−4049.

69. Bandosz, T. J.; Salame, I. I. Experimental Study of Water Adsorption on Activated Carbons.-*Langmuir* **1999**, *41*, 587–593.

70. Sircar, S.; Mohr, R.; Ristic, C.; Rao, M. B. Isosteric Heat of Adsorption: Theory and Experiment. *J. Phys. Chem. B* **1999**, *103*, 6539–6546.

SECTION

2. CONCLUSIONS

Sturdy, highly porous ceramic (SiC and Si_3N_4) and metallic (Co(0)) aerogels were synthesized carbothermally from *xerogel powder* compacts. Thus, the supercritical fluid drying, a common step in the preparation of aerogels, was bypassed making the overall process cost-effective. Also, the handling of powders instead of monoliths allowed faster solvent exchanges (time-efficient process) and an easy way to cast those aerogels in various shapes and sizes. Finally, polyurethane aerogels based on α- and β-cyclodextrins were synthesized and examined as desiccants.

In Paper I, SiC and Si_3N_4 aerogels were made from the same precursor (polymer-crosslinked APTES@TMOS xerogel powder) by two parallel processes under different pyrolysis conditions. Aerogels obtained from xerogels were beneficial for the formation of ceramics based on the topology of the reaction (at the SiC/SiO_2 interface). That synthetic design is not only cost- and time-effective but also materials-efficient i.e. a little over stoichiometric carbon was sufficient to obtain pure ceramic aerogels. The ceramic aerogels fabricated by the proposed methodology were very light-weight, highly porous (>80% v/v) and thermally stable up to about 1000 °C both under N_2 and O_2 environments. Due to their porous structure, those materials were very good thermal insulators in contrast to the bulk materials available in the market. The mechanical behavior of SiC and Si_3N_4 was found to be different, which was attributed to their different morphologies and sensitivity towards change in bulk density.

In Paper II, taking advantage of the generalizability of the proposed method in Paper I, the cobaltia system, which resists or takes time to gel, was diverted to the xerogel powder route to make Co(0) aerogels. Those pure metallic aerogels possessing about 70% v/v porosity, were filled with $LiClO_4$ to make monolithic thermites. They were ignited with a hot nichrome wire and the highest temperature reached during the thermite reaction was 1515 °C. It was found that the pore structure plays an important role in keeping the perchlorate intact within the Co(0) network during ignition. Co(0) that was made by pyrolysis at 800 °C had larger pores compared to the one that was made at 900 °C, due to sintering at higher temperature. That small change makes the morphology and pore structure of cobalt aerogels suitable as thermites.

In paper III, the polyol functionality of α- and β-cyclodextrins was reacted with a rigid-aromatic triisocyanate to form hierarchical structures referred to as α- and β-CDPU-xx aerogels. Those aerogels were examined as desiccants for ten cycles and were regenerated at room temperature by just reducing the relative humidity of the environment. In general, α-CDPU-2.5 showed the highest water adsorption capacity. That can be explained on the basis of its highest surface area and porosity, which makes the hydrophilic sites readily available for water. Moreover, water adsorption does not only depend on the hydrophilicity of the sample, but also on the extent of water-water interactions. α-CDPU-2.5 has the highest pore volume which allows water to get adsorbed in a multilayer fashion, which is also confirmed from the isosteric heats of water adsorption leading to very high water uptake (108% w/w). Also, due to the balance of the enthalpic and entropic factors of water adsorption in mesopores with pore sizes at about 20 nm or less, adsorbed water is released by reducing the relative humidity of the environment.

APPENDIX

RELATIVE GAS ADSORPTION STUDY ON α- and β-CDPU-xx AEROGELS

1. CARBON DIOXIDE CAPTURE BY CDPU AEROGELS

Micromeritics Tristar II 3020 version 3.02 was utilized for a relative adsorption study for N_2, CH_4, H_2, and CO_2 up to 760 torr (0.03 relative pressure) at 273 K and 298 K.

The highest CO_2 sorption was obtained at 273 K and 1 bar from the lowest density aerogels, α-CDPU-2.5 and β-CDPU-2.5, at 8.8 % w/w and 6.0 % w/w, respectively (Figure 1A). Those values are comparable to those reported from several porous polymers including conjugated microporous polymers CMP-1-$(CH_3)_2$ (7.2 % w/w)[1], porous polymer network PPN-6-SO_3Li (5.4 % w/w)[2] and NUTs (8.2 – 2.7 % w/w)[3], covalent organic frameworks COF-103 (7.4 % w/w),[4,5] metal organic frameworks (MOFs) ZIF-79 (6.4 % w/w),[6] and nanoporous amide networks NAN-2 (6.5 % w/w).[7] The CO_2 sorption capacity of CDPU aerogels decreased with decreasing surface area and porosity and dropped to 4.1 % w/w and 3.6 % w/w for α-CDPU-15 and β-CDPU-15, respectively (Table 1). The causes for those trends were investigated by measuring isosteric heats of CO_2 adsorption (Q_{st}) for all materials of this study using the Virial fitting method (described below). Thus, based on the amount of CO_2 uptake at 273 K and 298 K, the zero-coverage isosteric enthalpies of CO_2 adsorption, Q_o, were found equal to 35, 33, 28 and 23 kJ·mol^{-1} for α-CDPU-2.5, β-CDPU-2.5, α-CDPU-15 and β-CDPU-15, respectively (Table 1, Figure 1B).

During physisorption, the energy of adsorption is appreciably enhanced when it takes place in vary narrow pores.[8] Thus, the decreasing trend of Q_o with increasing density of the CDPU aerogels is attributed to the decreasing micropore area (Table 1). In that regard, both α- and β-CDPU-2.5 include practically the same micropore area. That combined with the fact that the two materials have very close Q_o values, points to an initial indiscriminate surface adsorption of CO_2 in the micropore. However, the amounts of CO_2 adsorbed by the two materials at 1 bar differ significantly. Thereby, once micropores have taken a monolayer coverage of CO_2 other factors begin to become important. As monolayer adsorption approaches completion, with further increase in relative pressure, multilayer adsorption takes place due to lateral interactions of CO_2 molecules. At this stage, the extent of multilayer formation depends on the available pore volumes. α-CDPU-2.5 possesses the highest micropore volume (Table 2, paper III), thereby multilayer adsorption of CO_2 is expected to be enhanced,, a fact which is supported by the increasing Q_{st} vs coverage plot, leading to the highest overall CO_2 uptake. A noticeable decreasing trend of Q_{st} with the adsorbed amount of CO_2 for α-CDPU-15 and β-CDPU-15 (Figure 1C) is consistent with the decrease in their micropore volumes. It suggests that the adsorption of CO_2 by those samples occurs due to interactions of the polarizable CO_2 molecules with the active sites of CDPU (monolayer adsorption) rather than the gas-gas interaction and aggregation of the CO_2 molecules themselves (multilayer adsorption).

In addition to the high CO_2 uptake, the selectivity for CO_2 over other adsorbates (N_2, H_2 and CH_4) is equally crucial from the practical application perspective. Selectivity for one gas over another was evaluated from the ratios of the Henry's law constants, K_H, for the gases under consideration. The K_H values were obtained from the slopes of the linear parts of the isotherms of Figure 1C at low pressures (<0.1 bar). High CO_2/N_2 selectivity is one of the essential aspects for post-combustion CO_2 capture. The CO_2/N_2 selectivity values for CDPUs were in the range of 50:1 to 67:1 at 273 K and 1 bar, comparable to that of other existing materials such as nanoporous amide networks NANs (57:1 to 74:1),[9] and porous, electron-rich covalent organonitridic frameworks PECONFs (51:1 to 83:1).[10] Similarly, the CO_2/H_2 pair showed significantly high selectivity in the range of 63:1 to 281:1. However, α-CDPU-2.5 showed the highest selectivity for CO_2 over CH_4 (10:1). Selectivity data for all CDPU samples are shown in Table 1 and Figure 1D.

2. CALCULATION OF ISOSTERIC HEATS OF CO_2 ADSORPTION (Q_{st})

They were calculated via the Virial method.[11] For this, the CO_2 adsorption isotherms at 273 K and 298 K were fitted simultaneously with a Virial-type equation (Eq 1) using the OriginPro 8.5.1 software package.

$$\ln P = \ln N + \frac{1}{T}\sum_{i=0}^{m} a_i N^i + \sum_{i=0}^{n} b_i N^i \tag{1}$$

(P is pressure in Torr, N is the adsorbed amount in mmol g^{-1}, T is the absolute temperature, a_i and b_i are the Virial coefficients, and m and n are the number of coefficients needed in order to fit the isotherms adequetly.) Using the least squares method, the values of m and n were gradually increased until the sum of the squared deviations of the experimental points from the fitted isotherm was minimized. $m = 5$ and $n = 2$ are used for all CDPU samples. The values of a_o to a_m were introduced into Eq 2 and isosteric heats of adsorption (Q_{st}) were calculated as a function of the surface coverage (N).

$$Q_{st} = -R\sum_{i=0}^{m} a_i N^i \tag{2}$$

(R is the universal gas constant of (8.314 J mol^{-1} K^{-1}) and Q_{st} is given in kJ mol^{-1}.) The common term in Eq 5 for all N, Q_0, corresponds to $i = 0$ and is given by Eq 3.

$$Q_0 = -Ra_0 \tag{3}$$

Q_0 is the heat of adsorption as coverage goes to zero, and is a sensitive evaluator of the affinity of the adsorbate for the surface.[12]

3. CALCULATION OF ADSORPTION SELECTIVITIES

The gas sorption selectivities were calculated with Henry's law: $C = K_H \times p$, where C = concentration (mmol g^{-1}) in phase I; p = pressure (bar) in phase II; k_H = Henry's law constant (mmol g^{-1} bar^{-1}),[13] from the ratios of the low-pressure slopes (<0.1 bar) of the corresponding isotherms.[14,15]

Table 1. Gas sorption capacities, isosteric heats of CO_2 adsorption and selectivity data of CDPU aerogels

Sample	CO_2 adsorption (% w/w)		Q_o (kJmol^{-1})	N_2 adsorption (% w/w)	H_2 adsorption (% w/w)	CH_4 adsorption (% w/w)	Selectivity*		
	273 K	298 K		273 K	273 K	273 K	CO_2/N_2	CO_2/H_2	CO_2/CH_4
α-CDPU-2.5	8.78 ± 0.99	3.39	35	0.07	0.020	0.56	62.29	62.59	10.48
β-CDPU-2.5	5.99 ± 0.39	3.61	33	0.07	0.006	0.52	51.18	139.44	8.72
α-CDPU-15	4.09 ± 0.04	2.86	28	0.12	0.003	0.56	57.6	263.67	5.84
β-CDPU-15	3.63 ± 0.42	2.86	23	0.11	0.004	0.50	66.79	280.82	5.94

*calculated from the Henery's low constant, obtained from the low-pressure slopes of the corresponding isotherms.

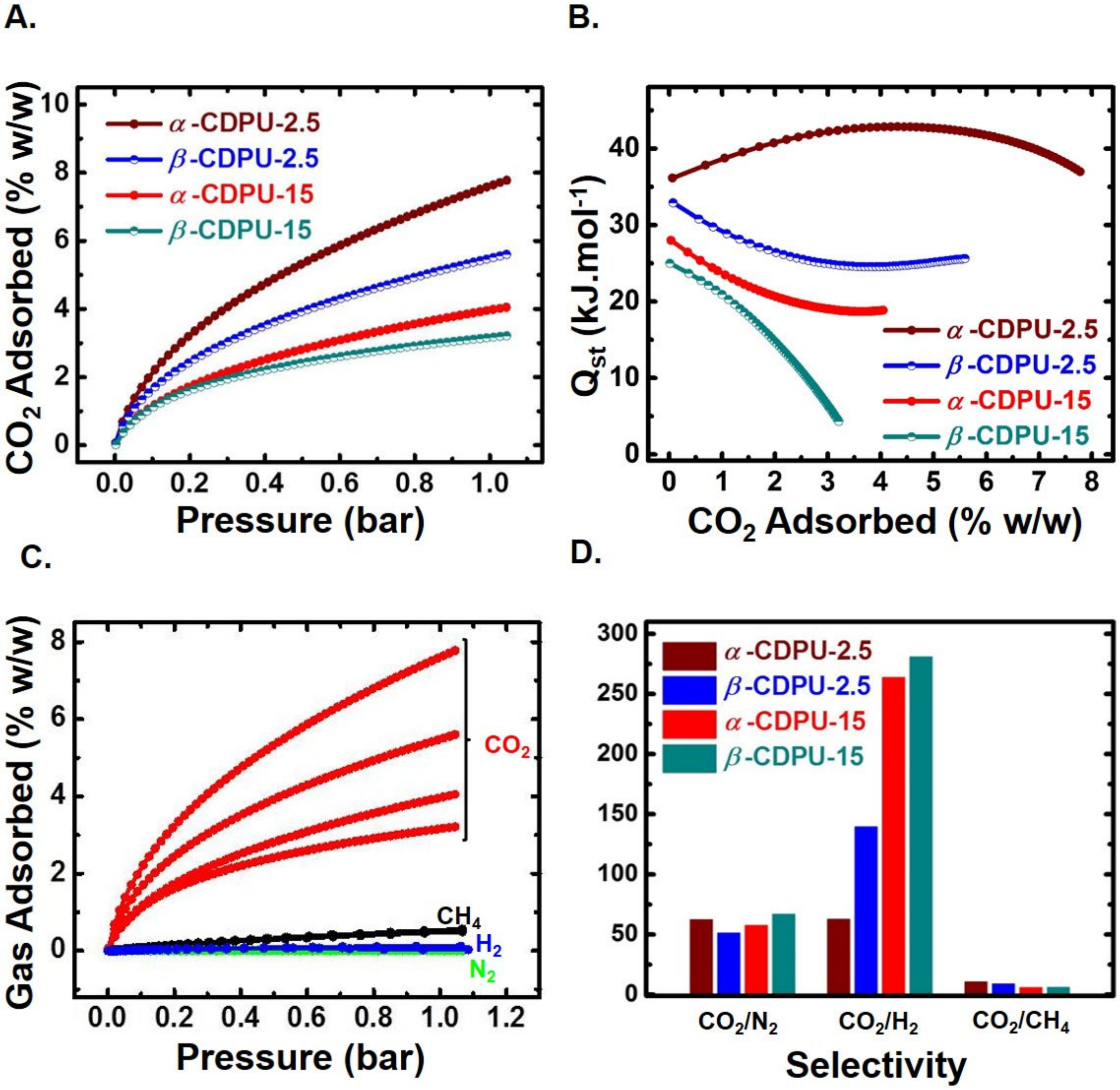

Figure 1. A. CO_2 sorption isotherms of *α*- and *β*-CDPU-xx at 273 K. B. Isosteric heats of CO_2 adsorption calculated via virial method for *α*- and *β*-CDPU-xx at 273 K. C. Adsorption isotherms at 273 K up to 1.1 bar of the four gases. (Note that isotherms cluster closely together at each xx level for N_2 and H_2, and all isotherms might not be visible.) D. Comparisons of Gas Selectivity by *α*- and *β*-CDPU-xx.

REFERENCES

1. Dawson, R.; Adams, D. J.; Cooper, A. I. Chemical Tuning of CO_2 Sorption in Robust Nanoporous Organic Polymers. *Chem. Sci*. **2011**, *2*, 1173–1177.

2. Lu, W.; Yuan, D.; Sculley, J.; Zhao, D.; Krishna, R.; Zhou, H.-C. Sulfonate-Grafted Porous Polymer Networks for Preferential CO_2 Adsorption at Low Pressure. *J. Am. Chem. Soc*. **2011**, *133*, 18126–18129.

3. Sun, L. B.; Kang, Y. H.; Shi, Y. Q.; Jiang, Y.; Liu, X. Q. Highly Selective Capture of the Greenhouse Gas CO_2 in Polymers. *ACS Sustain. Chem. Eng*. **2015**, *3*, 3077–3085.

4. Dawson, R.; Stöckel, E.; Holst, J. R.; Adams, D. J.; Cooper, A. I. Microporous Organic Polymers for Carbon Dioxide Capture. *Energy Environ. Sci*. **2011**, *4*, 4239–4245.

5. Furukawa, H; Yaghi, O. M. Storage of Hydrogen, Methane, and Carbon Dioxide in Highly Porous Covalent Organic Frameworks for Clean Energy Applications. *J. Am. Chem. Soc*., **2009**, *131*, 8875–8883.

6. Banerjee, R.; Furukawa, H.; Britt, D.; Knobler, C.; Keeffe, M. O.; Yaghi, O. M. Control of Pore Size and Functionality in Isoreticular Zeolitic Imidazolate Frameworks and their Carbon Dioxide Selective Capture Properties. *J. Am. Chem. Soc*. **2009**, *131*, 3875–3877.

7. Zulfiqar, S.; Mantione, D.; El Tall, O.; Sarwar, M. I.; Ruipérez, F.; Rothenberger, A.; Mecerreyes, D. Nanoporous Amide Networks Based on Tetraphenyladamantane for Selective CO_2 Capture. *J. Mater. Chem. A* **2016**, *4*, 8190–8197.

8. Rouquerol, F; Rouquerol, J; Sing, K; Maurin, G; Llewellyn, P. Introduction. In *Adsorption by Powders and Porous Solids*; **2014**; Chapter 1, pp 1–24, DOI: 10.1016/B978-0-08-097035-6.00001-2.

9. Xiang, Z.; Cao, D. Porous Covalent–organic Materials: Synthesis, Clean Energy Application and Design. *J. Mater. Chem. A* **2013**, *1*, 2691–2718.

10. Mohanty, P.; Kull, L. D.; Landskron, K. Porous Covalent Electron-Rich Organonitridic Frameworks as Highly Selective Sorbents for Methane and Carbon Dioxide. *Nat. Commun*. **2011**, *2, 1–6.*

11. Li, R.; Li, M.; Zhou, X.; Li, D.; O'Keeffe, M. A Highly Stable MOF with a Rod SBU and a Tetracarboxylate Linker: Unusual Topology and CO_2 Adsorption Behaviour under Ambient Conditions. *Chem. Commun*. **2014**, *50*, 4047–4049.

12. S. Sircar, R. Mohr, C. Ristic, M. B. Rao, Isosteric Heat of Adsorption: Theory and Experiment, *J. Phys. Chem. B* **1999**, *103*, 6539–6546.

13. *Perry's Chemical Engineer's Handbook*, 6th ed.; Green, D. W., Perry, R. H, Eds.; McGraw-Hill, 1984; pp 9−14.

14. Kim, H.; Kim, Y.; Yoon, M.; Lim, S.; Park, S. M.; Seo, G.; Kim, K. Highly Selective Carbon Dioxide Sorption in an Organic Molecular Porous Materials. *J. Am. Chem. Soc.* **2010**, *132*, 12200−12202.

15. Dawson, R.; Cooper, A. I.; Adams, D. J. Chemical Functionalization Strategies for Carbon Dioxide Capture in Microporous Organic Polymers. *Polym. Int.* **2013**, *62*, 345−352.

BIBLIOGRAPHY

1. Vareda, J. P.; Lamy-Mendes, A.; Durães, L. A Reconsideration on the Definition of the Term Aerogel Based on Current Drying Trends. *Microporous Mesoporous Mater.* **2018**, *258*, 211–216.

2. Rechberger, F.; Niederberger, M. Synthesis of Aerogels: from Molecular Routes to 3-Dimensional Nanoparticle Assembly. *Nanoscale Horizons* **2017**, *2*, 6–30.

3. Fricke, J.; Emmerling, A. Aerogels-Recent Progress in Production Techniques and Novel Applications. *J. Sol-Gel Sci. Technol.* **1998**, *13*, 299–303.

4. Gesser, H. D.; Goswami, P. C. Aerogels and Related Porous Materials. *Chem. Rev.* **1989**, *89,* 765–788.

5. Hüsing, N.; Schubert, U. Aerogels-Airy Materials: Chemistry, Structure, and Properties. *Angew. Chem. Int. Ed.* **1998**, *37*, 22–45.

6. Fricke, J.; Emmerling, A. Aerogels. *J. Am. Ceram. Soc.* **1992**, *75*, 2027–2035.

7. Armori, J. N.; Carlson, E. J.; Carrasquillo, G. Metallic Aerogels: A Novel Synthesis of Very Fine Copper Powder Materials *Letters* **1989**, *4*, 373–376.

8. Dardel, G.; Henning, S. A.; Svensson, L. C. Silica Aerogel. U.S. Patent No. 4,402,927, 1981.

9. Rubin, M.; Lampert, C. M. Transparent Silica Aerogels for Window Insulation *Solar Energy Mater.* 1983, 7, 393–400.

10. Henning, S.; Svensson, L. Production of Silica Aerogel *Physica Scripta* **1981**, *23*, 697–702.

11. Lundquist, Jr., J.T.; Lundsager, C.B. Alkaline Battery with Seperator of High Surface Area. U.S. Patent No. 4,287,276, 1979.

12. Krieble, R.H.; Elliott, J.R. Organosilicon-silica Sols, Gels, and Aerogels. US. Patent No. 2,441,422, 1945.

13. Oxford Jr., W.F. Drilling Fluid. U.S. Patent No. 2,455,188, 1946.

14. Rayl, L.L. Lightweight Insulating Structural Concrete. U.S. Patent No. 4,268,317, 1978.

15. McWilliams, J.A. Tharmal Insulation Containing Silica Aerogel and Alumina. U.S. Patent No. 4,221,672, 1978.

16. Armor, J.N.; Carlson, E.J. Palladium on Alumina Aerogel Catalyst Composition and Process for Making Same. U.S. Patent No. 4,469,816, 1982.

17. Leventis, N.; Donthula, S.; Mandal, C.; Ding, M. S.; Sotiriou-Leventis, C. Explosive versus Thermite Behavior in Iron(0) Aerogels Infiltrated with Perchlorates. *Chem. Mater.* **2015**, *27*, 8126–8137.

18. Mahadik-Khanolkar, S.; Donthula, S.; Bang, A.; Wisner, C.; Sotiriou-Leventis, C.; Leventis, N. Polybenzoxazine Aerogels. 2. Interpenetrating Networks with Iron Oxide and the Carbothermal Synthesis of Highly Porous Monolithic Pure Iron(0) Aerogels as Energetic Materials. *Chem. Mater.* **2014**, *26*, 1318–1331.

19. Blanchard, F.; Pommier, B.; Reymond, J. P.; Teichner, S. J. in: Preparation of catalysts, Vol. 3, eds. Poncelet, G.; Grange, P.; Jacobs, P. A. (Elsevier, Amsterdam, 1983, pp 39s.

20. Zarzycki, J. W.; Prassas, M.; Phalippou, J. E. H. Preparation of Monolithic Silica Aerogels, The Aerogels Thus Obtained and Their Use for the Preparation of Silica Glass Articles and of Heat-insulating Materials. U.S. Patent No. 4,432,956, 1981.

21. Cheng, F.; Kelly, S. M.; Lefebvre, F.; Clark, S.; Supplit, R.; Bradley, J. S. Preparation of a Mesoporous Silicon Nitride via a Non-aqueous Sol-gel Route. *J. Mater. Chem.* **2005**, *15*, 772–777.

22. Brinker, C. J.; Scherer, G. W. *Sol-Gel Science: The Physics and Chemistry of Sol-Gel Processing*, 1st ed.; Academic Press: San Diego, 1990.

23. Brinker, C. J.; Scherer, G. W. *Sol-Gel Science: The Physics and Chemistry of Sol-Gel Processing*, 1st ed.; Academic Press: New York: p461.

24. Aleman1 J, Chadwick AV, He J, Hess M, Horie K, Jones RG, Kratochvil P, Meisel I, Mita I, Moad G, Penczek S, Stepto RFT (2007) Definitions of terms relating to the Structure and Processing of sols, gels, Networks, and Inorganic-organic Hybrid Matetials (IUPAC recommendations 2007). Pure Appl. Chem. 79: 1801-1829.

25. Freundlich, H. Colloid and capillary chemistry, Duttom Ed., New York, 1923.

26. Aegerter, M. A.; Leventis, N.; Koebel, M. M. *Aerogels Handbook*; Springer: New York, NY, USA, 2011.

27. Ebelmen, I. Untersuchungen über die Verbindungen der Borsäure und Kieselsäure mit Aether. *Ann. Chem. Pharm.* **1846**, *57*, 319–355.

28. (a) Gesser, H. D.; Goswami, P. C. Aerogels and Related Porous Materials. *Chem. Rev.* **1989**, *89*, 765–788. (b) Hüsing, N.; Schubert, U. Aerogels-Airy Materials: Chemistry, Structure, and Properties. *Angew. Chem. Int. Ed.* **1998**, *37*, 22–45. (c) Pierre, A. C.; Pajonk, G. M. Chemistry of Aerogels and Their Applications. *Chem. Rev.* **2002**, *102*, 4243–4265. (d) Leventis, N. Three-Dimensional Core-Shell Superstructures: Mechanically Strong Aerogels. *Acc. Chem. Res.* **2007**, *40*, 874–884. (e) Capadona, L. A.; Meador, M. A. B.; Alunni,A.; Fabrizio, E. F.; Vassilaras, P.; Leventis, N. Flexible, Low-Density Polymer Crosslinked Silica Aerogels. *Polymer* **2006**, *47*, 5754–5761. (f) Zhang, G.; Dass, A.; Rawashdeh, A.-M. M.; Thomas, J.; Counsil, J. A.; Sotiriou-Leventis, C.; Fabrizio, E. F.; Ilhan, F.; Vassilaras, P.; Scheiman, D. A.; McCorkle, L.; Palczer, A.; Johnston, J. C.; Meador, M. A.; Leventis, N. Isocyanate-Crosslinked Silica Aerogel Monoliths: Preparation and Characterization. *J. Non-Cryst. Solids* **2004**, *350*, 152–164. (g) Leventis, N.; Sotiriou-Leventis, C.; Zhang, G.; Rawashdeh, A.-M. M. Nanoengineering Strong Silica Aerogels. *Nano Lett.* **2002**, *2*, 957–960.

29. (a) Baumann, T. F.; Gash, A. E.; Chinn, S. C.; Sawvel, A. M.; Maxwell, R. S.; Satcher, J. H. Synthesis of High-surface-area Alumina Aerogels without the Use of Alkoxide Precursors. *Chem. Mater.* **2005**, *17*, 395–401. (b) Baumann, T. F.; Kucheyev, S. O.; Gash, A. E.; Satcher, J. H. Facile Synthesis of a Crystalline, High-surface-area SnO2 Aerogel. *Adv. Mater.* **2005**, *17*, 1546–1548. (c) Gash, A. E.; Satcher, J. H.; Simpson, R. L. Strong Akaganeite Aerogel Monoliths Using Epoxides: Synthesis and Characterization. *Chem. Mater.* **2003**, *15*, 3268–3275. (d) Gash, A. E.; Satcher, J. H.; Simpson, R. L. Monolithic Nickel (II)-Based Aerogels Using an Organic Epoxide: The Importance of the Counterion. *J. Non-Cryst. Solids* **2004**, *350*, 145–151. (e) Kucheyev, S. O.; Sadigh, B.; Baumann, T. F.; Wang, Y. M.; Felter, T. E.; van Buuren, T.; Gash, A. E.; Satcher, J. H.; Hamza, A. V. Electronic Structure of Chromia Aerogels from Soft X-ray absorption spectroscopy. *J. Appl. Phys.* **2007**, *101*, 124315:1–124315:8. (f) Gan, L. H.; Yue, T. Y.; Chen, L. W.; Li, G. M.; Zhou, B. Preparation and Characterization of beta-FeOOH Aerogels. *Acta Phys. Chim. Sin.* **1997**, *13*, 48–51. (g) Leventis, N.; Vassilaras, P.; Fabrizio, E. F.; Dass, A. J. Polymer Nanoencapsulated Rare Earth Aerogels: Chemically Complex but Stoichiometrically Similar Core-Shell Superstructures with Skeletal Properties of Pure Compounds. *Mater. Chem.* **2007**, *17*, 1502–1508.

30. (a) Pala, I. R.; Brock, S. L. ZnS Nanoparticle Gels for Remediation of Pb^{2+} and Hg^{2+} Polluted Water. *ACS Appl. Mater. Interfaces* **2012**, *4*, 2160–2167. (b) Ganguly, S.; Zhou, C.; Morelli, D.; Sakamoto, J.; Brock, S. L. Synthesis and Characterization of Telluride Aerogels: Effect of Gelation on Thermoelectric Performance of Bi_2Te_3 and $Bi_{2-x}Sb_xTe_3$ Nanostructures. *J. Phys. Chem. C.* **2012**, *116*, 17431–17439. (c) Yu, H.; Bellair, R.; Kannan, R. M.; Brock, S. L. Engineering Strength, Porosity, and Emission Intensity of Nanostructured CdSe Networks by Altering the Building-Block Shape. *J. Am. Chem. Soc.* **2008**, *130*, 5054–5055. (d) Kalebaila, K. K.; Georgiev, D. G.; Brock, S. L. Synthesis and Characterization of Germanium Sulfide Aerogels. *J. Non-Cryst. Solids* **2006**, *352*, 232–240. (e) Arachchige, I. U.; Brock, S. L. Sol-gel Assembly of CdSe Nanoparticles to Form Porous Aerogel networks. *J. Am. Chem. Soc.* **2006**, *128*, 7964–7971.

31. (a) Pekala, R. W. Organic Aerogels from the Polycondensation of Resorcinol with Formaldehyde. *J. Mater. Sci.* **1989**, *24*, 3221–3227. (b) Pekala, R. W. Low Density, Resorcinol-Formaldehyde Aerogels. U.S. Patent No. 4,873,218, 1989. (c) Majedi Far, H.; Donthula, S.; Taghvaee, T.; Saeed, A. M.; Garr, Z.; Sotiriou-Leventis, C.; Leventis, N. Air-oxidation of Phenolic Resin Aerogels: Backbone Reorganization, Formation of Ring-fused Pyrylium Cations, and the Effect on Microporous Carbons with Enhanced Surface Areas *RSC Adv.* **2017**, *7*, 51104–51120.

32. (a) Mahadik-Khanolkar, S.; Donthula, S.; Sotiriou-Leventis, C.; Leventis, N. "Polybenzoxazine aerogels. 1. High-yield Room-temperature Acid-catalyzed Synthesis of Robust Monoliths, Oxidative Aromatization and Conversion to Microporous Carbons *Chem. Mater.* **2014**, *26*, 1303-1317. (b) Mahadik-Khanolkar, S.; Donthula, S.; Bang, A.; Wisner, C.; Sotiriou-Leventis, C.; Leventis, N. Polybenzoxazine Aerogels. 2. Interpenetrating Networks with Iron Oxide and the Carbothermal Synthesis of Highly Porous Monolithic Pure Iron(0) Aerogels as Energetic Materials," *Chem. Mater.* **2014**, *26*, 1318-1331.

33. Mohite, D. P.; Mahadik-Khanolkar, S.; Luo, H.; Lu, H.; Sotiriou-Leventis, C.; Leventis, C. Polydicyclopentadiene Aerogels Grafted with PMMA: II. Nanoscopic Characterization and Origin of Macroscopic Deformation. *Soft Mat.* **2013**, *9*, 1531-1539.

34. Sadekar, A. G.; Mahadik, S. S.; Bang, A. N.; Larimore, Z. J.; Wisner, C. A.; Bertino, M. F.; Kalkan, A. K.; Mang, J. T.; Sotiriou-Leventis, C.; Leventis, N. ′Green′ Aerogels and Porous Carbons by Emulsion Gelation of Acrylonitrile *Chem. Mater.* **2012**, *24*, 26-47.

35. (a) Zou, J. H.; Liu, J. H.; Karakoti, A. S.; Kumar, A.; Joung, D.; Li, Q. A.; Khondaker, S. I.; Seal, S.; Zhai, L. Ultralight Multiwalled Carbon Nanotube Aerogel. *ACS Nano* **2010**, *4*, 7293–7302. (b) Aliev, A. E.; Oh, J. Y.; Kozlov, M. E.; Kuznetsov, A. A.; Fang, S. L.; Fonseca, A. F.; Ovalle, R.; Lima, M.D.; Haque, M. H.; Gartstein, Y. N.; et al. Giant-Stroke, Superelastic Carbon Nanotube Aerogel Muscles. *Science* **2009**, *323*, 1575–1578.

36. (a) Xu, Z.; Zhang, Y.; Li, P. G.; Gao, C. Strong, Conductive, Lightweight, Neat Graphene Aerogel Fibers with Aligned Pores. *ACS Nano* **2012**, *6*, 7103–7113. (b) Worsley, M. A.; Pauzauskie, P. J.; Olson, T. Y.; Biener, J.; Satcher, J. H.; Baumann, T. F. Synthesis of Graphene Aerogel with High Electrical Conductivity. *J. Am. Chem. Soc.* **2010**, *132*, 14067–14069.

37. (a) Chen, K.; Bao, Z. H.; Liu, D.; Zhu, X. R.; Zhang, Z. H.; Zhou, B. Confined Synthesis and Properties of Porous Silicon from Silica Aerogel Templates by Magnesiothermic Reduction. *Acta Phys. Chim. Sin.* **2011**, *27*, 2719–2725 (b) Leventis, N.; Sadekar, A.; Chandrasekaran, N.; Sotiriou-Leventis, C. Click Synthesis of Monolithic Silicon Carbide Aerogels from Polyacrylonitrile-coated 3D Silica Networks. *Chem. Mater.* **2010**, *22*, 2790–2803. (c) Worsley, M. A.; Kuntz, J. D.; Pauzauskie, P. J.; Cervantes, O.; Zaug, J. M.; Gash, A. E.; Satcher, J. H.; Baumann, T. F. High surface Area Carbon Nanotube-supported Titanium Carbonitride Aerogels. *J. Mater. Chem.* **2009**, *19*, 5503–5506.

38. (a) Leventis, N.; Sotiriou-Leventis, C.; Zhang, G.; Rawashdeh, A. -M. M. Nanoengineering Strong Silica Aerogels *NanoLett.* **2002**, *2*, 957–960. (b) Leventis, N.; Sotiriou-Leventis, C. Methods and Composition for Preparing Silica Aerogels. U.S. Patent No. 7,771,609, 2010. (c) Leventis, N. Three-Dimensional Core-Shell Superstructures: Mechanically Strong Aerogels *Acc. Chem. Res.* **2007**, *40*, 874–884.

39. (a) Hæreid, S.; Anderson, J.; Einarsrud, M. A.; Hua, D. W.; Smith, D. M. Thermal and temporal aging of TMOSbased aerogel precursors in water. *J Non-Cryst Solids* **1995**, *185*, 221–226. (b) Lucas, E. M.; Doescher, M. S.; Ebenstein, D. M.; Wald, K. J.; Rolison, D. R. Silica aerogels with enhanced durability, 30-nm mean pore-size, and improved immersibility in liquids. *J Non-Cryst Solids* **2004**, *350*, 244–252.

40. (a) Katti, A.; Shimpi, N.; Roy, S.; Lu, H.; Fabrizio, E. F.; Dass, A.; Capadona, L. A.; Leventis, N. Chemical, Physical, and Mechanical Characterization of Isocyanate Cross-linked Amine-Modified Silica Aerogels. *Chem. Mater.* **2006**, *18*, 285–296. (b) Meador, M. A.; Capadona, L. A.; McCorkle, L.; Papadopoulos, D. S.; Leventis, N. Structure−Property Relationships in Porous 3D Nanostructures as a Function of Preparation Conditions: Isocyanate Cross-Linked Silica Aerogels. *Chem. Mater.* **2007**, *19*, 2247–2260. (c) Ilhan, U. F.; Fabrizio, E. F.; McCorkle, L.; Scheiman, D. A.; Dass, A.; Palczer, A.; Meador, M. A. B.; Johnston, J. C.; Leventis, N. Hydrophobic Monolithic Aerogels by Nanocasting Polystyrene on Amine-Modified Silica. *J. Mater. Chem.* **2006**, *16*, 3046–3054. (d) Mulik, S.; Sotiriou-Leventis, C.; Churu, G.; Lu, H.; Leventis, N. Cross-Linking 3D Assemblies of Nanoparticles into Mechanically Strong Aerogels by Surface-Initiated Free-Radical Polymerization. *Chem. Mater.* **2008**, *20*, 5035–5046.

41. Meador, M. A. B.; Fabrizzio, E. F.; Ilhan, F.; Dass, A.; Zhang, G.; Vassilaras, P.; Johnston, J. C.; Leventis, N. Cross-linking Amine-Modified Silica Aerogels with Epoxies: Mechanically Strong Lightweight Porous Materials *Chem. Mater.* **2005**, *17*, 1085–1098.

42. Leventis, N.; Sotiriou-Leventis, C.; Chandrasekaran, N.; Mulik, S.; Larimore, Z. J.; Lu, H.; Churu, G.; Mang, J. T. Multifunctional Polyurea Aerogels from Isocyanates and Water. A Structure-Property Case Study *Chem. Mater.* **2010**, *22*, 6692–6710.

43. Husing, N.; Schubert, U.; Mezer, R.; Fratzl, P.; Riegel, B.; Kiefer, W.; Kohler, D.; Mader, W. Formation and Structure of Gel Networks from $Si(OEt)_4/(MeO)_3Si(CH_2)_3NR'_2$ Mixtures ($NR'_2 = NH_2$ or $NHCH_2CH_2NH_2$) *Chem. Mater.* **1999**, *11*, 451–457.

44. Leventis, N.; Chandrasekaran, N.; Sotiriou-Leventis, C.; Mumtaz, A. Smelting in the Age of Nano: Iron Aerogels *J. Mater. Chem.* **2009**, *19*, 63–65.

45. Leventis, N.; Sadekar, A.; Chandrasekaran, N.; Sotiriou-Leventis, C. Click Synthesis of Monolithic Silicon Carbide Aerogels from Polyacrylonitrile-Coated 3D Silica Networks *Chem. Mater.* **2010**, *22*, 2790–2803.

46. Saunders, J. H.; Frisch, K. C. In Polyurethane Chemistry and Technology I. Chemistry, Interscience publishers, New York, NY, USA, 1963, pp 63–118.

47. Bayer, O. Das Di-Isocyanat-Polyadditionsverfahren (Polyurethane). *Angew. Chem.* **1947**, *59*, 257–272.

48. Seymour, R. B.; Kauffman, G. B. Polyurethanes: A Class of Modern Versatile Materials *J. Chem. Educ.* **1992**, *69*, 909–910.

49. (a) Islam, M. R.; Beg, M. D. H.; Jamari, S. S. Development of Vegetable-Oil-Based Polymers, *J. Appl. Polym. Sci.* **2014**, *131*, 40787–40790. (b) Delebecq, E.; Pascault, J.-P.; Boutevin, B.; Ganachaud, F. O. On the Versatility of Urethane/Urea Bonds: Reversibility, Blocked Isocyanate, and Nonisocyanate Polyurethane. *Chem. Rev.* **2012**, *113*, 80–118. (c) Pigott, K.A. Polyurethanes, in Encyclopedia of Polymer Science and Technology, Vol. 11.; John Wiley & Sons, Inc.: New York, NY, 1989; pp 506–563. (d) Hepburn, C. In *Polyurethane Elastomers;* Elsevier Science Publishing Co., Inc.: New York, 1982, p 402.

50. Jarfelt, U.; Ramnas, O. In *10th International Symposium on District Heating and Cooling* **2006**, pp. 1-11.

51. Kistler, S. S. Coherent expanded aerogels *J. Phys. Chem.* **1932**, *63*, 52–64.

52. Tabor, R. Microporous isocyanate-based polymer compositions and method of preparation. US Patent No. 5,478,867, 1995.

53. Biesmans, G.; Randall, D.; Francais, E.; Perrut, M. Polyurethane-based Organic Aerogels' Thermal Performance *J. Non-Cryst. Solids* **1998**, *225*, 36–40.

54. Tan, C.; Fung, B. M.; Newman, J. K.; Vu, C. Organic Aerogels with Very High Impact Strength *Adv. Mater.* **2001**, *13*, 644–646.

55. Chidambareswarapattar, C.; McCarver, P. M.; Luo, H.; Lu, H.; Sotiriou-Leventis, C.; Leventis, N. Fractal Multiscale Nanoporous Polyurethanes: Flexible to Extremely Rigid Aerogels from Multifunctional Small Molecules *Chem. Mater.* **2013**, *25*, 3205−3224.

56. (a) Donthula, S.; Mandal, C.; Leventis, T.; Schisler, J.; Saeed, A. M.; Sotiriou-Leventis, C.; Leventis, N. Shape Memory Superelastic Poly(isocyanurate-urethane) Aerogels (PIR-PUR) for Deployable Panels and Biomimetic Applications *Chem. Mater.* **2017**, *29*, 4461−4477. (b) Donthula, S.; Mandal, C.; Schisler, J.; Leventis, T.; Meador, M. A. B.; Sotiriou-Leventis, C.; Leventis, N. Nanostructure-Dependent Marcus-Type Correlation of the Shape Recovery Rate and the Young's Modulus in Shape Memory Polymer Aerogels *ACS Appl. Mater. Interfaces* **2018**, *10*, 23321−23334.

57. Harada, A. Cyclodextrin-Based Molecular Machines. *Acc. Chem. Res*. **2001**, *34*, 456–464.

58. Potolinca, V. O.; Oprea, S.; Ciobanu, A.; Lungu, N. C. Synthesis and Characterization of Cyclodextrin Polyurethane with Scavenging Properties. *J. Optoelectron. Adv. Mater.* **2011**, 1246–1250.

59. Mizobuchi, A; Tanaka, M; Kawaguchi, Y; Shono, T. Sorption Behavior of Low Molecular Organic Vapors on *β*-Cyclodextrin Polyuretjane Resins. *Bull. Chem. Soc. Jpn*. **1981**, *54*, 2487–2490.

60. Sreenivasan, K. On the Biostability of a Novel *β*-Cyclodextrin Based Hydrophilic Polyurethane. *Polym. Degrad. Stab*. **1996**, *53*, 73–77.

61. Crini, G.; Morcellet, M. Synthesis and Applications of Adsorbents Containing Cyclodextrins. *J. Sep. Sci*. **2002**, *25*, 789–813.

62. Appell, M.; Jackson, M. A. Synthesis and Evaluation of Cyclodextrin-Based Polymers for Patulin Extraction from Aqueous Solutions. *J. Incl. Phenom. Macrocycl. Chem*. **2010**, *68*, 117–122.

63. Yilmaz, E.; Memon, S.; Yilmaz, M. Removal of Direct Azo Dyes and Aromatic Amines from Aqueous Solutions Using Two *β*-Cyclodextrin-Based Polymers. *J. Hazard. Mater*. **2010**, *174*, 592–597.

64. Mirzajani, R.; Pourreza, N.; Najjar, S. S. A. *β*-Cyclodextrin-Based Polyurethane (*β*-CDPU) Polymers as Solid Media for Adsorption and Determination of Pb(II) Ions in Dust and Water Samples. *Res. Chem. Intermed*. **2014**, *40*, 2667–2679.

65. (a) Cao, X. Q.; Vassen, R.; Stoever, D. Ceramic Materials for Thermal Barrier Coatings. *J. Eur. Ceram. Soc.* **2004,** *24*, 1–10. (b) Koebel, M.; Rigacci, A.; Achard, P. Aerogel-based Thermal Superinsulation: An overview. *J. Solgel Sci. Techn.* **2012**, *63*, 315–339. (c) Bheekhun, N.; Abu Talib, A. R.; Hassan, M. R. Aerogels in Aerospace: An Overview. *Adv. Mater. Sci. Eng.* **2013**, 406065. (d) Pierre, A. C.; Pajonk, G. M. Chemistry of Aerogels and their Applications. *Chem. Rev.* **2002**, *102*, 4243–4265. (e) Baetens, R.; Jelle, B. P.; Gustavsen, A. Aerogel Insulation for Building Applications: A State-of-the-art Review. *Energy Build.* **2011**, *43*, 761–769.

66. (a) Zu, G.; Shen, J.; Zou, L.; Wang, W.; Lian, Y.; Zhang, Z.; Du, A. Nanoengineering Super Heat-Resistant, Strong Alumina Aerogels. *Chem. Mater.* **2013**, *25*, 4757–4764. (b)Si, Y.; Yu, J.; Tang, X.; Ge, J.; Ding, B. Ultralight Nanofibre-assembled Cellular Aerogels with Superelasticity and Multifunctionality. *Nat. Commun.* **2014**, *5*, 5802.

67. Geiger, G. Ultra-High Temperature Ceramics: Materials for Extreme Environment Applications, edited by Fahrenholtz, W. G.; Wuchina, E.; Lee, W. E. John Wiley & Sons, Incorporated, 2014.

68. (a) Walker, L. S.; Marotto, V. R.; Rafiee, M. A.; Koratkar, N.; Corral, E. L. Toughening in Graphene Ceramic Composites *ACS Nano* **2011**, *5*, 3182-3190. (b) Bansal, N. P.; Lamon. N. Ceramic Matrix Composites: Materials, Modeling and Technology, John Wiley & Sons, Incorporated, 2014. (c) Bauer, J.; Hengsbach, S.; Tesari, I.; Schwaiger, R.; Kraft, O. High-strength cellular ceramic composites with 3D microarchitecture *Proceedings of the National Academy of Sciences of the United States of America* **2014**, *111*, 2453-2458. (d) Li, X.; Yin, X.; Zhang, L.; Cheng, L.; Qi, Y. Mechanical and Dielectric Properties of Porous Si_3N_4–SiO_2 Composite Ceramics *Materials Science and Engineering A* **2009**, *500*, 63–69.

69. (a) Wang B, Wang Y, Lei Y, Wu N, Gou Y, Han C, et al. Hierarchically Porous SiC Ultrathin Fibers Mat with Enhanced Mass Transport, Amphipathic Property and High_Temperature Erosion Resistance. *J Mater Chem A.* **2014**, *2*, 20873–20881. (b) Wang Y, Han C, Zheng D, Lei Y. Large Scale, Flexible and High Temperature Resistant ZrO_2/SiC Ultrafine Fibers with a Radial Gradient Composition. *J Mater Chem A.* **2014**, *2*, 9607–9612. (c) Sung I-K, Christian , Mitchell M, Kim D-P, Kenis PJA. Tailored Macroporous SiCN and SiC Structures for High_Temperature Fuel Reforming. *Adv Funct Mater.* **2005**, *15*, 1336–1342. (d) Pradeep VS, Ayana DG, Graczyk-Zajac M, Soraru GD, Riedel R. High Rate Capability of SiOC Ceramic Aerogels with Tailored Porosity as Anode Materials for Li Ion Batteries. *Electrochim Acta.* **2015**, *157*, 41–45. (e) Sun H, Zhao KJ. Atomistic Origins of High Capacity and High Structural Stability of Polymer-derived SiOC Anode Materials. *ACS Appl Mater Interfaces.* **2017**, *9*, 35001–35009.

70. Sasikumar PVW, Zera E, Graczyk-Zajac M, Riedel R, Soraru GD. Structural Design of Polymer-derived SiOC Ceramic Aerogels for High-rate Li Ion Storage Applications. *J Am Ceram Soc.* **2016**, *99*, 2977–2983.

71. Zera E, Nickel W, Hao GP, Vanzetti L, Kaskel S, Sorarù GD. Nitrogen Doped Carbide Derived Carbon Aerogels by Chlorine Etching of a SiCN Aerogel. *J Mater Chem A.* **2016**, *4*, 4525–4533.

72. Chu P, Liu HL, Li YJ, Zhang H, Li J. Synthesis of SiC-TiO_2 Hybrid Aerogel via Supercritical Drying Combined PDCs Route. *Ceram Int.* **2016**, *42*, 17053–17058.

73. Assefa D, Zera E, Campostrini R, Soraru GD, Vakifahmetoglu C. Polymer-derived SiOC Aerogel with Hierarchical Porosity through HF Etching. *Ceram Int.* **2016**, *42*, 11805–11809.

74. Nguyen VL, Zera E, Perolo A, Campostrini R, Li W, Sorarù GD. Synthesis and Characterization of Polymer-derived SiCN Aerogel. *J Eur Ceram Soc.* **2015**, *35*, 3295–302.

75. Zera E, Campostrini R, Aravind PR, Blum Y, Soraru GD. Novel SiC/C Aerogels through Pyrolysis of Polycarbosilane Precursors. *Adv Eng Mater.* **2014**, *16*, 814–819.

76. (a) Meng, G. W.; Cui, Z.; Zhang, L. D.; Phillipp, F. J. Growth and Characterization of Nanostructured β-SiC via Carbothermal Reduction of SiO_2 Xerogels Containing Carbon Nanoparticles *Cryst. Growth* **2000**, *209*, 801–806. (b) Klinger, N.; Strauss, E. L.; Komarek, K. L. Reactions between Silica and Graphite *J. Am. Ceram. Soc.* **1966**, *49*, 369–375.

77. Mehner, H. German Patent No. 88999, 1896.

78. (a) Lin, Z.; Xuanhui, Q.; Bohua, D.; Xinbo. H. Progress in Research on Porous Silicon Carbide *J. Powder Metallurgy Technology* **2007**, *25*, 139−144. (b) She, J. H.; Yang, J. F.; Kondo, N.; Ohji, T.; Kanzaki, S.; Deng, Z. Y. High-strength Porous Silicon Carbide Ceramics by an Oxidation Bonding Technique *J. Am. Ceram. Soc.* **2002**, *85*, 2852−2854. (c) Verdenell, I. M.; Paarola, S.; Chassagneux, F.; Letoffe, J. M.; Vincent, H.; Scharff, J. P. J. Sol-gel Preparation and Thermomechanical Properties of Porous $x\mathrm{Al_2O_3}y\mathrm{SiO_2}$ Coatings on SiC Hi-Nicalon Fibres *J. Eur. Ceram. Soc.* **2003**, *23*, 1207−1213. (d) Eom, J. H.; Kim, Y. W.; Song, I. H.; Kim, H. D. Microstructure and Properties of Porous Silicon Carbide Ceramics Fabricated by Carbothermal Reduction and Subsequent Sintering Process *Mater. Sci. and Eng. A* **2007**, *464*, 129−134. (e) Qian, J. M.; Wang, P.; Qiao, G.; Jin, Z. H. Preparation of Porous SiC Ceramic with a Wood like Microstructure by Sol-gel and Carbothermal Reduction Processing *J. Eur. Ceram. Soc.* **2004**, *24*, 3251−3259. (f) Wang, C.; Wang, J.; Park, C. B.; Kim, Y. W. Crosslinking Behavior of a Polysiloxane in Ceramic Foam Processing J. Mater. Sci. **2004**, *39*, 4913−4915. (g) Shi, L. M.; Zhao, H. S.; Yan, Y. H.; Tang, C. H. Fabrication of High Purity Porous SiC Ceramics using Coatmix Process *Mater. Sci. and Eng. A*, **2007**, *460*, 645−647.

79. Zheng, Y.; Zheng, Y.; Lin, L. X.; Ni, J.; Wei, K. M. Synthesis of a Novel Mesoporous Silicon Carbide with a thorn-ball-like Shape *Scr. Mater.* **2006**, *55*, 883−886.

80. Zhao, X. T.; Wang, H. L.; Shang, W.; Chen, J. B.; Xu, H. L.; Lu, H. X.; Chen, D. L.; Fan, B. B.; Zhang, R. Properties and Processing of Porous Si_3N_4 Ceramics. *Key Eng. Mater.* **2014**, *602–603*, 375–379.

81. Burpo, F.; Nagelli, E.; Morris, L.; McClure, J.; Ryu, M.; Palmer, J. Direct Solution Based Reduction Synthesis of Au, Pd, And Pt Aerogels. *J. Mater. Res.* **2017**, *32*, 4153-4165.

82. Liu, W.; Herrmann, A. -K.; Bigall, N. C.; Rodriguez, P.; Wen, D.; Oezaslan, M.; Schmidt, T. J.; Gaponik, N.; Eychmüller, A. Noble Metal Aerogels—Synthesis, Characterization, and Application as Electrocatalysts. *Acc. Chem. Res.* **2015**, *48*, 154−162.

83. (a) Chandrasekaran, N.; and Muthusamy, S. Binderless, Free-Standing Porous Interconnects of Ni–Fe Alloy Decorated Reduced Graphene Oxide for Oxygen Evolution Reaction. *Langmuir* **2017**, *33*, 2−10. (b) Liu, Y.; Gorgutsa, S.; Santato, C.; Skorobogatiy, M. Flexible, Solid Electrolyte based Lithium Battery Composed of $LiFePO_4$ Cathode and $Li_4Ti_5O_{12}$ Anode for Applications in Smart Textiles. *J. Electrochem. Soc.* **2012**, *159*, A349-A356.

84. Leventis, N.; Donthula, S.; Mandal, C.; Ding, M. S.; Sotiriou-Leventis, C. Explosive versus Thermite Behavior in Iron(0) Aerogels Infiltrated with Perchlorates. *Chem. Mater.* **2015**, *27*, 8126–8137.

85. Ng, E.-P.; Mintova, S. Nanoporous Materials with Enhanced Hydrophilicity and High-water Sorption Capacity *Microporous Mesoporous Mater.* **2008**, *114*, 1–26.

86. Liu, L.; Tan, S. J.; Horikawa, T.; Do, D. D.; Nicholson, D.; Liu, J. Water adsorption on carbon - A review. *Adv. Colloid Interface Sci.* **2017**, *250*, 64–78.

87. Iskander, M.; Sadekar, S.; Ge, L. Geotechnical Properties of Silica Gel: in Modelling with Transparent Soils: Visualizing Soil Structure Interaction and Multi Phase Flow, Non-Intrusively; Springer: Science & Business Media, 2010, pp. 85–115.

88. (a) Martin, C. L.; Folkedahl, B. C.; Dunham, D. J.; Kay, J. P. Application of liquid desiccant dehumidification to amine-based carbon capture systems *Int. J. Greenh. Gas Con.* **2016**, *54*, 557–565. (b) Subramanyam, N.; Maiya, M. P.; Murthy, S. S. Application of Desiccant Wheel to Control Humidity in Air-conditioning Systems. *Appl. Therm. Eng.* **2004**, *24*, 2777–2788. (c) Daou, K.; Wang, R. Z.; Xia, Z. Z. Desiccant Cooling Air Conditioning: A Review *Renew. Sust. Energ. Rev.* **2006**, *10*, 55–77. (d) Yildirim, S.; Röcker, B.; Pettersen M. K.; Nilsen-Nygaard, J.; Zehera, A.; Rutkaite, R.; Radusin, T.; Suminska, P.; Marcos, B.; Coma, V. Active Packaging Applications for Food *Compr. Rev. Food Sci. Food Saf.* **2018**, *17*, 165–199. (e) Gaikwad, K. K.; Singh, S.; Ajji, A. Moisture Absorbers for Food Packaging Applications *Environ. Chem. Let.* **2019**, *17*, 609–628. (f) Mbuge, D. O.; Negrini, R.; Nyakundi, L. O.; Kaute, S. P. Application of Superabsorbent Polymers (SAP) as Desiccants to Dry Maize and Reduce Aflatoxin Contamination. *J. Food Sci. Technol.* **2016**, *53*, 3157–3165. (g) Henninger, S. K.; Schmidt, F. P.; Henning, H.-M. A Water Adsorption Characteristics of Novel Materials for Heat Transformation Applications *Appl. Therm. Eng.* **2010**, *30*, 1692–1702.

89. (a) Brennan, J. K.; Bandosz, T. J.; Thomson, K. T.; Gubbins, K. E. Water in porous carbons. *Colloids Surf A: Physicochemical Eng. Aspects* **2001**, *187–188*, 539–568. (b) Furmaniak, S.; Gauden, P. A.; Terzyk, A. P.; Rychlicki, G. Water Adsorption on Carbons--Critical Review of the Most Popular Analytical Approaches. *Adv. Colloid Interface Sci.* **2008**, *137*, 82–143. (c) Slasli, A. M.; Jorge, M.; Stoekli, F. Water Adsorption by Activated Carbons in Relation to their Microporous Structure *Carbon* **2003**, *41*, 479–486. (d) Fastyn, P.; Kornacki, W.; Gierczak, T.; Gawlowski, J.; Niedzielski J. Adsorption of Water Vapor from Humid Air by Selected Carbon Adsorbents *J. Chromatogr. A* **2005**, *1078*, 7–12.

90. (a) Kenyó, C.; Renner, K.; Móczó, J.; Fekete, E.; Kröhnke, C.; Pukánszky, B. Effect of Desiccant Characteristics on the Properties of PS/zeolite Functional Packaging Materials. *Polym. Compos.* **2014**, *35*, 2112–2120. (b) Mudiyanselage, T. K.; Neckers, D. C. Highly Absorbing Super-absorbent Polymer. *J. Polym. Sci. Part A: Polym. Chem.* **2008**, *46*, 1357–1364. (c) Yang, T. Poly(vinyl alcohol)/sulfated β-cyclodextrin for Direct Methanol Fuel Cell Applications. *Int J Hydrogen Energy* **2009**, *34*, 6917–6924. (d)Chen, C.-H.; Hsu, C.-Y.; Chen, C.-C.; Chen, S.-L. Silica Gel Polymer Composite Desiccants for Air Conditioning Systems *Energy Buildings* **2015**, *101*, 122–132. (e) Dai, L.; Yao, Y.; Jiang, F.; Yang, X.; Zhou, X.; Xiong, P. Sorption and Regeneration Performance of Novel Solid Desiccant based on PVA-LiCl Electrospun Nanofibrous Membrane *Polym. Test.* **2017**, *64*, 242–249. (f) Lee, J.; Lee, D.-Y. Sorption Characteristics of a Novel Polymeric Desiccant. *Int J Refrigeration* **2012**, *35*, 1940–1949. (g) Kallenberger, P. A.; Fröba, M. Water Harvesting from Air with a Hygroscopic Salt in a Hydrogel–derived Matrix *Commun. Chem.* **2018**, *1*, 28.

91. (a) Tretiak, C. S.; Abdallah, N. B. Sorption and Desorption Characteristics of a Packed Bed of Clay–$CaCl_2$ Desiccant Particles *Solar Energy* **2009**, *83*, 1861–1870. (b) Mohan, R. P. An Expatiate View of Solid Clay Based Desiccant Mould with Varying Void Fraction on Absorption *Advanced Materials Research* **2014**, *984-985*, 94–99. (c) Bridgeman, C. H.; Buckingham, A. D.; Skipper, N. T.; Payne, M. C. Ab-initio Energy Study of Uncharged 2 : 1 Clays and their Interaction with Water. *Mol. Phys.* **1996**, *89*, 879–888. (d) Delville, A.; Letellier, M. Structure and Dynamics of Simple Liquids in Heterogeneous Condition: An NMR Study of the Clay-water Interface. *Langmuir* **1995**, *11*, 1361–1367.

92. (a) Cao, T.; Lee, H.; Hwang, Y.; Radermacher, R.; Chun, H.-H. Experimental Investigations on Thin Polymer Desiccant Wheel Performance *Int J Refrigeration* **2014**, *44*, 1–11. (b) Du, C.; Yang, H. Synthesis and Characterization of Zeolite 4A-type Desiccant from Kaolin *American Mineralogist* **2010**, *95*, 741-746. (c) Jentys, A.; Warecka, G.; Derewinski, M.; Lercher, J. A. Adsorption of Water on ZSM5 Zeolites *J. Phys. Chem.* **1989**, *93*, 4837-4843. (d) Tatlier, M.; Munza, G.; Henningera, S. K. Relation of Water Adsorption Capacities of Zeolites with their Structural Properties *Microporous and Mesoporous Mater.* **2018**, *264*, 70–75.

93. Yuann, Y.; Zhang, H.; Yang, F.; Zhang, N.; Cao, X. Inorganic Composite Sorbents for Water Vapor Sorption: A Research Progress *Renew. Sust. Energ. Rev.* **2016**, *54*, 761–776.

VITA

Parwani M. Rewatkar graduated from the Institute of Chemical Technology (ICT, formerly U.D.C.T.), Mumbai, India and received her Bachelor of Technology degree in Dyestuff Technology and Intermediates in 2013. She then joined a dyestuff manufacturing industry – Vedant Dyestuff and Intermediates, Mumbai, India as a Research and Development Executive. After working for a year, she moved to Rolla, Missouri, USA in the Fall of 2014 to pursue a Ph.D. degree in Chemistry from Missouri University of Science and Technology (Missouri S&T) in Prof. Chariklia Sotiriou-Leventis' research group. Her work at Missouri S&T involved study of a wide range of light-weight porous materials (aerogels) for targeted applications. From Missouri S&T, Parwani had three papers as a first author in *Chemistry of Materials*, *ACS Applied Sciences and Interfaces*, and *Journal of Sol-gel Science and Technology*. She co-authored five more published papers with other members of the research group and was also a co-inventor of a U.S. patent filed in 2018. She presented her research in numerous ACS meetings. She won the Chemistry Department's Best Teaching Assistant Award in 2018, and Outstanding Graduate Researcher Award in 2019. She received her Doctor of Philosophy in Chemistry from Missouri S&T in July of 2019.